

Université François Rabelais de Tours

Università degli Studi di Padova



École Doctorale « Santé, Sciences et Technologies »  
LMP Laboratoire de Microélectronique de Puissance

Scuola di Dottorato in Ingegneria dell'Informazione  
DEI Dipartimento di Ingegneria dell'Informazione

**THÈSE EN COTUTELLE** présentée par  
**TESI IN COTUTELA** presentata da  
**CO-TUTORED THESIS** submitted by

**Benoît BIDOGLIA**

soutenue le/discussa li/defended on  
2 Décembre/Dicembre/December 2009

pour obtenir les grades de/per conseguire i titoli di/for the award of the degrees of

« **DOCTEUR DE L'UNIVERSITÉ DE TOURS** » et/e / and  
« **DOTTORE DI RICERCA DELL'UNIVERSITÀ DI PADOVA** »

Discipline/Disciplina/Subject:  
Électronique de puissance/Elettronica di potenza/Power electronics

## **FUEL CELL AND POWER CONVERTER SYSTEMS: MODEL AND DESIGN**

### **THÈSE dirigée par/RELATORI DI DOTTORATO/ADVISORS**

Monsieur BUSO Simone                      Professore, Università di Padova, Italy  
Monsieur VENTURA Laurent              Professeur, Université de Tours, France

### **RAPPORTEURS/ESAMINATORI/EXAMINERS**

Monsieur BERTHON Alain                  Professeur, Université de Franche-Comté, France  
Monsieur KÆR Søren Knudsen          Professor, Aalborg Universitet, Denmark

---

### **JURY/COMMISSIONE/COMMITTEE**

Monsieur BERNING Torsten              Assistant professor, Aalborg Universitet, Denmark  
Monsieur BERTHON Alain                  Professeur, Université de Franche-Comté, France  
Monsieur BUSO Simone                      Professore, Università di Padova, Italy  
Monsieur FERRIEUX Jean-Paul          Professeur, Université de Grenoble, France  
Monsieur KÆR Søren Knudsen          Professor, Aalborg Universitet, Denmark  
Monsieur LEQUEU Thierry                Maître de Conférences, Université de Tours, France  
Monsieur SPIAZZI Giorgio                Professore, Università di Padova, Italy  
Monsieur VENTURA Laurent              Professeur, Université de Tours, France

benoit.bidoggia@gmail.com

Last compiled on 11 January, 2010

*To my parents, Liliane and Roberto,  
and to all my friends.*

Tours, December 2, 2009



## RÉSUMÉ

Les piles à combustible sont des dispositifs qui permettent de transformer directement l'énergie chimique potentielle d'un carburant en énergie électrique. Elles sont presque toujours couplées à un convertisseur de puissance et l'ensemble est ici appelé « système à pile à combustible ». Le comportement de ces systèmes, les interactions entre ses composants, ainsi que leurs réponses aux stimulations extérieures ont été analysés, étudiés et mesurés. A cet effet, un système à pile à combustible complet a été modélisé. Des critères de dimensionnement pour cas où ni la pile à combustible ni le convertisseur de puissance sont à priori connus ont été identifiés et un prototype a été dimensionné et réalisé. D'autres aspects corrélatifs intéressants ont également été développés et étudiés, comme le fonctionnement du convertisseur à la limite entre les modes de conduction continu et discontinu, ainsi que son contrôle à fréquence de commutation variable. Des résultats expérimentaux et de simulation pour le système et pour les différentes parties dont il est composé sont présentés.

*Mots clefs.* — Pile à combustible, alimentation à découpage, hacheur élévateur, modèle, fréquence variable.

## RIASSUNTO

Le celle a combustibile sono dei dispositivi in cui l'energia chimica potenziale di un combustibile è direttamente convertita in energia elettrica. Quasi sempre le celle a combustibile sono accoppiate a un convertitore di potenza e l'insieme è qui chiamato « sistema a celle a combustibile ». Il comportamento di questi sistemi, le interazioni tra i diversi componenti, nonché le loro risposte a stimoli esterni sono stati analizzati, studiati e misurati. A tal fine, un sistema completo a celle a combustibile è stato modellizzato. Sono stati identificati dei criteri di dimensionamento per casi in cui né la cella a combustibile, né il convertitore sono noti a priori, e un prototipo è stato dimensionato e realizzato. Altri interessanti aspetti correlati sono stati sviluppati e studiati, come il funzionamento del convertitore di potenza al limite fra modo di conduzione discontinuo e continuo, e il suo controllo a frequenza di commutazione variabile. Risultati sperimentali e di simulazione per il sistema e le diverse parti che lo compongono sono presentati.

*Parole chiave.* — Celle a combustibile, alimentatore a commutazione, boost, modello, frequenza variabile.

## SUMMARY

Fuel cells are devices in which a fuel's chemical potential energy is directly converted into electrical energy. They are almost always coupled to a power converter and the ensemble is here called "fuel cell system." The behaviour of such systems, the interactions between their components, and their responses to external stimulations have been analysed, studied and measured. For this purpose, a complete fuel cell system has been modelled. Sizing criteria for cases where neither the fuel cell nor the power converter are a priori known have been identified, and a prototype has been sized and built. Other interesting correlative aspects have also been developed and studied, like the operation of the power converter on the border between the discontinuous and continuous conduction modes, and its control with a variable switching frequency. Experimental and simulation results for the system and for the different parts that compose it are presented.

*Key words.* — Fuel cell system, switch mode power supply, boost, model, variable frequency.



## ACKNOWLEDGMENTS

I would like to thank the institutions without whose financial support I could not have carried out my PhD, namely the French *Région Centre* for my 3-year PhD scholarship, the *Fondazione Ing. Aldo Gini* of Padova, Italy, for its one-time scholarship, and the *Université Franco-Italienne* for paying my numerous displacements between France and Italy. I also have to thank *Aalborg Universitet* and its Institute for Energy Technology for letting me finish my thesis during my first months in Aalborg, and for the *rundstykker* — bread rolls — offered during the traditional Friday coffee break, too.

I also feel indebted to two companies: Exergy Fuel Cells — formerly Arcotronics Fuel Cells — from Sasso Marconi, Bologna, Italy, and M.C.A. Elettrotecnica from Gardigiano, Venezia, Italy. I am grateful to Exergy Fuel Cells for the enriching scientific and industrial partnership and for the interest in my work that Claudio Lanciotti and Angelo D’Anzi showed. I would like to express my gratitude to M.C.A. Elettrotecnica for all the help, friendship, material support and pizzas I have been given, and particularly to Elisabetta and Armando Secchi, and Samuele Berton.

Special thanks go to the assessment committee for the interest in this thesis and for coming to its defence, and to my advisors, for the suggestions and help they provided me with in these three years, which were not always related to power electronics or engineering. So, thanks to Prof. Jean-Paul Ferrieux from *Université de Grenoble*, France, to Prof. Alain Berthon from *Université de Franche-Comté*, France, to Prof. Søren Knudsen Kær and to Dr. Torsten Berning from *Aalborg Universitet*, Denmark, to Prof. Laurent Ventura and to Dr. Thierry Lequeu from *Université François Rabelais de Tours*, France, and to Prof. Simone Buso and Prof. Giorgio Spiazzi from *Università degli Studi di Padova*, Italy.

When I left Tours in November 2008, I was sad leaving all my colleagues and friends in Tours, whom I hope to visit quite often in the future: Chaw-

ki, Damien, Anne-Zab, Luong-Viêt, Fred, Djamel, Olivier, Sébastien, Loïc, Gaël, Laurent(s), Daniel(s), Jérôme, Adelphe, Malika, Ambroise, Yves, Jean-Charles, Nathalie, Fabien, Antonella, Antoine... I really appreciated the great time we had together.

I cannot forget all the staff of the formerly called *Département de Productique* of the *Ecole Polytechnique de Tours* for the chance and resources I have been given in teaching microcontrollers, and all the staff of the *Département GEII* of the *Institut Universitaire de Tours* for organising all our convivial dinners.

Many thanks also go to all the friends that have been so kind to host me for a while: Clément, Aude and little Anouck in Lyon, Laurence and Gilles in Amiens, Béatrice and Bernard in their beautiful countryside and in *their* Splendid Island,<sup>1</sup> Marie and Florian in Paris, Sandra, Léane, Quentin and Thierry in Tours, and Marcia and Rudy in Tours.

I am also grateful to Joel for our English-themed lunches, to Sarane and *La Bazoche* choir for our musical Mondays, to Annie, Isabelle and all the skaters of the *Club Multi Patinage de Tours* for all the hours spent skating on ice.

I will not forget all the students I have had in these three years: I hope they do not mind if I am not writing all their names here.

I was also sad to leave my colleagues in Padova, whom I wish to thank: Elisabetta, Vladimir, Luisa, Rosapaola, Luca, Renato, Paolo. Many thanks go to Mattia Morandin and Sandro Fasolo for their contribution to the project. Many thanks also go to the technical and administrative staff of the Department of Information Engineering of Padova, Italy — Federico, Sabrina, Enrico, Angela — and to Prof. Paolo Tenti, its former director, for their support.

Wide and sincere hugs to all my Italian friends, who have not forgotten me yet, even if I only appear from time to time: Elisabetta and Samuele, Valentina and Simone, Anna and Marco, Marika and Daniele, Marco and Caterina, Giuseppe and Serena, Luca and Elisa, Tiziana, Francesco, Marco, Luca, Maida, Laura, Pasquale...

I would like to cite my new colleagues in Aalborg, who helped me in my first steps in this new city and with whom I have started playing table football again — after years of inactivity — during our breaks: Erik, Torben, Søren, Vincenzo, Samuel, Mihai, Dezso, Laszlo, Tamas, Peiyuan, Alexandros, Mads, Yash, Ram, Hernan, Anders, Jakob, Rasmus, Simon...

---

<sup>1</sup>The “Île d’Yeu”, of course!



Also, many thanks go to all the international students I met here, who shared their Erasmus experience with me — Marco, Massimo, Fabio, Cata, Andrei, Claudia, Lucille, Jean-Michel, Morris, Umberto, Elif, Weronika, Mirko, Lorenzo, Damiano, Diana, Anna, Giulia, Elisa... — and who organised the best surprise birthday party ever.

Many, many thanks go to Federico Chiariotti, Cecilia Poletto and Marcia Bate for proofreading the manuscript.

I am also extremely grateful to my parents Liliane and Roberto for standing my stubbornness, for taxiing me home from the different airports and for the huge practical help in accomplishing my work. Thanks again for the Saturday and Sunday traditional breakfasts at the *café*, which I particularly miss here in Aalborg.

To everybody, including those I may have forgotten here:

thank you very much!



## CONTENTS

<b>Acknowledgments</b> . . . . .	vii
<b>Abbreviations</b> . . . . .	1
<b>Introduction</b> . . . . .	7
<b>Chapter 1. Context</b> . . . . .	11
1.1. Fuel cells . . . . .	11
1.1.1. Historical information . . . . .	11
1.1.2. Types . . . . .	16
1.1.2.1. Proton Exchange Membrane Fuel Cell (PEMFC) . . . . .	17
1.1.2.2. Direct Methanol Fuel Cell (DMFC) . . . . .	19
1.1.2.3. Direct Ethanol Fuel Cell (DEFC) . . . . .	20
1.1.2.4. Phosphoric Acid Fuel Cell (PAFC) . . . . .	21
1.1.2.5. Alkaline Fuel Cell (AFC) . . . . .	22
1.1.2.6. Solid Oxide Fuel Cell (SOFC) . . . . .	24
1.1.2.7. Molten Carbonate Fuel Cell (MCFC) . . . . .	25
1.1.3. Publications on fuel cells . . . . .	26
1.2. Fuel cell systems . . . . .	27
1.2.1. Automotive applications . . . . .	29
1.2.1.1. Conclusion . . . . .	31
1.2.2. Stationary applications . . . . .	32
1.2.2.1. Conclusion . . . . .	36
1.2.3. Backup applications . . . . .	36

1.2.3.1. Grid connected cases: Diesel (1) versus fuel cell (2) . . . . .	36
1.2.3.2. Grid connected cases: battery (3) versus fuel cell with electrolyser (4) . . . . .	39
1.2.3.3. Stand-alone cases: Diesel (5) versus fuel cell with renewable sources (6) . . . . .	42
1.2.3.4. Stand-alone cases: renewable (7) with battery versus renewable with fuel cell and electrolyser (8) . . . . .	42
1.2.3.5. Conclusion . . . . .	43
1.2.4. Conclusion . . . . .	43
1.3. Power electronics for fuel cell systems . . . . .	44
1.4. Conclusion . . . . .	46
<b>Chapter 2. Sizing procedure . . . . .</b>	<b>55</b>
2.1. Power converter types . . . . .	55
2.1.1. Input current ripple . . . . .	59
2.1.2. Inductance current ripple . . . . .	60
2.1.3. Sizing factor . . . . .	61
2.1.4. Conclusion . . . . .	63
2.2. Sizing and design procedure . . . . .	66
2.2.1. Fuel cell active surface . . . . .	66
2.2.2. Cost of a fuel cell system . . . . .	68
2.2.2.1. Fuel cell stack cost . . . . .	68
2.2.2.2. Power converter cost . . . . .	70
2.2.2.3. Total cost and general considerations . . . . .	72
2.2.2.4. Conclusion . . . . .	73
2.2.3. Voltage matching . . . . .	74
2.2.4. Storage system . . . . .	76
2.3. Conclusion . . . . .	77
<b>Chapter 3. System . . . . .</b>	<b>79</b>
3.1. Introduction . . . . .	80
3.2. Overall system sizing . . . . .	81
3.2.1. Fuel cell sizing . . . . .	82
3.2.2. Power converter sizing . . . . .	86

3.2.2.1. Design specification . . . . .	86
3.2.2.2. Number of phases and efficiency . . . . .	87
3.2.2.3. Frequency modulation . . . . .	87
3.2.2.4. Fuel cell characteristics . . . . .	89
3.2.2.5. Converter design . . . . .	91
3.2.2.6. Average and RMS current computations . . . . .	102
3.2.2.7. Inductor design . . . . .	106
3.2.2.8. Estimation of the power losses . . . . .	108
3.2.3. Control implementation . . . . .	113
3.2.3.1. Current control implementation . . . . .	113
3.2.3.2. Variable frequency control implementa- tion . . . . .	117
3.3. Conclusion . . . . .	119
<b>Chapter 4. System modelling . . . . .</b>	<b>121</b>
4.1. Fuel Cell . . . . .	121
4.1.1. Bibliographical excursus . . . . .	122
4.1.2. Molar rates and current . . . . .	123
4.1.3. Electromotive force . . . . .	124
4.1.4. Voltage drops . . . . .	125
4.1.5. Dynamic effects . . . . .	132
4.1.6. Power density and efficiency . . . . .	133
4.1.7. Water production . . . . .	135
4.1.8. Model description . . . . .	137
4.2. Power converter . . . . .	141
4.2.1. Buck converter . . . . .	142
4.2.2. Boost converter . . . . .	143
4.2.3. Buck-boost converter . . . . .	145
4.2.4. Output capacitor . . . . .	147
4.2.5. Interleaving . . . . .	147
4.3. Controller . . . . .	150
4.4. Conclusion . . . . .	155

<b>Chapter 5. Hardware</b> . . . . .	157
5.1. Prototype . . . . .	158
5.1.1. Fuel cell stack . . . . .	158
5.1.2. Power converter . . . . .	158
5.2. Acquisition system . . . . .	162
5.2.1. Generic implementation of the interface . . . . .	165
5.2.2. Fuel cell single element voltage measurement . . . . .	166
5.2.3. Basic software voltage control . . . . .	167
5.2.4. Conclusion . . . . .	169
5.3. Conclusion . . . . .	171
<b>Chapter 6. Results and discussions</b> . . . . .	175
6.1. Fuel cell stack measurements . . . . .	176
6.1.1. Static characteristic . . . . .	176
6.1.2. Dynamic characteristic . . . . .	177
6.2. Fuel cell stack simulations . . . . .	178
6.2.1. Step response . . . . .	178
6.2.2. Sinusoidal stimuli . . . . .	179
6.3. Power converter measurements . . . . .	181
6.3.1. Constant voltage source test . . . . .	181
6.3.2. Fuel cell emulation test . . . . .	183
6.4. Simulations of the whole system . . . . .	187
6.4.1. Step transients . . . . .	189
6.4.1.1. Fuel cell voltage response . . . . .	190
6.4.1.2. Output voltage response . . . . .	192
6.4.1.3. Switching frequency response . . . . .	194
6.4.1.4. Voltage-current and frequency-power maps . . . . .	196
6.4.2. Sinusoidal transients . . . . .	198
6.5. Experimental results on fuel cell stack prototype . . . . .	201
6.6. Conclusion . . . . .	201
<b>Chapter 7. Conclusion</b> . . . . .	203

<b>Appendix A. Energetics considerations</b> . . . . .	207
A.1. Efficiencies . . . . .	207
A.2. Carbon dioxide emission calculation . . . . .	208
A.3. Primary sources of some country grid systems . . . . .	210
<b>Appendix B. The beginning of electrical lighting</b> . . . . .	211
<b>Appendix C. Statistics on published articles</b> . . . . .	213
<b>Appendix D. Fuel cell equations</b> . . . . .	217
D.1. Molar rates and current . . . . .	217
D.2. Electromotive force . . . . .	218
<b>Appendix E. Control implementation details</b> . . . . .	225
E.1. Current control implementation . . . . .	225
E.2. Output voltage control implementation . . . . .	230
E.3. Conclusion . . . . .	233
<b>Appendix F. Area specific and density variables</b> . . . . .	237
F.1. Area specific resistance . . . . .	237
F.2. Conductance density . . . . .	237
F.3. Capacitance density . . . . .	238
F.4. Area specific inductance . . . . .	238
<b>Appendix G. Step and log functions with continuous derivative</b> . . . . .	239
<b>Appendix H. Converter sizing details</b> . . . . .	243
H.1. Input inductor sizing . . . . .	243
H.2. Core power density interpolation function . . . . .	245
<b>Appendix I. Generic implementation of the input/output interface</b> . . . . .	247
I.1. Digital input interface . . . . .	247
I.2. Digital output interface . . . . .	248
I.3. Analog input interface . . . . .	249

I.4. Analog output interface . . . . .	251
<b>Appendix J. The fuel cell power electronics laboratory . . . . .</b>	<b>253</b>
<b>Appendix K. Result details . . . . .</b>	<b>261</b>
K.1. Fuel cell stack measurements . . . . .	261
K.2. Fuel cell simulations . . . . .	261
K.3. Power converter measurements . . . . .	261
K.4. Simulation of the whole system . . . . .	267
<b>References . . . . .</b>	<b>273</b>



## LIST OF FIGURES

1.1. Temperature ranges for the most common fuel cell (FC) types. The orange ranges represent newer fuel cell types. Acronyms: Proton Exchange Membrane (PEM), Direct Methanol (DM), Direct Ethanol (DE), Low temperature Alkaline (LA), High temperature Direct Methanol (HDM), High temperature Proton Exchange Membrane (HPEM), Phosphoric Acid (PA), Alkaline (A), Molten Carbonate (MC), Planar Solid Oxide (PSO), Tubular Solid Oxide (TSO). These ranges of temperature have been taken from different sources, like [6, 17, 2]. . . . .	17
1.2. Principle structure of a fuel cell. Reactants flowing in the gas channels diffuse through the gas diffusion layers to the catalyst layers, where reactions take place. Anions or cations, depending on the fuel cell type, cross the electrolyte, while electrons follow the external electric circuit. Acronyms: Anode (A), Cathode (C), Membrane Electrode Assembly (MEA). . . . .	18
1.3. Schematic representation of a Proton Exchange Membrane Fuel Cell (PEMFC). Acronyms: Anode (A), Cathode (C), Proton Exchange Membrane (PEM), Dihydrogen ( $H_2$ ), Dioxygen ( $O_2$ ), Water ( $H_2O$ ), Hydrogen ion ( $H^+$ ), Electron ( $e^-$ ). . . . .	18
1.4. Schematic representation of a Direct Methanol Fuel Cell (DMFC). Acronyms: Anode (A), Cathode (C), Proton Exchange Membrane (PEM), Methanol ( $CH_3OH$ ), Dioxygen ( $O_2$ ), Water ( $H_2O$ ), Carbon dioxide ( $CO_2$ ), Hydrogen ion ( $H^+$ ), Electron ( $e^-$ ). . . . .	20
1.5. Schematic representation of a Direct Ethanol Fuel Cell (DEFC). Acronyms: Anode (A), Cathode (C), Proton Exchange Membrane (PEM), Ethanol ( $C_2H_5OH$ ), Dioxygen ( $O_2$ ), Water ( $H_2O$ ), Carbon dioxide ( $CO_2$ ), Hydrogen ion ( $H^+$ ), Electron ( $e^-$ ). . . . .	21

1.6. Schematic representation of a Phosphoric Acid Fuel Cell (PAFC). Acronyms: Anode (A), Cathode (C), Phosphoric acid ( $\text{H}_3\text{PO}_4$ ), Dihydrogen ( $\text{H}_2$ ), Dioxygen ( $\text{O}_2$ ), Water ( $\text{H}_2\text{O}$ ), Hydrogen ion ( $\text{H}^+$ ), Electron ( $\text{e}^-$ ). . . . .	22
1.7. Schematic representation of an Alkaline Fuel Cell (AFC). Acronyms: Anode (A), Cathode (C), Potassium hydroxide (KOH), Dihydrogen ( $\text{H}_2$ ), Dioxygen ( $\text{O}_2$ ), Water ( $\text{H}_2\text{O}$ ), Hydroxyl anion ( $\text{OH}^-$ ), Electron ( $\text{e}^-$ ). . . . .	23
1.8. Schematic representation of a Solid Oxide Fuel Cell (SOFC). Acronyms: Anode (A), Cathode (C), Yttria-Stabilised Zirconia (YSZ), Gadolinium Doped Ceria (GDC), Dihydrogen ( $\text{H}_2$ ), Dioxygen ( $\text{O}_2$ ), Water ( $\text{H}_2\text{O}$ ), Oxide anion ( $\text{O}^{2-}$ ), Electron ( $\text{e}^-$ ). . . . .	24
1.9. Schematic representation of a Molten Carbonate Fuel Cell (MCFC). Acronyms: Anode (A), Cathode (C), Lithium carbonate ( $\text{Li}_2\text{CO}_3$ ), Potassium carbonate ( $\text{K}_2\text{CO}_3$ ), Dihydrogen ( $\text{H}_2$ ), Dioxygen ( $\text{O}_2$ ), Water ( $\text{H}_2\text{O}$ ), Carbon dioxide ( $\text{CO}_2$ ), Carbonate anion ( $\text{CO}_3^{2-}$ ), Electron ( $\text{e}^-$ ). . . . .	26
1.10. Ratio $\pi_1$ of fuel cell related articles over all the articles published by Elsevier, ordered by year $t$ . Search criteria for fuel cell related articles used within the “science direct” site: terms “fuel cell” in “Abstract, Title, Keywords” among “All journals (include article in press)” and “All sciences” as subject. Search criteria for all the articles: terms “*” in “Abstract, Title, Keywords” among “All journals (include article in press)” and “All sciences” as subject.	27
1.11. The four grid connected configurations. (1) and (3) are the traditional configurations, while (2) and (4) are their fuel cell based counterparts. (1) and (2) represent two grid connected fuel fed backup solutions, while (3) and (4) represent two grid connected storage based backup solutions. . . . .	37
1.12. The four stand-alone configurations. (5) and (7) are the traditional configurations, while (6) and (8) are their fuel cell based counterparts. (5) and (6) represent two fuel fed electric generators, while (7) and (8) represent two storage based backup solutions for stand-alone systems. . . . .	38
1.13. Normalised production of $\text{CO}_2$ emissions $\mu$ versus normalised operation time $\tau_{\text{op}}$ , for fuel cell and Diesel systems in four electricity production scenarios: either only from coal, from oil, from natural gas, or from no- $\text{CO}_2$ emitting sources. . . . .	40

1.14. Normalised production of CO <sub>2</sub> emissions $\mu$ versus normalised operation time $\tau_{op}$ , for fuel cell and Diesel systems in three electricity production scenarios: American, French, and Italian. . . . .	40
1.15. Normalised production of CO <sub>2</sub> emissions $\mu$ versus normalised operation time $\tau_{op}$ , for fuel cell-electrolyser and battery systems in three scenarios of electricity production: either only from coal, from oil, or from natural gas. . . . .	41
1.16. Normalised production of CO <sub>2</sub> emissions $\mu$ versus normalised operation time $\tau_{op}$ , for fuel cell-electrolyser and battery systems in three scenarios of electricity production: American, French, and Italian. . . . .	41
1.17. Voltage $v$ and power density $q$ of a single fuel cell typical element versus its current density $j$ . The voltage varies from about 1 V to about 0.5 V when the power goes from zero to its maximum value. . . . .	44
1.18. Ratio $\pi_2$ of fuel cell related articles over all the articles published by the Institute of Electrical and Electronics Engineers (IEEE) society, ordered by year $t$ . Search criteria for fuel cell related articles within the “ieeexplore” site: terms “fuel cell” in “All Fields”. Search criteria for all the articles: terms “e*” in “All Fields”. . .	45
1.19. The different paths through which power flows from oil, coal and natural gas fossil sources to the final user in automotive applications. Different efficiencies and different CO <sub>2</sub> emissions of the overall process depend on the different paths, primary sources and final user solutions. Left side. . . . .	48
1.20. The different paths through which power flows from oil, coal and natural gas fossil sources to the final user in automotive applications. Different efficiencies and different CO <sub>2</sub> emissions of the overall process depend on the different paths, primary sources and final user solutions. Right side. . . . .	49
1.21. The different paths through which power flows from oil, coal and natural gas fossil sources to a fixed user, like a domestic or industrial one. The user can use just electric energy, or can use both electric and thermal energy. In the latter case Combined Heat and Power (CHP) systems will be adopted and the overall efficiency will be higher. Different efficiencies and different CO <sub>2</sub> emissions of the overall process depend on the different paths, primary sources and final user solutions. Left side. . . . .	50

1.22.	The different paths through which power flows from oil, coal and natural gas fossil sources to a fixed user, like a domestic or industrial one. The user can use just electric energy, or can use both electric and thermal energy. In the latter case Combined Heat and Power (CHP) systems will be adopted and the overall efficiency will be higher. Different efficiencies and different CO <sub>2</sub> emissions of the overall process depend on the different paths, primary sources and final user solutions. Right side. . . . .	51
1.23.	The different paths through which power flows from oil, coal and natural gas fossil sources to the final user in backup applications. Different efficiencies and different CO <sub>2</sub> emissions of the overall process depend on the different paths, primary sources and final user solutions. Left side. . . . .	52
1.24.	The different paths through which power flows from oil, coal and natural gas fossil sources to the final user in backup applications. Different efficiencies and different CO <sub>2</sub> emissions of the overall process depend on the different paths, primary sources and final user solutions. Right side. . . . .	53
2.1.	Principle schematics of the buck (a), boost (c) and buck-boost (e) converters, and their control characteristics (b),(d) and (f). $V_i$ is the input voltage, $V_o$ is the output voltage, $\Pi = V_i/V_o$ is the ratio between input and output voltages, $\delta$ is the duty cycle, and $\lambda_o$ is the normalised output current. In the control characteristics, the area on the left of the DCM/CCM limit represents the points in which the converter can operate in Discontinuous Conduction Mode (DCM), while the right area represents the points in which the converter can operate in Continuous Conduction Mode (CCM). . . . .	58
2.2.	Normalised value of the inductance current ripple in a buck converter $\Delta\Lambda_{L,BU}$ , a boost converter $\Delta\Lambda_{L,BO}$ , and a buck-boost converter $\Delta\Lambda_{L,BB}$ versus the transfer ratio $\Pi$ . . . . .	61
2.3.	Global sizing factor $\Gamma$ for buck, boost and buck boost converters, versus (a) the transfer ratio $\Pi$ , (b) the duty cycle $\delta$ . The minimum points for the three topologies are shown. $\kappa_S$ indicates the incidence of the switch sizing factor on the global sizing factor, being $0 \leq \kappa_S \leq 1$ . $\kappa_D = 1 - \kappa_S$ indicates the incidence of the diode sizing factor on the global sizing factor. . . . .	64

- 2.4. Global sizing factor  $\Gamma$  variation for buck, boost and buck boost converters, versus (a) the transfer ratio  $\Pi$ , (b) the duty cycle  $\delta$ , when  $\kappa_S$  varies from 0 to 1.  $\kappa_S$  indicates the incidence of the switch sizing factor on the global sizing factor, being  $0 \leq \kappa_S \leq 1$ .  $\kappa_D = 1 - \kappa_S$  indicates the incidence of the diode sizing factor on the global sizing factor. 65
- 2.5. The static polarisation  $v(j)$  and the power density  $q(j)$  curves for a single fuel cell element in the  $V - J$  and  $Q - J$  plans respectively, where  $J$  stands for a current density,  $V$  a voltage, and  $Q$  a power density. The maximum power density point  $(J_{Q,M}, Q_M)$ , the operating point  $(J_{FC,n}, Q_n)$ , and the technology current limit  $J_{t,M}$  are shown. 67
- 2.6. Cost of a fuel cell stack  $C_{FC}$  as a function of the element surface  $S$  in the plane  $S - C$ , where  $S$  is a surface and  $C$  is a cost. The minimum point  $(S^*, C_{FC}^*)$  is shown. 69
- 2.7. Cost of a fuel cell stack  $C_{FC}$  and of the overall system  $C_T$  as a function of the element surface  $s$ . The minimum points  $*$  and  $**$  are located in  $S^*$  and  $S^{**}$  and their values are  $C_{FC}^*$  and  $C_T^{**}$ . 73
- 2.8. Behaviour of a bundle of  $V - P$  characteristics representing different fuel cell stacks with the same total surface  $S_T$ , but with different element numbers  $N$ , where  $P$  is a power and  $V$  a voltage. The operation power range  $[P_{FC,m} \dots P_{FC,n}]$  and the converter output voltage  $[V_{o,m} \dots V_{o,M}]$  defined by the user define a working area in gray and the two limit curves  $i$  and  $j$ . 75
- 2.9. (a) Electrical energy  $E_e$  that can be obtained by a fuel cell system and (b) mass of gaseous hydrogen stored in a pressurised cylinder system whose total geometrical volume is  $v$ . The standard pressure is 200 bar, but two other hypothetical storing pressures are also plotted. The standard geometrical volume of a 50 L cylinder is 40 L. A cylinder pack is generally composed of 9 cylinders, thus its total geometrical volume is equal to 360 L. 78
- 3.1. Functional diagram of a telecommunication power supply system. The lead-acid batteries of a standard telecommunication power supply could be replaced by fuel cell based modules. Storage elements can be added, if the dynamic performance of the fuel cell solution is inadequate. 80
- 3.2. Voltage  $v$  and power density  $q$  of a single Exergy Fuel Cells fuel cell element versus its current density  $j$ . 82
- 3.3. Fuel cell voltage  $V_{FC}$  versus power  $P_{FC}$  for the fuel cell stack configuration 140/116, where the element surface is  $140 \text{ cm}^2$  and the number of elements is 116. 84

3.4. Fuel cell voltage $V_{FC}$ versus power $P_{FC}$ for the fuel cell stack configuration 278/58, where the element surface is 278 cm <sup>2</sup> and the number of elements is 58. . . . .	84
3.5. Fuel cell voltage $V_{FC}$ versus power $P_{FC}$ for the fuel cell stack configuration 325/50, where the element surface is 325 cm <sup>2</sup> and the number of elements is 50. . . . .	85
3.6. Fuel cell voltage $V_{FC}$ versus power $P_{FC}$ for the fuel cell stack configuration 500/32, where the element surface is 500 cm <sup>2</sup> and the number of elements is 32. . . . .	85
3.7. Conditions imposed on the inductor current in order to ensure the operation of the power converter on the border between CCM and DCM. $V_i$ and $V_o$ are the input and output voltage, $I_{L,a}$ is the inductor average current, $T_{on}$ is switch on-time, $T_s$ is the switching period. . . . .	88
3.8. Minimum voltage $V_{i,m}$ , current $I_{i,m}$ and power $P_{i,m}$ required for the boost operation versus the reference output voltage $V_o$ . . . . .	91
3.9. Switching frequency $f_s$ versus fuel cell current $I_{FC}$ , with the output voltage $V_o$ as a parameter. . . . .	93
3.10. Voltage ratio $\Pi$ versus fuel cell current $I_{FC}$ , with the output voltage $V_o$ as a parameter. . . . .	94
3.11. Average input current $I_{i,a}$ and input current limit $I_{i,l}$ versus fuel cell current $I_{FC}$ , with the output voltage $V_o$ as a parameter. . . . .	94
3.12. Switch $\delta_s$ , diode $\delta_d$ and total $\delta_t$ duty cycles versus fuel cell current $I_{FC}$ , with the output voltage $V_o$ as a parameter. . . . .	96
3.13. Phase input current $i_i$ versus time $t$ , with the output voltage $V_o$ as a parameter. . . . .	97
3.14. Total input current $i_{i,T}$ versus time $t$ , with the output voltage $V_o$ as a parameter. . . . .	97
3.15. Input current ripple $\Delta I_{i,T}$ versus fuel cell current $I_{FC}$ and output voltage $V_o$ for different values of the number of phases $N_p$ . . . . .	98
3.16. Maximum input current ripple $\Delta I_{i,M}$ versus output voltage $V_o$ at nominal fuel cell current $I_{FC,n}$ and $\Delta I_{i,M}$ versus fuel cell current $I_{FC}$ at minimum output voltage $V_{o,m}$ . . . . .	99
3.17. Total output current $i_{o,T}$ versus time $t$ , with the output voltage $V_o$ as a parameter. . . . .	100
3.18. Output current ripple $\Delta I_{o,T}$ versus fuel cell current $I_{FC}$ and output voltage $V_o$ . . . . .	101
3.19. Output capacitance $C_{o,T}$ versus the output voltage $V_o$ . . . . .	102

3.20. Diode average current ratio $I_{d,rms}/I_{d,a}$ and diode average current $I_{d,a}$ versus the fuel cell current $I_{FC}$ , with the output voltage $V_o$ as a parameter. . . . .	104
3.21. Switch average current ratio $I_{s,rms}/I_{s,a}$ and diode average current $I_{s,a}$ versus the fuel cell current $I_{FC}$ , with the output voltage $V_o$ as a parameter. . . . .	104
3.22. Inductor $I_{L,rms}$ and output capacitor $I_{c,rms}$ RMS current versus the fuel cell current $I_{FC}$ , with the output voltage $V_o$ as a parameter. . . . .	106
3.23. Power ratio of the power losses in (a) the inductance $P_L$ , (b) the output capacitor $P_C$ , (c) the switch $P_s$ , (d) the diode $P_d$ over the output base power $P_b = I_{FC} V_{o,n}$ , (e) MOSFET drive and (g) turn off power losses. All the plot are versus fuel cell current $I_{FC}$ . . . . .	109
3.24. Total power losses $P_{l,T}$ and power converter efficiency $\eta_{exp}$ versus the fuel cell current $I_{FC}$ , with the output voltage $V_o$ as a parameter. . . . .	113
3.25. Equivalent model for a fuel cell and power converter system. Acronyms: fuel cell open-circuit voltage $V_{FC}$ , number of converter phases $N_p$ , fuel cell internal equivalent resistance $R_{FC}$ , boost input capacitor $C_i$ . . . . .	114
3.26. Block diagram of the relation between the peak current $I_{L,pk}$ and the input voltage $V_i$ . . . . .	114
3.27. Block diagram of the relation between the input voltage $V_i$ and the on-time $T_{on}$ . . . . .	115
3.28. Block diagram of the power converter control system. Acronym: Microcontroller Unit (MCU), Digital to Analog converter (D/A), Voltage Controller Oscillator (VCO), reference signal ( $m$ ), gate signals ( $g_1 \dots g_6$ ). . . . .	118
4.1. Main blocks that compose a fuel cell system. Acronyms: Fuel Cell (FC), Power Converter (PC), PC input and output voltages ( $v_i$ and $v_o$ ), PC input and output currents ( $i_i$ and $i_o$ ), PC gate signal control ( $g$ ), FC voltage and current ( $v_{FC}$ and $i_{FC}$ ). . . . .	122
4.2. Effect of the bare activation losses for different values of the exchange current density $J_0$ . . . . .	127
4.3. Schematic view of the fuel crossover and internal current effects. . . . .	128
4.4. Zoom of the first part of the polarisation curve of a proton exchange membrane fuel cell, where the effect of the internal current density is most evident. . . . .	128
4.5. Effect of the activation losses, of the ohmic voltage drop and of the internal currents. . . . .	129

4.6. Partial pressure curve shape of the reactant flowing from the gas chamber to the reaction sites. . . . .	130
4.7. The effect of concentration losses and the voltage of a fuel cell with all losses taken into account. . . . .	132
4.8. Typical plots of fuel cell voltage $v$ , power density $q$ and efficiency $\eta$ versus current density $j$ for a low temperature PEM fuel cell. . .	136
4.9. Efficiency plots for a single low temperature PEM fuel cell $\eta_{FC,a}$ and for a fuel cell system $\eta_{FC}$ for different values of the stoichiometric ratio $\lambda$ versus current density $j$ . . . . .	136
4.10. Density power $q$ and water production density $\dot{o}_{H_2O}$ versus current density $j$ for a typical low temperature PEM fuel cell. . . . .	137
4.11. Electrical model of a Proton Exchange Membrane Fuel Cell (PEMFC). . . . .	137
4.12. First block model configuration for the capacitor, activation and diffusion voltage drop loop. The capacitive effect is represented by a derivative block. . . . .	138
4.13. Second block model configuration for the capacitor, activation and diffusion voltage drop loop. The capacitive effect is represented by an integral block. The $j_a$ current density is a function of the activation voltage drop. . . . .	139
4.14. Third block model configuration for the capacitor, activation and diffusion voltage drop loop. The capacitive effect is represented by an integral block. The $j_a$ current density is a function of the diffusion voltage drop. . . . .	139
4.15. Block model of a fuel cell stack after derivation from the electrical equivalent model. . . . .	142
4.16. Main blocks that compose a power converter model, where $v_i$ and $v_o$ are the input and output voltages, $i_i$ and $i_o$ the input and output currents, $g$ the switch command, and $i_2 = i_C + i_o$ while $i_C$ stands for the capacitor current. . . . .	142
4.17. Electric schematic of a buck converter. . . . .	143
4.18. Block model of a buck converter. . . . .	144
4.19. Electric schematic of a boost converter. . . . .	145
4.20. Block model of a boost converter. . . . .	146
4.21. Electric schematic of a buck-boost converter. . . . .	147
4.22. Block model of a buck-boost converter. . . . .	148
4.23. Block model of the output capacitor, valid for buck, boost and buck-boost converters. . . . .	149



4.24.	Block representation of the parallel of more switching cells. . .	149
4.25.	The overall control system, composed of the digital voltage controller and of the analog current controller. Acronyms: inductance currents ( $I_L$ ), input and output voltages ( $V_i$ and $V_o$ ), output current ( $I_o$ ), gate commands ( $g$ ), Digital to Analog converter (DAC). . . . .	150
4.26.	Normalised input current of an interleaved boost (a) and buck (b) converters (black line) and a non-interleaved boost (a) and buck (b) converters (dashed line), with the same average value and operating in CCM. The current of the different phases of the interleaved converter are plotted in gray and shown as a reference. .	151
4.27.	(a) The overall voltage digital controller, composed of the voltage control and of the frequency adjustment blocks. Acronyms: input and output voltages ( $V_i$ and $V_o$ ), output current ( $I_o$ ), master frequency ( $f_{mas}$ ), inductance current reference ( $I_{ref}$ ). (b) The frequency adjustment block. Acronyms: input and output voltages ( $V_i$ and $V_o$ ), master frequency ( $f_{mas}$ ). . . . .	152
4.28.	The digital PI voltage controller. Acronyms: output voltage and current ( $V_o$ and $I_o$ ), output voltage reference ( $V_{o,ref}$ ), inductance current reference ( $I_{ref}$ ). . . . .	153
4.29.	The analog PI current control. Acronyms: inductance current ( $I_L$ ), inductance current reference ( $I_{ref}$ ), reference signal ( $m$ ). . . . .	153
4.30.	The modulator block. Acronyms: clock signal (Clk), voltage modulator reference value ( $V_{ref,mod}$ ), gate command ( $g$ ). . . . .	153
4.31.	The overall current controller, composed by six independent modulator and current control blocks, fed by a clock generator and the six current transducers. Acronyms: inductance currents ( $I_L$ ), inductance current reference ( $I_{ref}$ ), master frequency ( $f_{mas}$ ), clock signal (Clk), reference signal ( $m$ ), gate commands ( $g$ ). . . .	154
5.1.	Detail of the fuel cell stack before installing it. The gas inlets with their pressure regulators and the solenoid valves are on the left of the stack. The electrical terminals are located on the top (negative) and on the bottom (positive) of the stack. The black pipes carry the coolant (demineralised water). . . . .	159
5.2.	The fuel cell stack with the coolant tank, pump and radiator. On the right of the stack, there are the two outlet valves. . . . .	159
5.3.	A detail of the fuel cell stack, showing 51 wires used to acquire and measure the 50 differential voltages of every single element. . . .	160

- 5.4. The fuel cell stack after installation. The inlet valves are connected to the hydrogen and oxygen systems with two flowmeters in series. The outlet valves are connected to two pipes that carry the gasses outside. The radiator has been oversized and put under the table. A 100 k $\Omega$  resistance is always connected in parallel to the stack, in order to avoid to keep it in an open circuit state. . . . . 160
- 5.5. The boost prototype with its input bars on the rear side and its output bars on the front side. The six modules are visible, each with its input and output capacitors, its inductance, its current sensor and its current control board. . . . . 161
- 5.6. A detail of one of the six modules. The MOSFET and the diode are located under the main board, in contact with the aluminium heat sink. . . . . 161
- 5.7. The control boards. The board on the left provides the logic required to dispatch the clock and the current reference signals to the modules. On the right side is the DSP board, which will implement the voltage and frequency control loops. At the present time, it is only used to prevent the output voltage rises above the maximum acceptable value. . . . . 162
- 5.8. General diagram of the system: the fuel cell stack (FC) and the power converter are interfaced to a dSPACE board, which is programmed with Simulink and accessed via a Graphical User Interface (GUI). . . . . 163
- 5.9. General diagram of the fuel cell system. Acronyms: manual pressure regulator (MPR), hydrogen and oxygen Mass flow meter (MH2 and MO2), input and output solenoid Valves (EVI and EVO), hydrogen and oxygen temperature ( $T_{H_2}$ ,  $T_{O_2}$ ), hydrogen and oxygen pressures ( $P_{H_2}$ ,  $P_{O_2}$ ), water heat exchanger (ECW), water pump (PCW), water temperature ( $T_1$ ,  $T_2$ ,  $T_3$ ). . . . . 163
- 5.10. Diagram of the input stage of the DS1104 dSPACE acquisition interface. ADCH<sub>1</sub> ... ADCH<sub>8</sub> are analog inputs. ADCH<sub>1</sub> ... ADCH<sub>4</sub> are internally multiplexed. IO<sub>0</sub> ... IO<sub>19</sub> are digital input/output lines. . . . . 164
- 5.11. Connections of the differential voltages of the fuel cell elements ( $E_0$  ...  $E_{8n+7}$ ), with their separated grounds (GND<sub>0</sub> ... GND<sub>n</sub>). . . . 166
- 5.12. Fuel cell element differential voltage module. The left and right sides of the module are referred to different grounds. Acronyms: positive voltage ( $V_P$ ), negative voltage ( $V_N$ ), differential voltage ( $V_D$ ), optocoupling stage input voltage ( $V_{IN}$ ), optocoupling stage output voltage ( $V_{O_2}$ ), module output voltage ( $V_O$ ). . . . . 167

5.13.	Block diagram of the DEMUX element. Acronyms: own address (OAD), address lines (ADD), clock line (CLK), input multiplexed voltage ( $V_{IN}$ ), output demultiplexed voltage ( $V_O$ ), lower voltage limit ( $V_{min}$ ), single voltage enable (VOK), sample and hold element (S&H). . . . .	167
5.14.	Representation of the multiplexer board for the acquisition of the fuel cell element voltages, with its eight signal modules, its analog multiplexer and its isolated power supply. . . . .	168
5.15.	Representation of the entire system for the acquisition of the fuel cell element voltages, with the multiplexer boards, controlled by the microcontroller boards. Each microcontroller controls two multiplexer boards. . . . .	168
5.16.	Block diagram of the software voltage demultiplexer and control. Acronyms: control lines (CTR), address lines (ADD), clock line (CLK), select line (SE), input line (IN), analog line (AN), fire line (F), single voltage enable (VOK), global voltage enable (OK), analog input channel (ADCH). . . . .	169
5.17.	Block diagram of ADDRESS GENERATOR element. Acronyms: address lines (ADD), clock line (CLK), select line (SE), input line (IN), analog line (AN), fire line (F), up counter (UP CNT), extraction of bit $x$ (BIT $x$ ), pulse generator (PGEN). . . . .	169
5.18.	Time diagram of the selection of an analog channel. Acronyms: counter (CNT), extraction of bit $x$ (CNT ( $x$ )), pulse generator (PGEN), fire signal (FIRE), sample and hold (S&H) action. . . .	170
5.19.	Picture of one of the racks for the acquisition of up to 64 fuel cell element voltages. From left to right: the first board is the microcontroller board, the other eight ones are the multiplexer boards. The LEDs on the front display the power supplies and the signal selection. . . . .	172
5.20.	Detail of one the signal modules of the multiplexer board. . . .	172
5.21.	Picture of one of the multiplexer boards. From left to right: the analog multiplexer module, the eight signal modules, and the LED module. . . . .	173
5.22.	Detail of the bottom of the rack with the isolated power supplies. . . . .	173
6.1.	Fuel cell stack current $I_{FC}$ , voltage $V_{FC}$ and power $P_{FC}$ for a 325 cm <sup>2</sup> 50 element stack. . . . .	177

6.2. Simulated and experimental voltage fuel cell stack response to a 0 A–300 A current step, and relative error between the simulated and the experimental data. Fuel cell stack: 325 cm <sup>2</sup> , 20 elements. The boxes represent the absolute errors: $\Xi_v = 0.1$ V, $\Xi_t = 1$ ms. . . .	179
6.3. Voltage fuel cell stack response to a sinusoidal current injection, for different frequencies. Fuel cell stack: 325 cm <sup>2</sup> , 50 elements. . .	180
6.4. Power fuel cell stack response to a sinusoidal current injection, for different frequencies. Fuel cell stack: 325 cm <sup>2</sup> , 50 elements. . . . .	180
6.5. Plots of the 6 boost input currents acquired with a digital oscilloscope, under the condition of input power $P_i = 10$ kW. . . . .	182
6.6. Plots of 2 of the 6 boost input currents, of the input voltage and of the total input current acquired with a digital oscilloscope, under the condition of input power $P_i = 10$ kW. . . . .	182
6.7. Electric diagram of the connection during the fuel cell emulation test. Acronyms: Adjustable Power Supply (APS), Active Load (AL). . . . .	184
6.8. Analytical fuel cell stack voltage $V_{FC}$ and experimental converter input voltage $V_i$ versus fuel cell stack current and converter input current $I_{FC} = I_i$ working points of the tested power converter, for three different values of the output voltage reference $V_o$ : $V_{o,m} = 42$ V, $V_{o,n} = 48$ V and $V_{o,M} = 60$ V. The relative error $\varepsilon$ between $V_{FC}$ and $V_i$ is indicated. . . . .	185
6.9. Analytical fuel cell stack power $P_{FC}$ and experimental converter input power $P_i$ versus fuel cell stack current and converter input current $I_{FC} = I_i$ working points of the tested power converter, for three different values of the output voltage reference $V_o$ : $V_{o,m} = 42$ V, $V_{o,n} = 48$ V and $V_{o,M} = 60$ V. The relative error $\varepsilon$ between $P_{FC}$ and $P_i$ is indicated. . . . .	185
6.10. Experimental converter efficiency $\eta$ versus converter output power $P_o$ , for three different values of the output voltage reference $V_o$ : $V_{o,m} = 42$ V, $V_{o,n} = 48$ V and $V_{o,M} = 60$ V. Dashed curves represent the upper and lower limits of the error bars. . . . .	186
6.11. The four different transient types used to test the whole system. $P_1$ and $P_2$ represent the lower and higher power limits respectively, $t_1$ and $t_2$ the beginning and end instants of the ramp transient, and $T = 1/f$ the period of the sinusoidal stimulus. (a) Ramp transients. (b) Sinusoidal transients. . . . .	187

6.12. Hypothesis on the power variation ramp for a standard 3 kW rectifier for telecommunication applications, compared to the grid voltage phases. . . . .	190
6.13. Fuel cell voltage responses to different ramp transients on the output power for three different values of the output voltage reference: $V_{o,m}$ , $V_{o,n}$ and $V_{o,M}$ . Fuel cell stack: 325 cm <sup>2</sup> , 50 elements. . . . .	191
6.14. System output voltage responses to different ramp transients on the output power for three different values of the output voltage reference: $V_{o,m}$ , $V_{o,n}$ and $V_{o,M}$ . Fuel cell stack: 325 cm <sup>2</sup> , 50 elements. . . . .	193
6.15. Power converter switching frequency responses to different ramp transients on the output power for three different values of the output voltage reference: $V_{o,m}$ , $V_{o,n}$ and $V_{o,M}$ . Fuel cell stack: 325 cm <sup>2</sup> , 50 elements. . . . .	195
6.16. Fuel cell voltage versus current maps (left column) and power converter switching frequency versus output power maps (right column) under different ramp transients on the output power for three different values of the output voltage reference: $V_{o,m}$ , $V_{o,n}$ and $V_{o,M}$ . Fuel cell stack: 325 cm <sup>2</sup> , 50 elements. . . . .	197
6.17. Fuel cell voltage responses to sinusoidal transients on the output power for three different values of the output voltage reference: $V_{o,m}$ , $V_{o,n}$ and $V_{o,M}$ . Fuel cell stack: 325 cm <sup>2</sup> , 50 elements. . . . .	199
6.18. System output voltage responses (a) and (b), power converter switching frequency responses (c) and (d), fuel cell voltage versus current map (e) and power converter switching frequency versus output power map (f) under sinusoidal transients on the output power for three different values of the output voltage reference: $V_{o,m}$ , $V_{o,n}$ and $V_{o,M}$ . Fuel cell stack: 325 cm <sup>2</sup> , 50 elements. . . . .	200
E.1. Small signal equivalent circuit for the boost converter operating in Discontinuous Conduction Mode (DCM). . . . .	225
E.2. Fuel cell equivalent resistance $R_{FC}$ versus fuel cell current $I_{FC}$ . . . . .	227
E.3. Simplified schematic of the constant on-time modulator. Acronym: input signal $m$ , reference voltage $V_{ref}$ . . . . .	228
E.4. Constant on-time modulator basic operation signals versus time $t$ . Acronym: input signal $m$ , integrator output voltage $v_{int}$ , switching period $T_s$ . . . . .	228
E.5. Overview of the control organisation. The current reference is provided by an outer digital voltage controller through a D/A converter. The phase current controller is made up of an analog PI compensator and a constant on-time modulator. . . . .	231

E.6. Small signal equivalent circuit for the current controller boost converter. . . . .	232
E.7. Design of the current controller. Bode diagrams of the converter transfer function $G_{ID}(s)$ , open loop current gain, closed loop current gain. . . . .	235
E.8. Design of the voltage controller. Bode diagrams of the converter transfer function $G_{VI}(s)$ , open loop voltage gain, closed loop voltage gain. . . . .	235
G.1. Approximation of a step function using continuous functions, with different values of the parameter $k$ . . . . .	241
G.2. Approximation of square waves using continuous functions. . . .	241
I.1. Diagram of the generic digital input interface. Acronyms: digital inputs ( $I_0 \dots I_7$ ), bus input lines ( $DI_0 \dots DI_3$ ), address lines ( $A_0 \dots A_7$ ), control lines (SE, IN, AN, F), enable signal (EN), clock signal (CK). . .	247
I.2. Time diagram of the transmission towards a digital input interface. Acronyms: most/less significant (MS/LS), bus input lines ( $DI_0 \dots DI_3$ ), address lines ( $A_0 \dots A_7$ ), MS/LS selection line (SE), input selection line (IN), analog selection line (AN), fire line (F). . . . .	248
I.3. Diagram of the generic digital output interface. Acronyms: digital outputs ( $O_0 \dots O_7$ ), bus output lines ( $DO_0 \dots DO_3$ ), address lines ( $A_0 \dots A_7$ ), control lines (SE, IN, AN, F), clock signal (CK). . . . .	249
I.4. Time diagram of the transmission towards a digital output interface. Acronyms: most/less significant (MS/LS), bus output lines ( $DO_0 \dots DO_3$ ), address lines ( $A_0 \dots A_7$ ), MS/LS selection line (SE), input selection line (IN), analog selection line (AN), fire line (F). . . .	249
I.5. Diagram of the generic analog input interface. Acronyms: analog inputs ( $AI_0 \dots AI_7$ ), analog input channels ( $ADCH_1 \dots ADCH_4$ ), address lines ( $A_0 \dots A_7$ ), control lines (SE, IN, AN, F), clock signal (CK). . . . .	250
I.6. Time diagram of the selection (a) and deselection (b) of an analog input channel. Acronyms: address lines ( $A_0 \dots A_7$ ), MS/LS selection line (SE), input selection line (IN), analog selection line (AN), fire line (F). . . . .	250
I.7. Diagram of the generic analog output interface. Acronyms: analog outputs ( $AO_0 \dots AO_7$ ), analog output channels ( $DACH_1 \dots DACH_4$ ), address lines ( $A_0 \dots A_7$ ), control lines (SE, IN, AN, F), clock signal (CK). . . . .	251

I.8. Time diagram of the selection (a) and deselection (b) of an analog output channel. Acronyms: address lines ( $A_0 \dots A_7$ ), MS/LS selection line (SE), input selection line (IN), analog selection line (AN), fire line (F). . . . .	252
J.1. The container in the courtyard of the Department of Information Engineering (DEI) of the University of Padova. Its surface is equal to $9.6 \text{ m}^2$ . It is connected to the department electrical grid ( $P_{e,M} = 20 \text{ kW}$ ) and to the department Local Area Network (LAN). . . . .	253
J.2. The table on the right is for the computerised controller system. The table on the left is for the fuel cell stack being tested. . . . .	254
J.3. The table on the right is for the fuel cell stack under test. The table on the left is for the power electronics converter connected to the fuel cell stack. . . . .	254
J.4. The table on the left is for the power electronics converter connected to the fuel cell stack. The table on the right is for the fuel cell stack begin tested. . . . .	255
J.5. The gas safety system. On the left are the hydrogen and oxygen concentration measurement units. On the right is the panel with all the safety controls (green lights). The gas solenoid valves (red lights) are open only if all the safety controls are passed. . . . .	255
J.6. Main electric panel. . . . .	256
J.7. Hydrogen concentration sensor. . . . .	257
J.8. Hydrogen and oxygen concentration measurement units. . . . .	257
J.9. Fuel cell stack and fittings before installation. . . . .	258
J.10. High and medium pressure hydrogen fittings. . . . .	258
J.11. Oxygen and hydrogen cylinder cabinets. The cylinder in use must have the yellow label " <i>Bombola in uso</i> " ("Cylinder in use"). The new cylinder must have the yellow label " <i>Bombola carica</i> " ("Full cylinder"). Empty cylinders must have the red label " <i>Bombola scarica</i> " ("Empty cylinder"). . . . .	259
J.12. Safety signs inside and on the door of the laboratory. . . . .	259
K.1. Fuel cell stack current $I_{FC}$ , voltage $V_{FC}$ and power $P_{FC}$ on a $325 \text{ cm}^2$ 20 element stack. (a) Data, (b) Plot. Average temperature of the stack: $44 \text{ }^\circ\text{C}$ . The boxes represent the absolute errors. . . . .	263
K.2. Voltage fuel cell stack response to a $0 \text{ A}$ – $300 \text{ A}$ current step. Experimental data ( $v_{FC}$ ). Fuel cell stack: $325 \text{ cm}^2$ , 20 elements. The boxes represent the absolute errors: $\Xi_v = 0.1 \text{ V}$ , $\Xi_t = 1 \text{ ms}$ . . . . .	263

K.3. Voltage fuel cell stack response to a sinusoidal current injection, whose parameters are: amplitude 150 A, offset 150 A, frequency: (a) 0.1 Hz, (b) 1 Hz, (c) 10 Hz, (d) 100 Hz, (e) 1 kHz, (f) 10 kHz. Results from Matlab/Simulink simulation. Fuel cell stack: 325 cm <sup>2</sup> , 50 elements. . . . .	264
K.4. Plots of the 6 boost input currents acquired with a digital oscilloscope, on condition of input power $P_i = 5$ kW. . . . .	265
K.5. Plots of the 6 boost input currents acquired with a digital oscilloscope, on condition of input power $P_i = 3$ kW. . . . .	265
K.6. Experimental converter efficiency $\eta$ versus converter output power $P_o$ , for output voltage (a) $V_{o,m} = 42$ V, (b) $V_{o,m} = 48$ V, (c) $V_{o,m} = 60$ V. Error bars are indicated. . . . .	268
K.7. Output conductance of the system for the different ramp transients for three different values of the output voltage reference: $V_{o,m}$ , $V_{o,n}$ and $V_{o,M}$ . Fuel cell stack: 325 cm <sup>2</sup> , 50 elements. . . . .	269
K.8. Output conductance (a), (b) of the system for the 4 Hz sinusoidal transient tests. Output conductance (c), (d) of the system and fuel cell voltage responses (e), (f) for the 10 Hz sinusoidal transient tests. For three different values of the output voltage reference: $V_{o,m}$ , $V_{o,n}$ and $V_{o,M}$ . Fuel cell stack: 325 cm <sup>2</sup> , 50 elements. . . . .	270
K.9. System output voltage responses (a) and (b), power converter switching frequency responses (c) and (d), fuel cell voltage versus current map (e) and power converter switching frequency versus output power map (f) for the 10 Hz sinusoidal transient tests. For three different values of the output voltage reference: $V_{o,m}$ , $V_{o,n}$ and $V_{o,M}$ . Fuel cell stack: 325 cm <sup>2</sup> , 50 elements. . . . .	271



## LIST OF TABLES

1.1. Efficiencies from the primary fossil energy sources to the final user for automotive applications. Acronyms: Internal Combustion Engine (ICE), Fuel Cell (FC), Battery (BAT), Diesel (D), Gasoline (B), Natural gas (N), Methanol (M), Gaseous Hydrogen (GH), Liquid Hydrogen (LH), hydrogen by Reforming (R), hydrogen by Electrolysis (E). . . . .	31
1.2. Normalised CO <sub>2</sub> production from different fossil sources. Acronyms: Internal Combustion Engine (ICE), Fuel Cell (FC), Battery (BAT), Diesel (D), Gasoline (B), Natural gas (N), Gaseous Hydrogen (GH), Liquid Hydrogen (LH), hydrogen by Reforming (R), hydrogen by Electrolysis (E). . . . .	32
1.3. Efficiencies from the primary fossil energy sources to the final user for stationary applications, without Combined Heat and Power systems. Acronyms: Internal Combustion Engine (ICE), Fuel Cell (FC), Grid (GR), Diesel (D), Gasoline (B), Natural gas (N), Methanol (M), Gaseous Hydrogen (GH), Liquid Hydrogen (LH), hydrogen by Reforming (R), hydrogen by Electrolysis (E). . . . .	34
1.4. Efficiencies from the primary fossil energy sources to the final user for stationary applications, with Combined Heat and Power systems. Acronyms: Internal Combustion Engine (ICE), Fuel Cell (FC), Grid (GR), Diesel (D), Gasoline (B), Natural gas (N), Methanol (M), Gaseous Hydrogen (GH), Liquid Hydrogen (LH), hydrogen by Reforming (R), hydrogen by Electrolysis (E). . . . .	34
1.5. Normalised CO <sub>2</sub> production from different fossil sources without Combined Heat and Power systems. Acronyms: Internal Combustion Engine (ICE), Fuel Cell (FC), Grid (GR), Diesel (D), Gasoline (B), Natural gas (N), Methanol (M), Gaseous Hydrogen (GH), Liquid Hydrogen (LH), hydrogen by Reforming (R), hydrogen by Electrolysis (E). . . . .	35

1.6. Normalised CO <sub>2</sub> production from different fossil sources with Combined Heat and Power systems. Acronyms: Internal Combustion Engine (ICE), Fuel Cell (FC), Grid (GR), Diesel (D), Gasoline (B), Natural gas (N), Methanol (M), Gaseous Hydrogen (GH), Liquid Hydrogen (LH), hydrogen by Reforming (R), hydrogen by Electrolysis (E). . . . .	35
1.7. Summary of the main actors and events in the fuel cell history, where the most significant ones have been highlighted. Acronyms: Gaseous Voltaic Battery (GVB), Direct Coal Fuel Cell (DCFC), Solid Oxide Fuel Cell (SOFC), Molten Carbonate Fuel Cell (MCFC), Alkaline Fuel Cell (AFC), Phosphoric Acid Fuel Cell (PAFC), Direct Methanol Fuel Cell (DMFC), Proton Exchange Membrane Fuel Cell (PEMFC), National Fuel Cell Center Research (NFCR), Southern California (SCA). . . . .	47
3.1. Main values of the power converter when the phase number $N_p$ varies, calculated at nominal conditions. Acronyms: input inductance $L_n$ , output capacitor power losses $P_C$ , input inductance power losses $P_L$ , switch and diode power losses $P_{SD}$ , switch drive power losses $P_{drv}$ , off power losses $P_{off}$ , total power losses $P_{i,T}$ , power converter efficiency $\eta_{PC}$ , improvement in power converter efficiency $\Delta\eta_{PC}$ , inductance maximum current ripple $\Delta I_{i,T}$ , output capacitor $C_o$ , diode average current $I_{d,a}$ , diode RMS current $I_{d,rms}$ , switch average current $I_{s,a}$ , switch RMS current $I_{s,rms}$ , inductor peak current $I_{i,pk}$ . . . . .	88
5.1. Table of the correspondences between the digital input/output lines of the dSPACE board and the lines of the designed bus. . .	165
A.1. Distribution of the energy produced in Italy, France and USA across the different energy sources. . . . .	210
C.1. Data about articles concerning fuel cells published by Elsevier. .	214
C.2. Data about articles concerning fuel cells published by the IEEE. .	215
K.1. Fuel cell stack current $I_{FC}$ , voltage $V_{FC}$ and power $P_{FC}$ on a 325 cm <sup>2</sup> 20 element stack. (a) Data, (b) Plot. Average temperature of the stack: 44 °C. The boxes represent the absolute errors. . . . .	262
K.2. Data related to the low frequency ripple of the total input current, where $P_i$ is the input power, $\Delta I_{i,T}$ is the total input current ripple, $f_i$ is the low frequency of the ripple, $f_s$ is the switching frequency for every phase, and $f_t$ is the total apparent switching frequency. . .	262

K.3. Converter input voltage $V_i$ , input current $I_i$ , output power $P_o$ and efficiency $\eta_{PC}$ , with their respective absolute errors $\Xi_{V,i}$ , $\Xi_{I,i}$ , $\Xi_{P,o}$ , $\Xi_{\eta,PC}$ , and relative errors $\varepsilon_{V,i}$ , $\varepsilon_{I,i}$ , $\varepsilon_{P,o}$ , $\varepsilon_{\eta,PC}$ . Voltage output reference $V_o = 42$ V. . . . .	266
K.4. Converter input voltage $V_i$ , input current $I_i$ , output power $P_o$ and efficiency $\eta_{PC}$ , with their respective absolute errors $\Xi_{V,i}$ , $\Xi_{I,i}$ , $\Xi_{P,o}$ , $\Xi_{\eta,PC}$ , and relative errors $\varepsilon_{V,i}$ , $\varepsilon_{I,i}$ , $\varepsilon_{P,o}$ , $\varepsilon_{\eta,PC}$ . Voltage output reference $V_o = 48$ V. . . . .	266
K.5. Converter input voltage $V_i$ , input current $I_i$ , output power $P_o$ and efficiency $\eta_{PC}$ , with their respective absolute errors $\Xi_{V,i}$ , $\Xi_{I,i}$ , $\Xi_{P,o}$ , $\Xi_{\eta,PC}$ , and relative errors $\varepsilon_{V,i}$ , $\varepsilon_{I,i}$ , $\varepsilon_{P,o}$ , $\varepsilon_{\eta,PC}$ . Voltage output reference $V_o = 60$ V. . . . .	267



## ABBREVIATIONS

The symbols and letters used for physical quantities will be detailed in the following. As a general rule:

- Roman letters are generally used to indicate dimension quantities, while Greek letters are generally used to indicate dimensionless quantities;
- uppercase letters generally indicate time independent variables (constants), while lowercase letters generally indicate time dependent variables.

The derivative operation is often indicated with a dot on the variable ( $\frac{dx}{dt} = \dot{x}$ ). Measurement units generally comply with the *Système international* (SI), with some exceptions:

- [L] has also been used to indicate volumes;
- [A/cm<sup>2</sup>] has also been used to indicate current densities;
- [bar] has also been used to indicate pressures;
- [°C] has also been used to indicate temperatures;
- [a] has also been used to indicate time (year).

The indices M, n and m indicate maximum, nominal and minimum values respectively.

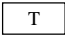
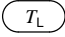
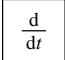


### Physical quantities

Symbol	Unit	Description
$\gamma$	–	Molar concentration
$\Gamma$	–	Sizing factor
$\delta$	–	Duty cycle
$\eta$	–	Efficiency
$\Xi_{\eta}$	–	Efficiency absolute error
$\varepsilon_{\eta}$	–	Efficiency relative error
$\kappa$	–	Coefficient
$\lambda$	–	Stoichiometry ratio
$\mu$	–	Normalised mass
$\mu_0$	$H/m$	Free space permeability
$\mu_e$	–	Relative permeability
$\Pi$	–	Voltage ratio
$\rho$	$\Omega \cdot m$	Resistivity
$\tau$	–	Normalised time
$\tau$	s	Time constant
$\omega$	$rad/s$	Angular frequency
$\mathfrak{R}$	H	Reluctance
$a$	–	Chemical activity
$A$	$m^2$	Area
$A$	V	Tafel constant
$B$	T	Magnetic field
$B$	V	Diffusion constant
$\bar{c}$	$J/mol \cdot K$	Molar specific heat capacity
$c$	$\text{€}/m^2$	Variable cost
$C$	€	Fixed cost
$C$	F	Capacitance

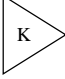
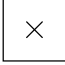
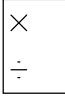
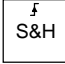
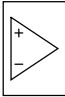
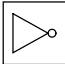
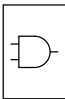
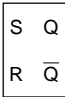

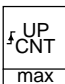
$e, E$	V	Electromotive force, element voltage.
$\Delta e$	V	Variation in electromotive force
$E$	J	Energy
$f$	Hz	Frequency
$g$	S	Conductance
$g$	J	Gibbs free energy
$\bar{g}$	$\text{J}/\text{mol}$	Molar Gibbs free energy
$\Delta\bar{g}$	$\text{J}/\text{mol}$	Variation in molar Gibbs free energy
$h$	J	Enthalpy
$\bar{h}$	$\text{J}/\text{mol}$	Molar enthalpy
$i, I$	A	Current
$\Delta I$	A	Current variation, current ripple
$\Xi_I$	A	Current absolute error
$\varepsilon_i$	A	Current relative error
$j, J$	$\text{A}/\text{m}^2$	Current density
$l$	m	Length
$L$	H	Inductance
$m$	kg	Mass
$\dot{m}$	$\text{kg}/\text{s}$	Mass flow rate
$M$	$\text{kg}/\text{mol}$	Molar mass
$\dot{n}$	$\text{mol}/\text{s}$	Molar flow rate
$N$	–	Number of elements, number of turns
$\dot{o}$	$\text{kg}/\text{s}\cdot\text{m}^2$	Mass flow rate density
$P$	Pa	Pressure
$p, P$	W	Power
$\Xi_P$	W	Power absolute error
$\varepsilon_P$	–	Power relative error
$q, Q$	$\text{W}/\text{m}^2$	Power density
$Q$	C	Electric charge

$r$	$\Omega \cdot \text{m}^2$	Area specific resistance
$R$	$\Omega$	Resistance
$s$	J	Entropy
$\bar{s}$	$\text{J}/_{\text{mol}}$	Molar entropy
$S$	$\text{m}^2$	Surface, cross section
$t$	m	Thickness
$t$	$^{\circ}\text{C}$	Temperature
$T$	K	Temperature
$T$	s	Interval, period
$V$	$\text{m}^3$	Volume
$v, V$	V	Voltage
$\Xi_V$	V	Voltage absolute error
$\varepsilon_V$	–	Voltage relative error
$\Delta V$	V	Voltage variation, voltage ripple
$w$	J	Work
$w$	m	Width
$x$	m	Space
$Z$	$\Omega$	Impedance

### Symbols

Symbol	Description
	Constant
	Variable input, variable output
	Derivator
	Integrator (with reset)
	Saturator



	Proportional
	Multiplier
	Divider
	Sample and hold
	Comparator
	Logical not
	Logical and
	Set-reset flip-flop
	Pulse generator
	Up counter

---



## INTRODUCTION

Fuel cells are electrochemical devices in which the chemical potential energy of a fuel is directly converted into electrical energy, without involving thermodynamic cycles. This results in possible advantages, like higher efficiencies and absence of mechanical vibrations. Despite these advantages, fuel cells almost always need to be coupled with power converters in order to be practically used: they adapt the electrical characteristics of the fuel cell to the electrical characteristics the load requires. Such an ensemble is called a fuel cell system [1].

In the literature, the interest around fuel cell systems has never stopped growing during the last two decades. The final applications in which fuel cells can be employed have expanded beyond the military and aerospace laboratories, and have started penetrating the end-user market, too. The literature is rich of articles concerning fuel cells and — more recently — power electronics applications to fuel cells.

In spite of this large amount of information covering all aspects of fuel cells and power converters separately, information concerning such systems' overall behaviour has been harder to get. Their operation is quite far from being easily comprehensible, due to the mutual interactions between the different components the system is made of.

Hence, the first goal of this work is to analyse, study and measure — when possible — the behaviour of a fuel cell system, the interactions between its main components, along with their responses to external stimulation. This will eventually lead to shape, characterise and simulate a complete fuel cell system.

The actual production of such a system, which is the second aim of this work, is a consequence of the experimental validation of the theoretical approach developed in the first part. A review of the different application domains of fuel cells has shown that fuel cell systems, when used as energy backup solutions, can be valid competitors to traditional technologies. A prototype of a fuel cell based backup system for telecommunication applications has then been sized, studied and produced.

Thanks to the participation in this project of an industrial fuel cell manufacturer and of two power electronics laboratories, the sizing process enjoyed a large freedom. This leads to the third main goal of this work: the identification of criteria that could help sizing such systems, in which neither the fuel cell nor the power converter are previously known.

During the development of this thesis, other interesting topics showed up, leading to minor aims, which have also been developed and studied. For example, one of the interesting aspects related to the power converter which will be studied, concerns its peculiar operation on the border between the discontinuous and continuous conduction modes, and its control with a variable switching frequency, both aimed at increasing the power converter efficiency.

The thesis ends with the experimental and simulation results for the different parts that compose the system and for the system itself. Simulation results for the fuel cell and for the complete system will be presented, with particular care to the behaviour of the system during the most common types of transients. Experimental results concerning both the fuel cell and the power converter will be given, thereby showing a quite high efficiency of the power converter.

∴

The details of the chapters composing this thesis follow.

In Chapter 1, a list of applications in which fuel cells can be useful will be presented. In this list, some applications will be identified and proved more interesting than traditional systems, based on a CO<sub>2</sub> emission level criterion. Once their competitiveness is demonstrated, an introduction about power electronics applied to fuel cells will be given.

After dealing with the different aspects that should be taken into account in sizing such systems, Chapter 2 will give a sizing procedure, in which both the

fuel cell stack and the power converter will be taken into account, and the mutual implications in the choice of these two elements will be described.

In Chapter 3, the procedure and considerations described in the previous chapter will be applied to a particular case, in which a 5 kW fuel cell based backup system for telecommunication applications will be sized.

In Chapter 4, a complete Simulink model of such a system will be developed. Both the fuel cell and the power converter models will be illustrated. An example of a digital control system will also be given. Thanks to this, the mutual interactions between fuel cell, power converter and load in this complex system will be studied.

Before discussing the results, the hardware used during the experimental tests will be introduced. Chapter 5 will present the fuel cell stack and the power converter prototypes. This will be followed by the description of the realised acquisition system, needed to operate the fuel cell stack under safe conditions.

The simulation and experimental results obtained for the fuel cell, the power converter and the entire system will be shown and discussed in Chapter 6.

Since the fuel cell activity was completely new, the whole equipment and space had to be conceived and built up. As an example, Appendix J will show some pictures of the newly built laboratory.



## CHAPTER 1

### CONTEXT

Since the late 1990s, fuel cell systems have been drawing more and more attention, and their applications have been spreading from niche domains — like space or military technology — to others, like backup power supplies, automotive or portable devices, which have always used traditional energy technologies.

In this chapter, after an overview of fuel cell history and of the most common fuel cell types, an organisation of the domains and applications in which fuel cell systems could be interesting will be proposed. They will be analysed, identifying some of the criteria and reasons that do or do not justify the use of fuel cell technology instead of traditional ones.

Then, since practical applications of fuel cells require the use of power electronics converters as interface devices, some brief historical information on the impact of fuel cell systems in power electronics will be given.

#### 1.1. Fuel cells

##### 1.1.1. Historical information

Fuel cell history is briefly exposed, in a non-traditional way: presenting it in a strict chronological order — without separating the different fuel cell type

evolutions — should make it easier to highlight the effect-cause relationships between the milestones of this history and to correlate it with the history of electricity where appropriate.

A detailed description of the evolution of fuel cell technology is beyond the scope of this dissertation and can be found in many sources (see [2] for a complete description).

In this work, fuel cell history has been divided in four periods from its origin to the present day, characterised by different approaches towards the fuel cell phenomenon.

The first period, which ranges from 1800 to the second half of 1800s, witnessed the birth of electrochemistry and the discovery of the fuel cell phenomenon, which still remained a scientific curiosity.

In 1800, W. Nicholson and J. Ritter, United Kingdom, decomposed water into hydrogen and oxygen [3]. About thirty years later, M. Faraday, United Kingdom, formulated the two fundamental laws of electrochemistry [3], and C.F. Schönbein, Germany, observed the principle of what would be later called a fuel cell. In 1839, W.R. Grove, United Kingdom, built his “gaseous voltaic battery” — the first fuel cell — using platinum electrodes and sulphuric acid as an electrolyte. Some years later, Grove realised the importance of the reaction surface and in 1843 Schönbein, after reading Grove’s work, published his results.

The second period began in the 1880s, when fuel cells started to be perceived as a viable solution for practical applications, and studies were conducted in order to improve their performance. In 1882, J.W. Strutt Rayleigh, United Kingdom, achieved the first improvement by using platinum gauze as electrodes. He also was the first to attempt to feed a gaseous voltaic battery with coal gas, all the previous experiments having been conducted using pure hydrogen. In 1889, L. Mond and C. Langer, United Kingdom, built the first prototype of a practical fuel cell, in which a porous, non-conducting matrix was soaked with a liquid electrolyte. They coined the term “fuel cell” [3]. In the same year, C.R. Alder Wright and C. Thompson, United Kingdom, published information about an apparatus similar to Mond and Langer’s that they had built in 1887: the interest in the production of such systems was spreading in the scientific community. They also foresaw the use of liquid fuels as a source of energy. In the same years, F.W. Ostwald, Germany, provided much of the theoretical understanding of fuel cell operation [3].

It should be noticed how the last years of the 19<sup>th</sup> century were also characterised by the wide diffusion of gas power in cities — for lighting, but for do-



mestic use as well. These years also witnessed the first days of commercial electricity production and distribution: amongst the numerous important discoveries and scientists, the first electric power plants, which date back to 1882 and 1883 thanks to the work of T.A. Edison [4], are worth mentioning. In that context, as heritage of the industrial revolutions, coal was still the main energy source. It was used to produce both mechanical work and electricity via steam machines, whose efficiency was very low — less than 10 %. As a consequence, the ambition of reaching higher efficiencies led to the interest in the direct transformation of coal into electricity with the first direct coal fuel cell systems.

The third period began when fuel cell research started to be oriented towards the solutions of practical problems.

Between 1894 and 1896, Ostwald recognised that electrochemistry was a more efficient means of producing electricity directly from coal, while W.W. Jacques, USA, produced a fuel cell able to do it, which also set the basis for two new types of fuel cells: the solid oxide and molten carbonate fuel cells. In 1899, W.H. Nernst, Germany, investigated solid conductors at high temperatures and observed the positive relation between conductivity of melted salts and temperatures. The next year, Nernst and W. Wild, Germany, built their electrolytic glow body, a light lamp using a ceramic rod that is heated to incandescence [5].

The fourth period began in 1902, with the first attempt to produce an alkaline fuel cell, documented by a US patent [6]. This period was characterised by the coexistence of many different fuel cell types and their commercial development.

F. Haber, Germany, and Sir J.T. Brunner, United Kingdom, continued the work of Jacques on direct coal fuel cells, concluding that the expectations of Jacques' coal cell were low due to the electrolyte consumption in the reaction. E. Baur and H. Ehrenberg, Germany, also researched direct coal fuel cells independently from Jacques' work.

After a break from 1912 to 1932, very likely due to World War 1, F.T. Bacon, United Kingdom, started thinking about the reversibility of the water electrolysis process and built his own fuel cell, an alkaline fuel cell. In 1937, E. Baur, Germany, and Brunner continued research on direct coal fuel cells, with molten carbonate electrolytes, opening the way to both solid oxide fuel cells and molten carbonate fuel cells. Two years later, Baur and H. Preis, Switzerland, started developing the first solid oxide fuel cell in order to avoid the problems of molten electrolytes. After seven years of work, Bacon succeeded in

designing an alkaline fuel cell with economically viable catalysts and practical high pressure equipments.

After a pause probably due to World War 2, information about fuel cell research started to circulate again in 1946, when O.K. Davatyan, USSR, developed a high temperature fuel cell using a solid ionic conductor as electrolyte and fed with coal gas. He also carried out some experiments on low temperature alkaline fuel cells. In the same year, Bacon continued his work on alkaline fuel cells and developed a complete fuel cell system.

In 1951, K. Kordesch and A. Marko made the first attempt to create a direct methanol fuel cell. In the 1950s alkaline fuel cells were developed. Despite the many practical successful prototypes, these attempts ended up having no commercial applications. Worth mentioning is the fuel cell tractor made by Allis Chalmers, USA, in 1959 with a 1008 element alkaline fuel cell, which was one of the first fuel cell based vehicles [2].

Davtyan's work on high temperature fuel cells was carried on by G.H.J. Broers and J.A.A. Ketelaar, Netherland, who deduced that the electrolyte used by Davtyan was actually two-phase, starting research on molten carbonate fuel cells. They designed a new fuel cell with a molten carbonate electrolyte held in a matrix. They made several tests, feeding the fuel cell with hydrogen gas, town gas, carbon monoxide and natural gas with internal reforming. In the same year, there were other works on molten carbonate fuel cells, like Baker's, Douglas' and Bacon's.

The first solid polymer fuel cell was developed in 1960 by T. Grubb and L. Niedrach, at General Electric, USA using a polymer sheet made of cross-linked polystyrene and, two years later, J. Weissbart and R.J. Ruka, at the Westinghouse Electric Corporation, USA, built a solid oxide fuel cell fed with pure oxygen and either hydrogen or methane [2].

For what concerns alkaline fuel cells, Allis Chalmers first used an electrolyte matrix instead of a flowing liquid electrolyte, and Pratt and Whitney, USA, developed a fuel cell to supply power to the auxiliary units of the Apollo space module: the lack of commercial applications for alkaline fuel cells was filled in by space and military applications. General Electric, USA, built a proton exchange membrane fuel cell for the Gemini Space project, but its lifetime was extremely short, less than 500 h [6].

Twelve years after the first attempts in 1951, Murray and Grimes, at Allis Chalmers, USA, produced a direct methanol fuel cell with an alkaline electrolyte. In 1965, Williams, at Shell, Netherland, and Tarmy and Ciprios, at Esso, USA, built a direct methanol fuel cell with an aqueous acid electrolyte.

In the same year, the National Aeronautics and Space Administration (NASA), USA, used proton exchange membrane fuel cells in its Gemini project, since Gemini 5 mission. Because of the low operation temperature (21 °C) and the problems in the water management of the first proton exchange membrane fuel cells, NASA switched to the alkaline fuel cell made by Pratt and Whitney and based on Bacon's design in 1965.

1965 also witnessed a new product that utterly changed the water management of low temperature fuel cells: polytetrafluoroethylene (PTFE), whose commercial name is "Teflon" by DuPont, USA. Niedrach and Alford, at General Electric, USA, used it in the electrodes to achieve controlled wetting at the gas-electrolyte interface.

In the next year, during the Lunar Orbiter Program — a series of five unmanned lunar missions — redesigned alkaline fuel cells were used. In 1967, Pratt and Whitney Aircraft Division of the United Technologies Corporation started working on phosphoric acid fuel cells with the "Target" program.

In 1972, W.G. Grot, at DuPont, invented a new polymer named "XR", whose good chemical and temperature stability derive from its PTFE backbone: its commercial name is "Nafion" and it gave new life to the proton exchange membrane fuel cell type [7].

From 1975 to 1977, two prototypes of electrical power systems supplied with natural gas and based on phosphoric acid fuel cells were presented: the "PC-11" 12.5 kW prototype and the "PC-19" 1 MW prototype.

In 1986, Raistrick at the Los Alamos National Laboratory, USA, devised a method to reduce the amount of catalyst required in the electrodes, paving the way to effective and cheaper proton exchange membrane fuel cells.

Three years later, Verbrugge at General Motors Research Laboratories, USA, modelled the transport of methanol across perfluorinated ion-exchange membrane, which was fundamental for the further development of direct methanol fuel cells [8].

In 1990, Ballard Power Systems, Canada, began developing solid polymer fuel cell technology, with the goal of creating a system functioning on hydrogen and air, and to demonstrate operation on products of reformed hydrocarbon fuels: the "MK-4" prototype [9, 10].

In 1991, a 11 MW phosphoric acid fuel cell power plant in Goi, Japan, was built. This proved the maturity of phosphoric acid fuel cell technology. In 1992, the Jet Propulsion Laboratory, USA, began developing a direct methanol fuel cell

with a Nafion membrane: for the first time methanol could be injected in a liquid form, rather than as a solution through the electrolyte.

Among the several demonstrations of proton exchange membrane fuel cell systems for stationary applications, one of the most publicised was Plug Power's, USA, in 1998 [11]. Other projects and industrial partners are described in [12].

In 2000, the National Fuel Cell Research Center and Southern California Edison, USA, evaluated a solid oxide fuel cell with microturbine generator, in which the fuel cell was made by Siemens Westinghouse and the microturbine by Northern Research and Engineering Corporation [13].

The FCX Clarity car is one of the most important projects integrating fuel cell technology in automotive applications. It is a proton exchange membrane fuel cell based car made by Honda and marketed "beginning in the summer of 2008" [14].

A recent research domain, aiming at miniaturising fuel cell at the micrometre scale, has been started using techniques that pertain to the semiconductor and MicroElectroMechanical System (MEMS) industry [15, 16].

At the end of the chapter, Table 1.7 (page 47) sums up the main events and actors of the fuel cell history.

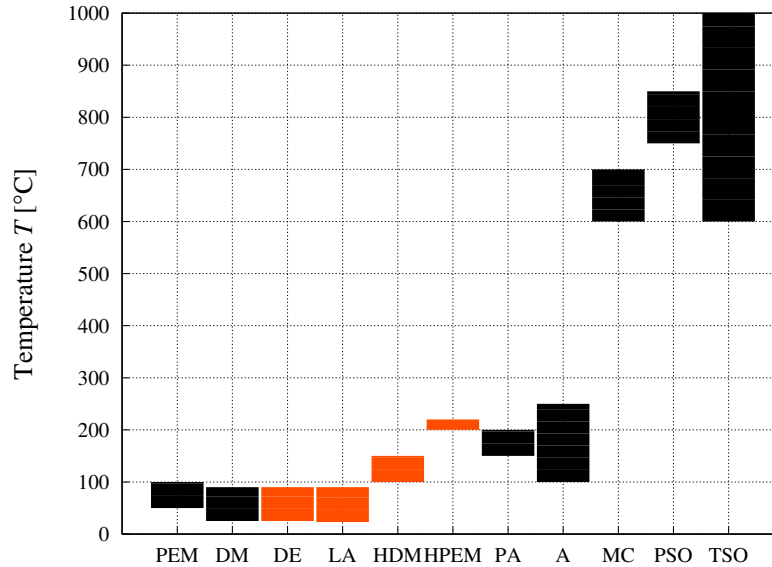
### 1.1.2. Types

One of the criteria that can be used to classify fuel cell types is based on their nominal temperature ranges, which leads to a rough distinction between low temperature and high temperature fuel cells. Figure 1.1 shows the temperature ranges in the most common fuel cell types.

Since many operative aspects of fuel cells are strictly related to their operation temperature, fuel cells in the same temperature range generally display the same advantages and disadvantages.

On the one hand, high temperature fuel cells enjoy the advantages of good reaction kinetics, of internal reforming possibility, of inexpensive catalyst use, and of insensitivity to CO poisoning.

On the other hand, low temperature fuel cells neither need special alloys to resist to the highly corrosive media common to high temperature fuel cells, nor thermal shielding. They do not suffer from thermal dilatation problems



**Figure 1.1.** Temperature ranges for the most common fuel cell (FC) types. The orange ranges represent newer fuel cell types. Acronyms: Proton Exchange Membrane (PEM), Direct Methanol (DM), Direct Ethanol (DE), Low temperature Alkaline (LA), High temperature Direct Methanol (HDM), High temperature Proton Exchange Membrane (HPEM), Phosphoric Acid (PA), Alkaline (A), Molten Carbonate (MC), Planar Solid Oxide (PSO), Tubular Solid Oxide (TSO). These ranges of temperature have been taken from different sources, like [6, 17, 2].

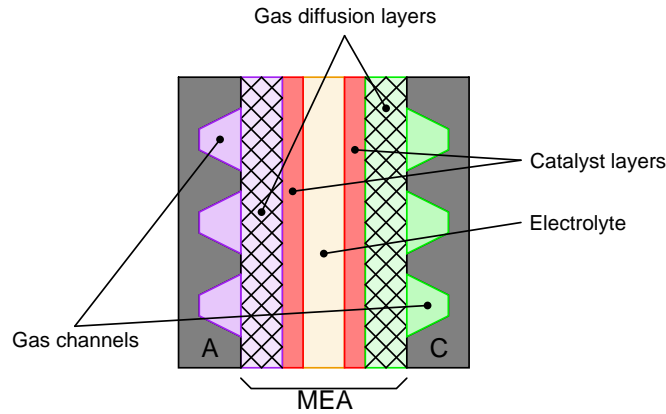
and they enjoy faster start-up processes compared to high temperature fuel cells. Aqueous electrolytes can only be used in low temperature fuel cells.

All the different fuel cell types share the same principle structure described in Figure 1.2. Further details can be found in [6, 17, 2].

Fuel cell efficiency will be meant in the following comparison as the ratio between the maximum electrical energy that can be achieved by the fuel cell and the chemical energy the fuel is able to deliver. This will be expressed by the Higher Heating Value (HHV), which is the energy released by a fuel during its combustion.

#### 1.1.2.1. Proton Exchange Membrane Fuel Cell (PEMFC)

The schematic representation of a PEMFC, whose main characteristics follow, is shown in Figure 1.3. The overall chemical reactions occurring at the anode and cathode respectively are described by 1.1.1 and 1.1.2, in which

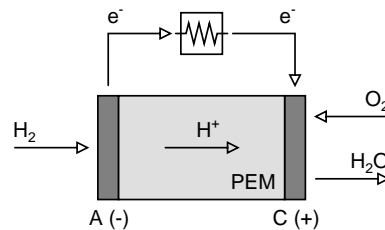


**Figure 1.2.** Principle structure of a fuel cell. Reactants flowing in the gas channels diffuse through the gas diffusion layers to the catalyst layers, where reactions take place. Anions or cations, depending on the fuel cell type, cross the electrolyte, while electrons follow the external electric circuit. Acronyms: Anode (A), Cathode (C), Membrane Electrode Assembly (MEA).

gaseous hydrogen ( $H_2$ ) and oxygen ( $O_2$ ) react to produce electrical energy, heat and water ( $H_2O$ ) in a gas-liquid two-phase state.



- Operating temperature: from 50 °C to 100 °C for standard PEMFC and up to 220 °C for high temperature PEMFC.
- Fuel: pure hydrogen; gaseous hydrocarbons with external reforming.

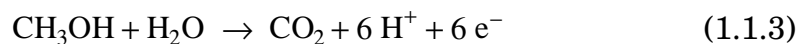


**Figure 1.3.** Schematic representation of a Proton Exchange Membrane Fuel Cell (PEMFC). Acronyms: Anode (A), Cathode (C), Proton Exchange Membrane (PEM), Dihydrogen ( $H_2$ ), Dioxygen ( $O_2$ ), Water ( $H_2O$ ), Hydrogen ion ( $H^+$ ), Electron ( $e^-$ ).

- Electrolyte: a proton exchange membrane, also called polymer exchange membrane; the most common is Nafion by DuPont, operating at maximum 90 °C; others exist: a new type based on polybenzimidazole (PBI)<sup>1</sup> could allow temperatures up to 220 °C.
- Charge carrier: hydrogen ion H<sup>+</sup>.
- Status: production.
- Power range: from less than 1 kW to about 250 kW.
- Applications: main power sources in vehicles, stationary backup systems and sometime used in small distributed generation and portable applications.
- Advantages: compactness, less corrosion problems thanks to the solid electrolyte, no electrolyte management system, insensitivity to orientation in space, highest power density.
- Disadvantages: water management is crucial, expensive platinum catalyst is required [18, 19], they are sensitive to CO.
- Maximum efficiency: around 60 %.
- Research activities: increasing catalytic activity, reducing poisoning effects, aging mechanisms [20].

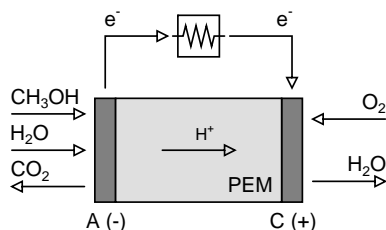
#### 1.1.2.2. *Direct Methanol Fuel Cell (DMFC)*

The schematic representation of a DMFC, whose main characteristics follow, is shown in Figure 1.4. The overall chemical reactions occurring at the anode and cathode respectively are described by 1.1.3 and 1.1.4, in which liquid methanol (CH<sub>3</sub>OH) and gaseous oxygen (O<sub>2</sub>) react to produce electrical energy, heat, gaseous carbon dioxide (CO<sub>2</sub>) and water (H<sub>2</sub>O) in a gas-liquid two-phase state.




---

<sup>1</sup>Polybenzimidazole or PBI fibre is a synthetic fibre with an extremely high melting point that also does not ignite [21, 22].

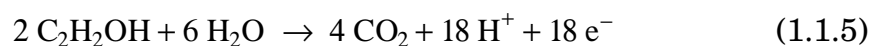


**Figure 1.4.** Schematic representation of a Direct Methanol Fuel Cell (DMFC). Acronyms: Anode (A), Cathode (C), Proton Exchange Membrane (PEM), Methanol ( $\text{CH}_3\text{OH}$ ), Dioxygen ( $\text{O}_2$ ), Water ( $\text{H}_2\text{O}$ ), Carbon dioxide ( $\text{CO}_2$ ), Hydrogen ion ( $\text{H}^+$ ), Electron ( $\text{e}^-$ ).

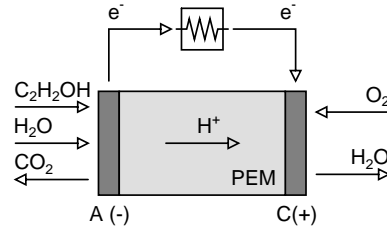
- Operating temperature: from 25 °C to 90 °C for standard DMFC and from 100 °C to 150 °C for high temperature DMFC.
- Fuel: liquid methanol.
- Electrolyte: a proton exchange membrane; the same for hydrogen PEMFC.
- Charge carrier: hydrogen ion  $\text{H}^+$ .
- Status: under development with limited success; research and development is about three years behind standard hydrogen PEMFC.
- Power range: from less than 1 W to about 100 W.
- Applications: portable applications.
- Advantages: methanol is more energy dense than gaseous and liquid hydrogen, methanol distribution networks already exist.
- Disadvantages: low efficiency, methanol toxicity, expensive platinum catalyst is required.

#### 1.1.2.3. Direct Ethanol Fuel Cell (DEFC)

The schematic representation of a DEFC, whose main characteristics follow, is shown in Figure 1.5. The overall chemical reactions occurring at the anode and cathode respectively are described by 1.1.5 and 1.1.6, in which liquid ethanol ( $\text{C}_2\text{H}_5\text{OH}$ ) and gaseous oxygen ( $\text{O}_2$ ) react to produce electrical energy, heat, gaseous carbon dioxide ( $\text{CO}_2$ ) and water ( $\text{H}_2\text{O}$ ) in a gas-liquid two-phase state.







**Figure 1.5.** Schematic representation of a Direct Ethanol Fuel Cell (DEFC). Acronyms: Anode (A), Cathode (C), Proton Exchange Membrane (PEM), Ethanol ( $C_2H_5OH$ ), Dioxygen ( $O_2$ ), Water ( $H_2O$ ), Carbon dioxide ( $CO_2$ ), Hydrogen ion ( $H^+$ ), Electron ( $e^-$ ).

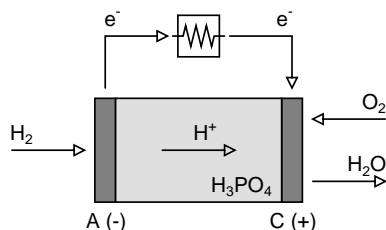


- Operating temperature: from 25 °C to 90 °C.
- Fuel: liquid ethanol.
- Electrolyte: a proton exchange membrane; the same for hydrogen PEMFC.
- Charge carrier: hydrogen ion  $H^+$ .
- Status: under development with some prototypes.
- Applications: portable applications.
- Advantages: same considerations for DMFC, ethanol innocuousness.
- Disadvantages: expensive platinum catalyst is required.
- Research activities: new electrocatalyst nanostructures based on non-noble metals.

#### 1.1.2.4. Phosphoric Acid Fuel Cell (PAFC)

The schematic representation of a PAFC, whose main characteristics follow, is shown in Figure 1.6. The overall chemical reactions occurring at the anode and cathode respectively are described by 1.1.7 and 1.1.8, in which gaseous hydrogen ( $H_2$ ) and oxygen ( $O_2$ ) react to produce electrical energy, heat, and water ( $H_2O$ ) in a steam form due to the high temperatures at which the cell operates.





**Figure 1.6.** Schematic representation of a Phosphoric Acid Fuel Cell (PAFC). Acronyms: Anode (A), Cathode (C), Phosphoric acid ( $\text{H}_3\text{PO}_4$ ), Dihydrogen ( $\text{H}_2$ ), Dioxygen ( $\text{O}_2$ ), Water ( $\text{H}_2\text{O}$ ), Hydrogen ion ( $\text{H}^+$ ), Electron ( $\text{e}^-$ ).



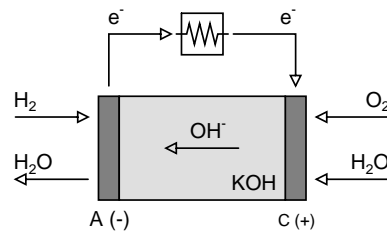
- Operating temperature: from 150 °C to 200 °C (the electrolyte solidifies at 40 °C).
- Fuel: hydrogen; hydrocarbons with external reforming.
- Electrolyte: liquid concentrated phosphoric acid ( $\text{H}_3\text{PO}_4$ ) soaked in a matrix.
- Charge carrier: hydrogen ion  $\text{H}^+$ .
- Status: in production.<sup>2</sup>
- Power range: from 150 kW to 11 MW.
- Applications: stationary applications, distributed generation, experiments on some large vehicles.
- Advantages: commercially available, insensitivity to CO.
- Disadvantages: low power densities, continuous operation.
- Maximum efficiency: around 42 %. The global efficiency for a Combined Heat and Power (CHP) system can reach 80 %.

#### 1.1.2.5. Alkaline Fuel Cell (AFC)

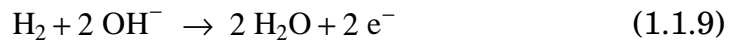
The schematic representation of an AFC, whose main characteristics follow, is shown in Figure 1.7. The overall chemical reactions occurring at the anode

<sup>2</sup>PAFC has been for long the most advanced fuel cell type, which has been dominating the on-site stationary fuel cell market.

and cathode respectively are described by 1.1.9 and 1.1.10, in which gaseous hydrogen ( $H_2$ ) and oxygen ( $O_2$ ) react to produce electrical energy, heat, and water ( $H_2O$ ) in a steam form for high temperature AFC and in a gas-liquid two-phase form for low temperature AFC.



**Figure 1.7.** Schematic representation of an Alkaline Fuel Cell (AFC). Acronyms: Anode (A), Cathode (C), Potassium hydroxide (KOH), Dihydrogen ( $H_2$ ), Dioxygen ( $O_2$ ), Water ( $H_2O$ ), Hydroxyl anion ( $OH^-$ ), Electron ( $e^-$ ).

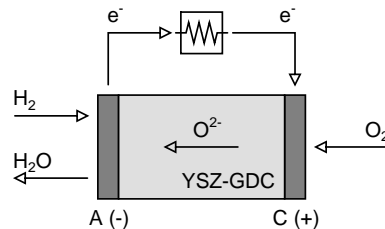


- Operating temperature: from 100 °C to 250 °C for standard AFC and from 23 °C to 70 °C for low temperature AFC.
- Fuel: pure hydrogen.
- Oxidant: pure oxygen, or air with external  $CO_2$  scrubber.
- Electrolyte: alkaline solution, generally potassium hydroxide (KOH); both structures with static electrolyte soaked in a matrix and structures with flowing electrolyte exist.
- Charge carrier: hydroxyl anion  $OH^-$ .
- Status: the oldest practical fuel cell type, currently used in particular market niches.
- Power range: from 100 W to 100 kW.
- Applications: mainly space and defence applications; some unsuccessful examples for consumer applications.
- Advantages: high performance, non-noble metal catalyst required.

- Disadvantages: electrolyte sensitivity to CO<sub>2</sub> poisoning requires external CO<sub>2</sub> scrubbers or frequent electrolyte changes, short lifetime (about 5 000 h).
- Maximum efficiency: 60 %.
- Research activities: solid-state alkaline fuel cells in which the electrolyte is an anion-exchange membrane rather than a liquid.

#### 1.1.2.6. Solid Oxide Fuel Cell (SOFC)

The schematic representation of an SOFC, whose main characteristics follow, is shown in Figure 1.8. The overall chemical reactions occurring at the anode and cathode respectively are described by 1.1.11 and 1.1.12, in which gaseous hydrogen (H<sub>2</sub>) — directly fed, or produced by internal reforming of some hydrocarbon — and oxygen (O<sub>2</sub>) react to produce electrical energy, heat, and water (H<sub>2</sub>O) in a steam form due to the high temperatures at which the cell operates.



**Figure 1.8.** Schematic representation of a Solid Oxide Fuel Cell (SOFC). Acronyms: Anode (A), Cathode (C), Yttria-Stabilised Zirconia (YSZ), Gadolinium Doped Ceria (GDC), Dihydrogen (H<sub>2</sub>), Dioxygen (O<sub>2</sub>), Water (H<sub>2</sub>O), Oxide anion (O<sup>2-</sup>), Electron (e<sup>-</sup>).

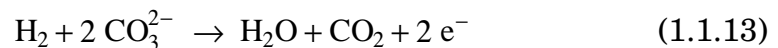


- Operating temperature: from 600 °C to 1000 °C for tubular SOFC, and from 750 °C to 850 °C for planar.

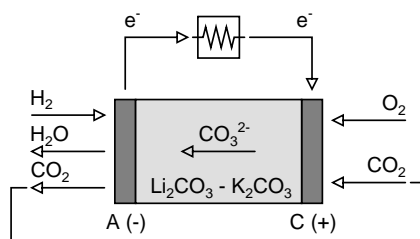
- Fuel: hydrogen, hydrocarbons (methane, propane, butane, natural gas), fermentation gas, gasified biomass, paint fumes; no sulphur components have to be present.
- Electrolyte: solid oxides like yttria-stabilised zirconia (YSZ) or gadolinium doped ceria (GDC).
- Charge carrier: oxide anion  $O^{2-}$ .
- Status: prototypes.
- Power range: from less than 1 kW to 3 MW.
- Applications: stationary applications for cogeneration, large distributed generation, some experiments on vehicles like refrigerated trucks and auxiliary power source on vehicles.
- Advantages: high efficiency, long-term stability, fuel flexibility, suitable for hybrid cycles and combined heat and power (CHP) systems, several catalysts used, insensitivity to CO, internal reforming.
- Disadvantages: significant ohmic losses.
- Maximum efficiency: from 43 % to 60 %.

#### 1.1.2.7. Molten Carbonate Fuel Cell (MCFC)

The schematic representation of an MCFC, whose main characteristics follow, is shown in Figure 1.9. The overall chemical reactions occurring at the anode and cathode respectively are described by 1.1.13 and 1.1.14, in which gaseous hydrogen ( $H_2$ ) — directly fed, or produced by internal reforming of some hydrocarbon — and oxygen ( $O_2$ ) react to produce electrical energy, heat, and water ( $H_2O$ ) in a steam form due to the high temperatures at which the cell operates. It may be noticed carbon dioxide ( $CO_2$ ) is produced and required during the reaction, but its global balance is zero.



- Operating temperature: from 600 °C to 700 °C.
- Fuel: virtually any, even coal.



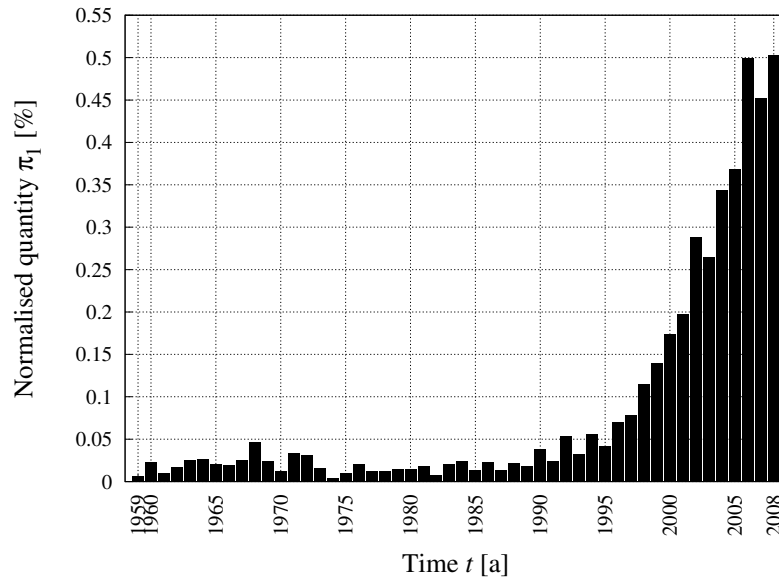
**Figure 1.9.** Schematic representation of a Molten Carbonate Fuel Cell (MCFC). Acronyms: Anode (A), Cathode (C), Lithium carbonate ( $\text{Li}_2\text{CO}_3$ ), Potassium carbonate ( $\text{K}_2\text{CO}_3$ ), Dihydrogen ( $\text{H}_2$ ), Dioxygen ( $\text{O}_2$ ), Water ( $\text{H}_2\text{O}$ ), Carbon dioxide ( $\text{CO}_2$ ), Carbonate anion ( $\text{CO}_3^{2-}$ ), Electron ( $e^-$ ).

- Electrolyte: alkali carbonate in a chemically inert ceramic matrix, typically  $\text{Li}_2\text{CO}_3$  and  $\text{K}_2\text{CO}_3$ .
- Charge carrier: carbonate anion  $\text{CO}_3^{2-}$ .
- Status: prototypes.
- Power range: from less than 1 kW to 1 MW.
- Applications: stationary applications for cogeneration, large distributed generation.
- Advantages: durability, high efficiency, fuel flexibility, suitable for combined heat and power (CHP) systems, variety of catalysts, insensitivity to CO, internal reforming.
- Disadvantages: significant ohmic losses.
- Maximum efficiency: from 47 % to 60 %.

### 1.1.3. Publications on fuel cells

The histogram of Figure 1.10 gives an idea of the trend in publication production related to fuel cells. Although the number of articles only relates to those published by Elsevier, this analysis should be still representative since Elsevier is “the world’s leading publisher of science and health information” [23] and it publishes several journals about different branches of science. Furthermore, instead of plotting the absolute numbers of articles, the ratio  $\pi_1$  of

fuel cell related articles over the total number of articles has been represented. The detailed data are presented in Appendix C.



**Figure 1.10.** Ratio  $\pi_1$  of fuel cell related articles over all the articles published by Elsevier, ordered by year  $t$ . Search criteria for fuel cell related articles used within the “science direct” site: terms “fuel cell” in “Abstract, Title, Keywords” among “All journals (include article in press)” and “All sciences” as subject. Search criteria for all the articles: terms “\*” in “Abstract, Title, Keywords” among “All journals (include article in press)” and “All sciences” as subject.

The figure shows an increasing interest in fuel cells starting from about 1990, the same year of the “MK-4” PEMFC prototype from Ballard. As underlined in [24], which studied the number of fuel cell related articles published in the Journal of the Electrochemical Society, a quite moderate interest in fuel cells had also been shown in the years preceding the 1973 oil crisis.

## 1.2. Fuel cell systems

Among all the fuel cell applications and systems that can be found in the literature and in the market, four domains can be defined, characterised by the role played by the fuel cells [25, 1]:

- automotive: a fuel cell is used as the main energy source in a vehicle;
- stationary: a fuel cell supplies electricity, and possibly heat, to a fixed — generally domestic or industrial — user;
- backup: a fuel cell supplies electricity to a sensitive load, whose power supply should be guaranteed;
- portable: a miniaturised fuel cell supplies power to a portable device and it is intended as a replacement for batteries.

The advantages and disadvantages of such systems with respect to their traditional counterparts can be analysed from different points of view, such as — for instance — cost, safety, volume, weight, efficiency, CO<sub>2</sub> emissions.

The following analysis is limited to efficiency and CO<sub>2</sub> emission considerations, in which only the emissions due to the fuel consumption have been considered. The interests in the portable domain being dominated by other criteria than these, only the first three domains will be taken into account [26, 27].

Hydrogen and methanol are energy vectors that can be produced from different energy sources, with several techniques. They can be directly derived from fossil fuels — like coal, oil or natural gas — or they can be produced by electrochemical means. In the latter case, the electrical energy needed for the process can come from thermoelectrical, nuclear and/or renewable energy power plants [28].

The CO<sub>2</sub> emission level index for the different solutions that can be figured out only allows a direct comparison between fossil fuel based solutions, since nuclear and renewable energy based solutions always have a zero CO<sub>2</sub> emission level. Nevertheless, there are no actual zero emission power plant systems in the world so far, and thus the considerations based on CO<sub>2</sub> emission levels are still valid.

In order to show the impact of real mixed power plant systems, tables about CO<sub>2</sub> emissions contain six columns: the first is related to an oil based system, the second to a coal based system, the third to a natural gas system, the fourth to the USA system, the fifth to the French system and the last to the Italian system. These three real examples have been chosen since they are representative of three typical cases, the USA system being mainly dominated by oil, the French one by nuclear, and the Italian one being largely based on natural gas.



The details and sources on which these analyses were based can be found in Appendix A.

### 1.2.1. Automotive applications

Using the diagrams shown in Figures 1.19 and 1.20, displayed at the end of the chapter (pages 48 and 49), efficiencies  $\eta$  and normalised CO<sub>2</sub> emissions  $\mu$  were calculated for the following scenarios, in which the vehicles are propelled by:

- (ICE) an Internal Combustion Engine, fed with:
  - (D) Diesel;
  - (G) Gasoline;
  - (N) Natural gas;
  - (GHNR) Gaseous Hydrogen produced by Natural gas Reforming;
  - (GHE) Gaseous Hydrogen produced by Electrolysis;
  - (LHNR) Liquid Hydrogen produced by Natural gas Reforming;
  - (LHE) Liquid Hydrogen produced by Electrolysis;
  - (GHMR) Gaseous Hydrogen produced by onboard Methanol Reforming;
  - (M) Methanol;
  
- (FC) an electric motor and a Fuel Cell, fed with:
  - (GHNR) Gaseous Hydrogen produced by Natural gas Reforming;
  - (GHE) Gaseous Hydrogen produced by Electrolysis;
  - (LHNR) Liquid Hydrogen produced by Natural gas Reforming;
  - (LHE) Liquid Hydrogen produced by Electrolysis;

- (GHMR) Gaseous Hydrogen produced by onboard Methanol Reforming;
  - (M) Methanol;
- (BAT) an electric motor and a BAttery bank.

Tables 1.1 and 1.2 respectively show the efficiencies and the CO<sub>2</sub> emissions of these different scenarios.

The first table takes into account the efficiencies of the processes required to produce the mechanical power needed by the vehicle from the primary energy sources and involving several energy vectors: hydrogen, methanol and electricity. In the case of the electrical vehicle, it also includes the efficiency of the charge/discharge process of the batteries.

The second table shows the CO<sub>2</sub> emission level of the different solutions, taking into account the efficiencies previously shown and the CO<sub>2</sub> emissions proper to the different primary sources and to the different power plant systems of USA, France and Italy.

The efficiency of the battery based systems (case BAT from Oil:  $\eta = 25\%$ , from Coal:  $\eta = 23\%$ , from Natural gas:  $\eta = 32\%$ ) is always the best one in every column, immediately followed by the Diesel internal combustion engine solution in the oil column (case ICE.D:  $\eta = 22\%$ ) and the hydrogen fuel cell system on the other two (cases FC.GHE from Coal:  $\eta = 9.4\%$ , and FC.GHNR:  $\eta = 26\%$ ).

From the point of view of CO<sub>2</sub> emissions, battery based systems (case BAT from Oil:  $\mu = 4.0$ , from Coal:  $\mu = 5.6$ , from Natural gas:  $\mu = 2.3$ ) all have the lowest emission levels, but hydrogen fuel cell systems have similar emission levels when the hydrogen is produced by natural gas reforming and stored under a high pressurised gas (case FC.GHNR:  $\mu = 2.9$ ). Furthermore, both a direct methanol fuel cell system (case FC.M:  $\mu = 3.7$ ) and a hydrogen fuel cell system with onboard methanol reforming (case FC.GHMR:  $\mu = 3.4$ ) show about the same emission levels. Both levels are lower than the ones in standard internal combustion engine vehicles (cases ICE.D:  $\mu = 4.5$ , ICE.G:  $\mu = 5.3$  and ICE.N:  $\mu = 3.8$ ).

Notice that even a hydrogen internal combustion engine vehicle (case ICE.GHNR:  $\mu = 5.2$ ) has lower emissions than standard gasoline internal combustion engine vehicles (case ICE.G:  $\mu = 5.3$ ).

**Table 1.1.** Efficiencies from the primary fossil energy sources to the final user for automotive applications. Acronyms: Internal Combustion Engine (ICE), Fuel Cell (FC), Battery (BAT), Diesel (D), Gasoline (B), Natural gas (N), Methanol (M), Gaseous Hydrogen (GH), Liquid Hydrogen (LH), hydrogen by Reforming (R), hydrogen by Electrolysis (E).

	Efficiency ( $\eta$ )		
	Oil [%]	Coal [%]	Natural gas [%]
ICE.D	22	–	–
ICE.G	18.9	–	–
ICE.N	–	–	20
ICE.GHNR	–	–	14.6
ICE.GHE	5.7	5.3	7.3
ICE.LHNR	–	–	11.6
ICE.LHE	4.6	4.3	5.8
ICE.GHMR	–	–	12.5
ICE.M	–	–	14.7
FC.GHNR	–	–	26
FC.GHE	10.1	9.4	12.9
FC.LHNR	–	–	20
FC.LHE	8.0	7.5	10.3
FC.GHMR	–	–	22
FC.M	–	–	20
BAT	25	23	32

Among the problems of fuel cells for the automotive domain, the subzero start-up and operation should be cited. An interesting presentation introducing the problem can be found in [29].

#### 1.2.1.1. Conclusion

In terms of CO<sub>2</sub> emissions, electricity based solutions are strictly related to the electricity production means. They are generally better than standard hydrocarbon internal combustion solutions, and even in the worst case — when electricity only comes from coal — they are only slightly worse.

Fuel cell solutions with gaseous hydrogen from natural gas reforming are always better than standard solutions. Methanol fuel cell solutions are also good choices, where the advantage of methanol is the presence of an existent infrastructure.

**Table 1.2.** Normalised CO<sub>2</sub> production from different fossil sources. Acronyms: Internal Combustion Engine (ICE), Fuel Cell (FC), Battery (BAT), Diesel (D), Gasoline (B), Natural gas (N), Gaseous Hydrogen (GH), Liquid Hydrogen (LH), hydrogen by Reforming (R), hydrogen by Electrolysis (E).

Normalised CO <sub>2</sub> production ( $\mu$ )						
	Oil	Coal	Natural gas	USA	France	Italy
	[–]	[–]	[–]	[–]	[–]	[–]
ICE.D	4.5	–	–	–	–	–
ICE.G	5.3	–	–	–	–	–
ICE.N	–	–	3.8	–	–	–
ICE.GHNR	–	–	5.2	–	–	–
ICE.GHE	17.5	24	10.3	14.2	1.65	11.3
ICE.LHNR	–	–	6.5	–	–	–
ICE.LHE	22	31	12.9	17.8	2.1	14.1
ICE.GHMR	–	–	6.0	–	–	–
ICE.M	–	–	5.1	–	–	–
FC.GHNR	–	–	2.9	–	–	–
FC.GHE	9.9	13.8	5.8	8.1	0.94	6.4
FC.LHNR	–	–	3.7	–	–	–
FC.LHE	12.5	17.3	7.3	10.1	1.18	8.0
FC.GHMR	–	–	3.4	–	–	–
FC.M	–	–	3.7	–	–	–
BAT	4.0	5.6	2.3	3.3	0.38	2.6

### 1.2.2. Stationary applications

From what Figures 1.21 and 1.22, displayed at the end of the chapter (pages 50 and 51), show, efficiencies  $\eta$  and normalised CO<sub>2</sub> emissions  $\mu$  were calculated for the following scenarios, in which the power is produced by:

- (ICE) an Internal Combustion Engine based electric generator, fed with:
  - (D) Diesel;
  - (G) Gasoline;
  - (N) Natural gas;
  - (M) Methanol;

- (GR) the national power plant system, and transmitted and distributed by the national grid;
- (FC) a fuel cell, fed with:
  - (GHNR) Gaseous Hydrogen produced by Natural gas Reforming;
  - (GHE) Gaseous Hydrogen produced by Electrolysis;
  - (LHNR) Liquid Hydrogen produced by Natural gas Reforming;
  - (LHE) Liquid Hydrogen produced by Electrolysis;
  - (GHMR) Gaseous Hydrogen produced by onboard Methanol Reforming;
  - (M) Methanol.

Tables 1.3 and 1.5 respectively show the efficiencies and the CO<sub>2</sub> emissions of the different scenarios without the adoption of Combined Heat and Power (CHP) systems, while tables 1.4 and 1.6 respectively show the same data for the same scenario but with the adoption of CHP systems.

From the point of view of efficiency, among non-CHP systems the best solution is always the grid connected one (cases GR:  $\eta = 35\%$ ,  $\eta = 33\%$  and  $\eta = 44\%$ ). In the case of CHP systems, the solutions with the highest efficiency are the traditional ones (cases ICE.D:  $\eta = 51\%$ , ICE.G:  $\eta = 46\%$ , ICE.N:  $\eta = 48\%$ ), along with the fuel cell system fed with gaseous hydrogen produced by natural gas reforming (case FC.GHNR:  $\eta = 48\%$ ).

From the point of view of CO<sub>2</sub> emissions, instead, the best source is the electric grid (case GR) with a predominant production by natural gas (case GR, from Natural gas:  $\mu = 1.69$ ), if CHP systems are not used. Otherwise, if CHP systems are used, the energy sources with the lowest emissions are the fuel cell systems fed by gaseous hydrogen produced by natural gas reforming and the natural gas CHP system (cases FC.GHNR and ICE.N:  $\mu = 1.57$ ).

The interest in using fuel cell systems to give power to stationary users when the electric grid is accessible is real, but limited to CHP systems. Otherwise, the use of fuel cells cannot be justified by CO<sub>2</sub> reduction or efficiency improvement reasons, except in the case in which the electric energy distributed by the grid comes almost totally from coal (case GR, from Coal:  $\mu = 4.0$ ).

**Table 1.3.** Efficiencies from the primary fossil energy sources to the final user for stationary applications, without Combined Heat and Power systems. Acronyms: Internal Combustion Engine (ICE), Fuel Cell (FC), Grid (GR), Diesel (D), Gasoline (B), Natural gas (N), Methanol (M), Gaseous Hydrogen (GH), Liquid Hydrogen (LH), hydrogen by Reforming (R), hydrogen by Electrolysis (E).

	Efficiency ( $\eta$ )		
	Oil [%]	Coal [%]	Natural gas [%]
ICE.D	20	–	–
ICE.G	17.0	–	–
ICE.N	–	–	17.7
GR	35	33	44
FC.GHNR	–	–	26
FC.GHE	10.1	9.4	12.9
FC.LHNR	–	–	20
FC.LHE	8.0	7.5	10.3
FC.GHMR	–	–	22
FC.M	–	–	17.2

**Table 1.4.** Efficiencies from the primary fossil energy sources to the final user for stationary applications, with Combined Heat and Power systems. Acronyms: Internal Combustion Engine (ICE), Fuel Cell (FC), Grid (GR), Diesel (D), Gasoline (B), Natural gas (N), Methanol (M), Gaseous Hydrogen (GH), Liquid Hydrogen (LH), hydrogen by Reforming (R), hydrogen by Electrolysis (E).

	Efficiency ( $\eta$ )		
	Oil [%]	Coal [%]	Natural gas [%]
ICE.D	51	–	–
ICE.G	46	–	–
ICE.N	–	–	48
FC.GHNR	–	–	48
FC.GHE	18.7	17.5	24
FC.LHNR	–	–	38
FC.LHE	15.0	14.0	19.1
FC.GHMR	–	–	41
FC.M	–	–	39

**Table 1.5.** Normalised CO<sub>2</sub> production from different fossil sources without Combined Heat and Power systems. Acronyms: Internal Combustion Engine (ICE), Fuel Cell (FC), Grid (GR), Diesel (D), Gasoline (B), Natural gas (N), Methanol (M), Gaseous Hydrogen (GH), Liquid Hydrogen (LH), hydrogen by Reforming (R), hydrogen by Electrolysis (E).

Normalised CO <sub>2</sub> production ( $\mu$ )						
	Oil	Coal	Natural gas	USA	France	Italy
	[–]	[–]	[–]	[–]	[–]	[–]
ICE.D	5.1	–	–	–	–	–
ICE.G	5.9	–	–	–	–	–
ICE.N	–	–	4.2	–	–	–
GR	2.9	4.0	1.69	2.3	0.27	1.85
FC.GHNR	–	–	2.9	–	–	–
FC.GHE	9.9	13.8	5.8	8.1	0.94	6.4
FC.LHNR	–	–	3.7	–	–	–
FC.LHE	12.5	17.3	7.3	10.1	1.18	8.0
FC.GHMR	–	–	3.4	–	–	–
FC.M	–	–	4.4	–	–	–

**Table 1.6.** Normalised CO<sub>2</sub> production from different fossil sources with Combined Heat and Power systems. Acronyms: Internal Combustion Engine (ICE), Fuel Cell (FC), Grid (GR), Diesel (D), Gasoline (B), Natural gas (N), Methanol (M), Gaseous Hydrogen (GH), Liquid Hydrogen (LH), hydrogen by Reforming (R), hydrogen by Electrolysis (E).

Normalised CO <sub>2</sub> production ( $\mu$ )						
	Oil	Coal	Natural gas	USA	France	Italy
	[–]	[–]	[–]	[–]	[–]	[–]
ICE.D	2.0	–	–	–	–	–
ICE.G	2.2	–	–	–	–	–
ICE.N	–	–	1.57	–	–	–
GR	–	–	–	–	–	–
FC.GHNR	–	–	1.57	–	–	–
FC.GHE	5.3	7.4	3.1	4.3	0.50	3.4
FC.LHNR	–	–	2.0	–	–	–
FC.LHE	6.7	9.3	3.9	5.4	0.63	4.3
FC.GHMR	–	–	1.83	–	–	–
FC.M	–	–	1.90	–	–	–

It is also interesting to observe that the different forms of hydrogen storage other than compressed gaseous hydrogen (case FC.GHNR:  $\mu = 1.57$ ) — liquid hydrogen (case FC.LHNR:  $\mu = 2.0$ ), reformed methanol (case FC.GHMR:  $\mu = 1.83$ ), direct methanol (case FC.M:  $\mu = 1.9$ ) — display quite the same values of efficiency and CO<sub>2</sub> production.

Other stationary configurations like isolated systems with renewable sources are possible. They are included in section 1.2.3 with backup systems.

#### 1.2.2.1. *Conclusion*

In terms of CO<sub>2</sub> emissions, grid connected solutions are the best if CHP systems are not taken into account. Otherwise, the most interesting solutions are CHP fuel cell systems fed with hydrogen produced by natural gas reforming and CHP systems fed with natural gas.

#### 1.2.3. Backup applications

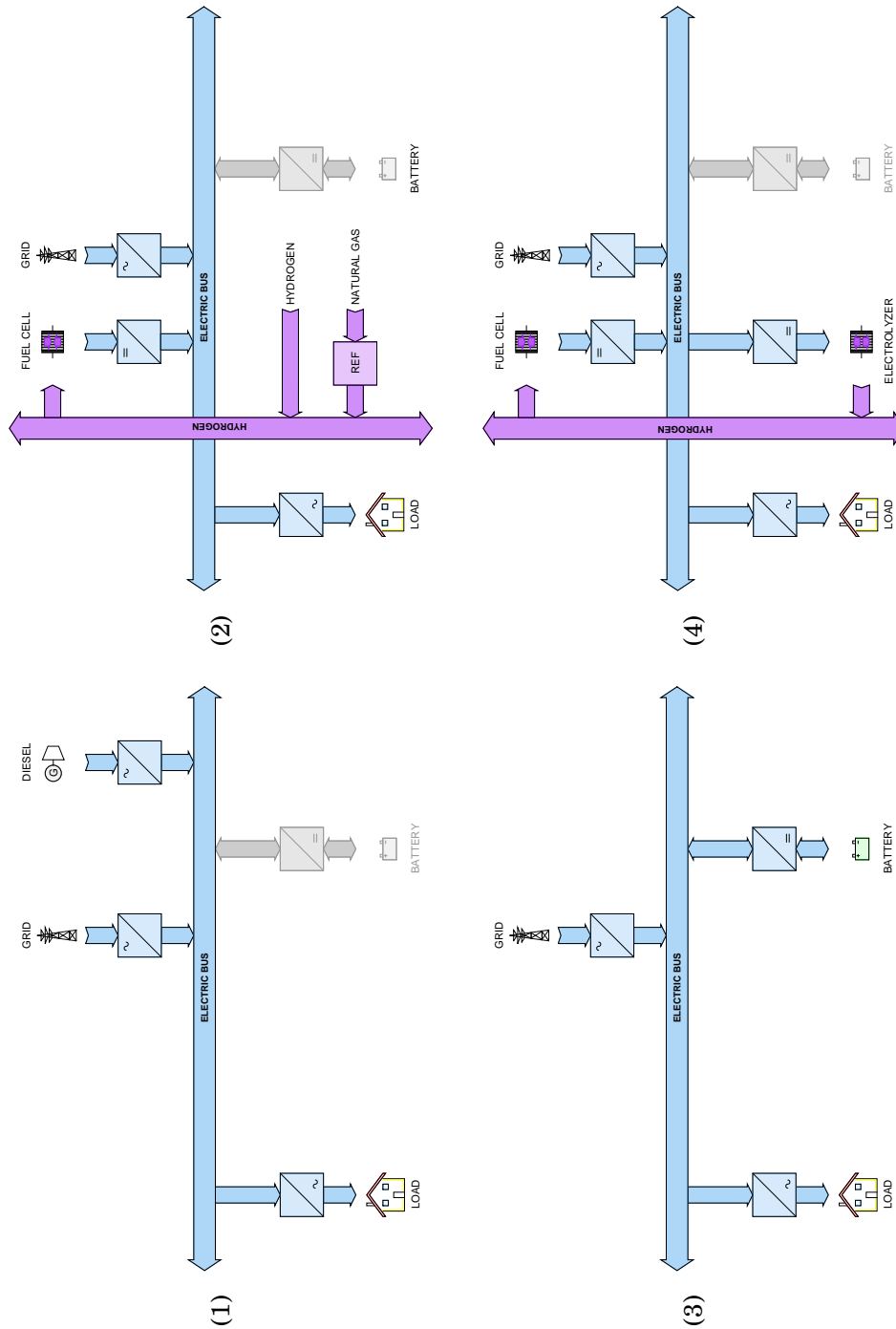
Systems belonging to this domain have been divided into the “grid connected” and the “stand-alone” subdomains, represented in Figures 1.11 and 1.12 respectively. For each subdomain, two traditional systems were compared to two fuel cell based systems with the same function.

The following considerations on efficiency  $\eta$  and normalised CO<sub>2</sub> emissions  $\mu$  are based on Figures 1.23 and 1.24, displayed at the end of the chapter (page 52 and 53), as in sections 1.2.1 and 1.2.2. Nevertheless, in every case in which fuel cells are involved, the system was supposed to use either natural gas via an external reformer or pure hydrogen produced by the reforming of natural gas and stored as a gas in high pressure tanks, since this is the way to produce hydrogen that has the lowest CO<sub>2</sub> emissions, and also the most common today.

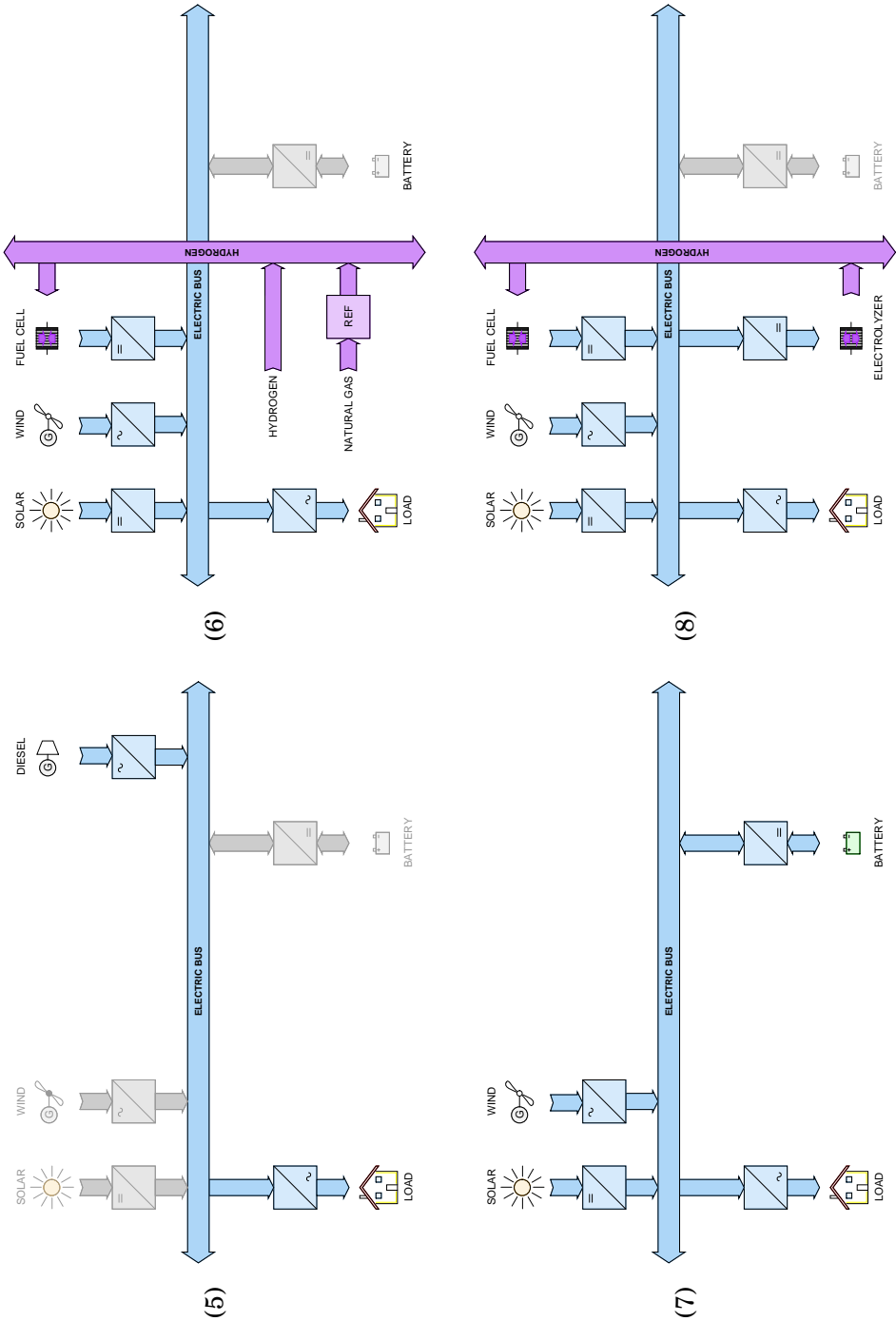
##### 1.2.3.1. *Grid connected cases:* *Diesel (1) versus fuel cell (2)*

In cases 1 and 2, represented in Figure 1.11 (1) and (2), the loads are always connected to the grid, but an auxiliary generator is also present. The case 1 is the standard case in which the auxiliary generator is a Diesel electric generator, while in the case 2 the latter is substituted by a fuel cell. In both cases, auxiliary batteries could be required to match the load dynamic requirements,





**Figure 1.11.** The four grid connected configurations. (1) and (3) are the traditional configurations, while (2) and (4) are their fuel cell based counterparts. (1) and (2) represent two grid connected fuel fed backup solutions, while (3) and (4) represent two grid connected storage based backup solutions.



**Figure 1.12.** The four stand-alone configurations. (5) and (7) are the traditional configurations, while (6) and (8) are their fuel cell based counterparts. (5) and (6) represent two fuel fed electric generators, while (7) and (8) represent two storage based backup solutions for stand-alone systems.

but since this does not affect the CO<sub>2</sub> emission comparison, it has been omitted.

The total CO<sub>2</sub> emissions  $\mu_1$  and  $\mu_2$ , for the first and second case respectively, are functions of the normalised operation time of the auxiliary generators  $\tau_{op}$  — defined as the operation time of the auxiliary system over the total operation time of the system —, of the auxiliary system emissions  $\mu_D$  and  $\mu_{FC}$ , for the Diesel and fuel cell systems respectively, and of the emission  $\mu_G$  related to the production and distribution of the electricity taken from the grid:

$$\mu_1 = \mu_D \tau_{op} + \mu_G (1 - \tau_{op}) \quad (1.2.1)$$

$$\mu_2 = \mu_{FC} \tau_{op} + \mu_G (1 - \tau_{op}) \quad (1.2.2)$$

where  $\mu_D = 5.1$ ,  $\mu_{FC} = 2.9$ , and  $\mu_G$  depends on the power plant composition.

Figure 1.13 compares the CO<sub>2</sub> emissions of these two systems in the cases when the power plants are either only coal, oil, or natural gas based. Figure 1.14 makes the same comparison with respect to the American, French and Italian power plant compositions.

Whatever the composition of the power plant, the use of a fuel cell system for this purpose is justified, since the CO<sub>2</sub> emissions of such a system are always lower than those produced by a Diesel system.

#### 1.2.3.2. *Grid connected cases:*

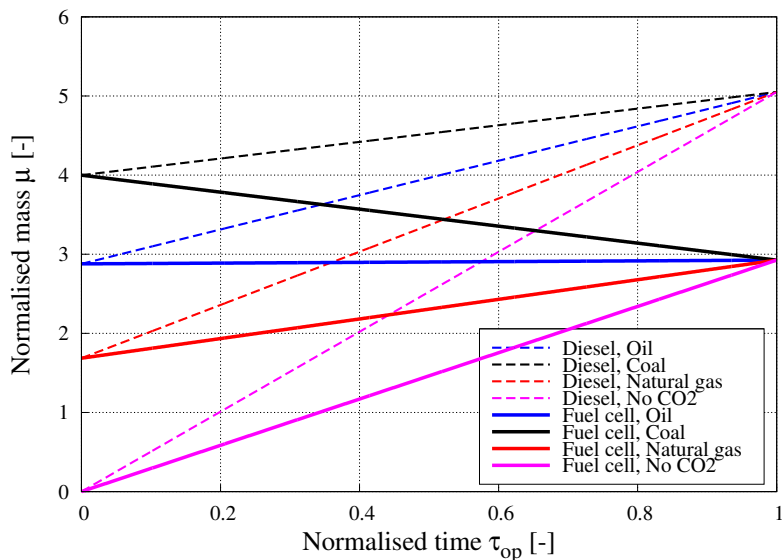
##### *battery (3) versus fuel cell with electrolyser (4)*

In cases 3 and 4, represented in Figure 1.11 (3) and (4), the loads are always connected to the grid, but a storage based backup system is present. In case 3 the backup system is ensured by a traditional bank of batteries, while in case 4 the energy storage system consists in an electrolyser producing hydrogen, and a fuel cell converting hydrogen back into electricity.

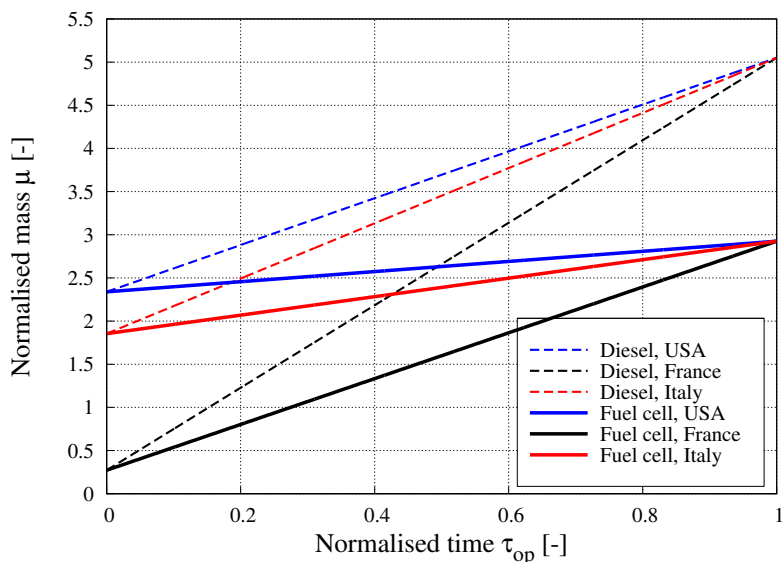
The total CO<sub>2</sub> emissions  $\mu_3$  and  $\mu_4$ , for the third and fourth case respectively, are functions of the normalised operation time of the auxiliary generators  $\tau_{op}$ , of the storage system emissions  $\mu_B$  and  $\mu_{FCE}$ , for the battery and fuel cell-electrolyser systems respectively, and of the emission  $\mu_G$  related to the production and distribution of the electricity taken from the grid:

$$\mu_3 = \mu_B \tau_{op} + \mu_G (1 - \tau_{op}) \quad (1.2.3)$$

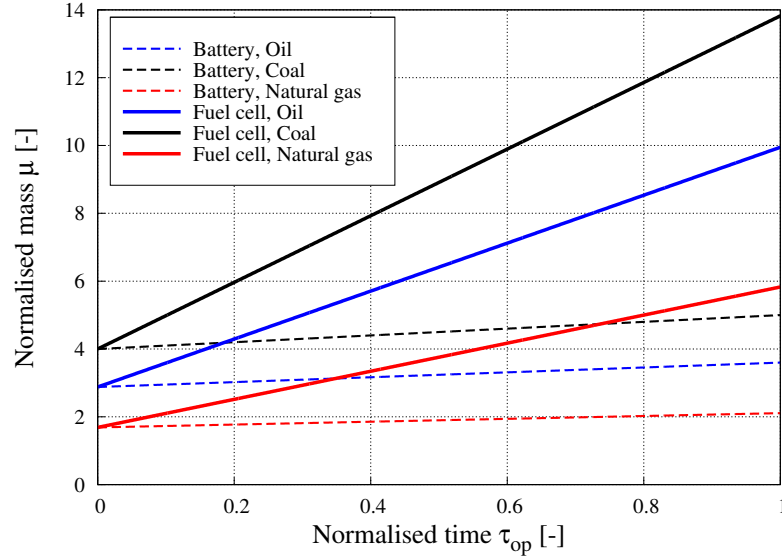
$$\mu_4 = \mu_{FCE} \tau_{op} + \mu_G (1 - \tau_{op}) \quad (1.2.4)$$



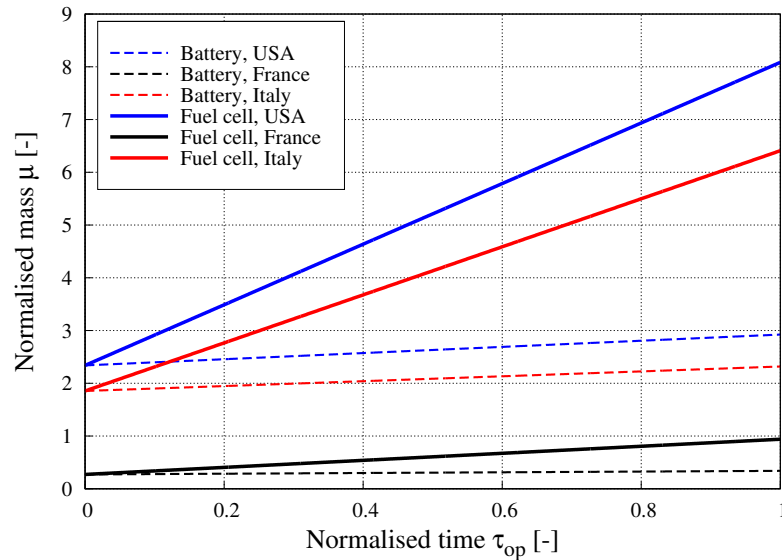
**Figure 1.13.** Normalised production of CO<sub>2</sub> emissions  $\mu$  versus normalised operation time  $\tau_{op}$ , for fuel cell and Diesel systems in four electricity production scenarios: either only from coal, from oil, from natural gas, or from no-CO<sub>2</sub> emitting sources.



**Figure 1.14.** Normalised production of CO<sub>2</sub> emissions  $\mu$  versus normalised operation time  $\tau_{op}$ , for fuel cell and Diesel systems in three electricity production scenarios: American, French, and Italian.



**Figure 1.15.** Normalised production of CO<sub>2</sub> emissions  $\mu$  versus normalised operation time  $\tau_{op}$ , for fuel cell-electrolyser and battery systems in three scenarios of electricity production: either only from coal, from oil, or from natural gas.



**Figure 1.16.** Normalised production of CO<sub>2</sub> emissions  $\mu$  versus normalised operation time  $\tau_{op}$ , for fuel cell-electrolyser and battery systems in three scenarios of electricity production: American, French, and Italian.

where  $\mu_B$ ,  $\mu_{FCE}$ , and  $\mu_G$  depend on the power plant composition.

Figure 1.15 compares the CO<sub>2</sub> emissions of these two systems in the cases when the power plants are either only coal, oil, or natural gas based. Figure 1.16 makes the same comparison with respect to the American, French and Italian power plant compositions.

Whatever the composition of the power plant, the use of a fuel cell system for this purpose is not justified since the CO<sub>2</sub> emissions are always higher than those related to a battery based backup system.

#### 1.2.3.3. *Stand-alone cases:*

##### *Diesel (5) versus fuel cell with renewable sources (6)*

In cases 5 and 6, represented in Figure 1.12 (5) and (6), the systems are isolated from the grid and a main power supply is required. In case 5 this is ensured by a Diesel electric generator — which is a traditional choice for giving power to remote telecommunication stations in countries like India or Africa, for example —, while in case 6 the main power source consists in a fuel cell. In this case the auxiliary contribution of solar and/or wind renewable sources is often present. Even if it is not traditionally done, it is possible to imagine the introduction of this kind of energy sources in diesel based generators, too. This is why the maximum CO<sub>2</sub> emissions are considered here: the higher the contribution of renewable sources is, the lower the actual CO<sub>2</sub> emissions are.

The maximum emissions in case 5 is  $\mu_{5,M} = \mu_D = 5.1$ , which is about 1.8 times the maximum emission in case 6  $\mu_{6,M} = \mu_{FC} = 2.9$ . This wholly justifies the use of a fuel cell system for such a purpose.

#### 1.2.3.4. *Stand-alone cases:*

##### *renewable (7) with battery versus renewable with fuel cell and electrolyser (8)*

In the last two cases, 7 and 8, represented in Figure 1.12 (7) and (8), the systems are isolated from the grid. Renewable sources — solar and wind energies — power the loads and a storage system is required to compensate the source fluctuations. The storage system consists in a battery bank in case 7 and in a fuel cell-electrolyser system in case 8.

The efficiency of the battery system is  $\eta_7 = \eta_B = 80\%$ , which is 2.5 times the efficiency of the hydrogen/electrolyser system  $\eta_8 = \eta_{FCE} = 32\%$ .

Nevertheless, since the grid is not involved — unlike the cases 3 and 4 —, long-term storage is often required. That is why in this case the fuel cell system, which does not suffer from the problem of self discharge typical of battery systems — hydrogen micro-leakages being neglected —, could win over the latter. The curves of solar and wind production, and the curve of load are mandatory to determine which of the two systems is better for that particular scenario.

#### 1.2.3.5. *Conclusion*

The use of a fuel cell system directly fed with pure hydrogen or natural gas via a reformer is always justified for cases (2) — grid connected fuel cell — and (6) — stand-alone fuel cell with renewable sources —, in which the fuel cell system is meant to be the energy source.

The use of a fuel cell-electrolyser system as a storage system could be justified for case (8) — stand-alone renewable with fuel cell and electrolyser —, due the long-term storage issue, but it is hardly justifiable in case (4) — grid connected fuel cell with electrolyser.

These conclusions are merely based on efficiency and CO<sub>2</sub> emission considerations. Taking into account other variables could lead to different conclusions: for example, there could be other advantages, like a reduction in maintenance or a higher reliability of a fuel cell system compared to a standard lead-acid battery system.

Furthermore, in a fuel cell-electrolyser storage system the maximum output power and the maximum energy that can be stored are independent, unlike in battery systems, and a fuel cell system can be seen as a possible solution for reducing the quantity of lead in telecommunication sites.

#### 1.2.4. Conclusion

Regarding CO<sub>2</sub> emission reduction, there can be advantages in substituting traditional systems with fuel cell systems in the automotive domain, in the stationary domain if both electricity and heat are used, and in the backup system domain.

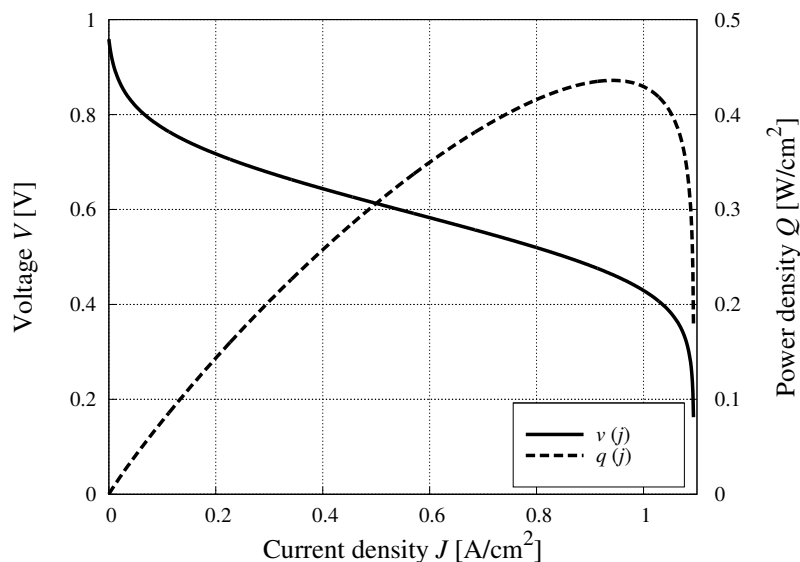
Other common cited advantages are the absence of noise and local pollutant problems, higher efficiencies at partial loads too, and less maintenance in relation to traditional systems.

As for the costs, it is reasonable to expect a standard technology maturity lifecycle. A curious historical example of technology and cost development can be found in Appendix B.

### 1.3. Power electronics for fuel cell systems

In order to use fuel cells practically, they generally need to be coupled with a power converter, since they provide a voltage strongly dependent on the power absorbed by the load, while the load itself generally requires a constant voltage. This is shown in Figure 1.17 for one element of a standard PEM fuel cell and referred to its current density  $J$ .

Thus, a power converter is required to adapt the electrical characteristics of the fuel cell to those required by the load, should this be a Direct Current (DC) or an Alternating Current (AC) one. The histogram in Figure 1.18 gives an idea of the trend of publication production ratio concerning fuel cells in the field of power electronics  $\pi_2$ . The number of articles only takes into account those published by the Institute of Electrical and Electronics Engineers



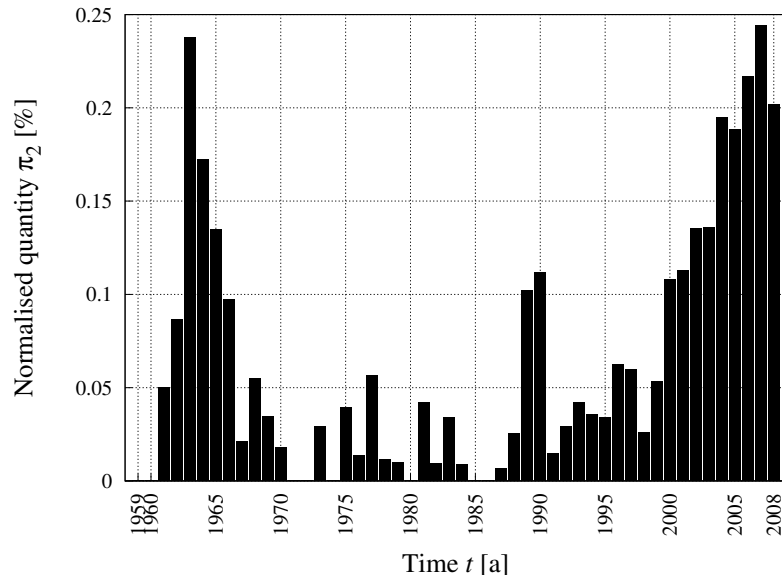
**Figure 1.17.** Voltage  $v$  and power density  $q$  of a single fuel cell typical element versus its current density  $j$ . The voltage varies from about 1 V to about 0.5 V when the power goes from zero to its maximum value.



(IEEE) society and it reflects the trend shown in Figure 1.10, highlighting the growing interest that started during the 1990s. The numerical data is presented in Appendix C.

Several types of converters and applications have been developed and described since the 1960s for different applications: from a 400 Hz DC/AC converter for aerospace of 1964 [30] to a DC/AC converter for hybrid photovoltaic and fuel cell applications of 1988 [31]; from considerations on the use of fuel cells for dispersed generation of 1973 [32] to the development of fuel cell power sources for bus transport of 1990 [33]. Furthermore, in the last years of the 20<sup>th</sup> century, works on direct methanol and proton exchange membrane fuel cells have also appeared, like those described in [34] and in [35] respectively.

Recently, and even more so in the last decade, articles about DC/DC converters have been published. They are used in combination with DC/AC converters [36 – 39], or alone [40 – 45]. Two quite recent articles of DC/AC converters for fuel cell applications should be cited [46, 47]. They present a solution for grid connected renewable DC sources, in which the DC/AC stage is realised with a line frequency commutated voltage source inverter.



**Figure 1.18.** Ratio  $\pi_2$  of fuel cell related articles over all the articles published by the Institute of Electrical and Electronics Engineers (IEEE) society, ordered by year  $t$ . Search criteria for fuel cell related articles within the “ieeexplore” site: terms “fuel cell” in “All Fields”. Search criteria for all the articles: terms “e\*” in “All Fields”.

Except these two last examples, the general trend in power converters reflects an increasing in the switching frequency and a decreasing in the power converter volume. This has led to the possibility of integrating the controller directly onto the silicon wafer, with switching frequencies in the range of mega Hertz [48].

Furthermore, reference [49] presents a special topology that cannot be reconducted to the standard structures present in the literature and leaves room for future developments.

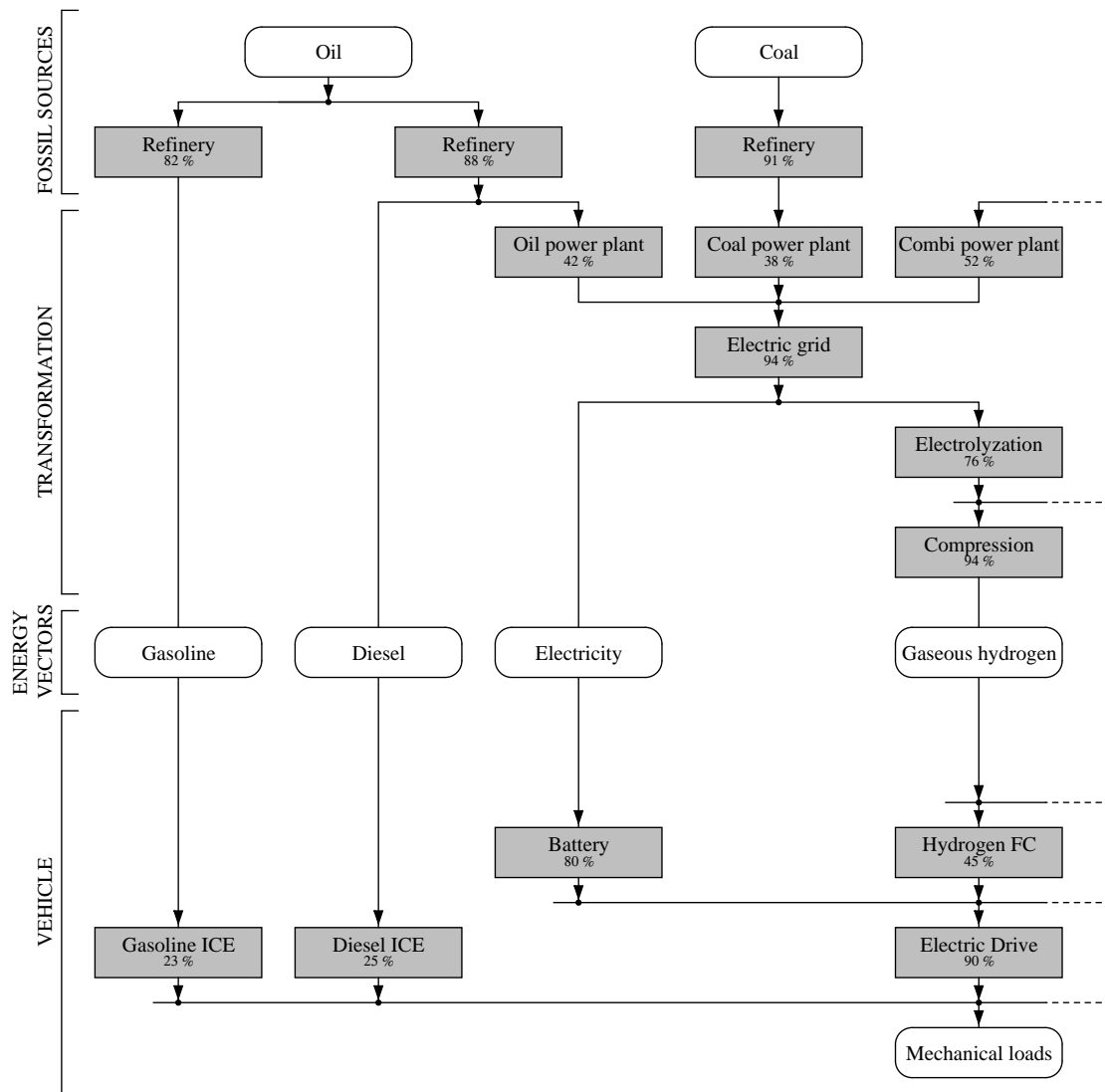
#### **1.4. Conclusion**

After presenting an excursus on fuel cell history and after introducing the most common types of fuel cells, the focus shifted on fuel cell systems and on their applications. Several possible applications of fuel cell systems have been analysed and compared using the CO<sub>2</sub> emission level as a comparison term. It turned out that there are cases in which fuel cell systems can be more interesting than their traditional counterparts: grid connected or stand-alone backup systems can be mentioned as an example. Then, the impact of fuel cells on power electronics has been shown, confirmed by the more and more abundant literature in these fields.

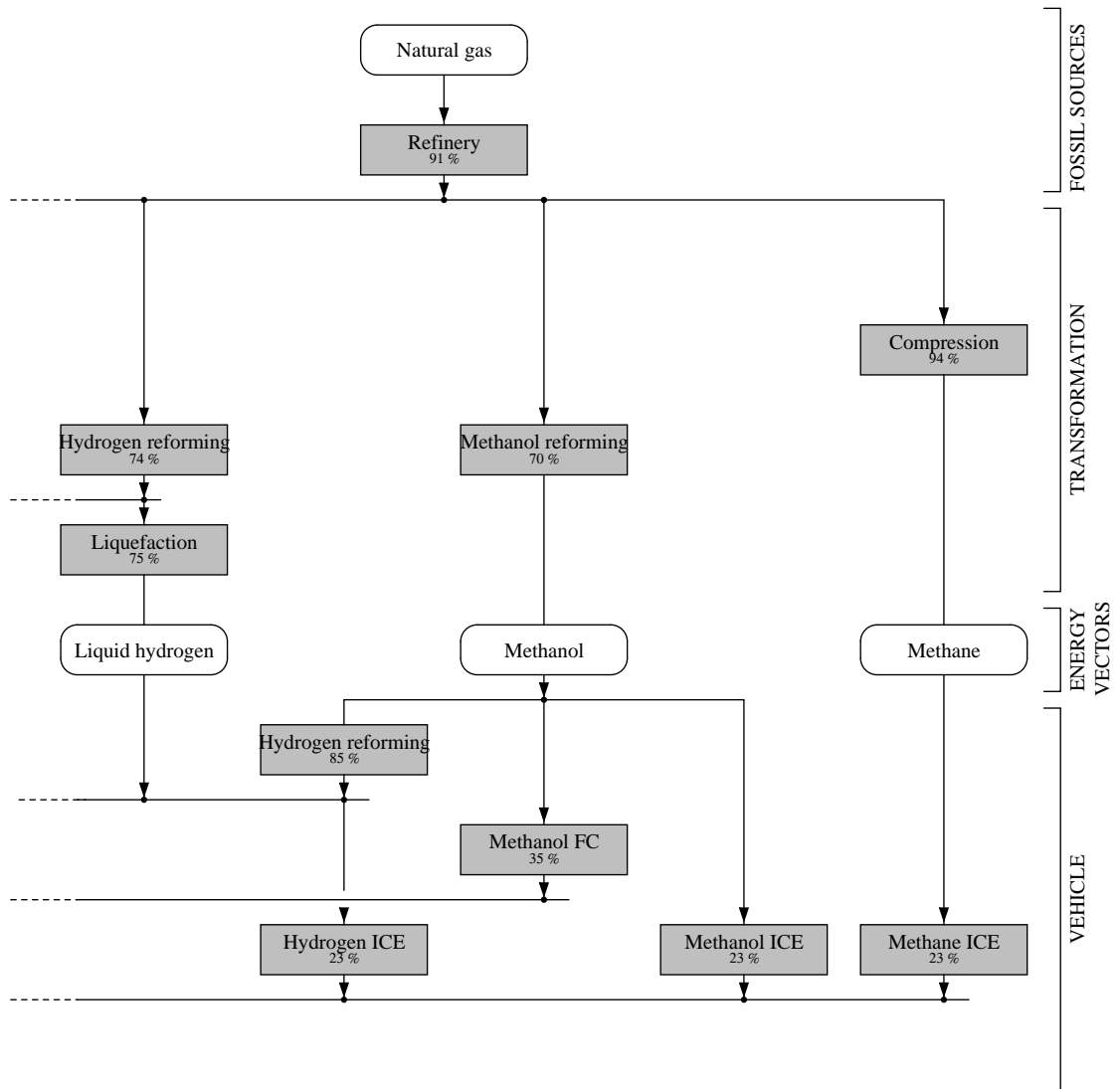
In the next chapter, a description of power converter types will be followed by a proposed sizing procedure for fuel cell systems.

	GVB	DCFC	SOFC	MCFC	AFC	PAFC	DMFC	PEMFC
1800	Nicholson & Ritter							
1832	Faraday							
1838	Schönbein							
1839	<b>Grove</b>							
1842	Grove							
1843	Schönbein							
1882	Strutt							
1889	<b>Mond &amp; Langer,</b> Wright & Thompson							
1893	Ostwald							
1894		Ostwald						
1896		<b>Jacques</b>						
1899			Nernst					
1900			Nernst & Wild					
1902					US Patent			
1904		Haber & Brunner						
1912		Baur & Ehrenberg						
1932					<b>Bacon</b>			
1935		<b>Baur &amp; Brunner</b>						
1937			<b>Baur &amp; Preis</b>					
1939					Bacon			
1946			<b>Davtyan</b>		Davtyan, Bacon			
1951							Kordesh & Marko	
1959					Allis Chalmers			
1960				<b>Broers &amp; Ketelaar,</b> Baker, Bacon				<b>Grubb &amp; Niedrach</b>
1962		<b>Weissbart &amp; Ruka</b>			Allis Chalmers, <b>Pratt &amp; Whitney</b>			General Electric
1963							Murray & Grimes	
1965					Pratt & Whitney, Niedrach & Alford		Williams, Termny & Ciprios, Binder	Gemini
1967						<b>Pratt &amp; Whitney</b>		
1972								<b>Grot</b>
1975						Pratt & Whitney		
1977						Pratt & Whitney		
1986								Raistrick
1989							<b>Verbrugge</b>	
1990								<b>Ballard</b>
1991						Goi		
1992							Jet Propulsion Lab	
1998								Plug Power
2000			NFCR & SCA Edison					
2008								<b>Honda</b>

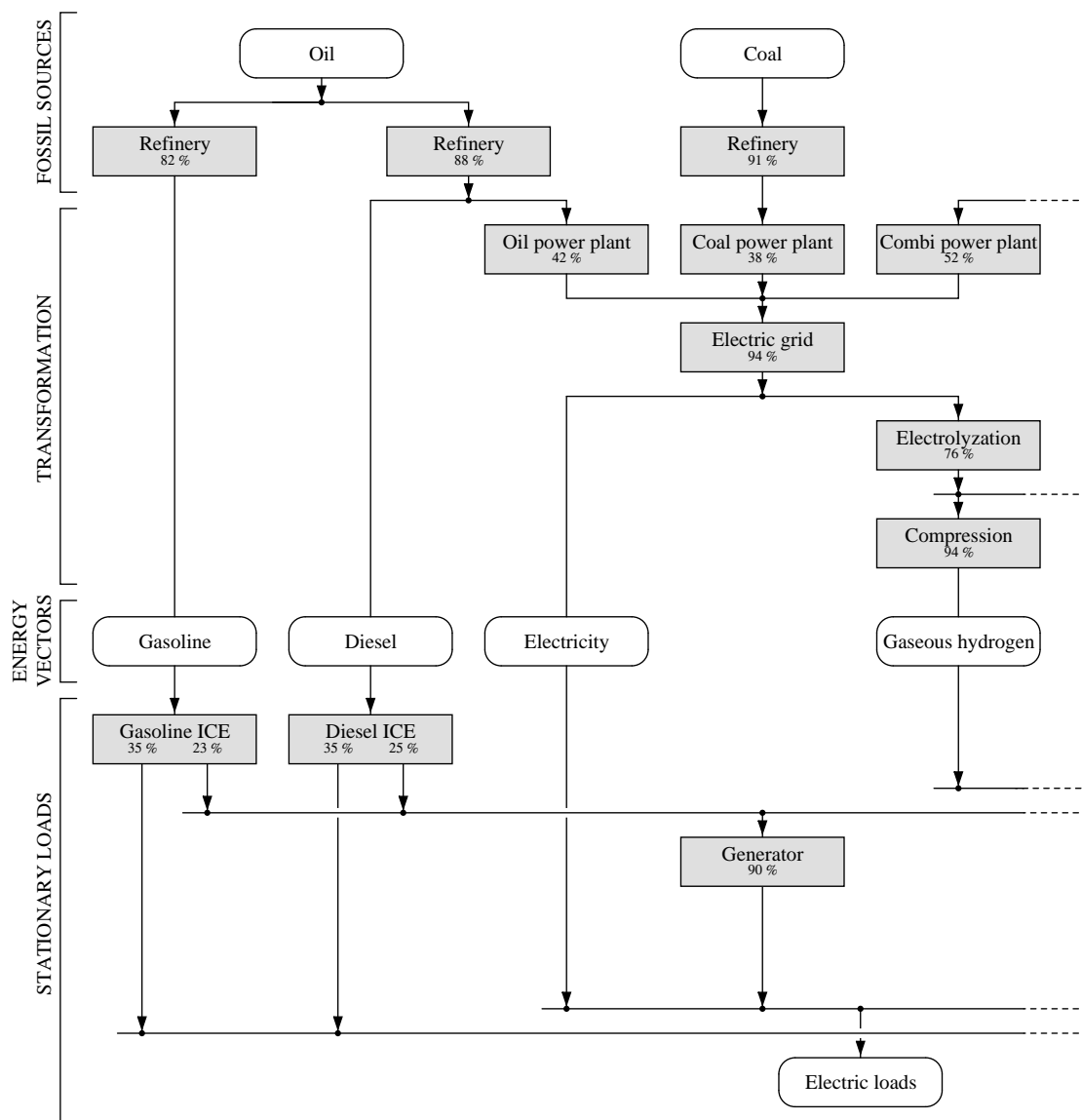
**Table 1.7.** Summary of the main actors and events in the fuel cell history, where the most significant ones have been highlighted. Acronyms: Gaseous Voltaic Battery (GVB), Direct Coal Fuel Cell (DCFC), Solid Oxide Fuel Cell (SOFC), Molten Carbonate Fuel Cell (MCFC), Alkaline Fuel Cell (AFC), Phosphoric Acid Fuel Cell (PAFC), Direct Methanol Fuel Cell (DMFC), Proton Exchange Membrane Fuel Cell (PEMFC), National Fuel Cell Center Research (NFCR), Southern California (SCA).



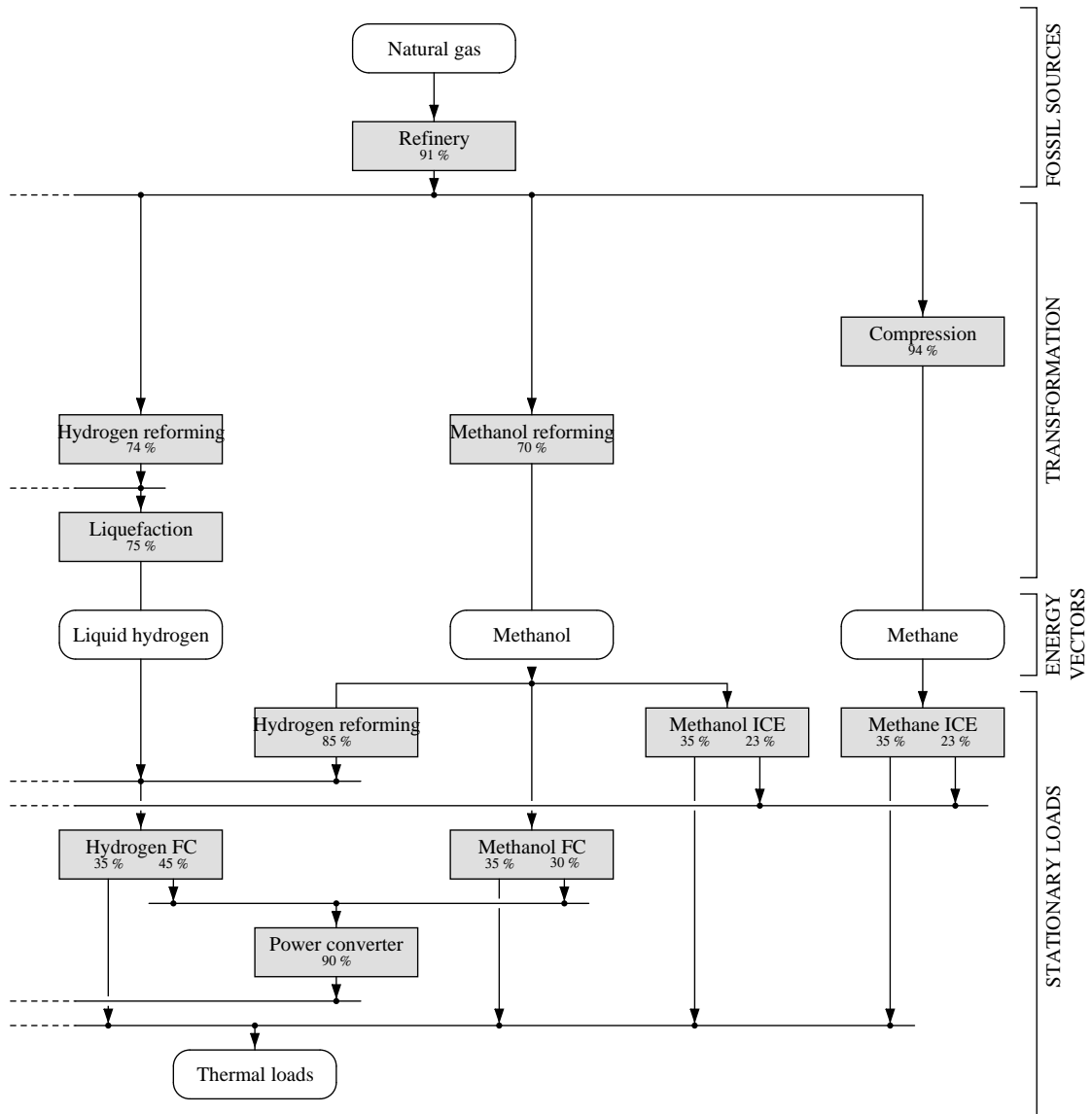
**Figure 1.19.** The different paths through which power flows from oil, coal and natural gas fossil sources to the final user in automotive applications. Different efficiencies and different CO<sub>2</sub> emissions of the overall process depend on the different paths, primary sources and final user solutions. Left side.



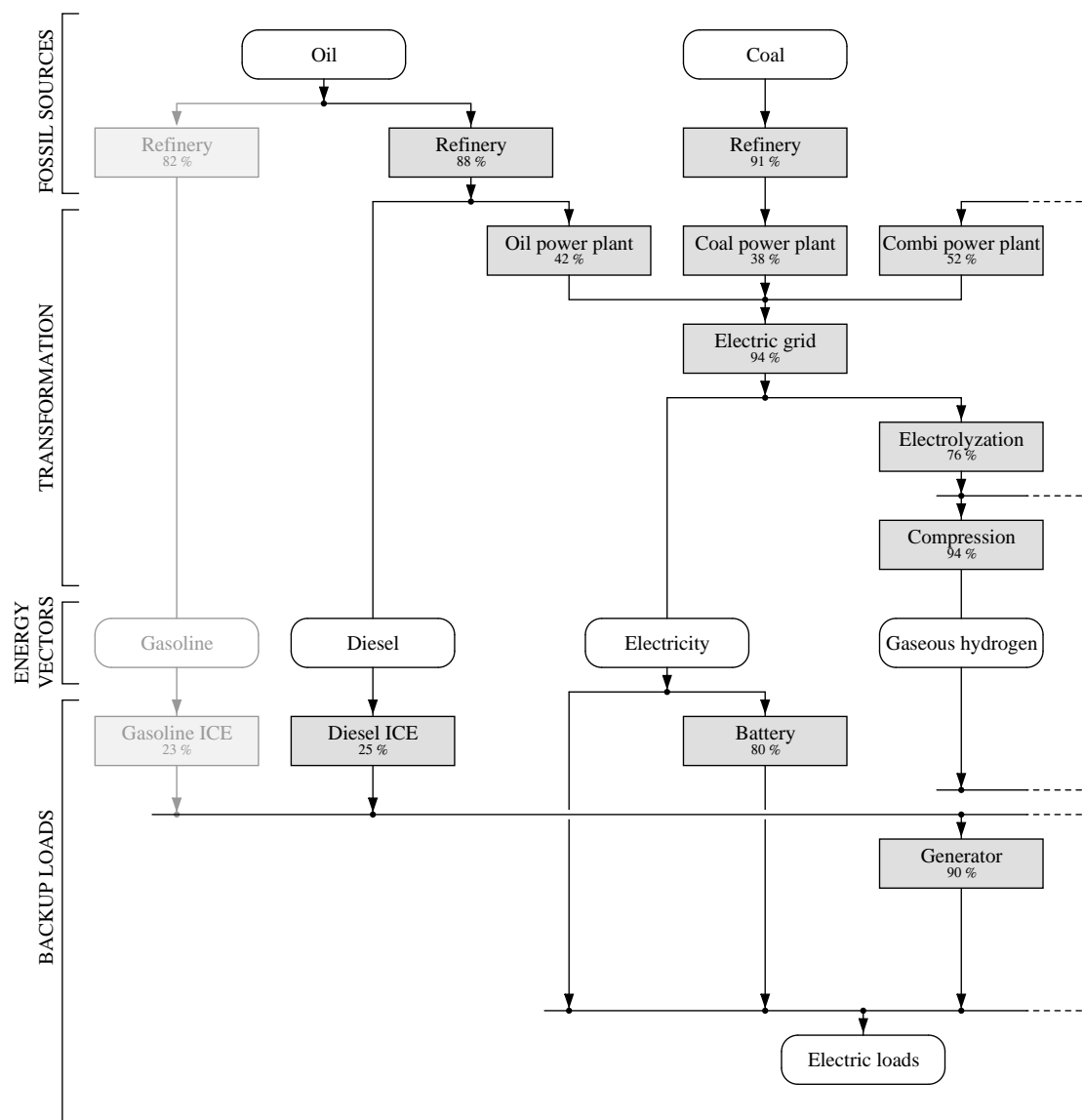
**Figure 1.20.** The different paths through which power flows from oil, coal and natural gas fossil sources to the final user in automotive applications. Different efficiencies and different CO<sub>2</sub> emissions of the overall process depend on the different paths, primary sources and final user solutions. Right side.



**Figure 1.21.** The different paths through which power flows from oil, coal and natural gas fossil sources to a fixed user, like a domestic or industrial one. The user can use just electric energy, or can use both electric and thermal energy. In the latter case Combined Heat and Power (CHP) systems will be adopted and the overall efficiency will be higher. Different efficiencies and different CO<sub>2</sub> emissions of the overall process depend on the different paths, primary sources and final user solutions. Left side.

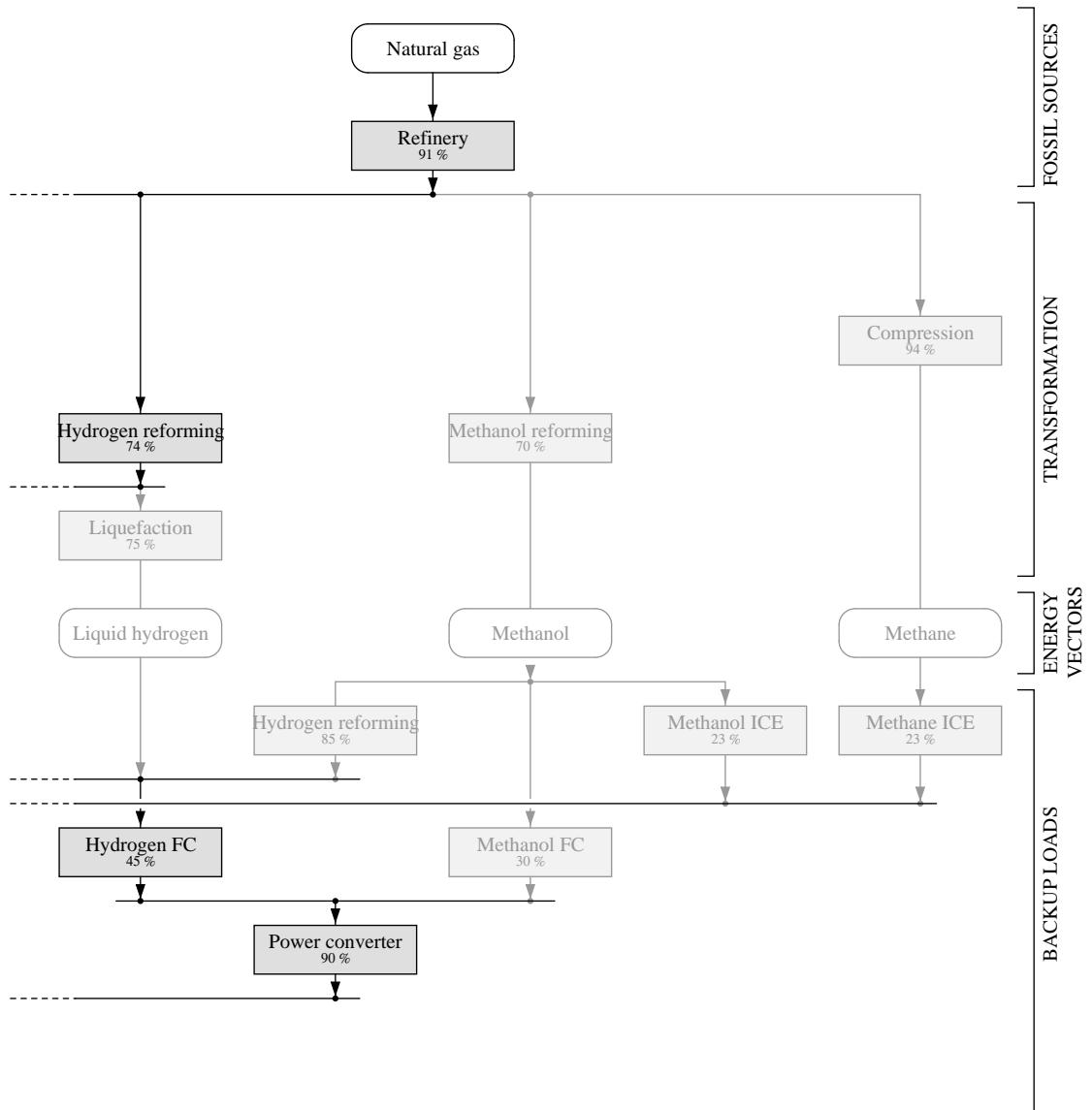


**Figure 1.22.** The different paths through which power flows from oil, coal and natural gas fossil sources to a fixed user, like a domestic or industrial one. The user can use just electric energy, or can use both electric and thermal energy. In the latter case Combined Heat and Power (CHP) systems will be adopted and the overall efficiency will be higher. Different efficiencies and different CO<sub>2</sub> emissions of the overall process depend on the different paths, primary sources and final user solutions. Right side.



**Figure 1.23.** The different paths through which power flows from oil, coal and natural gas fossil sources to the final user in backup applications. Different efficiencies and different CO<sub>2</sub> emissions of the overall process depend on the different paths, primary sources and final user solutions. Left side.





**Figure 1.24.** The different paths through which power flows from oil, coal and natural gas fossil sources to the final user in backup applications. Different efficiencies and different CO<sub>2</sub> emissions of the overall process depend on the different paths, primary sources and final user solutions. Right side.



## CHAPTER 2

### SIZING PROCEDURE

In this chapter an introduction on the basic types of power converters that can be used in fuel cell systems will be given. Then, a sizing and design procedure for fuel cell systems will be presented, in which the mutual implications in the choice of the fuel cell stack and of the power converter are presented.

#### 2.1. Power converter types

Power converter types can be classified between isolated and non-isolated converters. In isolated converters, the secondary side of the converter is floating in respect to the primary side, while in non-isolated converters the secondary side and the primary side are both referred to the same ground.

The insulation is achieved through at least one transformer, meaning that an isolated converter is generally bulkier, heavier and more expensive than a non-isolated converter with the same performance. On the other hand, insulation could be required for safety reasons, and the presence of a transformer, whose winding turn ratio can be arbitrarily chosen, leads to a higher flexibility in the voltage conversion ratio between input and output.

A second classification, both valid in the case of isolated and non-isolated converters, is based on the input  $V_i$  and output  $V_o$  voltages, in which converters are divided into step-down only, step-up only and step-up/step-down converters:

- step-down only converter, when  $V_o < V_i$ ;

- step-up only converter, when  $V_o > V_i$ ;
- step-up/step-down converter, when  $V_o < > V_i$ .

The number of topologies of such converters is very high, so the scope of this dissertation has been restricted to non-isolated DC/DC converters. Unless isolation is explicitly required, these topologies should be preferred: being simpler, they are also cheaper and more efficient. The three basic topologies for the three cases above are:

- the buck converter, as a step-down only converter;
- the boost converter, as a step-up only converter;
- the buck-boost converter, as a step-up/step-down converter.

The basic schematics of these three topologies are presented in Figure 2.1, along with their control characteristics. These three topologies are composed by one switch, one diode, one inductor and a capacitor. The switch gate is controlled by an external circuit, while the diode turns on and off naturally.

Their input/output average behaviour is described by the following functions — representing the transfer ratio  $\Pi$  between input and output voltages —, both for the Continuous Conduction Mode (CCM) and Discontinuous Conduction Mode (DCM), in which  $\Pi_{\text{BU}}$  stands for the buck converter,  $\Pi_{\text{BO}}$  for the boost converter, and  $\Pi_{\text{BB}}$  for the buck-boost converter [50]:

$$\Pi_{\text{BU}} = \begin{cases} \delta & \text{in CCM} \\ \frac{\delta^2}{1 + \frac{\delta^2}{2\lambda_o}} & \text{in DCM} \end{cases} \quad (2.1.1)$$

$$\Pi_{\text{BO}} = \begin{cases} \frac{1}{1 - \delta} & \text{in CCM} \\ 1 + \frac{\delta^2}{2\lambda_o} & \text{in DCM} \end{cases} \quad (2.1.2)$$

$$\Pi_{\text{BB}} = \begin{cases} \frac{\delta}{1-\delta} & \text{in CCM} \\ \frac{\delta^2}{2\lambda_o} & \text{in DCM} \end{cases} \quad (2.1.3)$$

where:

$$\Pi_{(\text{BU,BO,BB})} = \frac{v_o}{v_i}; \quad \delta = \frac{T_{\text{on}}}{T}; \quad \lambda_o = \frac{i_o}{I_b}; \quad I_b = \frac{V_i}{Lf} \quad (2.1.4)$$

and  $\delta$  the duty cycle,  $T_{\text{on}}$  the time during which the converter switch is closed,  $\lambda_o$  the normalised output current,  $I_b$  the base reference current,  $L$  the value of the inductance  $L$ , and  $f = 1/T$  the switching frequency, where  $T$  is the switching period.

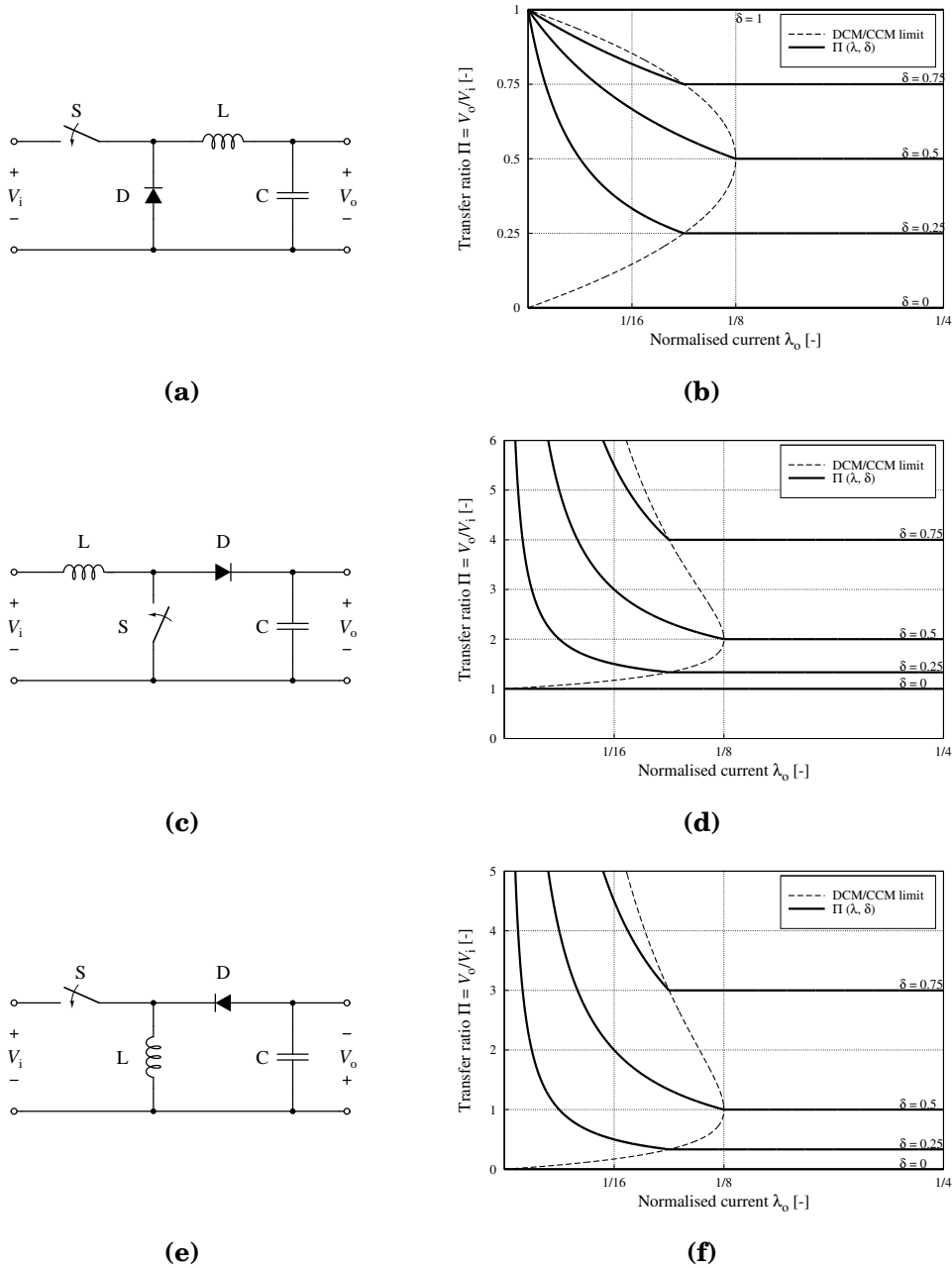
The distinction between CCM and DCM is necessary because the behaviour of each converter completely changes between the two modes. CCM is characterised by the fact that the inductance current and its magnetic field are always positive, while in DCM they may both reach zero.

The analysis of these topologies shows that, in CCM, the average value of the current in the inductance is imposed by the load, and thus the output voltage can be independently chosen. On the contrary, in DCM, the average value of the current in the inductance and the output voltage are no longer independent from each other [50, 51].

As a consequence, in CCM the voltage ratio  $\Pi$  is only a function of the duty cycle  $\delta$ , while in DCM the voltage ratio  $\Pi$  is both a function of the duty cycle  $\delta$  and of the output current, represented by the normalised output current  $\lambda_o$ .

In the choice of one of these three topologies, the following three factors should be taken into account:

- input current ripple;
- inductance current ripple;
- sizing factor.



**Figure 2.1.** Principle schematics of the buck (a), boost (c) and buck-boost (e) converters, and their control characteristics (b),(d) and (f).  $V_i$  is the input voltage,  $V_o$  is the output voltage,  $\Pi = V_i/V_o$  is the ratio between input and output voltages,  $\delta$  is the duty cycle, and  $\lambda_o$  is the normalised output current. In the control characteristics, the area on the left of the DCM/CCM limit represents the points in which the converter can operate in Discontinuous Conduction Mode (DCM), while the right area represents the points in which the converter can operate in Continuous Conduction Mode (CCM).

### 2.1.1. Input current ripple

In the literature, information concerning the effects of current ripple on a fuel cell stack was quite hard to find, according to what was stated in [52]: “At present there is little endurance data to show how such loads can affect the fuel cell over extended periods of time e.g., greater than several thousand hours!” (2003). The same article reported that a consensus has not even been reached yet on the definition of current ripple. This shows that this aspect has not been exhaustively studied yet. A quite recent article presented a case study of the effect of power electronics on fuel cells, in which two different stacks had been run for several hours: a constant DC current was imposed on the first one, while the second had the same constant DC current with a superimposed current ripple. The degradation of the two stacks was compared [53].

Nevertheless, when dealing with current ripples, [54] suggested to distinguish between:

- low frequency: 10 mHz – 1 Hz;
- medium frequency: 1 Hz – 10 kHz;
- high frequency: 10 kHz – 100 kHz.

Low frequency ripples are mainly related to load variations — fluctuating power from DC/AC power converters generates current ripples in the medium frequency range —, while high frequency ripples are due to power converter switching.

Medium frequency current ripples are characterised by a fundamental equal to twice the output AC frequency — generally 50 Hz or 60 Hz — and are present when single phase DC/AC converters are used. In [55], two limits were given: the first suggested to limit the current ripple to 15 % of the rated current, while the second limited the current ripple to 24.7 % RMS (35 % peak-peak).

As for the high frequency ripple — more than 10 kHz —, information is harder to find. Exergy Fuel Cells indicated a 10 % peak-peak limit, while [55] just mentioned that “it is easily filtered via a small high frequency capacitive filter”. Reference [54] noted that high frequency should be transparent to the fuel cell, because of the large double layer capacitor effect (see 4.1.5), too.

From the point of view of power converters, boost converters, when working in CCM, always absorb continuous currents: their input current ripple coincides

with the inductance current ripple. Instead, buck and buck-boost converters, whether working in CCM or in DCM, always absorb discontinuous currents: then, the input current ripple is higher. Choosing a buck or buck-boost converter leads to larger — and more expensive — input filters than choosing boost converters.

As a rule of thumb in the sizing process of a power converter for fuel cell systems, [52] reported that “to ensure minimal impact to the performance of the fuel cell, as well as its durability, fuel cell developers would prefer to specify as little ripple as possible, e.g., below 2 % of the theoretical fuel cell current”, and “that to ensure negligible inverter ripple impact, inverter frequencies need to be above 120 Hz, or have ripple factors less than 4 %.”

### 2.1.2. Inductance current ripple

One of the effects of the current ripple on the power converter inductance is to increase the ohmic losses in the inductor itself. A comparison between the inductance current ripple follows.

The amplitude of the normalised inductance L current ripples are shown in Figure 2.2 for the buck ( $\Delta\Lambda_{L,BU}$ ), boost ( $\Delta\Lambda_{L,BO}$ ) and buck-boost ( $\Delta\Lambda_{L,BB}$ ) in the case of CCM. They are defined as:

$$\Delta I_{L,BU} = \frac{V_i}{Lf} \Pi_{BU} (1 - \Pi_{BU}) \quad (2.1.5)$$

$$\Delta I_{L,BO} = \frac{V_i}{Lf} \frac{\Pi_{BO} - 1}{\Pi_{BO}} \quad (2.1.6)$$

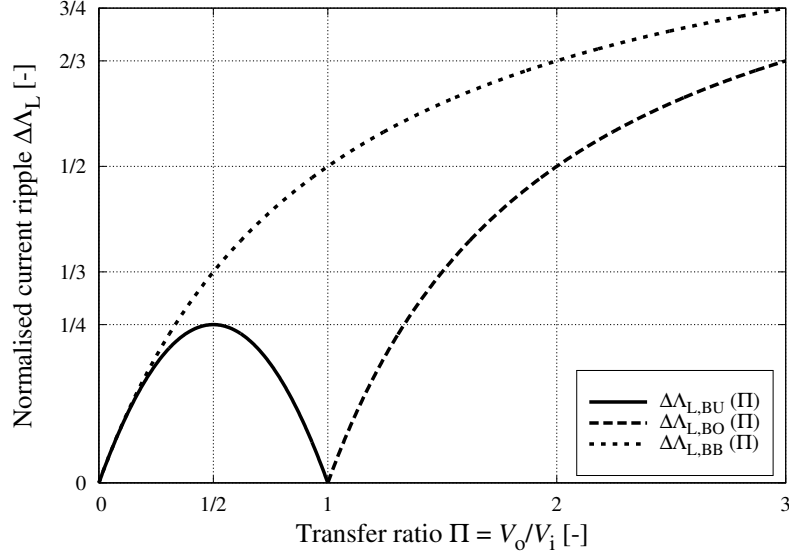
$$\Delta I_{L,BB} = \frac{V_i}{Lf} \frac{\Pi_{BB}}{1 + \Pi_{BB}} \quad (2.1.7)$$

and after normalisation using  $I_b$  as the base current

$$\Delta\Lambda_{L,BU} = \frac{\Delta I_{L,BU}}{I_b} = \Pi_{BU} (1 - \Pi_{BU}) \quad (2.1.8)$$

$$\Delta\Lambda_{L,BO} = \frac{\Delta I_{L,BO}}{I_b} = \frac{\Pi_{BO} - 1}{\Pi_{BO}} \quad (2.1.9)$$





**Figure 2.2.** Normalised value of the inductance current ripple in a buck converter  $\Delta\Lambda_{L,BU}$ , a boost converter  $\Delta\Lambda_{L,BO}$ , and a buck-boost converter  $\Delta\Lambda_{L,BB}$  versus the transfer ratio  $\Pi$ .

$$\Delta\Lambda_{L,BB} = \frac{\Delta I_{L,BB}}{I_b} = \frac{\Pi_{BB}}{1 + \Pi_{BB}}. \quad (2.1.10)$$

The buck-boost converter always shows the higher input current ripple, so using it in the case with  $\Pi \cong 1$  would constitute a poor solution. If possible, it would be preferable to size the system in order to have  $\Pi < 1$  and to use a buck converter, or to have  $\Pi > 1$  and to use a boost converter.

### 2.1.3. Sizing factor

A comparison between the different topologies can also be made about the sizing factor of the switching elements of power converters. As introduced in [56], it is defined as:<sup>1</sup>

$$\Gamma = \frac{V_M I_M}{P} \quad (2.1.11)$$

<sup>1</sup>In [56], the sizing factor (*facteur de dimensionnement*) was indicated with the symbol  $F_d$ . In accordance with the conventions used in this dissertation, dimensionless quantities are indicated with Greek letters, and thus the symbol  $\Gamma$  is used for the sizing factor.

where  $V_M$  and  $I_M$  are the maximum constraints of the switching element, while  $P$  is the power transferred by the power converter.

For buck, boost and buck-boost converters respectively, the sizing factors of the switching elements are:

$$\Gamma_{BU,S} = \frac{1}{\delta}; \quad \Gamma_{BU,D} = \frac{1-\delta}{\delta} \quad (2.1.12)$$

$$\Gamma_{BO,S} = \frac{1}{1-\delta}; \quad \Gamma_{BO,D} = 1 \quad (2.1.13)$$

$$\Gamma_{BB,S} = \frac{1}{\delta(1-\delta)}; \quad \Gamma_{BB,D} = \frac{1}{\delta} \quad (2.1.14)$$

where  $\Gamma_{BU,S}$  and  $\Gamma_{BU,D}$  are the sizing factors for the switch and diode of the buck converter,  $\Gamma_{BO,S}$  and  $\Gamma_{BO,D}$  are the sizing factors for the switch and diode of the boost converter, and  $\Gamma_{BB,S}$  and  $\Gamma_{BB,D}$  are the sizing factors for the switch and diode of the buck-boost converter [56].

The switch and diode sizing factors can then be combined, in order to obtain a global power converter sizing factor, defined as:

$$\Gamma_{(BU,BO,BB)} = \kappa_S \Gamma_{(BU,BO,BB),S} + \kappa_D \Gamma_{(BU,BO,BB),D} \quad (2.1.15)$$

where  $\kappa_S$  and  $\kappa_D$  determine the weights of the switch and of the diode on the global sizing factor. The following constraints apply to  $\kappa_S$  and  $\kappa_D$ :

$$0 \leq \kappa_S \leq 1 \quad (2.1.16)$$

$$0 \leq \kappa_D \leq 1 \quad (2.1.17)$$

$$\kappa_S + \kappa_D = 1. \quad (2.1.18)$$

Thus, the global sizing factors for buck  $\Gamma_{BU}$ , boost  $\Gamma_{BO}$  and buck-boost  $\Gamma_{BB}$  converters become:

$$\Gamma_{BU}(\delta) = \kappa_S + \frac{1-\delta}{\delta} \quad (2.1.19)$$

$$\Gamma_{BO}(\delta) = 1 + \kappa_S \frac{\delta}{1-\delta} \quad (2.1.20)$$

$$\Gamma_{BB}(\delta) = \frac{1}{\delta} + \kappa_S \frac{1}{1-\delta}. \quad (2.1.21)$$

In order to compare the three topologies, the sizing factors are rewritten as a function of the transfer ratios  $\Pi_{\text{BU}}$ ,  $\Pi_{\text{BO}}$  and  $\Pi_{\text{BB}}$  for the buck, boost and buck-boost converters respectively:

$$\Gamma_{\text{BU}}(\Pi_{\text{BU}}) = \kappa_S + \frac{1 - \Pi_{\text{BU}}}{\Pi_{\text{BU}}} \quad (2.1.22)$$

$$\Gamma_{\text{BO}}(\Pi_{\text{BO}}) = \kappa_S \Pi_{\text{BO}} + (1 - \kappa_S) \quad (2.1.23)$$

$$\Gamma_{\text{BB}}(\Pi_{\text{BB}}) = \frac{1 + \Pi_{\text{BB}}}{\Pi_{\text{BB}}} + \kappa_S (1 + \Pi_{\text{BB}}) \quad (2.1.24)$$

where:

$$\Pi_{\text{BU}} = \delta; \quad \Pi_{\text{BO}} = \frac{1}{1 - \delta}; \quad \Pi_{\text{BB}} = \frac{\delta}{1 - \delta}. \quad (2.1.25)$$

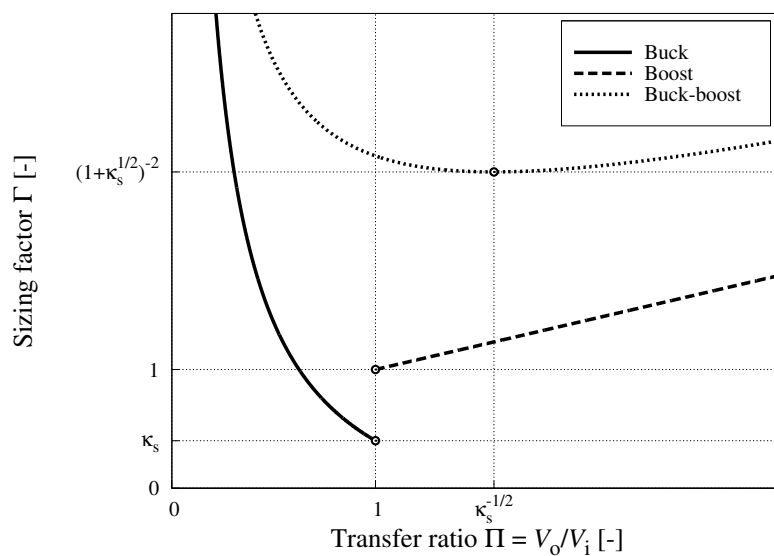
The global sizing factors are shown in Figure 2.3 (a) as a function of the transfer ratio. For completeness, Figure 2.3 (b) also shows the global sizing factors, as a function of the duty cycle. In Figure 2.4 the  $\kappa_S$  and  $\kappa_D$  incidence on the global sizing factors is plotted.

Notice that the buck-boost converter sizing factor is always higher than buck and boost converters, whatever the values of  $\kappa_S$  and  $\kappa_D$  are. As for the inductance current ripple, a buck or boost based solution is preferable to a buck-boost one.

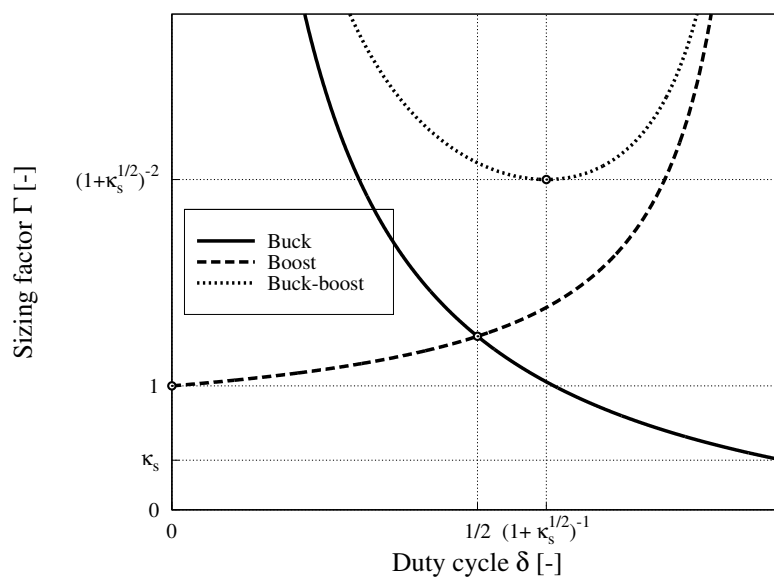
#### 2.1.4. Conclusion

Three basic topologies have been presented and the choice on using one depends on the relation between input and output voltage ranges. The output voltage range is set by the user, while the input voltage range depends on the fuel cell stack choice.

The procedures and considerations used to design such a system are the topic of the next section, in which both the fuel cell and the power converter sizing processes will be taken into account.

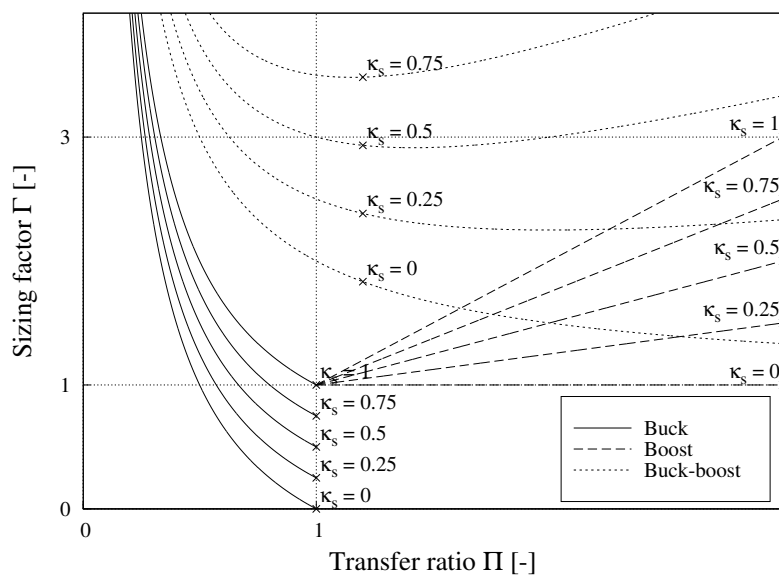


(a)

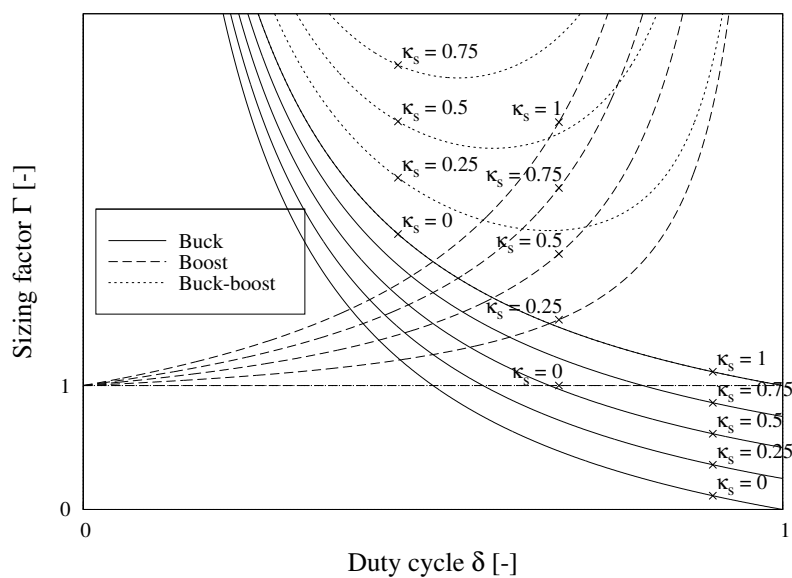


(b)

**Figure 2.3.** Global sizing factor  $\Gamma$  for buck, boost and buck boost converters, versus (a) the transfer ratio  $\Pi$ , (b) the duty cycle  $\delta$ . The minimum points for the three topologies are shown.  $\kappa_S$  indicates the incidence of the switch sizing factor on the global sizing factor, being  $0 \leq \kappa_S \leq 1$ .  $\kappa_D = 1 - \kappa_S$  indicates the incidence of the diode sizing factor on the global sizing factor.



(a)



(b)

**Figure 2.4.** Global sizing factor  $\Gamma$  variation for buck, boost and buck boost converters, versus (a) the transfer ratio  $\Pi$ , (b) the duty cycle  $\delta$ , when  $\kappa_s$  varies from 0 to 1.  $\kappa_s$  indicates the incidence of the switch sizing factor on the global sizing factor, being  $0 \leq \kappa_s \leq 1$ .  $\kappa_D = 1 - \kappa_s$  indicates the incidence of the diode sizing factor on the global sizing factor.

## 2.2. Sizing and design procedure

It is possible to calculate the total fuel cell active surface in the sizing and designing procedure of a fuel cell system, once the output voltage and power ranges are known. This partially defines the characteristics of the fuel cell stack and of the power converter.

Other criteria need to be taken into account to find the optimum solution. Considerations about the cost of a fuel cell system and about suitable power converter types will be presented.

Moreover, information on hydrogen storage systems will be given, as the equivalence between cylinder volume and stored electric energy.

### 2.2.1. Fuel cell active surface

Figure 2.5 shows the voltage  $v(j)$  and power density  $q(j)$  functions versus current density  $j$  of a single element of a fuel cell, in which the current density varies from 0 to the current density limit  $J_1$ .

Unlike the voltage  $v(j)$  function, which is monotonically decreasing, the power density  $q(j)$  function has a maximum  $Q_M$  in  $J_{Q,M}$ .

Therefore,  $J_{Q,M}$  is a current density limit, since making the fuel cell work with current densities  $j > J_{Q,M}$  would result in higher losses for the same output power. There is also a technological limit on the current density a fuel cell can carry. It is called  $J_{t,M}$  in this dissertation and it is related to many different factors, as — for instance — ohmic losses and speed of the reactants in the channels and pipes.

The absolute maximum current density is then defined as the lowest between the two previous current density limits:

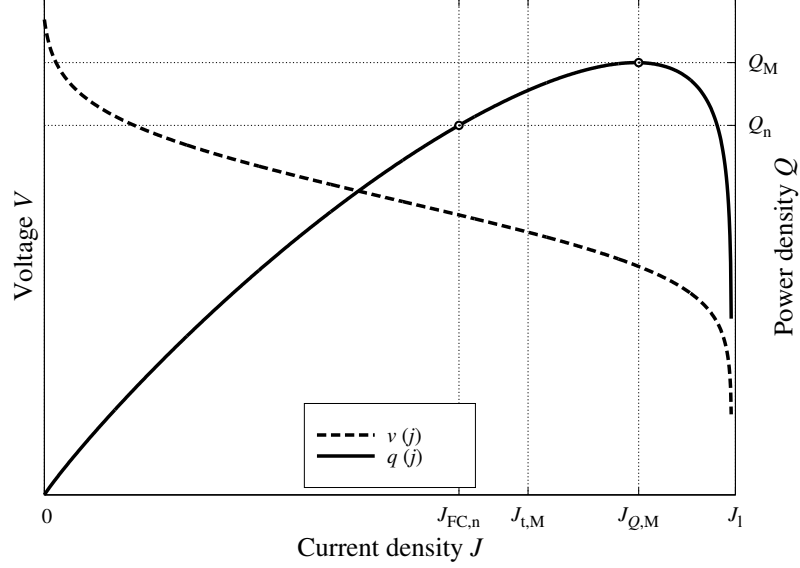
$$J_{a,M} = \min \left\{ J_{Q,M}, J_{t,M} \right\} \quad (2.2.1)$$

and the nominal operative current density is set as

$$J_{FC,n} = \kappa_{FC,n} J_{a,M} \quad (2.2.2)$$

where  $\kappa_{FC,n} < 1$  for safety reasons.

This also sets the nominal power density at which the fuel cell functions:



**Figure 2.5.** The static polarisation  $v(j)$  and the power density  $q(j)$  curves for a single fuel cell element in the  $V - J$  and  $Q - J$  plans respectively, where  $J$  stands for a current density,  $V$  a voltage, and  $Q$  a power density. The maximum power density point  $(J_{Q,M}, Q_M)$ , the operating point  $(J_{FC,n}, Q_n)$ , and the technology current limit  $J_{t,M}$  are shown.

$$Q_n = q(J_{FC,n}). \quad (2.2.3)$$

The nominal power the fuel cell stack needs to provide  $P_{FC,n}$  comes from the maximum system output power  $P_{o,n}$  and a target efficiency for the power converter  $\eta_{PC}$  in a direct calculation:

$$P_{FC,n} = \frac{P_{o,n}}{\eta_{PC}}. \quad (2.2.4)$$

Once the nominal power the fuel cell stack can produce ( $P_{FC,n}$ ) and the nominal power density at which each element can be operated ( $Q_n$ ) have both been established, the total membrane surface required is then determined by:

$$S_T = \frac{P_{FC,n}}{Q_n}. \quad (2.2.5)$$

From the total active membrane surface  $S_T$ , it is possible to find the number of elements  $N$  the fuel is made of, and their surface  $S$ :

$$S_T = S N = \frac{P_{FC,n}}{Q_n} \quad (2.2.6)$$

which has infinite solutions ( $S, N$ ).

Rather than including all the factors that could influence the choice of the best solution into the dissertation, it has been preferred to present the main factors and their mutual relationships:

- fuel cell and power converter costs;
- fuel cell, load and power converter voltage matching;
- types of power converters.

These considerations will lead to the identification of one or more possible solutions. Then, only the simulating-prototyping process, along with the technological and commercial experiences of an industrial partner, will determine the best solution.

### 2.2.2. Cost of a fuel cell system

First, a cost function of a fuel cell stack system will be determined, showing how its cost depends on the element surface. Then, it will be extended to a fuel cell system, in which both the fuel cell stack and the power converter costs will be taken into account. Later on, the cost function will be expressed as a function of the fuel cell element surface as well.

#### 2.2.2.1. Fuel cell stack cost

The total cost of a fuel cell stack  $C_{FC}$  is determined by the sum of three parts:

$$C_{FC} = C_1 + C_2 + C_3 \quad (2.2.7)$$

where  $C_1$  is the cost of the membrane electrode assembly (MEA),  $C_2$  of the bipolar plates, and  $C_3$  of the fuel cell stack heads and of other fixed costs.

The details of these three variables are:

$$C_1 = c_M S_T \quad (2.2.8)$$



$$C_2 = (c_P S + C_P) N = c_P S_T + C_P N \quad (2.2.9)$$

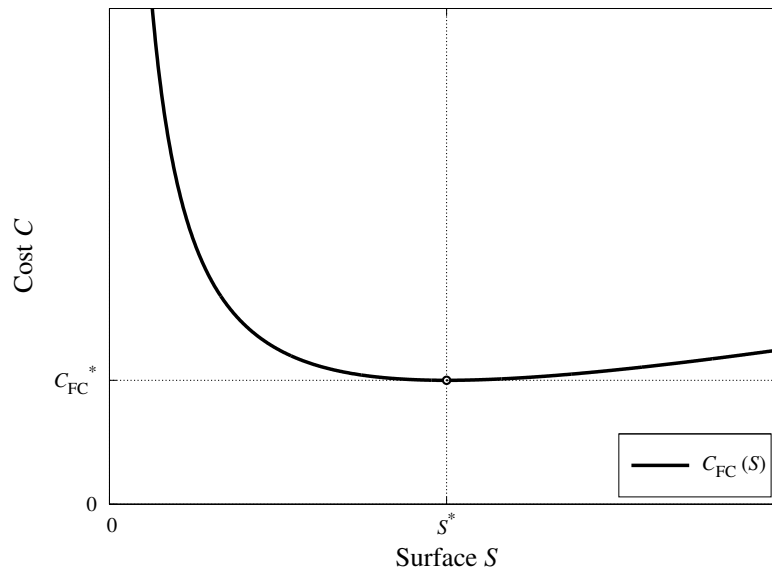
$$C_3 = c_H S + C_F \quad (2.2.10)$$

where  $c_M$  is the variable cost of the MEA,  $c_P$  is the variable cost of the bipolar plates,<sup>2</sup>  $C_P$  is the fixed cost of each bipolar plate,  $c_H$  is the variable cost for the fuel cell stack heads,<sup>3</sup> and  $C_F$  the fixed cost of a fuel cell stack.

The total cost of the fuel cell stack, which is expressed as a function of the element surface, becomes:

$$C_{FC}(S) = C_F + (c_M + c_P) S_T + c_H S + C_P S_T \frac{1}{S} \quad (2.2.11)$$

whose behaviour is plotted in Figure 2.6.



**Figure 2.6.** Cost of a fuel cell stack  $C_{FC}$  as a function of the element surface  $S$  in the plane  $S - C$ , where  $S$  is a surface and  $C$  is a cost. The minimum point  $(S^*, C_{FC}^*)$  is shown.

<sup>2</sup>The variable cost of the bipolar plates is the sum of the cost of the metal and of the machining operation, which are both directly proportional to the plate surface.

<sup>3</sup>The variable cost of the fuel cell stack heads is the sum of the cost of the metal and of the connecting system, which are both directly proportional to the plate surface, being the current directly proportional to the plate surface as well.

The function reaches a minimum in:

$$S^* = \sqrt{\frac{C_P}{c_H} S_T} \quad (2.2.12)$$

and its value is:

$$C_{FC}^* = C_F + (c_M + c_P) S_T + 2 \sqrt{c_H S_T C_P}. \quad (2.2.13)$$

If  $S^* > S_T$ , as in the case of the Italian manufacturer Exergy Fuel Cells, then all the possible values for  $S$  are located on the descending part of the curve. As a consequence, the cheapest fuel cell is the one with the largest surface per element.

#### 2.2.2.2. Power converter cost

Whichever converter type has been chosen, a maximum current limit associated to an assigned value of the power losses in conduction mode in the power converter switch can be determined by experimental and technological considerations.

Assuming the main switch is a MOSFET (Metal-Oxide-Semiconductor Field-Effect Transistor) switch, the resistance between drain and source during the conducting state is proportional to the maximum voltage the switch is able to block:

$$R_{DS,on} = K_{RV} V_M. \quad (2.2.14)$$

The maximum voltage is then proportional to the sum of the voltage the switch should block in ideal conditions and of the overvoltage due to the inductance of the connections:

$$V_M = V_B + L_C \left( \frac{di}{dt} \right)_M. \quad (2.2.15)$$

The relation between the current derivative and the nominal current depends on the commutation time, but they can be considered — in a first order approximation — directly proportional:

$$\left( \frac{di}{dt} \right)_M = K_{dt} I_{i,n}. \quad (2.2.16)$$

The conduction power losses on the switch are then:

$$P_{l,S,p} = R_{DS,on} I_{rms}^2 \quad (2.2.17)$$

$$I_{rms} = K_{rms} I_{i,n} \quad (2.2.18)$$

leading to:

$$P_{l,S,p} = K_{RV} K_{rms}^2 V_B \left[ \left( 1 + \frac{L_C K_{dl}}{V_B} I_{i,n} \right) I_{i,n}^2 \right]. \quad (2.2.19)$$

This means that once the switch technology is known — and so  $K_{RV}$  —, and once everything has been done to make  $L_C$  as low as possible, the power losses  $P_{l,S,p}$  only depend on the value of the maximum current  $I_{i,n}$ .

If  $N_p$  switching elements are put in parallel, the total nominal current  $I_{FC,n}$ , and the total switch power losses  $P_{l,S}$  are expressed by:

$$I_{i,n} = \frac{I_{FC,n}}{N_p} \quad (2.2.20)$$

$$P_{l,S} = N_p P_{l,S,p} = N_p K_{RV} K_{rms}^2 V_B \left[ \left( 1 + \frac{L_C K_{dl}}{V_B} I_{i,n} \right) I_{i,n}^2 \right] \quad (2.2.21)$$

$$= \frac{1}{N_p} K_{RV} K_{rms}^2 V_B \left[ \left( 1 + \frac{L_C K_{dl}}{V_B} \frac{I_{FC,n}}{N_p} \right) I_{FC,n}^2 \right]. \quad (2.2.22)$$

This means that increasing the number of phases a converter is made of would certainly improve efficiency. Unfortunately, this increases system cost as well.

Once the nominal current  $I_{i,n}$  per phase has been chosen — according to the technological constraints and to the accepted power losses per switch —, the number of phases  $N_p$  can be calculated:

$$I_{FC,n} = I_{i,n} N_p \quad (2.2.23)$$

$$I_{FC,n} = J_{FC,n} S \quad (2.2.24)$$

leading to:

$$N_p = \frac{I_{FC,n}}{I_{i,n}} = J_{FC,n} \frac{S}{I_{i,n}} = \frac{S}{S_p} \quad (2.2.25)$$

where:

$$S_p = \frac{I_{i,n}}{J_{FC,n}} \quad (2.2.26)$$

and where  $I_{FC,n}$  is the nominal current of the fuel cell stack corresponding to the nominal input current of the power converter,  $J_{FC,n}$  is the nominal current density of the fuel cell stack, and  $S_p$  is a fictitious surface, which is determined by the operating condition of the fuel cell  $J_{FC,n}$  and of the power converter  $I_{i,n}$ .

The total cost of the power converter  $C_{PC}$  is then proportional to the number of phases  $N_p$ :

$$C_{PC} = C_p N_p = \frac{C_p}{S_p} S = c_p S \quad (2.2.27)$$

where:

$$c_p = \frac{C_p}{S_p} \quad (2.2.28)$$

and where  $C_p$  is the fixed cost of one phase of the converter, and  $c_p$  a variable cost representative of the converter cost.

### 2.2.2.3. Total cost and general considerations

In this way all the considerations made before for the fuel cell stack cost can be applied again, taking into account the effect of the additional variable cost  $c_p$ .

The total cost of the system  $C_T$  is the sum of the fuel cell stack cost  $C_{FC}$  and of the power converter cost  $C_{PC}$ :

$$C_T(S) = C_{FC} + C_{PC} \quad (2.2.29)$$

$$= C_F + (c_M + c_p) S_T + (c_H + c_p) S + C_P S_T \frac{1}{S}. \quad (2.2.30)$$

The function has the same behaviour of the one represented in Figure 2.6 and both are represented in Figure 2.7, where  $C_T(s)$  presents its minimum in:

$$S^{**} = \sqrt{\frac{C_P}{c_H + c_p} S_T} \quad (2.2.31)$$

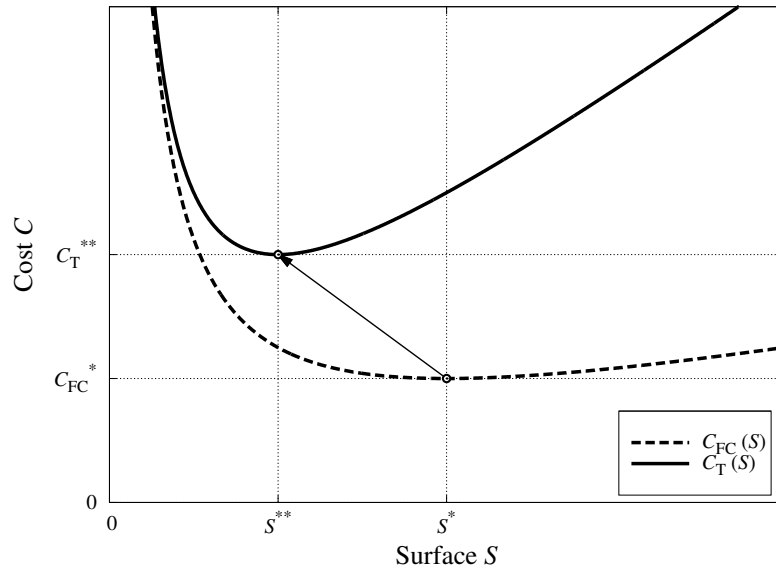
and the minimum cost is:

$$C_T^{**} = C_F + (c_M + c_P) S_T + 2\sqrt{(c_H + c_p) S_T C_P}. \quad (2.2.32)$$

The effect of taking into account the power converter, too, moves the minimum surface from  $S^*$  to  $S^{**}$ , where  $S^{**} < S^*$ . Thus, if  $S_T < S^{**}$  — and a fortiori  $S < S^{**}$  — the best solution is still the one with the higher surface  $S$ .

#### 2.2.2.4. Conclusion

Generally, the higher the element surface of a fuel cell stack is, the cheaper it becomes. Nevertheless, this leads to higher currents, which increase the power converter cost, and could compromise the gain obtained through the fuel cell stack.



**Figure 2.7.** Cost of a fuel cell stack  $C_{FC}$  and of the overall system  $C_T$  as a function of the element surface  $s$ . The minimum points  $^*$  and  $^{**}$  are located in  $S^*$  and  $S^{**}$  and their values are  $C_{FC}^*$  and  $C_T^{**}$ .

All the previous considerations have been made as if the fuel cell surface, the number of elements, the MOSFET maximum voltage and current were continuous variables. Naturally, this cannot be true, since all of them comply with technological constraints that limit the number of possible choices.

Nevertheless, the conclusion drawn through the continuous analysis is still useful to identify a limited number of cases, whose real components satisfy the conditions imposed by the continuous analysis. Then, a comparison between these real cases has to be made.

### 2.2.3. Voltage matching

The cost factor having been discussed in the previous section, the second factor — the relation between the fuel cell voltage, function of the number  $N$  of elements and of their surface  $S$ , and the input and output voltages for the different types of converter — will be covered in the following.

Once the total surface  $S_T$  and the output power and voltage ranges have been chosen, the two limit curves  $i$  and  $j$  of Figure 2.8 can be determined.

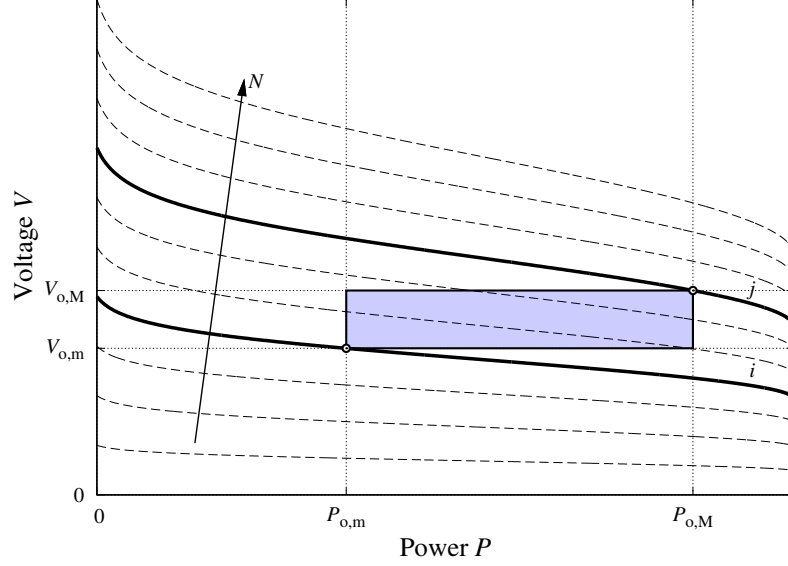
All characteristics in the region above the curve  $j$  belong to fuel cell stacks that need to be coupled with step-down only converters, while all characteristics in the region below the curve  $i$  belong to fuel cell stacks that need to be coupled with step-up only converters. All characteristics in the region included between the two curves belong to fuel cell stacks that need to be coupled with step-up/step-down converters.

Changing the surface  $S$  of a fuel cell stack means changing its number of elements  $N$ . It also means changing its characteristics in the  $V - P$  plan, and so the topology of the associated power converter.

These considerations should be taken into account, along with global cost considerations, since a step-up or step-down only converter could be favoured over a step-up/step-down converter, as previously discussed.

The real study is simplified by the limited number of possibilities for fuel cell stack configurations. The set of possible surfaces a fuel cell manufacturer can build has been called:

$$\left\{ S_{\text{tec},1}, S_{\text{tec},2} \dots S_{\text{tec},m} \right\}. \quad (2.2.33)$$



**Figure 2.8.** Behaviour of a bundle of  $V - P$  characteristics representing different fuel cell stacks with the same total surface  $S_T$ , but with different element numbers  $N$ , where  $P$  is a power and  $V$  a voltage. The operation power range  $[P_{FC,m} \dots P_{FC,n}]$  and the converter output voltage  $[V_{o,m} \dots V_{o,M}]$  defined by the user define a working area in gray and the two limit curves  $i$  and  $j$ .

For every different surface  $S_{tec,i}$ , a different  $N_{tec,i}$  can be found, in order to obtain:

$$S_T = S_{tec,i} N_{tec,i} \quad (2.2.34)$$

with:

$$N_{tec,i} = \text{Int}\left(\frac{S_T}{S_{tec,i}}\right) \quad (2.2.35)$$

where  $\text{Int}(\bullet)$  is the integer excess rounding function. This leads to  $m$  different fuel cell stack configurations, identified by the couples  $(S_{tec,i}, N_{tec,i})$ :

$$\left\{ (S_{tec,1}, N_{tec,1}), (S_{tec,2}, N_{tec,2}) \dots (S_{tec,m}, N_{tec,m}) \right\}. \quad (2.2.36)$$

Then, the  $V - P$  and  $I - P$  characteristics of these stacks need to be matched with the input and output characteristics of the possible power converters. Some examples of this process will be presented in the next chapter.

### 2.2.4. Storage system

Though far from being exhaustive, some information concerning hydrogen storage systems will integrate this chapter about the sizing procedure of fuel cell systems.

The relation between stored energy and hydrogen mass versus cylinders volume and pressure will be presented here for storage systems based on gaseous hydrogen. The commercial values used by Sapió — which is an Italian group operating in the field of technical and medical gases — have been chosen as a reference.

The standard commercial cylinder volume is 50 L, while its internal volume — called geometric volume — is  $V^* = 40$  L. It is regularly loaded with  $\bar{V}^* = 8$  Nm<sup>3</sup> of hydrogen, corresponding to a pressure  $P^* = 200$  bar at a temperature  $t = 0$  °C.

The “normal cubic metre” (Nm<sup>3</sup>) is a measure of the amount of substance for gases or gaseous mixtures, like the mole (mol), since it is defined as the volume of 1 m<sup>3</sup> at STP (Standard Temperature and Pressure), i.e.  $P_0 = 1$  atm and  $t_0 = 0$  °C, and in the SI (*Système International*)  $P_0 = 101\,325$  Pa and  $T_0 = 273.15$  K. So, the measure of the gas quantity in moles ( $n$ ) is directly proportional to the measure of the same quantity in normal cubic metres ( $\bar{V}$ ):

$$n = \frac{P_0}{R T_0} \bar{V} = K_{n\bar{V}} \bar{V} \quad (2.2.37)$$

where:

$$K_{n\bar{V}} = 44.034 \frac{\text{mol}}{\text{Nm}^3} \quad (2.2.38)$$

and  $R = 8.314 \frac{\text{J}}{\text{molK}}$  is the universal gas constant.

So, the amount of electric energy  $E_e$  that could be obtained from a fuel cell system can be calculated as a function of the hydrogen amount  $\bar{V}$ :

$$E_e = \eta_{\text{PC}} \eta \Delta H_{\text{LHV}} K_{n\bar{V}} \bar{V} \quad (2.2.39)$$

where  $\eta_{\text{PC}}$  is the power converter efficiency,  $\eta$  is the fuel cell efficiency, and  $\Delta H_{\text{LHV}}$  is the Lower Heating Value (LHV) of hydrogen.

It is also interesting to express the electric energy  $E_e$  as a function of the geometric volume  $v$  of hydrogen cylinders and of the nominal pressure  $p$ , loaded under the previously described conditions  $V^*$ ,  $\bar{V}^*$ ,  $P^*$ :



$$E_e(v,p) = \eta_{PC} \eta \Delta H_{LHV} K_n \bar{V} \bar{V}^* \frac{v}{V^*} \frac{P}{P^*} \quad (2.2.40)$$

and the total mass of hydrogen:

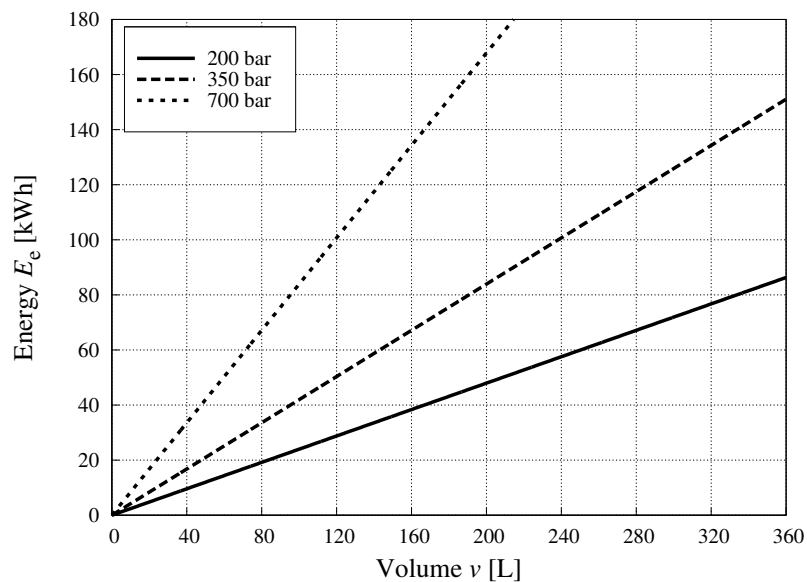
$$m_{H_2}(v,p) = M_{H_2} n = M_{H_2} K_n \bar{V} \frac{v}{V^*} \frac{P}{P^*} \quad (2.2.41)$$

where  $M_{H_2}$  is the molar mass of the gaseous hydrogen  $H_2$ . These new functions are plotted in Figure 2.9.

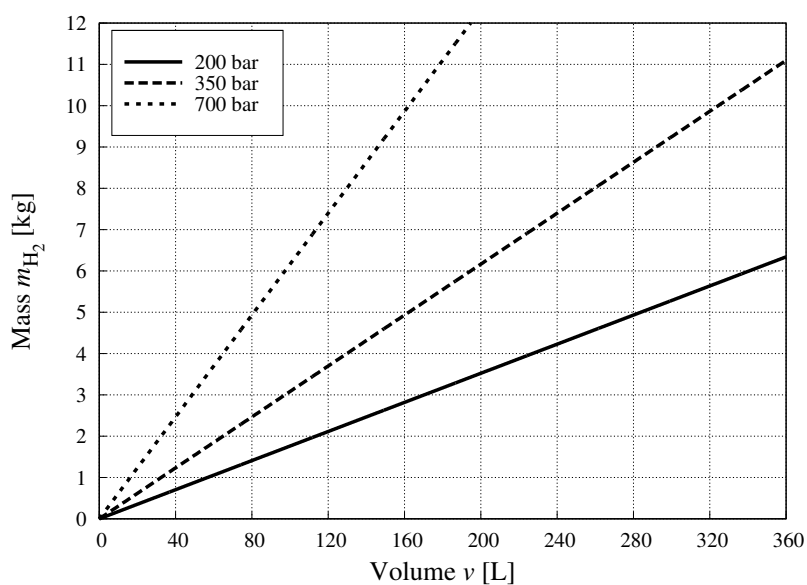
### 2.3. Conclusion

In the first part of this chapter, a survey of power converters has been presented. In the second part of the chapter, several considerations that should be taken into account in the design of a fuel cell system have been presented.

All these considerations and methods will be applied for the design of a prototype fuel cell system in the next chapter.



(a)



(b)

**Figure 2.9.** (a) Electrical energy  $E_e$  that can be obtained by a fuel cell system and (b) mass of gaseous hydrogen stored in a pressurised cylinder system whose total geometrical volume is  $v$ . The standard pressure is 200 bar, but two other hypothetical storing pressures are also plotted. The standard geometrical volume of a 50 L cylinder is 40 L. A cylinder pack is generally composed of 9 cylinders, thus its total geometrical volume is equal to 360 L.

## CHAPTER 3

### SYSTEM

In this chapter, after a description of the practical context in which the fuel cell system prototype is, the sizing process will be illustrated and the considerations made in the previous chapter will be applied.

It is relevant to report a quite extended analytical description of the operation of the power converter in its whole current range, since its operation mode is quite unusual:

- its input voltage is a function of the output power;
- in order to increase the efficiency, the power converter is forced to work on the border between CCM and DCM;<sup>1</sup>
- in order to guarantee the previous condition is met, the power converter needs to operate with a variable switching frequency;
- the saturation limits of the switching frequency influence the behaviour of all the other variables.

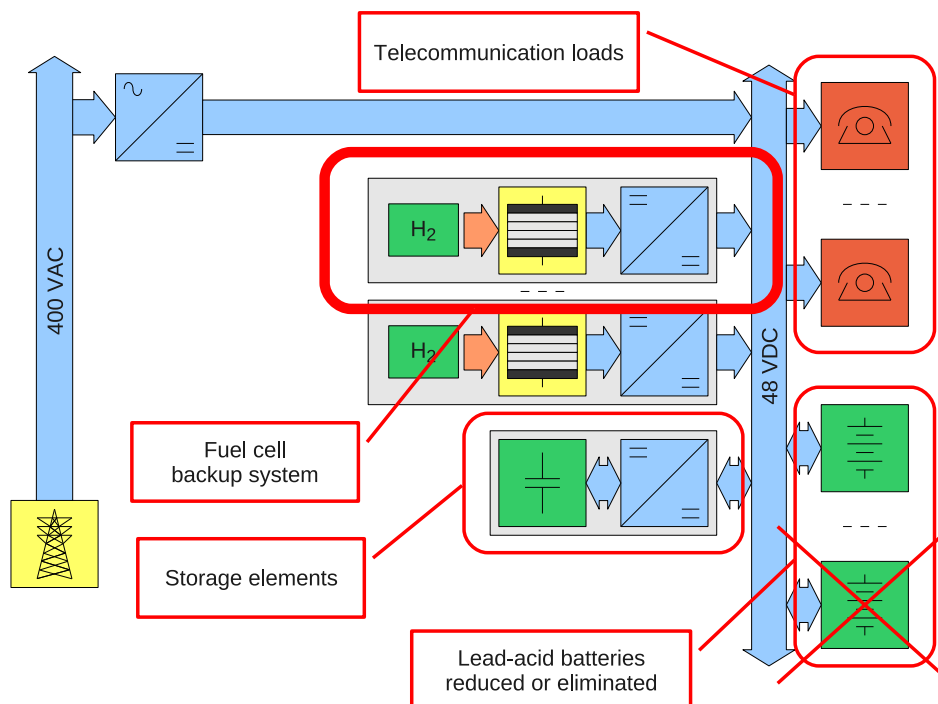
The chapter ends with the description of the peculiar control system implemented in the prototype.

---

<sup>1</sup>An analysis of the operation of a flyback converter on the border between CCM and DCM is presented in [57].

### 3.1. Introduction

Telecommunication applications need backup systems to guarantee full functionality for a predefined time span even during grid faults. Nowadays, this backup function is based on lead-acid battery banks, sometimes coupled with Diesel power generators (Figure 3.1).



**Figure 3.1.** Functional diagram of a telecommunication power supply system. The lead-acid batteries of a standard telecommunication power supply could be replaced by fuel cell based modules. Storage elements can be added, if the dynamic performance of the fuel cell solution is inadequate.

The aim of the project is the production of a modular backup system for telecommunication applications based on a Proton Exchange Membrane Fuel Cell (PEMFC) [58]. Such a system should allow the reduction or elimination of the standard lead-acid batteries. If all batteries were eliminated, other energy storage systems, like supercapacitors, would probably be required to match the dynamic requirements of the load with the dynamic response of the fuel cell.

Literature offers many articles in which fuel cells are suggested as a backup solution for telecommunication systems, like in [59 – 62]. Other present some working example of these systems [63 – 67]. Another interesting reference is [68], in which the behaviour of the parallel between a fuel cell stack and a lead-acid battery is studied.<sup>2</sup>

In the following sections, the sizing procedure for both the fuel cell stack and the DC/DC power converter will be described.

The electrical constraints of the system are:

$$P_{o,n} = 5\,500\text{ W} \quad (3.1.1)$$

$$P_{o,m} = 500\text{ W} \quad (3.1.2)$$

$$V_{o,M} = 60\text{ V} \quad (3.1.3)$$

$$V_{o,n} = 48\text{ V} \quad (3.1.4)$$

$$V_{o,m} = 42\text{ V} \quad (3.1.5)$$

$$\Delta V_{o,M} = 200\text{ mV} \quad (3.1.6)$$

$$\eta_{PC} = 0.9 \quad (3.1.7)$$

where  $P_{o,n}$  is the nominal output power,  $P_{o,m}$  is the minimum output power,  $V_{o,n}$  is the nominal output voltage, and  $V_{o,m}$  and  $V_{o,M}$  the minimum and maximum output voltage respectively,  $\Delta V_{o,M}$  is the maximum output voltage ripple, and  $\eta_{PC}$  is the minimum expected efficiency of the converter.

### 3.2. Overall system sizing

First, the fuel cell stack will be sized, then the power converter. The section ends with the sizing procedure of the control system.

---

<sup>2</sup> A similar connection between high temperature PEMFCs and Li-Ion batteries has been presented in [69], in which the targetted goal were fuel cell electrical vehicles.

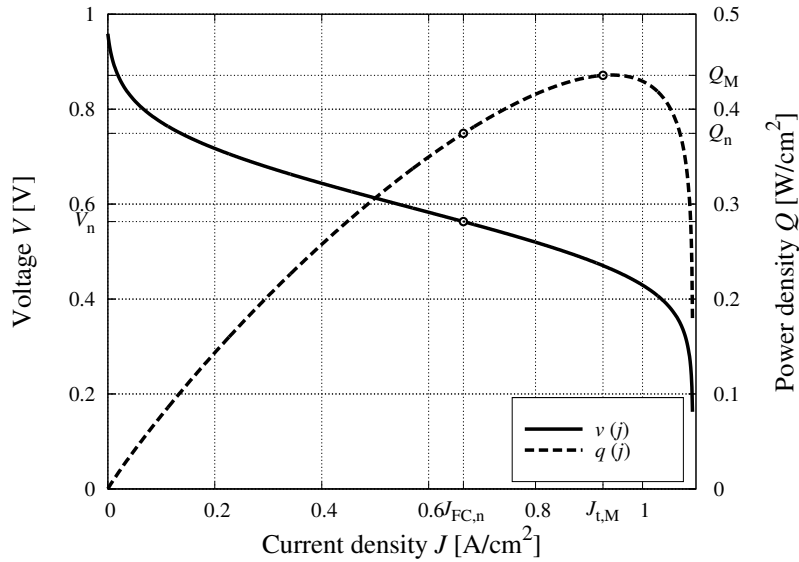
### 3.2.1. Fuel cell sizing

Following the procedure described in Chapter 2, the current density limit  $J_{Q,M}$ , the technological current density limit  $J_{t,M}$  and the absolute maximum current limit  $J_{a,M}$  are (Figure 3.2) given by the manufacturer and equal to:

$$J_{Q,M} = 0.939 \text{ A/cm}^2 \quad (3.2.1)$$

$$J_{t,M} = 0.926 \text{ A/cm}^2 \quad (3.2.2)$$

$$J_{a,M} = J_{t,M} = 0.926 \text{ A/cm}^2. \quad (3.2.3)$$



**Figure 3.2.** Voltage  $v$  and power density  $q$  of a single Exergy Fuel Cells fuel cell element versus its current density  $j$ .

The maximum operating current density can be chosen as:

$$J_{FC,n} = \kappa_{FC,n} J_{a,M} \quad (3.2.4)$$

where  $\kappa_{FC,n}$  is a safety coefficient, whose value depends on the technological choices made by the manufacturers. In this case it has been given as:

$$\kappa_{FC,n} = 0.72 \quad (3.2.5)$$

leading to:

$$J_{FC,n} = 0.665 \text{ A/cm}^2. \quad (3.2.6)$$

The nominal power density the fuel cell operates ( $Q_n$ ) at and the nominal power the fuel cell stack needs to provide ( $P_{FC,n}$ ) are then:

$$Q_n = 0.375 \text{ W/cm}^2 \quad (3.2.7)$$

$$P_{FC,n} = \frac{P_{o,n}}{\eta_{PC}} = 6 \text{ 100 W} \quad (3.2.8)$$

$$P_{FC,m} = \frac{P_{o,m}}{\eta_{PC}} = 560 \text{ W} \quad (3.2.9)$$

leading to the total membrane surface required:

$$S_{FC} = \frac{P_{FC,n}}{Q_n} = 16 \text{ 310 cm}^2. \quad (3.2.10)$$

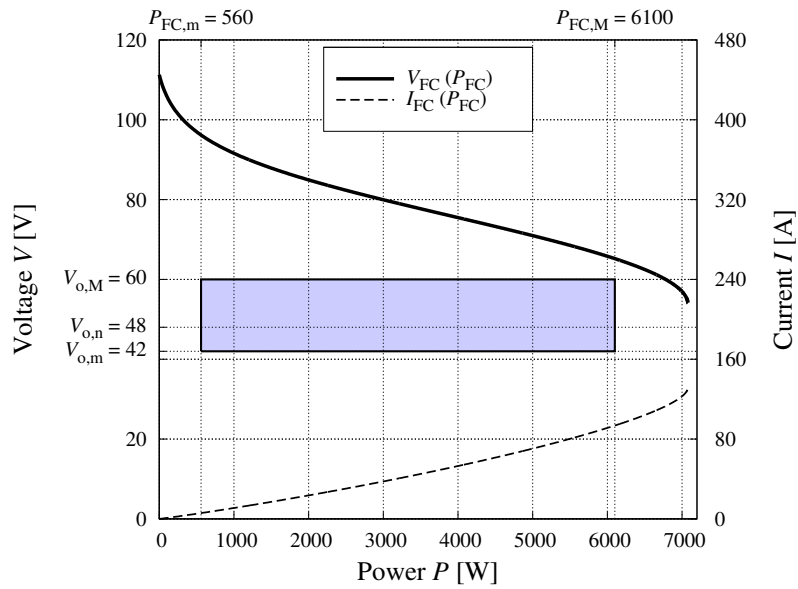
The standard fuel cell elements that could be used were  $S_{FC,1} = 140 \text{ cm}^2$ ,  $S_{FC,2} = 278 \text{ cm}^2$ ,  $S_{FC,3} = 325 \text{ cm}^2$ ,  $S_{FC,4} = 500 \text{ cm}^2$ , which give four possible stack configurations, whose number of elements was  $N_{FC,1} = 116$ ,  $N_{FC,2} = 58$ ,  $N_{FC,3} = 50$ ,  $N_{FC,4} = 32$ . From now on, a fuel cell stack configuration will be identified by the notation  $S_{FC,x}/N_{FC,x}$ .

According to what Section 2.2.2.3 stated and to the recommendations of the fuel cell manufacturer Exergy Fuel Cells, the cheapest fuel cell turned out to be the one with the largest surface per element.

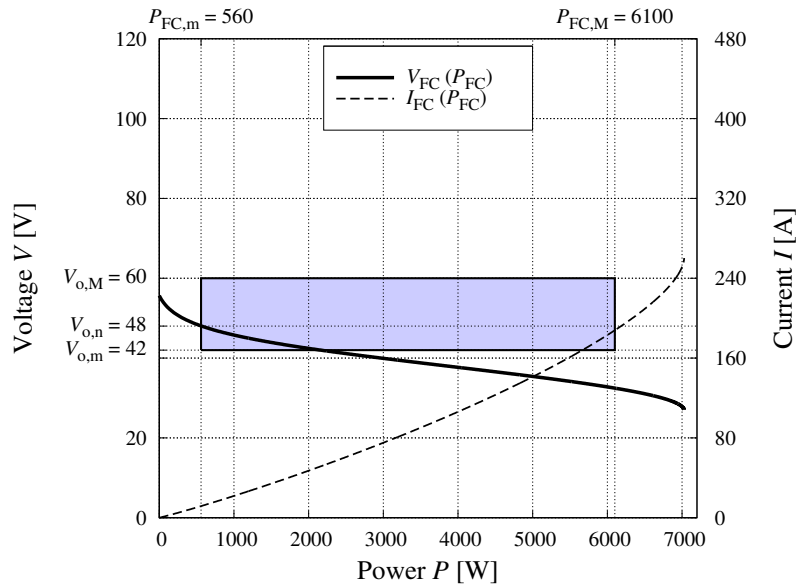
The voltage matching between the fuel cell stack and the power converter is shown in Figures 3.3, 3.4, 3.5 and 3.6 in all four cases, in which the plots of the fuel cell voltage and current versus power are traced. The diagrams also report the required minimum and maximum power, and the minimum, nominal and maximum voltage limits.

Solution 140/116 should be discarded since it leads to the most expensive fuel cell stack, due to the high number of elements, even if it has the advantage of high voltages, low currents and a step-down only converter.

Solution 278/58 should also be discarded since the voltage matching leads to a step-up/step-down converter, which is to be avoided, as previously discussed.

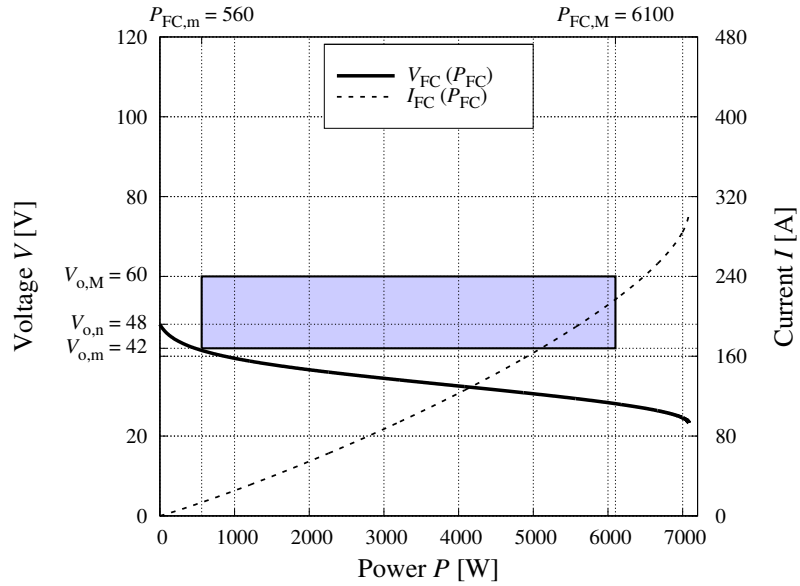


**Figure 3.3.** Fuel cell voltage  $V_{FC}$  versus power  $P_{FC}$  for the fuel cell stack configuration 140/116, where the element surface is 140 cm<sup>2</sup> and the number of elements is 116.

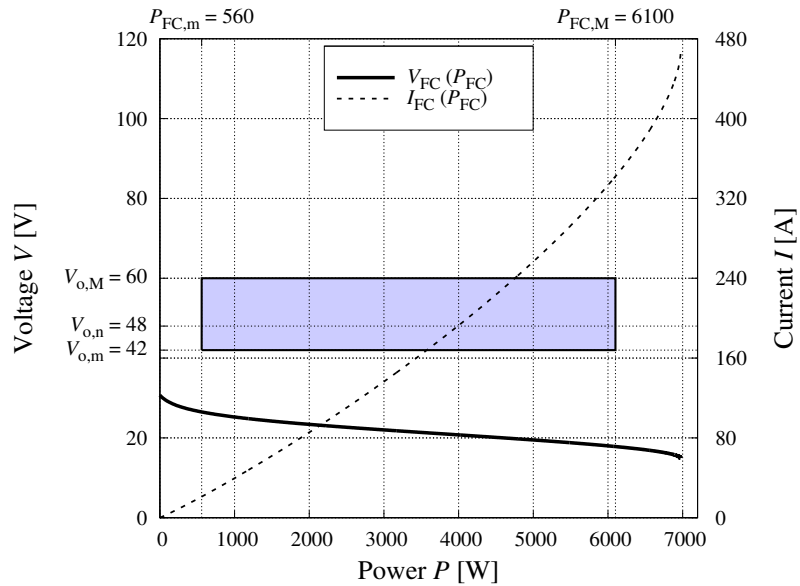


**Figure 3.4.** Fuel cell voltage  $V_{FC}$  versus power  $P_{FC}$  for the fuel cell stack configuration 278/58, where the element surface is 278 cm<sup>2</sup> and the number of elements is 58.





**Figure 3.5.** Fuel cell voltage  $V_{FC}$  versus power  $P_{FC}$  for the fuel cell stack configuration 325/50, where the element surface is 325 cm<sup>2</sup> and the number of elements is 50.



**Figure 3.6.** Fuel cell voltage  $V_{FC}$  versus power  $P_{FC}$  for the fuel cell stack configuration 500/32, where the element surface is 500 cm<sup>2</sup> and the number of elements is 32.

The two remaining candidates are the 325/50 and the 500/32. The second one has the advantage of the cheapest fuel cell stack, but the first one does not display such high current values as high as the second one's. The choice between these two stack configurations is far from obvious. After discussing with the stack manufacturer, the 325/50 version has been chosen as a first prototype.

### 3.2.2. Power converter sizing

In this section, the power converter sizing will be studied in detail. Its behaviour is interesting and far from obvious for several reasons:

- the input voltage is a function of the output power and can vary in a wide range;
- the switching frequency varies in a wide range, in order to keep the converter working on the border between CCM and DCM;
- the system is non-linear, presenting higher and lower saturation limits in the switching frequency.

For these reasons, the relations between all the variables have been analytically studied with the program Mathcad and the behaviour of the main variables is presented in the whole current range, for three different values of the output voltage reference.

#### 3.2.2.1. Design specification

The electrical constraints previously defined lead to the following output currents:

$$I_{o,n} = \frac{P_{o,n}}{V_{o,n}} = 115 \text{ A} \quad (3.2.11)$$

$$I_{o,m} = \frac{P_{o,n}}{V_{o,M}} = 92 \text{ A} \quad (3.2.12)$$

$$I_{o,M} = \frac{P_{o,n}}{V_{o,m}} = 131 \text{ A} \quad (3.2.13)$$

where  $I_{o,n}$ ,  $I_{o,m}$  and  $I_{o,M}$  are respectively called nominal, minimum and maximum output current.

The power converter is expected to always work in DCM, as close as possible to the border between CCM and DCM. This implies a variable switching frequency, whose relevant values are:

$$f_{s,m} = 50 \text{ kHz} \quad (3.2.14)$$

$$f_{s,n} = 60 \text{ kHz} \quad (3.2.15)$$

$$f_{s,M} = 160 \text{ kHz} \quad (3.2.16)$$

where  $f_{s,m}$ ,  $f_{s,n}$  and  $f_{s,M}$  are the minimum, nominal and maximum frequency respectively.

### 3.2.2.2. Number of phases and efficiency

As discussed in Chapter 2, the higher the phase number of a power converter is, the higher the efficiency, but also the more expensive the power converter will be. The sizing operation has been performed for different values of the phase number  $N_p = 3, 4 \dots 9$  and the results are reported in Tables 3.1 (a) and (b). It has been found that  $N_p = 6$  is a good compromise between good efficiency, a small current ripple and a small inductance. It should also be noticed that the increment in efficiency for  $N_p > 6$  is negligible or negative.

In what follows, the sizing procedure for  $N_p = 6$  is detailed.

### 3.2.2.3. Frequency modulation

As mentioned above, the converter is designed to operate in DCM. However, in order to mitigate the impact of the high switch RMS current and to achieve a better efficiency, the converter switching frequency is not kept constant. A feed-forward control is implemented in order to adjust the frequency so as to keep the converter as close as possible to the border between CCM and DCM.

The inductance voltage balance equation can be derived from Figure 3.7, which represents the inductance current during the border line operation mode:

$$\frac{V_i}{L} T_{on} + \frac{V_i - V_o}{L} (T_s - T_{on}) = 0 \quad (3.2.17)$$

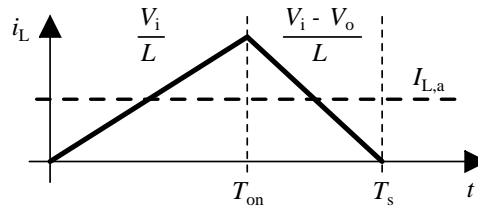
**Table 3.1.** Main values of the power converter when the phase number  $N_p$  varies, calculated at nominal conditions. Acronyms: input inductance  $L_n$ , output capacitor power losses  $P_C$ , input inductance power losses  $P_L$ , switch and diode power losses  $P_{SD}$ , switch drive power losses  $P_{drv}$ , off power losses  $P_{off}$ , total power losses  $P_{l,T}$ , power converter efficiency  $\eta_{PC}$ , improvement in power converter efficiency  $\Delta\eta_{PC}$ , inductance maximum current ripple  $\Delta I_{i,T}$ , output capacitor  $C_o$ , diode average current  $I_{d,a}$ , diode RMS current  $I_{d,rms}$ , switch average current  $I_{s,a}$ , switch RMS current  $I_{s,rms}$ , inductor peak current  $I_{i,pk}$ .

$N_p$	$L_n$	$\Delta I_{i,T}$	$C_o$	$I_{d,a}$	$I_{d,rms}$	$I_{s,a}$	$I_{s,rms}$	$I_{i,pk}$
[–]	[ $\mu$ H]	[A]	[ $\mu$ F]	[A]	[A]	[A]	[A]	[A]
3	1.20	46	230	38	66	27	55	153
4	1.60	27	98	29	49	20	42	115
5	2.0	17.5	49	23	39	16.2	33	92
6	2.4	10.3	28	19.1	33	13.5	28	76
7	2.8	8.0	18.0	16.4	28	11.6	24	66
8	3.2	6.4	12.0	14.3	25	10.2	21	57
9	3.6	4.4	9.0	12.7	22	9.0	18.5	51

(a)

$N_p$	$P_C$	$P_L$	$P_{SD}$	$P_{drv}$	$P_{off}$	$P_{l,T}$	$\eta_{PC}$	$\Delta\eta_{PC}$
[–]	[W]	[W]	[W]	[W]	[W]	[W]	[%]	[%]
3	8.0	51	370	0.54	40	470	92.3	-
4	3.3	61	290	0.72	40	400	93.5	1.2
5	1.68	74	250	0.90	40	360	94.0	0.5
6	0.94	90	220	1.09	40	350	94.3	0.3
7	0.60	109	194	1.27	40	350	94.3	0
8	0.38	131	178	1.45	40	350	94.3	0
9	0.27	156	165	1.63	40	360	94.1	-0.2

(b)



**Figure 3.7.** Conditions imposed on the inductor current in order to ensure the operation of the power converter on the border between CCM and DCM.  $V_i$  and  $V_o$  are the input and output voltage,  $I_{L,a}$  is the inductor average current,  $T_{on}$  is switch on-time,  $T_s$  is the switching period.

which leads to:

$$T_{\text{on}} = \frac{V_o - V_i}{V_o} T_s. \quad (3.2.18)$$

The constraint on the average current  $I_{L,a}$ , after inserting the previous equation, becomes:

$$I_{L,a} = \frac{V_i}{2L} T_{\text{on}} = \frac{V_i}{2L} \frac{V_o - V_i}{V_o} T_s = \frac{V_i}{2L} \frac{V_o - V_i}{V_o} \frac{1}{f_s} \quad (3.2.19)$$

which sets the following as a condition that needs to be satisfied:

$$f_s = \frac{V_i}{2L} \frac{V_o - V_i}{V_o} \frac{1}{I_{L,a}} \quad (3.2.20)$$

where  $f_s = 1/T_s$  is the switching frequency,  $V_i$  and  $V_o$  the power converter input and output voltage respectively,  $L$  the main inductance value,  $I_{L,a}$  the average value of the inductance current.

Therefore, the switching frequency regulation can be automatically operated, basing on Equation 3.2.20, applying a suitable safety margin on the calculated frequency. Furthermore, the individual phase frequency is limited to the range between 50 kHz and 160 kHz for practical use. The limits have been found by experiment, with the aim of keeping:

- a sufficiently high response speed;
- switching losses below maximum acceptable levels.

The graphical representation of the phase switching frequency as a function of the fuel cell current will be shown further on.

#### 3.2.2.4. Fuel cell characteristics

Since the converter design depends on its primary energy source, the characteristics of the chosen fuel cell will be analysed first.

The element surface  $S_{FC}$  and the element number  $N_{FC}$  of the chosen fuel cell stack are:

$$S_{FC} = 325 \text{ cm}^2 \quad (3.2.21)$$

$$N_{FC} = 50 \quad (3.2.22)$$

which lead to the following electrical values:

$$I_{FC,M} = 300 \text{ A} \quad (3.2.23)$$

$$V_{FC,m} = V_{FC}(I_{FC,M}) = 23 \text{ V} \quad (3.2.24)$$

$$P_{FC,M} = P_{FC}(I_{FC,M}) = 7 \text{ kW} \quad (3.2.25)$$

$$V_{FC,M} = V_{FC}(0) = 48 \text{ V}. \quad (3.2.26)$$

In nominal conditions, the fuel cell stack values are:

$$P_{FC,n} = \frac{P_{o,n}}{\eta_{PC}} = 6.1 \text{ kW} \quad (3.2.27)$$

$$I_{FC,n} = 220 \text{ A} \quad (3.2.28)$$

$$V_{FC,n} = V_{FC}(I_{FC,n}) = 28 \text{ V} \quad (3.2.29)$$

$$\Gamma_{FC} = \frac{P_{FC,n}}{P_{FC,M}} = 0.86. \quad (3.2.30)$$

Given that the power converter uses a boost topology, the input voltage needs to be lower than the output voltage, with a suitable safety margin. This is called minimum input voltage and defined as:

$$V_{i,m}(V_o) = \begin{cases} V_{FC,M} & \Leftarrow \kappa_V \cdot V_o > V_{FC,M} \\ \kappa_V \cdot V_o & \Leftarrow \kappa_V \cdot V_o \leq V_{FC,M} \end{cases} \quad (3.2.31)$$

where  $\kappa_V = 0.9$  is a margin coefficient.

In order to guarantee this voltage, a minimum current has to be absorbed, which is a function of  $V_o$  and implicitly defined as:

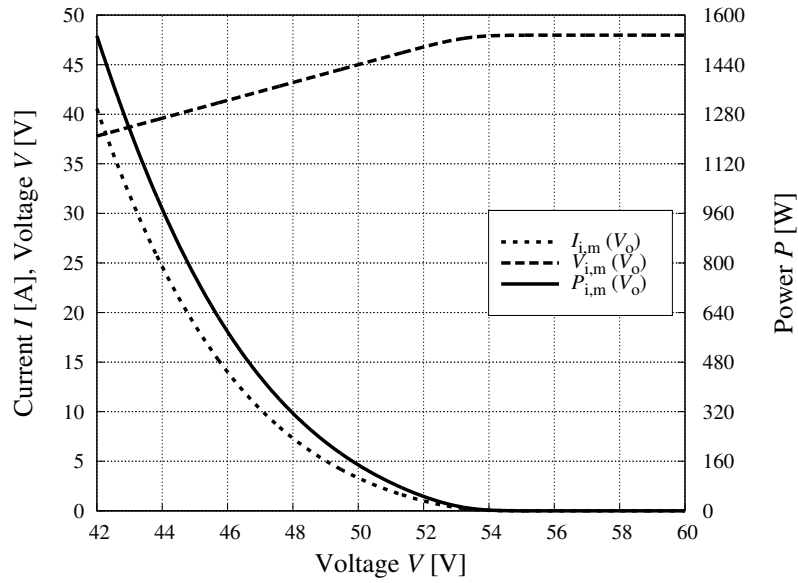
$$I_{i,m}(V_o) \mid V_{FC}(I_{i,m}(V_o)) = V_{i,m}(V_o). \quad (3.2.32)$$

This also leads to set a minimum power produced by the fuel cell stack to guarantee the boost operation:

$$P_{i,m}(V_o) = V_{i,m}(V_o) I_{i,m}(V_o). \quad (3.2.33)$$

The minimum input voltage, current and power are plotted in Figure 3.8, and their values for the nominal, minimum and maximum output voltage follow:

$$\begin{aligned}
 V_o = V_{o,n} &\Rightarrow V_{i,m} = 43 \text{ V} & I_{i,m} = 7.1 \text{ A} & P_{i,m} = 310 \text{ W} \\
 V_o = V_{o,m} &\Rightarrow V_{i,m} = 38 \text{ V} & I_{i,m} = 41 \text{ A} & P_{i,m} = 1530 \text{ W} \\
 V_o = V_{o,M} &\Rightarrow V_{i,m} = 48 \text{ V} & I_{i,m} = 0 & P_{i,m} = 0.
 \end{aligned} \tag{3.2.34}$$



**Figure 3.8.** Minimum voltage  $V_{i,m}$ , current  $I_{i,m}$  and power  $P_{i,m}$  required for the boost operation versus the reference output voltage  $V_o$ .

### 3.2.2.5. Converter design

In order to ensure the DCM operation, a maximum limit has to be imposed to the input inductance, which is a function of the input current  $I_{FC}$  and of the output voltage  $V_o$ :

$$L_M(I_{FC}, V_o) = \frac{V_{FC}(I_{FC})}{2f_{s,n}} \frac{I_{FC}}{N_p} \frac{V_o - V_{FC}(I_{FC})}{V_o}. \tag{3.2.35}$$

The maximum inductance is set so as to ensure the DCM operation at the nominal switching frequency, at the nominal current and at the nominal output voltage:

$$L_M = L_M(I_{FC,n}, V_{o,n}) = 2.7 \mu\text{H}. \quad (3.2.36)$$

A safety coefficient  $\kappa_L = 0.9$  has been applied to this value, leading to:

$$L = \kappa_L L_M \cong 2.4 \mu\text{H}. \quad (3.2.37)$$

In order to make the power converter always work on the border between CCM and DCM, the switching frequency needs to be adjusted as a function of the input current  $I_{FC}$  and of the output voltage  $V_o$ :

$$f_s(I_{FC}, V_o) = \frac{V_{FC}(I_{FC})}{2L} \frac{V_o - V_{FC}(I_{FC})}{\frac{I_{FC}}{N_p}} \kappa_f \quad (3.2.38)$$

where  $\kappa_f = 0.9$  is a safety coefficient. The switching frequency is also saturated at the minimum and maximum switching frequency limits  $f_{s,m}$  and  $f_{s,M}$ .

The switching frequency is plotted in Figure 3.9, and its values for the nominal current, and the nominal, minimum and maximum output voltage follow:

$$f_s(I_{FC,n}, V_{o,n}) = 60 \text{ kHz} \quad (3.2.39)$$

$$f_s(I_{FC,n}, V_{o,m}) = 50 \text{ kHz} \quad (3.2.40)$$

$$f_s(I_{FC,n}, V_{o,M}) = 77 \text{ kHz}. \quad (3.2.41)$$

The upper saturation limit is reached for both  $V_o = V_{o,M}$  and  $V_o = V_{o,n}$  for current values less than 100 A, while the lower saturation limits is reached for  $V_o = V_{o,m}$  for current values greater than 200 A. These saturation phenomena of the switching frequency will influence almost all the other variables of the converter.

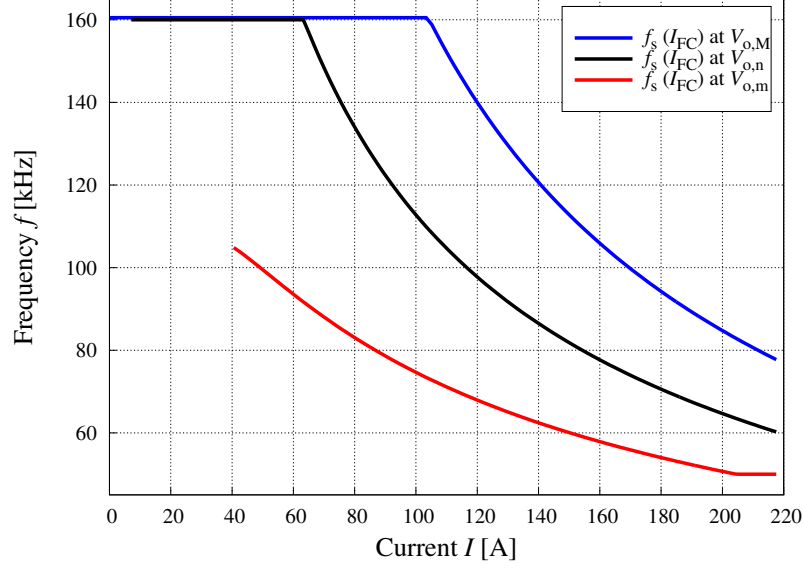
The ratio between the input voltage  $V_{FC}$  and the output voltage  $V_o$  is plotted in Figure 3.10 and expressed by:

$$\Pi(I_{FC}, V_o) = \frac{V_o}{V_{FC}(I_{FC})} \quad (3.2.42)$$

whose minimum and maximum values are:

$$\begin{aligned} V_o = V_{o,n} &\Rightarrow \Pi_m = 1.11 \quad \Pi_M = 1.71 \\ V_o = V_{o,m} &\Rightarrow \Pi_m = 1.11 \quad \Pi_M = 1.50 \\ V_o = V_{o,M} &\Rightarrow \Pi_m = 1.25 \quad \Pi_M = 2.1. \end{aligned} \quad (3.2.43)$$





**Figure 3.9.** Switching frequency  $f_s$  versus fuel cell current  $I_{FC}$ , with the output voltage  $V_o$  as a parameter.

The shape of the transfer ratio curve is inversely proportional to the fuel cell stack polarisation curve, since  $V_o$  is constant: the first part is then related to the quick voltage drop of the fuel cell voltage, while the second part is almost linear.

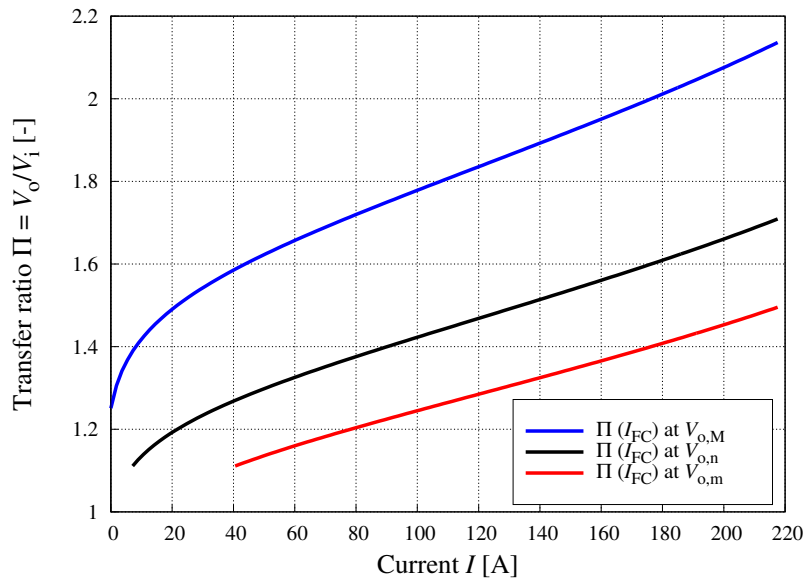
In order to verify the power converter is actually operating in DCM, the input current limit has been calculated:

$$I_{i,l}(I_{FC}, V_o) = \frac{V_o}{2f_s(I_{FC}, V_o)L} \frac{\Pi(I_{FC}, V_o) - 1}{\Pi^2(I_{FC}, V_o)}. \quad (3.2.44)$$

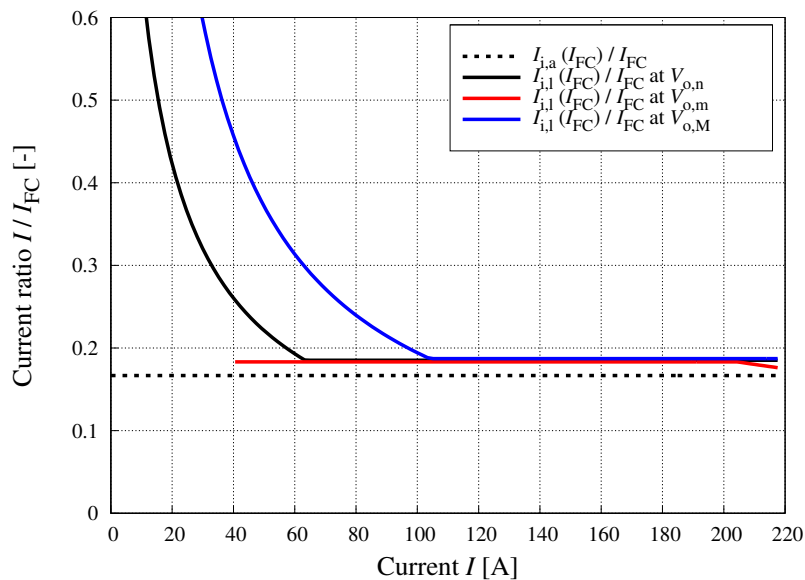
Figure 3.11 shows the ratio between the input current limit and the fuel cell current, compared to the ratio between the input current and the fuel cell current: it can be seen that the input current is always below the input current limit. This confirms it is working in DCM in all the current range.

The switch duty cycle is expressed by:

$$\delta_s(I_{FC}, V_o) = \sqrt{\left(\Pi(I_{FC}, V_o) - 1\right) \frac{\frac{I_{FC}}{N_p}}{\frac{V_o}{2f_s(I_{FC}, V_o)L}}} \quad (3.2.45)$$



**Figure 3.10.** Voltage ratio  $\Pi$  versus fuel cell current  $I_{FC}$ , with the output voltage  $V_o$  as a parameter.



**Figure 3.11.** Average input current  $I_{i,a}$  and input current limit  $I_{i,l}$  versus fuel cell current  $I_{FC}$ , with the output voltage  $V_o$  as a parameter.

whose minimum and maximum values are:

$$\begin{aligned} V_o = V_{o,n} &\Rightarrow \delta_{s,m} = 0.046 \quad \delta_{s,M} = 0.39 \\ V_o = V_{o,m} &\Rightarrow \delta_{s,m} = 0.095 \quad \delta_{s,M} = 0.32 \\ V_o = V_{o,M} &\Rightarrow \delta_{s,m} = 0 \quad \delta_{s,M} = 0.51. \end{aligned} \quad (3.2.46)$$

The diode duty cycle is expressed by:

$$\delta_d(I_{FC}, V_o) = \frac{V_{FC}(I_{FC})}{V_o - V_{FC}(I_{FC})} \delta_s(I_{FC}, V_o) \quad (3.2.47)$$

whose values at  $I_{FC} = I_{FC,n}$  are:

$$\begin{aligned} V_o = V_{o,n} &\Rightarrow \delta_d = 0.56 \\ V_o = V_{o,m} &\Rightarrow \delta_d = 0.65 \\ V_o = V_{o,M} &\Rightarrow \delta_d = 0.44. \end{aligned} \quad (3.2.48)$$

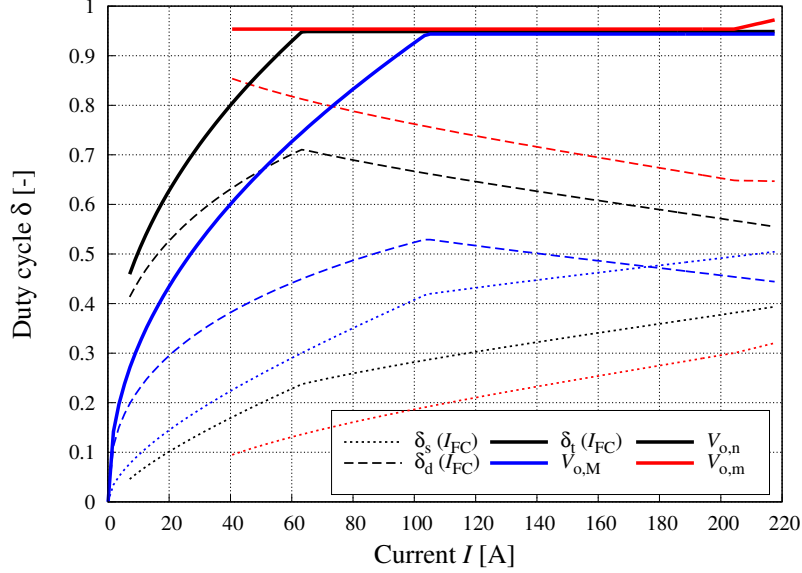
In order to verify the operation in DCM, the total duty cycle has been calculated:

$$\delta_t(I_{FC}, V_o) = \delta_s(I_{FC}, V_o) + \delta_d(I_{FC}, V_o). \quad (3.2.49)$$

Figure 3.12 shows the switch, diode and total duty cycles. Since  $\delta_t < 1$  in any condition, the power converter is always operating in DCM, even if the effect of the switching frequency saturations is noticeable: the upper saturation leads  $\delta_t$  to decrease and makes the converter work deeper in DCM, while the lower saturation leads  $\delta_t$  to increase and makes the converter work in a region closer to CCM. The effects of saturation are also illustrated in the switch and diode duty cycle plots, in which the relation is linear when the frequency is not saturated.

The input current of each module is plotted in Figure 3.13 for three different values of the output voltage  $V_o$ . It shows that, although the switching frequency and the duty cycle change, the power converter is always working on the border between CCM and DCM. It is interesting to see how both the shape and the frequency of the input current vary for the three different values of the output voltage reference, even if the average current is the same.

The total input current is the sum of all the input currents of each module and still a function of the input current  $I_{FC}$  and of the output voltage  $V_o$ , whose plot in Figure 3.14 shows the partial ripple cancellation phenomenon:



**Figure 3.12.** Switch  $\delta_s$ , diode  $\delta_d$  and total  $\delta_i$  duty cycles versus fuel cell current  $I_{FC}$ , with the output voltage  $V_o$  as a parameter.

$$i_{i,T}(I_{FC}, V_o) = \sum_{k=1}^{N_p} i_{i,k}(I_{FC}, V_o). \quad (3.2.50)$$

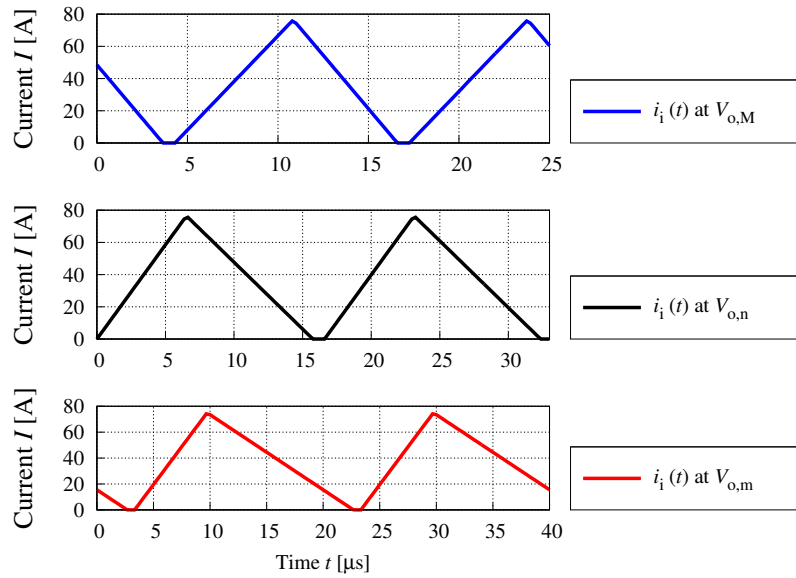
In order to understand the behaviour of the input current ripple, this has been plotted as a function of both the input current  $I_{FC}$  and of the output voltage  $V_o$  in Figure 3.15.

The current ripple forms parallel hills and valleys on the right side of the graphs, while the shape changes on the left side due to the saturation effects. As expected, the maximum value of the current ripple decreases when the number of phases increases.

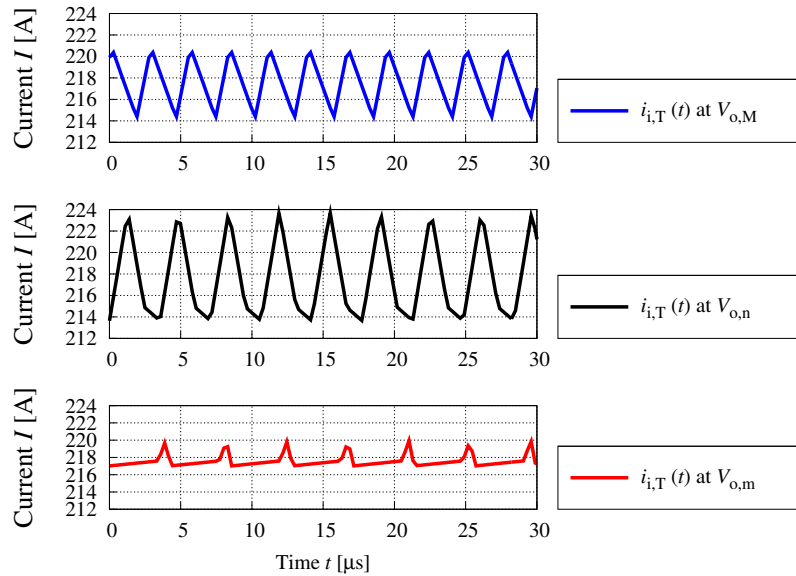
For the case  $N_p = 6$ , the maximum input current ripple values are located along the line  $I_{FC} = I_{FC,n}$  and the line  $V_o = V_{o,m}$ , whose projections are shown in Figure 3.16. The two maxima are the same as in Figure 3.15, while the behaviour of the input current ripple is far from being simple. The maximum input current ripple is:

$$\Delta I_{i,M} = 10.3 \text{ A} \quad (3.2.51)$$

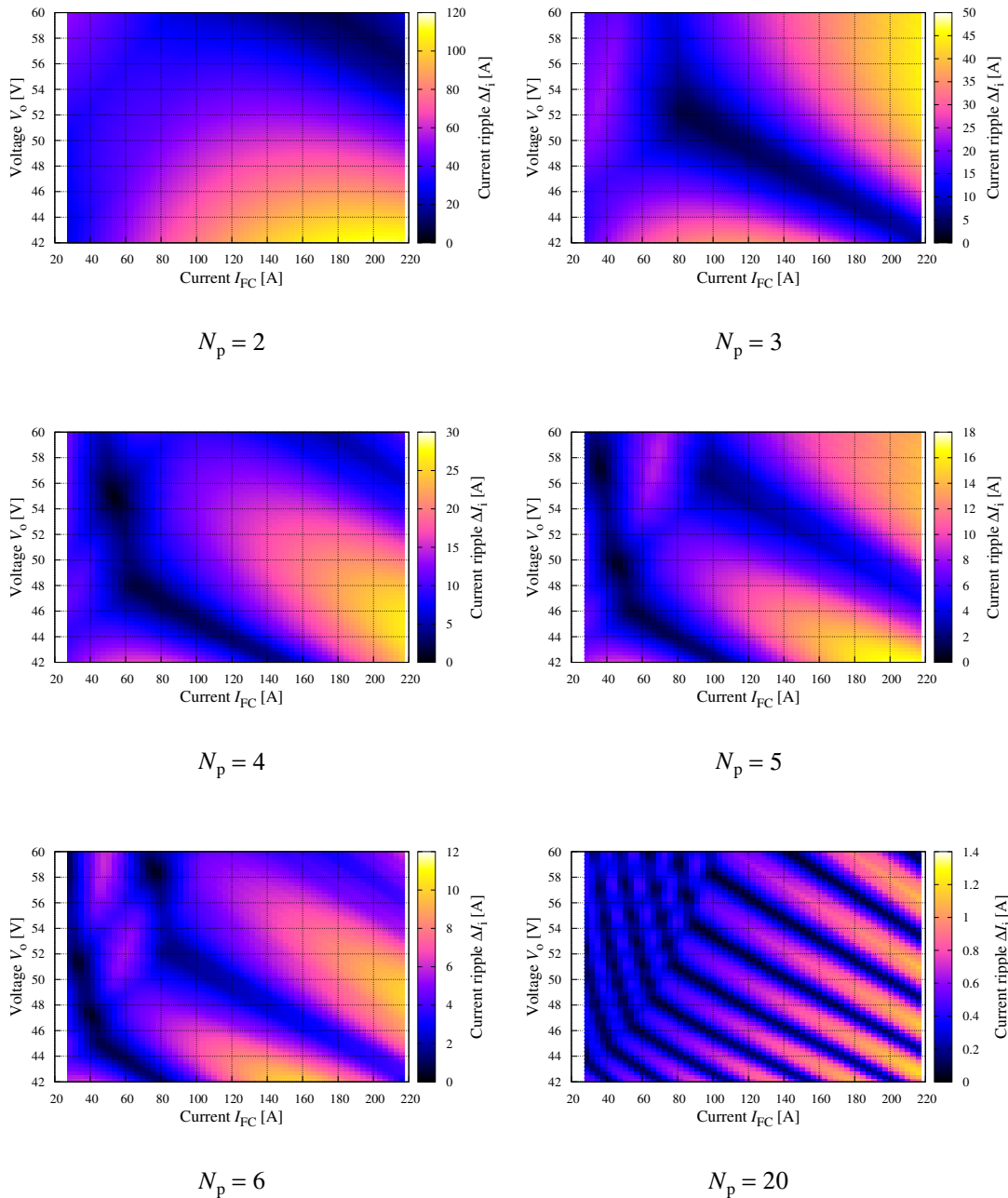
The relative input current ripple is:



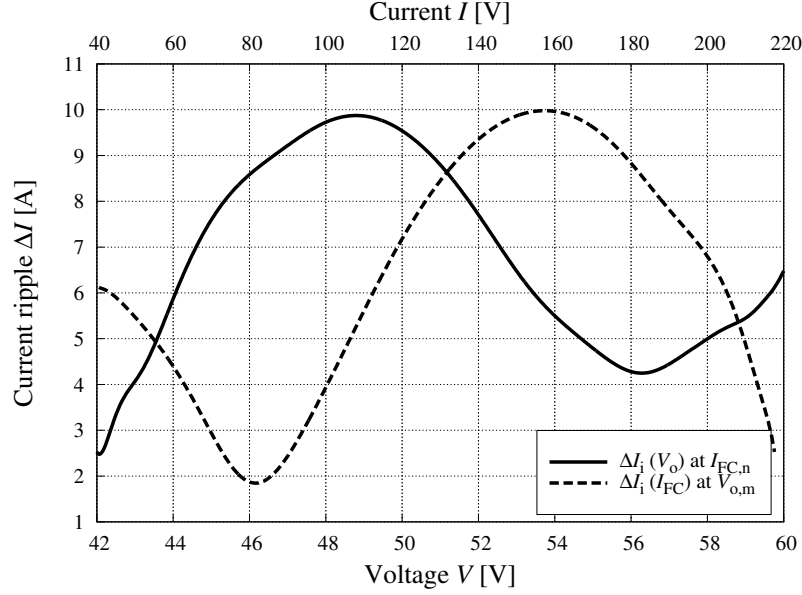
**Figure 3.13.** Phase input current  $i_i$  versus time  $t$ , with the output voltage  $V_o$  as a parameter.



**Figure 3.14.** Total input current  $i_{i,T}$  versus time  $t$ , with the output voltage  $V_o$  as a parameter.



**Figure 3.15.** Input current ripple  $\Delta I_{i,T}$  versus fuel cell current  $I_{FC}$  and output voltage  $V_o$  for different values of the number of phases  $N_p$ .



**Figure 3.16.** Maximum input current ripple  $\Delta I_{i,M}$  versus output voltage  $V_o$  at nominal fuel cell current  $I_{FC,n}$  and  $\Delta I_{i,M}$  versus fuel cell current  $I_{FC}$  at minimum output voltage  $V_{o,m}$ .

$$\Delta \Lambda_{i,M} = \frac{\Delta I_{i,M}}{I_{FC,n}} = 4.7 \% \quad (3.2.52)$$

which is compatible with what stated in Chapter 2 concerning current ripple.

Based on the diode current, the total output current can be calculated as:

$$i_{d,T}(I_{FC}, V_o) = \sum_{k=1}^{N_p} i_{d,k}(I_{FC}, V_o) \quad (3.2.53)$$

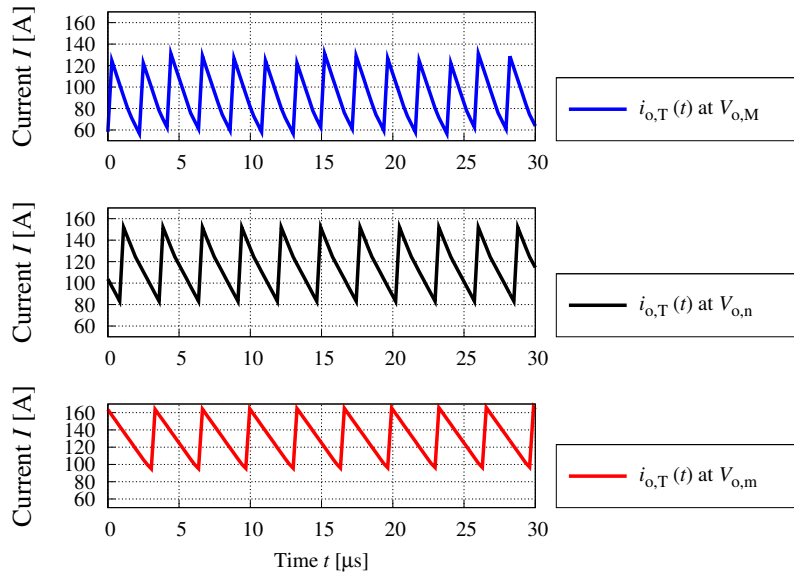
whose plot is shown in Figure 3.17.

In order to take into account the losses, assuming a known and constant efficiency, an equivalent current has been defined as:

$$I_{l,T}(I_{FC}, V_o) = \frac{P_{FC}(I_{FC})}{V_o} (1 - \eta_{PC}) \quad (3.2.54)$$

$$i_{o,T}(I_{FC}, V_o) = i_{d,T}(I_{FC}, V_o) - I_{l,T}(I_{FC}, V_o) \quad (3.2.55)$$

where  $i_{o,T}$  is the output current, and all the losses are supposed to take place at the output stage at the  $V_o$  voltage. The output current  $i_{o,T}$  is plotted in Figure 3.17. The Figure shows that the total output current trace shape is almost triangular, thanks to the interleaving control technique of the power converter's modules. The different average value of the current is related to the different output voltage, while the output power is the same.



**Figure 3.17.** Total output current  $i_{o,T}$  versus time  $t$ , with the output voltage  $V_o$  as a parameter.

The previous graph and considerations are endorsed by the behaviour of the output current ripple, which is plotted as a function of both the input current  $I_{FC}$  and of the output voltage  $V_o$ , as shown in Figure 3.18: it does not depend on the output voltage  $V_o$ , but only on the input current  $I_{FC}$ .

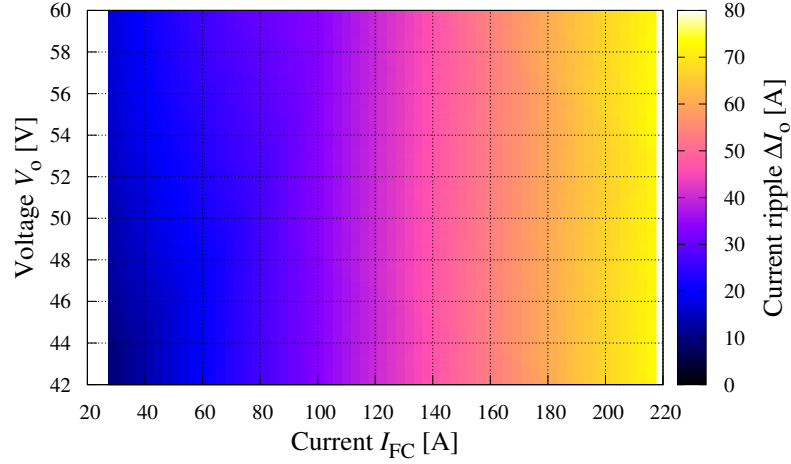
The maximum output current ripple values are reached when  $I_{FC} = I_{FC,n}$  and are almost independent from the output voltage  $V_o$ . Its maximum value is:

$$\Delta I_{o,M} = 73 \text{ A.} \quad (3.2.56)$$

The maximum relative output current ripple is:

$$\Delta \Lambda_{o,M} = \frac{\Delta I_{o,M}}{I_{o,a}(I_{FC}, V_o)} = 64 \%. \quad (3.2.57)$$





**Figure 3.18.** Output current ripple  $\Delta I_{o,T}$  versus fuel cell current  $I_{FC}$  and output voltage  $V_o$ .

The output capacitor current is calculated as:

$$i_{c,T}(I_{FC}, V_o) = i_{o,T}(I_{FC}, V_o) - I_{o,a}(I_{FC}, V_o) \quad (3.2.58)$$

whose plot is the same of the total output current, once its average component has been subtracted.

The output capacitor current ripple and the output current ripple are the same:

$$\Delta I_c(I_{FC}, V_o) = \Delta I_o(I_{FC}, V_o). \quad (3.2.59)$$

The output capacitance has been calculated, assuming that the interleaved converter is behaving like a standard converter in CCM mode:

$$\Delta Q(V_o) = \Delta I_{o,M} \frac{1}{8N_p f_s(I_{FC,n}, V_o)} \quad (3.2.60)$$

$$C_{o,T}(V_o) = \frac{\Delta Q(V_o)}{\Delta V_{o,M}}. \quad (3.2.61)$$

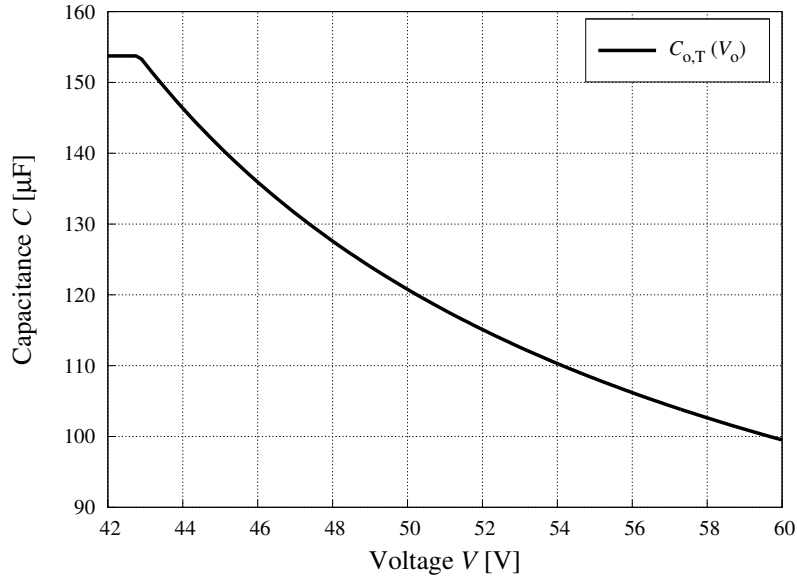
The plot of  $C_{o,T}(V_o)$  is shown in Figure 3.19. Its maximum value is:

$$C_{o,M} = 152 \mu\text{F}. \quad (3.2.62)$$

A safety coefficient  $\kappa_c = 0.9$  has been applied to this value, and the total capacity has been divided by the phase number, leading to:

$$C_o = \frac{C_{o,M}}{N_p} \frac{1}{\kappa_c} \cong 28 \mu\text{F} \quad (3.2.63)$$

where  $C_o$  is the output capacitor of every phase module.



**Figure 3.19.** Output capacitance  $C_{o,T}$  versus the output voltage  $V_o$ .

### 3.2.2.6. Average and RMS current computations

The phase average output current, which is equal to the diode average current, is defined as:

$$I_{o,a}(I_{FC}, V_o) = \frac{P_{FC}(I_{FC})}{N_p V_o} \eta_{PC} \quad (3.2.64)$$

$$I_{d,a}(I_{FC}, V_o) = I_{o,a}(I_{FC}, V_o) \quad (3.2.65)$$

which is plotted in Figure 3.20, and whose maximum values for  $I_{FC} = I_{FC,n}$  are:

$$\begin{aligned} V_o = V_{o,n} &\Rightarrow I_{d,a} = 19.1 \text{ A} \\ V_o = V_{o,m} &\Rightarrow I_{d,a} = 22 \text{ A} \\ V_o = V_{o,M} &\Rightarrow I_{d,a} = 15.3 \text{ A.} \end{aligned} \quad (3.2.66)$$

The diode RMS current is defined as:

$$I_{d,rms}(I_{FC}, V_o) = I_{i,pk}(I_{FC}, V_o) \sqrt{\frac{\delta_d(I_{FC}, V_o)}{3}} \quad (3.2.67)$$

which is plotted in Figure 3.20, and whose maximum values for  $I_{FC} = I_{FC,n}$  are:

$$\begin{aligned} V_o = V_{o,n} &\Rightarrow I_{d,rms} = 33 \text{ A} \\ V_o = V_{o,m} &\Rightarrow I_{d,rms} = 35 \text{ A} \\ V_o = V_{o,M} &\Rightarrow I_{d,rms} = 29 \text{ A.} \end{aligned} \quad (3.2.68)$$

For all the plots of the RMS and average current of the diodes and of the switches, the different behaviour presented depends on the saturation status of the switching frequency. Moreover, in non-saturation, the current ratio between RMS and average value is linear. Instead, when the fuel cell current decreases and the switching frequency saturates, the ratio increases, confirming the operation of the converter deeper and deeper in DCM.

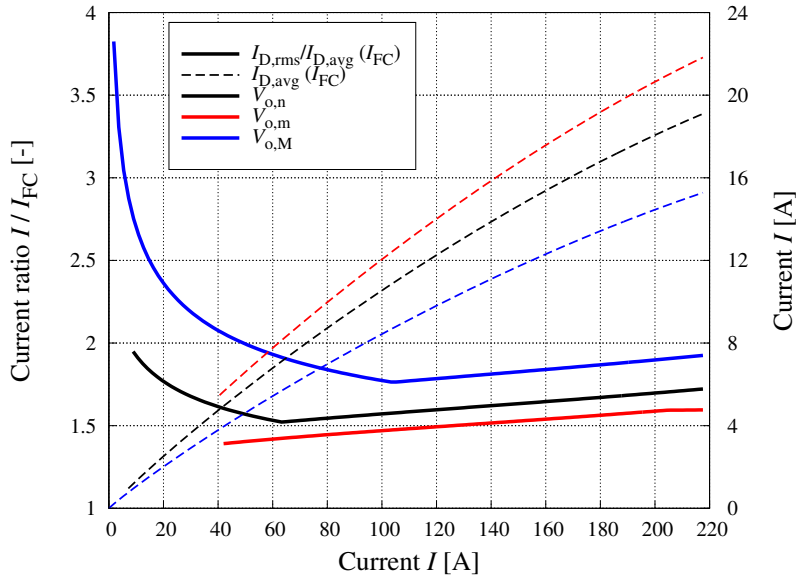
The switch average current is defined as:

$$I_{s,a}(I_{FC}, V_o) = I_{o,a}(I_{FC}, V_o) \frac{\delta_s(I_{FC}, V_o)}{\delta_d(I_{FC}, V_o)} \quad (3.2.69)$$

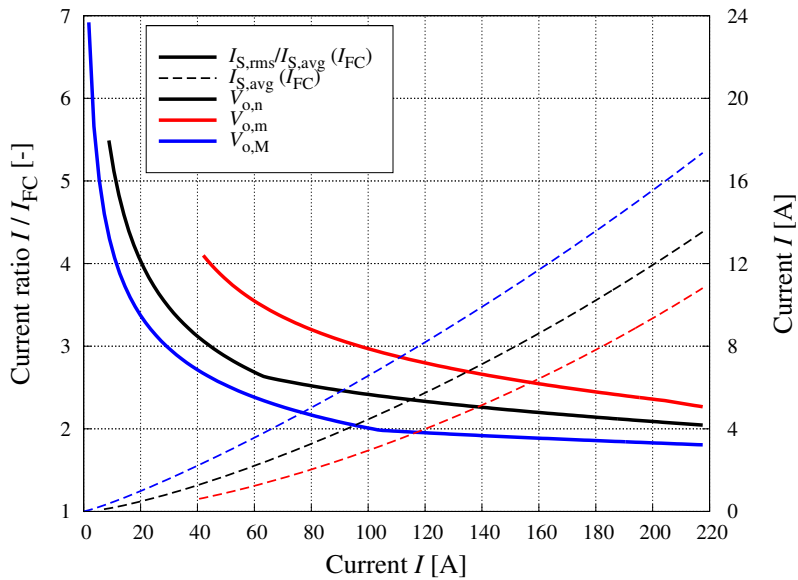
which is plotted in Figure 3.21, and whose maximum values for  $I_{FC} = I_{FC,n}$  are:

$$\begin{aligned} V_o = V_{o,n} &\Rightarrow I_{s,a} = 13.5 \text{ A} \\ V_o = V_{o,m} &\Rightarrow I_{s,a} = 10.8 \text{ A} \\ V_o = V_{o,M} &\Rightarrow I_{s,a} = 17.4 \text{ A} \end{aligned} \quad (3.2.70)$$

The switch RMS current is defined as:



**Figure 3.20.** Diode average current ratio  $I_{d,rms}/I_{d,a}$  and diode average current  $I_{d,a}$  versus the fuel cell current  $I_{FC}$ , with the output voltage  $V_o$  as a parameter.



**Figure 3.21.** Switch average current ratio  $I_{s,rms}/I_{s,a}$  and diode average current  $I_{s,a}$  versus the fuel cell current  $I_{FC}$ , with the output voltage  $V_o$  as a parameter.

$$I_{s,rms}(I_{FC}, V_o) = I_{i,pk}(I_{FC}, V_o) \sqrt{\frac{\delta_s(I_{FC}, V_o)}{3}} \quad (3.2.71)$$

which is plotted in Figure 3.21, and whose maximum values for  $I_{FC} = I_{FC,n}$  are:

$$\begin{aligned} V_o = V_{o,n} &\Rightarrow I_{s,rms} = 28 \text{ A} \\ V_o = V_{o,m} &\Rightarrow I_{s,rms} = 25 \text{ A} \\ V_o = V_{o,M} &\Rightarrow I_{s,rms} = 31 \text{ A}. \end{aligned} \quad (3.2.72)$$

The inductor peak current is defined as:

$$I_{i,pk}(I_{FC}, V_o) = \frac{V_{FC}(I_{FC})}{L} \frac{\delta_s(I_{FC}, V_o)}{f_s(I_{FC}, V_o)} \quad (3.2.73)$$

whose maximum values for  $I_{FC} = I_{FC,n}$  are:

$$\begin{aligned} V_o = V_{o,n} &\Rightarrow I_{i,pk} = 13.5 \text{ A} \\ V_o = V_{o,m} &\Rightarrow I_{i,pk} = 10.8 \text{ A} \\ V_o = V_{o,M} &\Rightarrow I_{i,pk} = 17.4 \text{ A}. \end{aligned} \quad (3.2.74)$$

The inductor average current is defined as:

$$I_{L,a}(I_{FC}, V_o) = I_{i,pk}(I_{FC}, V_o) \frac{\delta_s(I_{FC}, V_o) + \delta_d(I_{FC}, V_o)}{2} \quad (3.2.75)$$

which coincides with the phase average input current, whose maximum value is:

$$I_{L,a,M} = 36 \text{ A}. \quad (3.2.76)$$

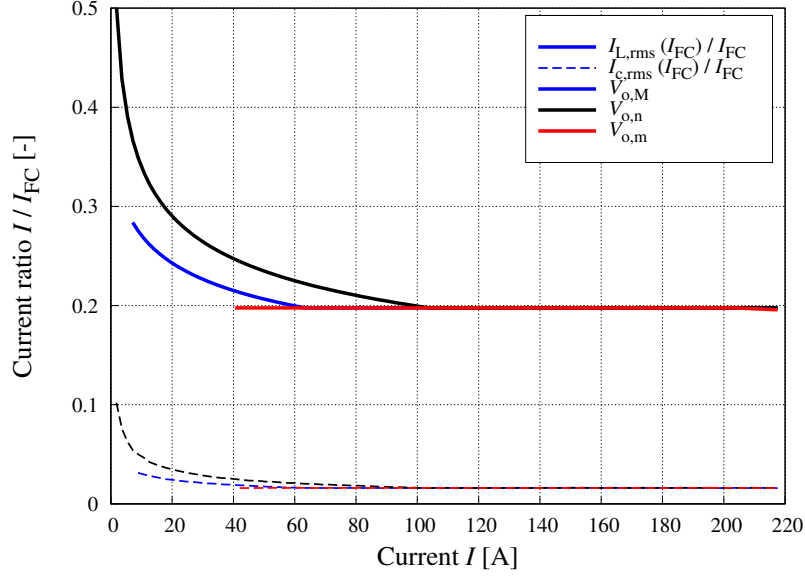
The inductor RMS current is defined as:

$$I_{L,rms}(I_{FC}, V_o) = \sqrt{I_{s,rms}^2(I_{FC}, V_o) + I_{d,rms}^2(I_{FC}, V_o)} \quad (3.2.77)$$

which is plotted in Figure 3.22, and whose maximum value is:

$$I_{L,a,M} = 43 \text{ A}. \quad (3.2.78)$$

The output capacitor RMS current for each module is defined as:



**Figure 3.22.** Inductor  $I_{L,rms}$  and output capacitor  $I_{c,rms}$  RMS current versus the fuel cell current  $I_{FC}$ , with the output voltage  $V_o$  as a parameter.

$$I_{c,rms}(I_{FC}, V_o) = \frac{\Delta I_c(I_{FC}, V_o)}{2\sqrt{3}} \frac{1}{N_p} \quad (3.2.79)$$

also plotted in Figure 3.22, and whose maximum value is:

$$I_{c,rms,M} = 3.4 \text{ A.} \quad (3.2.80)$$

Both the inductor and the output capacitor current ratios display similar behaviours, except that the inductor's current is about 10 times larger than the output capacitor's one.

### 3.2.2.7. Inductor design

The operating values of the inductor are:

$$I_{L,pk} = 76 \text{ A} \quad (3.2.81)$$

$$I_{L,rms} = 43 \text{ A} \quad (3.2.82)$$

$$I_{L,a} = 36 \text{ A} \quad (3.2.83)$$

$$L_n = 2.4 \mu\text{H} \quad (3.2.84)$$

$$T_{L_n} = 100 \text{ }^\circ\text{C} \quad (3.2.85)$$

where  $I_{L,\text{pk}}$  is the inductor peak current,  $I_{L,\text{rms}}$  its RMS current,  $I_{L,\text{a}}$  its average current,  $L_n$  the inductance value, and  $T_{L_n}$  the operating temperature.

Some important constants are:

$$\rho_{\text{Cu},T} = 23 \cdot 10^{-7} \text{ } \Omega\text{m} \quad (3.2.86)$$

$$\mu_0 = 4\pi \cdot 10^{-7} \text{ H/m} \quad (3.2.87)$$

$$D_p = 310 \text{ } \mu\text{m} \quad (3.2.88)$$

where  $\rho_{\text{Cu},T}$  is the copper resistivity at the operating temperature,  $\mu_0$  is the vacuum magnetic permeability, and  $D_p$  is the skin depth in copper at the nominal switching frequency.

The chosen core is a 3C90 material FerroxCube ETD 44/22/15 core, whose technical characteristics are given in Appendix H.

The width  $w_{\text{Cu}}$ , thickness  $t_{\text{Cu}}$  and section area  $S_{\text{Cu}}$  of the conductor are:

$$w_{\text{Cu}} = 25 \text{ mm} \quad (3.2.89)$$

$$t_{\text{Cu}} = 0.5 \text{ mm} \quad (3.2.90)$$

$$S_{\text{Cu}} = w_{\text{Cu}} t_{\text{Cu}} = 12.5 \text{ mm}^2 \quad (3.2.91)$$

where the thickness has been chosen in order to keep it as close as possible to the double of the skin depth.

This leads to a winding DC resistance and to winding power losses which are equal to:

$$R_{w,\text{DC}} = 142 \text{ m}\Omega \quad (3.2.92)$$

$$P_{w,l} = R_{w,\text{DC}} I_{L,\text{rms}}^2 = 260 \text{ mW}. \quad (3.2.93)$$

The maximum achievable inductance with  $N_t = 4$  turns is:

$$L_{N_t} = 2.3 \text{ } \mu\text{H}. \quad (3.2.94)$$

In order to achieve the nominal inductance  $L_n$ , an air gap is required:

$$t_a = 1.9 \text{ mm} \quad (3.2.95)$$

leading to the maximum induction level:

$$B_{M,l} = 265 \text{ mT} \quad (3.2.96)$$

which is compatible with the chosen core material.

The alternating part of the induction in the core is given by:

$$B_{AC}(I_{FC}, V_o) = \frac{1}{2} L_n \frac{I_{i,pk}(I_{FC}, V_o)}{N_t A_e} \quad (3.2.97)$$

whose value for nominal output voltage and nominal input current is:

$$B_{AC}(I_{FC,n}, V_{o,n}) = 133 \text{ mT}. \quad (3.2.98)$$

### 3.2.2.8. Estimation of the power losses

*Input inductor.* — A function interpolating the specific power loss as a function of peak flux density and frequency has been derived from the core material datasheet, and since both peak flux density and frequency are functions of the input current  $I_{FC}$  and output voltage  $V_o$ , total core losses can be expressed as:

$$P_{L,c}(I_{FC}, V_o) = P_V(I_{FC}, V_o) V_e \quad (3.2.99)$$

where  $P_V$  is the interpolating function and  $V_e$  is the core volume. Further details on the interpolating function  $P_V$  can be found in Appendix H.

The core losses for  $I_{FC} = I_{FC,n}$  are:

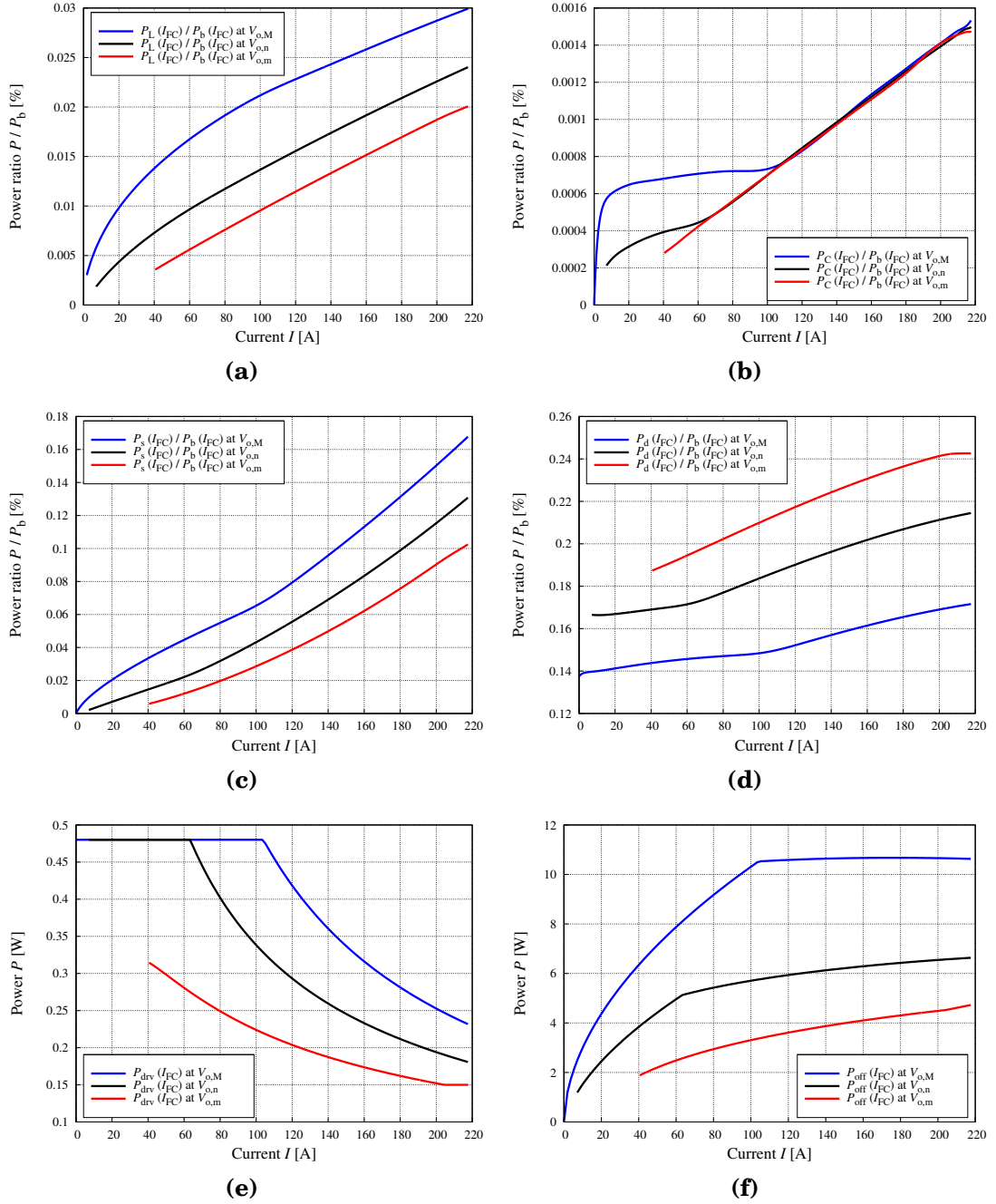
$$\begin{aligned} V_o = V_{o,n} &\Rightarrow P_{L,c} = 1.46 \text{ W} \\ V_o = V_{o,m} &\Rightarrow P_{L,c} = 1.07 \text{ W} \\ V_o = V_{o,M} &\Rightarrow P_{L,c} = 2.1 \text{ W}. \end{aligned} \quad (3.2.100)$$

Disregarding the skin effect, the losses on the inductor winding for each module are given by:

$$P_{w,DC}(I_{FC}, V_o) = N_t R_{w,DC} I_{L,rms}^2(I_{FC}, V_o) \quad (3.2.101)$$

The maximum values for the winding losses in the inductor are:





**Figure 3.23.** Power ratio of the power losses in (a) the inductance  $P_L$ , (b) the output capacitor  $P_C$ , (c) the switch  $P_s$ , (d) the diode  $P_d$  over the output base power  $P_b = I_{FC} V_{o,n}$ . (e) MOSFET drive and (g) turn off power losses. All the plot are versus fuel cell current  $I_{FC}$ .

$$\begin{aligned}
V_o = V_{o,n} &\Rightarrow P_{w,DC} = 1.05 \text{ W} \\
V_o = V_{o,m} &\Rightarrow P_{w,DC} = 1.03 \text{ W} \\
V_o = V_{o,M} &\Rightarrow P_{w,DC} = 1.05 \text{ W}
\end{aligned} \tag{3.2.102}$$

while the plots of the total losses in the inductor are shown in Figure 3.23 (a).

*Output capacitor.* — The total power losses on the output capacitors, plotted in Figure 3.23 (b), are given by:

$$P_C(I_{FC}, V_o) = R_{ESR} I_{c,rms}^2(I_{FC}, V_o) \tag{3.2.103}$$

where  $R_{ESR} = 13 \text{ m}\Omega$  is the capacitor equivalent series resistance (ESR), derived from an experimental capacitor characterisation. The maximum values for  $I_{FC} = I_{FC,n}$  are:

$$\begin{aligned}
V_o = V_{o,n} &\Rightarrow P_C = 0.152 \text{ W} \\
V_o = V_{o,m} &\Rightarrow P_C = 0.151 \text{ W} \\
V_o = V_{o,M} &\Rightarrow P_C = 0.154 \text{ W.}
\end{aligned} \tag{3.2.104}$$

*Switch and diode.* — The chosen module Microsemi APT10M11JVRU2 integrates both the power switch and the free-wheeling diode. Thus, it is suitable to implement the switching cell within a single ISOTOP package.

All the specifications can be found in Appendix H. However, the main values follow:

$$R_{DS,on} = 18 \text{ m}\Omega \tag{3.2.105}$$

$$V_F = 0.55 \text{ V} \tag{3.2.106}$$

$$R_F = 11 \text{ m}\Omega \tag{3.2.107}$$

$$V_{gs} = 10 \text{ V} \tag{3.2.108}$$

$$Q_g = 300 \text{ nC} \tag{3.2.109}$$

$$T_{off} = 60 \text{ ns} \tag{3.2.110}$$

where  $R_{DS,on}$  is the MOSFET drain-source on resistance,  $V_F$  is the free-wheeling diode forward voltage drop and  $R_F$  its equivalent series resistance,  $V_{gs}$  is

the MOSFET gate-source on voltage,  $Q_g$  is the MOSFET gate charge, and  $T_{\text{off}}$  a first order approximation of the turn-off time.

The switch ohmic losses are plotted in Figure 3.23 (c) and given by:

$$P_s(I_{\text{FC}}, V_o) = R_{\text{DS,on}} I_{\text{s,rms}}^2(I_{\text{FC}}, V_o) \quad (3.2.111)$$

whose values for  $I_{\text{FC}} = I_{\text{FC,n}}$  are:

$$\begin{aligned} V_o = V_{o,n} &\Rightarrow P_s = 13.7 \text{ W} \\ V_o = V_{o,m} &\Rightarrow P_s = 10.7 \text{ W} \\ V_o = V_{o,M} &\Rightarrow P_s = 17.5 \text{ W}. \end{aligned} \quad (3.2.112)$$

The diode losses are plotted in Figure 3.23 (d) and given by:

$$P_d(I_{\text{FC}}, V_o) = R_F I_{\text{d,rms}}^2(I_{\text{FC}}, V_o) + V_F I_{\text{d,a}}(I_{\text{FC}}, V_o) \quad (3.2.113)$$

whose values for  $I_{\text{FC}} = I_{\text{FC,n}}$  are:

$$\begin{aligned} V_o = V_{o,n} &\Rightarrow P_d = 22 \text{ W} \\ V_o = V_{o,m} &\Rightarrow P_d = 25 \text{ W} \\ V_o = V_{o,M} &\Rightarrow P_d = 17.9 \text{ W}. \end{aligned} \quad (3.2.114)$$

*Driving losses.* — The driving losses are plotted in Figure 3.23 (e) and given by:

$$P_{\text{drv}}(I_{\text{FC}}, V_o) = Q_g V_{\text{gs}} f_s(I_{\text{FC}}, V_o) \quad (3.2.115)$$

whose values for  $I_{\text{FC}} = I_{\text{FC,n}}$  are:

$$\begin{aligned} V_o = V_{o,n} &\Rightarrow P_{\text{drv}} = 0.181 \text{ W} \\ V_o = V_{o,m} &\Rightarrow P_{\text{drv}} = 0.150 \text{ W} \\ V_o = V_{o,M} &\Rightarrow P_{\text{drv}} = 0.23 \text{ W}. \end{aligned} \quad (3.2.116)$$

Since the driving losses are directly proportional to the switching frequency, they clearly present the same saturation behaviour as the switching frequency, as shown in the graph.

*Switching losses.* — Since in DCM the turn-on and diode recovery losses are inherently zero, the switching losses can be given by:

$$P_{\text{off}}(I_{\text{FC}}, V_o) = \frac{1}{2} I_{i,\text{pk}}(I_{\text{FC}}, V_o) V_o T_{\text{off}} f_s(I_{\text{FC}}, V_o) \quad (3.2.117)$$

and are plotted in Figure 3.23 (f). Their values for  $I_{\text{FC}} = I_{\text{FC},n}$  are:

$$\begin{aligned} V_o = V_{o,n} &\Rightarrow P_{\text{off}} = 6.6 \text{ W} \\ V_o = V_{o,m} &\Rightarrow P_{\text{off}} = 4.7 \text{ W} \\ V_o = V_{o,M} &\Rightarrow P_{\text{off}} = 10.6 \text{ W}. \end{aligned} \quad (3.2.118)$$

*Efficiency estimation.* — The total lost power is plotted in Figure 3.24 and given by:

$$P_{l,T}(I_{\text{FC}}, V_o) = N_p (P_C(I_{\text{FC}}, V_o) + P_{L,c}(I_{\text{FC}}, V_o) + P_{w,\text{DC}}(I_{\text{FC}}, V_o) + \quad (3.2.119)$$

$$+ P_s(I_{\text{FC}}, V_o) + P_d(I_{\text{FC}}, V_o) + P_{\text{drv}}(I_{\text{FC}}, V_o) \quad (3.2.120)$$

$$+ P_{\text{off}}(I_{\text{FC}}, V_o)) \quad (3.2.121)$$

whose values for  $I_{\text{FC}} = I_{\text{FC},n}$  are:

$$\begin{aligned} V_o = V_{o,n} &\Rightarrow P_{l,T} = 350 \text{ W} \\ V_o = V_{o,m} &\Rightarrow P_{l,T} = 320 \text{ W} \\ V_o = V_{o,M} &\Rightarrow P_{l,T} = 390 \text{ W}. \end{aligned} \quad (3.2.122)$$

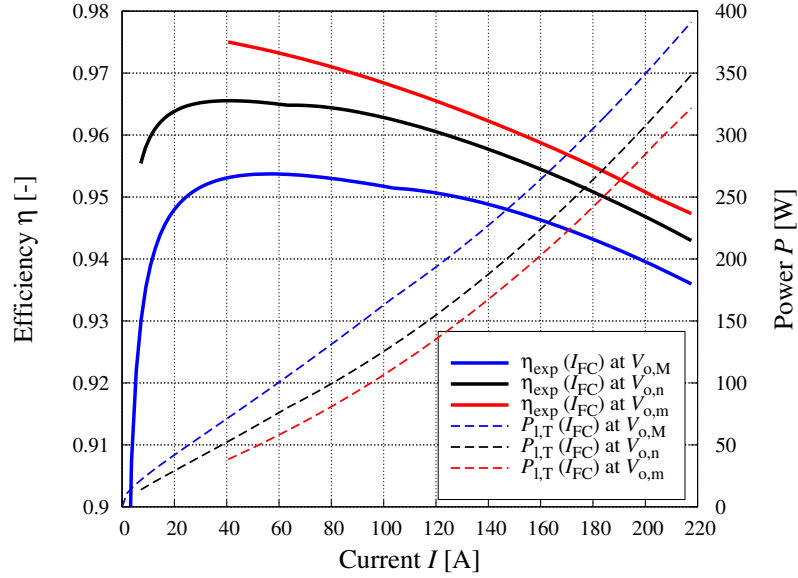
The power converter efficiency is plotted in Figure 3.24 and given by:

$$\eta_{\text{exp}}(I_{\text{FC}}, V_o) = 1 - \frac{P_{l,T}(I_{\text{FC}}, V_o)}{P_{\text{FC}}(I_{\text{FC}})} \quad (3.2.123)$$

whose values for  $I_{\text{FC}} = I_{\text{FC},n}$  are:

$$\begin{aligned} V_o = V_{o,n} &\Rightarrow \eta_{\text{exp}} = 0.943 \\ V_o = V_{o,m} &\Rightarrow \eta_{\text{exp}} = 0.947 \\ V_o = V_{o,M} &\Rightarrow \eta_{\text{exp}} = 0.936. \end{aligned} \quad (3.2.124)$$

The calculated efficiency is in the range between 0.93 and 0.98 for almost all its operation range.



**Figure 3.24.** Total power losses  $P_{l,T}$  and power converter efficiency  $\eta_{\text{exp}}$  versus the fuel cell current  $I_{\text{FC}}$ , with the output voltage  $V_o$  as a parameter.

### 3.2.3. Control implementation

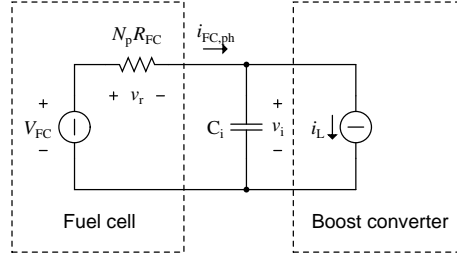
After presenting the sizing process of the hardware part, the implementation of its control strategy will be described.

#### 3.2.3.1. Current control implementation

The initial choice for the boost converter input current control strategy was the peak current mode control. Its inherent robustness and simplicity make it a perfect candidate for this application. However, an interesting instability phenomenon was observed during the early stages of the experimental tests.

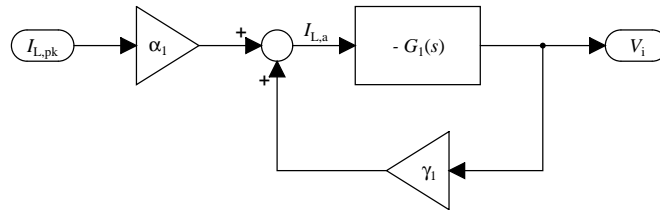
The fuel cell — the primary energy source — can be modelled, according to a Thévenin equivalent representation, as a constant voltage source  $V_{\text{FC}}$ , with a series resistance  $R_{\text{FC}}$ . They are both derivable from the typical fuel cell characteristic of Figure 3.5. The current controlled boost converter can be considered equivalent to a current source  $i_L$ , as shown in Figure 3.25.

It should be noted that even if the following analysis is referred to a single phase converter, it can also apply to a multi-phase topology as well, since the derived relations only involve average quantities. In the following discussion, the switching frequency is assumed as a constant.



**Figure 3.25.** Equivalent model for a fuel cell and power converter system. Acronyms: fuel cell open-circuit voltage  $V_{FC}$ , number of converter phases  $N_p$ , fuel cell internal equivalent resistance  $R_{FC}$ , boost input capacitor  $C_i$ .

The voltage across the input capacitor  $C_i$ , required to couple the voltage and current sources, is a function of the average value  $I_{L,a}$  of the input current  $i_L$ , among other parameters. In the peak current mode controller the latter is inherently related to the input voltage  $V_i$ . Then, an unwanted feedback loop is generated, as shown in Figure 3.26, and its stability needs to be assessed.



**Figure 3.26.** Block diagram of the relation between the peak current  $I_{L,pk}$  and the input voltage  $V_i$ .

The average input current of the boost converter can be expressed as:

$$I_{L,a} = \frac{1}{2} I_{L,pk}^2 \frac{L f_s}{V_i} \frac{V_o}{V_o - V_i} \tag{3.2.125}$$

where  $L$  is the converter phase inductance and  $f_s$  is the phase switching frequency.

By perturbing the previous equation with respect to  $I_{L,pk}$  and  $V_i$ , it is possible to calculate the parameter of the model representing the  $I_{L,a}$  intrinsic input feedback loop. These are given by the following relations and are valid assuming the DCM operation:

$$-G_1(s) = -\frac{N_p R_{FC}}{1 + s N_p R_{FC} C_i} \quad (3.2.126)$$

$$\alpha_1 = \frac{\partial I_{L,a}}{\partial I_{L,pk}} = \sqrt{\frac{2L f_s}{V_i} \frac{I_{L,a}}{1 - \frac{V_i}{V_o}}} \quad (3.2.127)$$

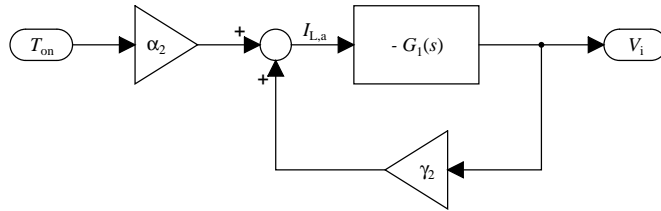
$$\gamma_1 = \frac{\partial I_{L,a}}{\partial V_i} = -\frac{I_{L,a}}{V_i} \frac{1 - 2 \frac{V_i}{V_o}}{1 - \frac{V_i}{V_o}}. \quad (3.2.128)$$

When  $V_i < V_o/2$ , the  $\gamma$  parameter becomes negative and this makes the loop unstable, since a positive feedback is introduced. It should be noted that this phenomenon is not related with the well known static instability of the peak current mode and cannot then be solved by any compensation ramp.

For this reason, a constant on-time modulator solution, shown in Figure 3.27, has been adopted. The control loop is inherently stable, since the  $\gamma$  parameter is always positive. The relation between the average input current  $I_{L,a}$  and the modulator output variable, the switch on-time  $T_{on}$ , is given by:

$$I_{L,a} = \frac{V_i f_s}{2L} \frac{V_o}{V_o - V_i} T_{on}^2. \quad (3.2.129)$$

By perturbing the previous equation with respect to  $T_{on}$  and  $V_i$ , it is possible to calculate the parameters of the model representing the intrinsic input feedback loop. This is expressed by the following relation and is valid assuming the DCM operation:



**Figure 3.27.** Block diagram of the relation between the input voltage  $V_i$  and the on-time  $T_{on}$ .

$$\alpha_2 = \frac{\partial I_{L,a}}{\partial T_{on}} = 2T_{on} \frac{V_i f_s}{2L} \frac{V_o}{V_o V_i} \quad (3.2.130)$$

$$\gamma_2 = \frac{\partial I_{L,a}}{\partial V_i} = \frac{I_{L,a}}{V_i} \frac{1}{1 - \frac{V_i}{V_o}}. \quad (3.2.131)$$

In this case, the  $\gamma$  parameter is inherently positive.

The same conclusion would also apply to the conventional Pulse-Width Modulation (PWM) modulator. Adopting the PWM solution has indeed been considered, but eventually discarded. The conventional analog PWM modulator is based on the comparison between a modulating signal and a suitable, triangular, carrier waveform. Then, the switch duty cycle must be proportional to the ratio between the modulating signal level and the carrier wave peak to peak amplitude. In this way, the switch duty cycle is independent from the switching and carrier wave frequency.

Instead, the converter proposed here is based on a interleaved, multiphase topology and variable switching frequency operation is advisable for the application. The interleaving requires the phase modulators to operate with precisely phase shifted modulating signals, but the implementation of several ( $N_p$ ) triangular carrier waveforms, which have a variable frequency, but maintain a constant phase lag between each other, is not exactly straightforward.

Non-conventional implementations of the PWM modulator could have been investigated, but the constant  $T_{on}$  modulator seemed to be preferable also for the following motivation.

Since the switching frequency is variable, a PWM modulator would not directly control the switch on-time. The power switches always present a minimum on-time  $T_{on,m}$ , below which no regulation is possible, as the switch simply does not turn on. When this limit is reached, the current controller which is driving the modulator will saturate. In order to properly take care of the saturation and avoid undesirable transients when linearity is restored — as those due to the integral controller wind-up —, information about the minimum/maximum allowed modulator input is important. Unfortunately the input's limits are undefined in the case of variable switching frequency with a conventional PWM modulator, as the modulator controls the duty-cycle, not the on-time — the same duty-cycle corresponds to different on-times, as the switching frequency varies. Therefore, the required anti-wind-up provisions are not easy to implement, since the saturation level becomes a function of the switching frequency.



The synchronisation between the phases is easy to achieve in the case of a constant on-time modulator, since the only required information is a clock signal to mark the start of each modulation period. The generation of  $N_p$  clock signals with variable frequency and assigned phase lag is much easier to implement with a controllable master clock frequency generator and a simple counter. Moreover, the modulator input related to the minimum on-time is unambiguously defined, independently from the switching frequency, and the outer control loop saturation can be properly managed. When the modulator operates at constant frequency, it actually behaves as a standard PWM modulator, at least as long as it operates in the linear region, i.e. for  $T_{on} > T_{on,m}$ . Under these conditions, there is no real difference between a standard PWM modulator and the constant  $T_{on}$  one in the input-output behaviour. Therefore, the analysis of the converter dynamic behaviour can be developed as if in the presence of a conventional PWM control, the only difference being the small signal modulator gain.

Based on the constant on-time modulator, an average current control loop has been implemented, which uses an analog Proportional Integral (PI) regulator. Voltage mode control has been considered as well, but not implemented. The reason is that having the full control of the fuel cell current in any condition is advisable, especially during transients and start-up/shut-down phases. This is impossible to achieve when voltage mode control is used. However, in order to regulate the converter output voltage, an additional, external feedback loop is needed, whose design will be discussed in E.2.

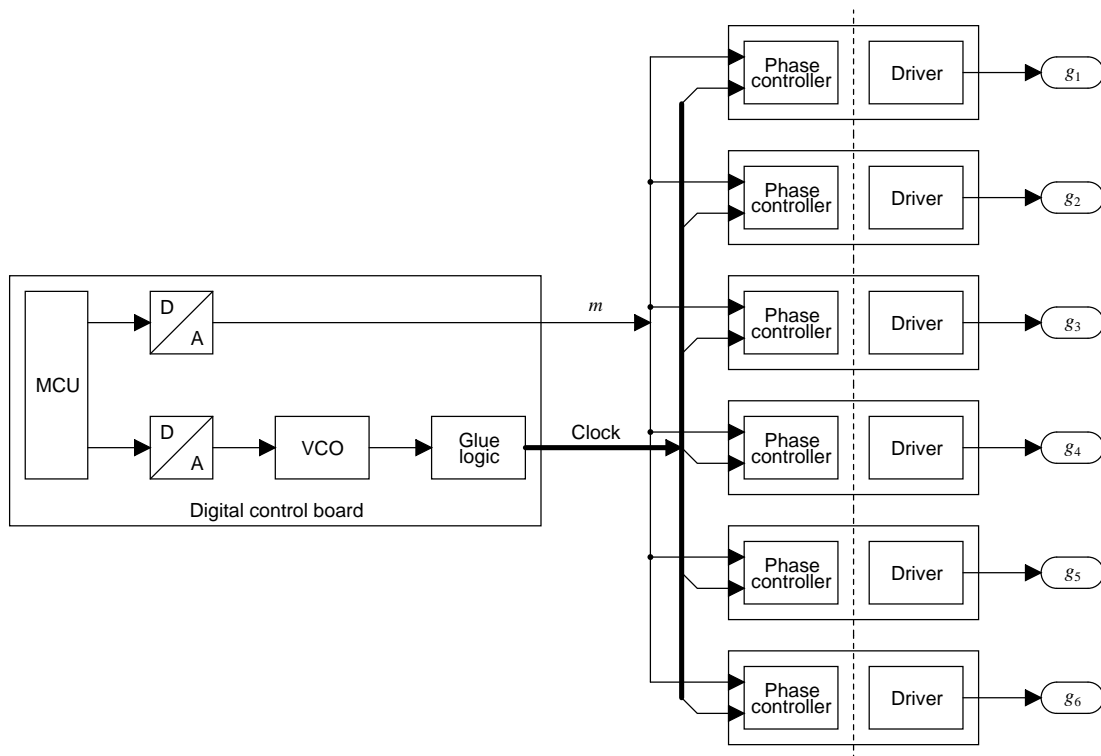
### 3.2.3.2. *Variable frequency control implementation*

The regulation action defined by Equation 3.2.20 is based on continuously acquired input and output voltage samples.

As far as the current is concerned, the reference value generated by the voltage controller is used directly. The speed of the regulation is determined by the repetition frequency of the calculation of Equation 3.2.20. This should not be very high, so as to limit the dynamic interactions with the current control loop. In the actual prototype, frequencies between 1 kHz and 2 kHz have been successfully tested. In the presence of load transients, the converter will temporarily operate at a switching frequency different from the one imposed by Equation 3.2.20, as the input current changes significantly within the frequency update period. This is not a problem if the load is decreased, as the only practical consequence will be the operation, for a limited amount of time, at a switching frequency lower than the best possible one. However, if the load is increased, the same phenomenon may determine the temporary operation

of the converter in CCM mode. Although this event implies an increase in the commutation losses of the power switches, its limited duration — typically lower than a few milliseconds — prevents any relevant thermal stress. In addition, it causes no control problems, since the average current controller is robust enough to compensate the gain variation determined by the operation in CCM.

Referring to Figure 3.28, more details on the control's design will follow. The digital controller is interfaced with six low level control boards, one for each phase, that implement the actual phase current regulation, exploiting the UC3823 analog integrated controller. The controllers are synchronised with the respective clock signals, thanks to a dedicated pin. The integrated circuit allows the implementation of both the constant on-time modulator and the analog Proportional Integral (PI) regulator. A power MOSFET driver is then used to provide gate signals for the switches.



**Figure 3.28.** Block diagram of the power converter control system. Acronym: Microcontroller Unit (MCU), Digital to Analog converter (D/A), Voltage Controller Oscillator (VCO), reference signal ( $m$ ), gate signals ( $g_1 \dots g_6$ ).

The set-points for the inductor average current and the clock signals for the modulators are generated by a digital control board, by means of a serial Digital to Analog (D/A) converter and a dedicated logic circuit respectively. The D/A converter is serially connected to a MicroController Unit (MCU), which periodically executes the voltage control loop and frequency adjustment algorithms. The former generates the current set-point that is directly sent to the phase controllers after D/A conversion. The latter provides a set-point for the synchronisation logic circuit. This circuit includes a Voltage Controlled Oscillator (VCO), fed by the second channel of the D/A converter. The VCO frequency is then divided by a binary counter, whose output bits are used as phase clock signals after being properly processed by simple combinatorial logic gates.

### 3.3. Conclusion

A 5 kW fuel cell system has been sized along with all its components: the fuel cell stack, the power converter and the controller.

The variable switching frequency behaviour of the power converter along with its adequate controller have been extensively studied.

An interesting instability phenomenon in the first version of the current control has been investigated and a working solution has been proposed and studied analytically.

A complete model of the system will be presented in the next chapter.



## CHAPTER 4

### SYSTEM MODELLING

A complete model of a fuel cell system will be presented in this chapter. It will be used to simulate the system with the Matlab Simulink tool. Figure 4.1 shows the main blocks that compose such a system:

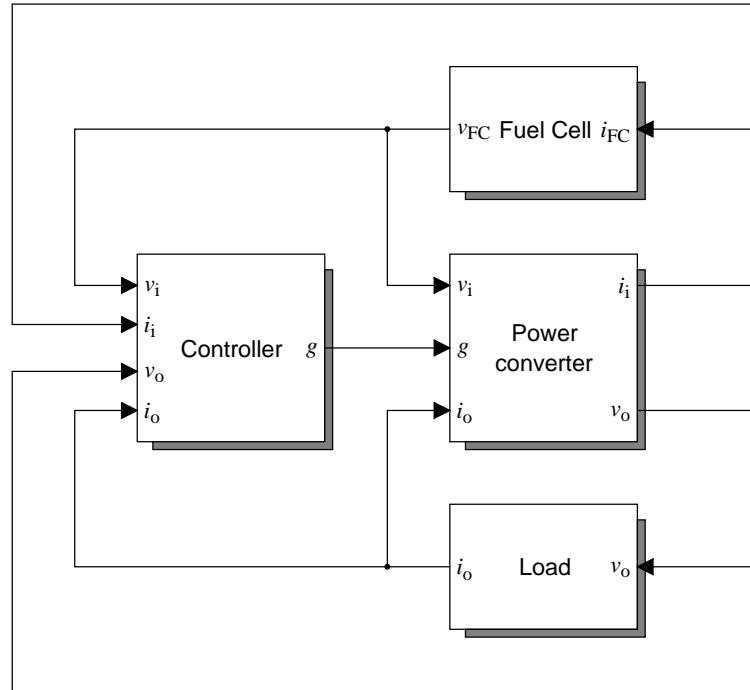
- the fuel cell;
- the power converter;
- the load;
- the controller.

In the following sections, the fuel cell block will be modelled and will be followed by the power converter block model. The chapter will end with the model of the controller block.

#### 4.1. Fuel Cell

After a bibliographical excursus on the fuel cell models, the relations between the output voltage of a fuel cell and the current the external load imposes will be expressed.

First, the relations between the reactant rates and the fuel cell current will be established. The electromotive force, the voltage drops on the cell and the dynamical effects will then be described.



**Figure 4.1.** Main blocks that compose a fuel cell system. Acronyms: Fuel Cell (FC), Power Converter (PC), PC input and output voltages ( $v_i$  and  $v_o$ ), PC input and output currents ( $i_i$  and  $i_o$ ), PC gate signal control ( $g$ ), FC voltage and current ( $v_{FC}$  and  $i_{FC}$ ).

Power density, efficiency and water production of a fuel cell will be calculated. A fuel cell model will then be proposed.

#### 4.1.1. Bibliographical excursus

Fuel cell models can be divided into four groups on the basis of two independent criteria:

- time criterion: steady-state models — in which the interest is focused on the polarisation curve of the fuel cell —, and dynamic models — in which the interest is focused on the dynamic behaviour of the fuel cell;
- space criterion: 0-dimensional models — in which variable relations are only a function of time —, and 1, 2 or 3-dimensional models — in which variable relations also involve one or more space variables.

The 1, 2, or 3-dimensional group is characterised by the use of diffusion equations to solve the problem. This does not probably suit the simulation of a system, since the interest is focused more on the interactions between the fuel cell and the other parts of the system than on the internal working of the fuel cell itself. Examples of 1-D models are described in [70 – 75], while a 2-D model example is presented in [76].

Instead, a 0-dimensional model only includes differential equations about the time variable: its numerical solution requires less resources, it can be represented as an electrical circuit or as a block diagram, and so it is suitable for the simulation of an entire system.

References [77, 78], published in 1990, are historically significant articles, in which the transport phenomena of ions are studied, mainly in relation with ion-exchange membranes. 1990 is also the year when Ballard presented its first PEMFC system (Section 1.1.1). These articles were followed by [79 – 81], which are some of the most referenced articles on fuel cell modelling: 1-D diffusion equations in the different parts a fuel cell is composed of are described thoroughly.

In 1995, references [9, 10] were written on this basis: they presented a semi-empirical 0-D model, used as a basis for many other 0-D models developed in the following years. Other articles presenting similar semi-empirical models are [82 – 87].

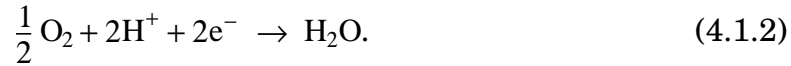
The model applied in this thesis is a 0-D dynamic one. The fuel cell voltage equation used is based on [9]. A systematic description of the several parts the equation is composed of can be found in [6, 88]. References [6, 54, 89 – 95] present the integration of some dynamic aspects and the electrical equivalent circuit.

Two reviews of fuel cell models are [96, 97].

Concerning fuel cell systems, references [98 – 102] deal with modelling and analysis in the automotive domain. For what concerns stationary applications, a small wind fuel cell hybrid system is described in [103].

#### 4.1.2. Molar rates and current

The two semi-reactions that take place in a PEMFC, at the anode and cathode respectively, are described by:



The relations between the current  $i$  and the molar rates of the different species — namely hydrogen  $\dot{n}_{\text{H}_2}$  oxygen  $\dot{n}_{\text{O}_2}$  flow rates, and water production  $\dot{n}_{\text{H}_2\text{O}}$  — are derived from the two semi-reactions 4.1.1 and 4.1.2 in Appendix D:

$$\dot{n}_{\text{H}_2} = \frac{i}{2F} \quad (4.1.3)$$

$$\dot{n}_{\text{O}_2} = \frac{i}{4F} \quad (4.1.4)$$

$$\dot{n}_{\text{H}_2\text{O}} = \frac{i}{2F}. \quad (4.1.5)$$

where  $F = 96\,485 \text{ C/mol}$  is the charge of a mole of electrons and is called Faraday constant.

This shows that the flow rates of the reactants are directly proportional to the current, and so imposed by the external circuit.

#### 4.1.3. Electromotive force

The calculation of the electromotive force of a fuel cell is based on the balance between the energy provided by the hydrogen and oxygen reaction and the electric work performed by the electrons along the electric circuit.

In Appendix D, the expression of the electromotive force is derived as a function of reactants' temperature, pressure and concentration, leading to:

$$e = E_0 + \Delta e_a$$

where  $E_0$  is the electromotive force at standard conditions and  $\Delta e_a$  is the variation of the electromotive force related to pressure and concentration variations.

From now on, the operating temperature and pressure values will be assumed to be constant and  $\Delta e_a$  will then represent the concentration losses. The



relation of  $\Delta e_a$  with the fuel cell density current will be expressed further on in this chapter.

#### 4.1.4. Voltage drops

The different voltage drops that are present in a fuel cell will be analysed in this part. Though in electrochemistry they are often called “overvoltages”, here they are referred to as voltage drops.

*Activation losses.* — A rigorous explanation of the phenomena of activation in electrochemistry can be found in many specialised books, like [104].

The voltage drop called “activation loss” is related to the “activity” of the reactions that take place in a fuel cell. Since the reactions at the cathode and anode are bidirectional, there is always an exchange flow of protons and electrons at the equilibrium — whose average value is zero. A current density  $J_0$  can be associated to this flow of charges and called “exchange” current density: the more active the surfaces are, the higher this current density becomes.

When electrons are subtracted from the anode and injected into the cathode — due to the current flowing into an external electric circuit —, the equilibrium of the reactions is shifted rightwards.

As long as the current density  $j_a$  of the electric circuit is less than the exchange current density  $J_0$ , no extra energy needs to be spent to produce the required charges. When the current density  $j_a$  is greater than the exchange current density  $J_0$ , new charges need to be “activated.” This requires extra energy and leads to a voltage drop, which is a function of the current density  $v_a(j_a)$ . For this reason, it is important that the current density  $J_0$  should be as high as possible.

This phenomenon can be formalised using multiple equations, like the Butler-Volmer or the Tafel ones [54]. In this work the Tafel equation has been chosen. It is a simpler form of the Butler-Volmer equation, but nonetheless provides good results. The equation applies separately to the anode and the cathode sides:

$$v_a(j_a) = A \ln\left(\frac{j_a}{J_0}\right) \quad (4.1.6)$$

which is only valid for  $j_a > J_0$  and where  $A$  is the Tafel constant.

Applying the equation for the anode and the cathode separately, the following relations can be obtained:

$$v_{a,A} = A_A \ln\left(\frac{j_a}{J_{0,A}}\right) \quad (4.1.7)$$

$$v_{a,C} = A_C \ln\left(\frac{j_a}{J_{0,C}}\right) \quad (4.1.8)$$

where  $A_A$  and  $A_C$  are the Tafel constants, and  $J_{0,A}$  and  $J_{0,C}$  the exchange current densities for the anode and cathode sides respectively.

Generally, since  $J_{0,A}$  and  $J_{0,C}$  are different, the activation loss expression is divided into three ranges, depending on the value of  $j_a$  as shown in:

$$1 : 0 \leq j_a < J_1 \quad (4.1.9)$$

$$2 : J_1 \leq j_a < J_2 \quad (4.1.10)$$

$$3 : J_2 \leq j_a \quad (4.1.11)$$

where:

$$J_1 = \min\{J_{0,A}, J_{0,C}\} \quad (4.1.12)$$

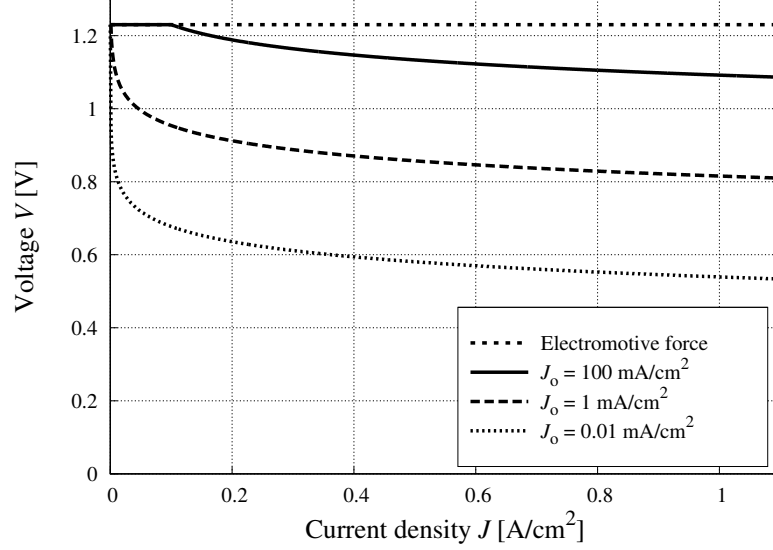
$$J_2 = \max\{J_{0,A}, J_{0,C}\}. \quad (4.1.13)$$

This leads to the following formulation:

$$v_a(j_a) = \begin{cases} 0 & 0 \leq j_a < J_1 \\ A' \ln\left(\frac{j_a}{J'}\right) & J_1 \leq j_a < J_2 \\ A'' \ln\left(\frac{j_a}{J''}\right) & J_2 \leq j_a \end{cases} \quad (4.1.14)$$

where  $J' = J_1$ , and  $A' = A_A$  if  $J_{0,A} < J_{0,C}$  and  $A' = A_C$  otherwise. The other significant values are:

$$A'' = A_A + A_C \quad (4.1.15)$$



**Figure 4.2.** Effect of the bare activation losses for different values of the exchange current density  $J_0$ .

$$J'' = J_{0,A} \frac{A_A}{A''} + J_{0,C} \frac{A_C}{A''}. \quad (4.1.16)$$

In the following,  $J''$  is referred to as  $J_0$ , and  $A''$  as  $A$ , whose typical values are:

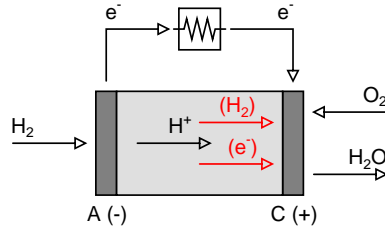
$$J_0 = 0.08 \frac{\text{mA}}{\text{cm}^2} \quad (4.1.17)$$

$$A = 0.06 \text{ V} \quad (4.1.18)$$

and whose effect is shown in Figure 4.2, for different values of the exchange current density  $J_0$ . The lower the exchange current density is, the more important the voltage drop will be. This is particularly noticeable for low values of the fuel cell current density  $J$ .

*Fuel crossover and internal currents.* — In real proton exchange membrane fuel cells, streams of electrons and of gaseous hydrogen can directly flow from the anode side to the cathode side across the proton exchange membrane: the first phenomenon is called “fuel crossover”, and the second “internal currents” (Figure 4.3).

Both subtract electrons to the external circuit and are associated, as a consequence, to an equivalent internal current density  $J_n$  which is always present.

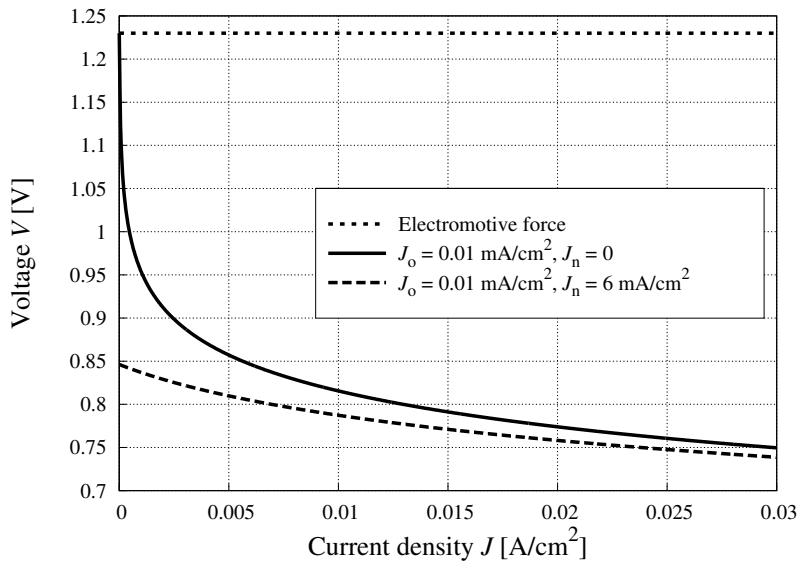


**Figure 4.3.** Schematic view of the fuel crossover and internal current effects.

Since this current density is always greater than the exchange current density  $J_0$ , the fuel cell voltage is always affected by the activation losses, and this is particularly noticeable when  $j_a$  is quite small (Figure 4.4). Due to this phenomenon, it is impossible to measure the electromotive force of a fuel cell. As shown in the figure, the fuel cell open circuit voltage is around 0.85 V, which is much lower than the electromotive force (around 1.23 V). More detailed information on the fuel crossover can be found in [105].

A typical value for  $J_n$  is:

$$J_n = 6 \text{ mA/cm}^2. \tag{4.1.19}$$



**Figure 4.4.** Zoom of the first part of the polarisation curve of a proton exchange membrane fuel cell, where the effect of the internal current density is most evident.

*Ohmic losses.* — An important percentage of the total voltage drop in a fuel cell is due to the ohmic losses, whose effect is shown in Figure 4.5, and whose formulation is given by:

$$v_r(j) = r j \quad (4.1.20)$$

where  $r$  is an area specific resistance (Appendix F). As shown in Figure 4.5, the ohmic effect is more conspicuous for high values of the fuel cell current density  $J$ .

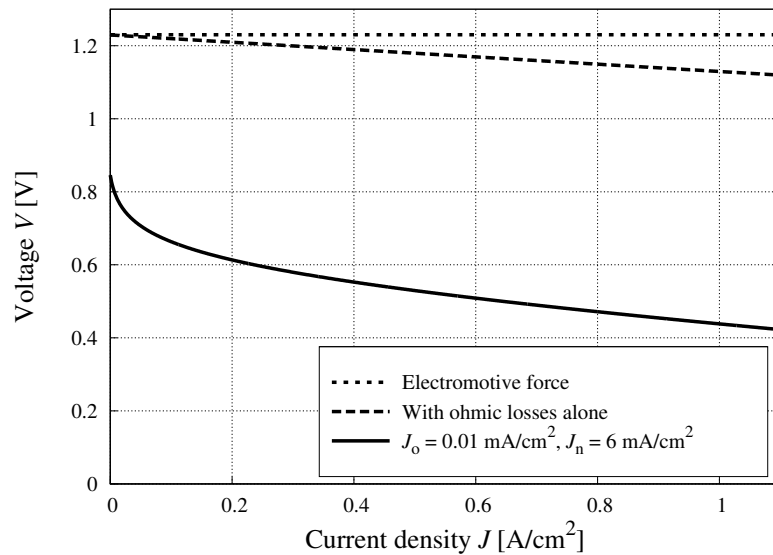
The total area specific resistance of a fuel cell is the sum of three main factors:

$$r = r_E + r_{BP} + r_C \quad (4.1.21)$$

where  $r_E$ ,  $r_{BP}$  and  $r_C$  are the area specific resistances of the electrolyte, of the bipolar plates and of the cell interconnections respectively. In the case of a proton exchange membrane fuel cell,  $r_E$  is dominant and strongly dependent on the hydration state of the membrane.

A typical value of  $r$  for a hydrated proton exchange membrane fuel cell is:

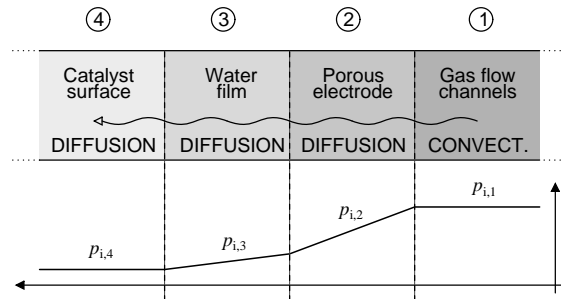
$$r = 22 \text{ m}\Omega \cdot \text{cm}^2. \quad (4.1.22)$$



**Figure 4.5.** Effect of the activation losses, of the ohmic voltage drop and of the internal currents.

*Diffusion losses.* — In the formulation of the electromotive force (in Appendix D), it has been shown that any variation in the reactant pressure and/or concentration is turned into variation of the electromotive force of the fuel cell (Equation D.2.28). Equations 4.1.3 and 4.1.4 show that the reactant mass flows are directly proportional to the current density. For this reason, diffusion losses are also called “mass transport losses” or “concentration losses”.

Reactants flowing from the gas channels to the catalyst layers have to cross several regions and undergo friction losses and diffusion phenomena. This leads to pressure and partial pressure drops of the reactants from the gas flow channel region, where the pressure and the concentration are at their highest, to the catalyst surface, where the pressure and the concentration are at their lowest and the reactions take place. The shape of the partial pressure curve of the reactant along its path is shown in Figure 4.6. The higher the current is, the higher the reactant flow rate is. Thus, the higher the partial pressure drop and the electromotive force due to the partial pressure drop are.



**Figure 4.6.** Partial pressure curve shape of the reactant flowing from the gas chamber to the reaction sites.

The partial pressure variation related to the electromotive force variation is the one in region ④, indicated by  $p_{i,4}$ , where  $i$  stands for the reactant — either hydrogen  $H_2$  or oxygen  $O_2$ .

When the current density  $j_d$  varies from  $J^*$  to  $J^{**}$ , to which the following partial pressures of the  $i$  reactant respectively correspond:

$$P_{i,4}^* = p_{i,4}(J^*) \quad (4.1.23)$$

$$P_{i,4}^{**} = p_{i,4}(J^{**}) \quad (4.1.24)$$

the formulation of the associated voltage drop is:

$$v_{p,* \rightarrow **} = \frac{R T}{\xi_i F} \ln \left( \frac{P_{i,4}^*}{P_{i,4}^{**}} \right) \quad (4.1.25)$$

where  $\xi_i = 2$  at the anode, and  $\xi_i = 4$  at the cathode.

Two hypotheses are formulated in [6] in order to obtain a mathematical relation between  $v_p$  and  $j_d$

- there is a current density  $J_1$ , called limit current density, which causes the partial pressure  $p_{i,4}$  to drop to zero;
- the partial pressure  $p_{i,4}$  linearly decreases from  $P_{i,4}^0$  when  $j_d = 0$  to zero when  $j_d = J_1$ .

$$\frac{p_{i,4}(j_d)}{P_{i,4}^0} = 1 - \frac{j_d}{J_1} \quad (4.1.26)$$

$$v_p(j_d) = \frac{R T}{\xi_i F} \ln \left( 1 - \frac{j_d}{J_1} \right) = B \ln \left( 1 - \frac{j_d}{J_1} \right) \quad (4.1.27)$$

where:

$$B = \frac{R T}{\xi_i F}. \quad (4.1.28)$$

This formulation is valid for both the anode and cathode sides, so the final voltage drop should be a linear combination of the two separate voltage drops. Nevertheless, the voltage drop on the cathode side — the air or oxygen side — is generally far higher than the anode side voltage drop — the hydrogen side. This still lets approximate the voltage drop with Equation 4.1.27, where  $B$  is now an experimental parameter, whose typical value for a proton exchange membrane fuel cell is:

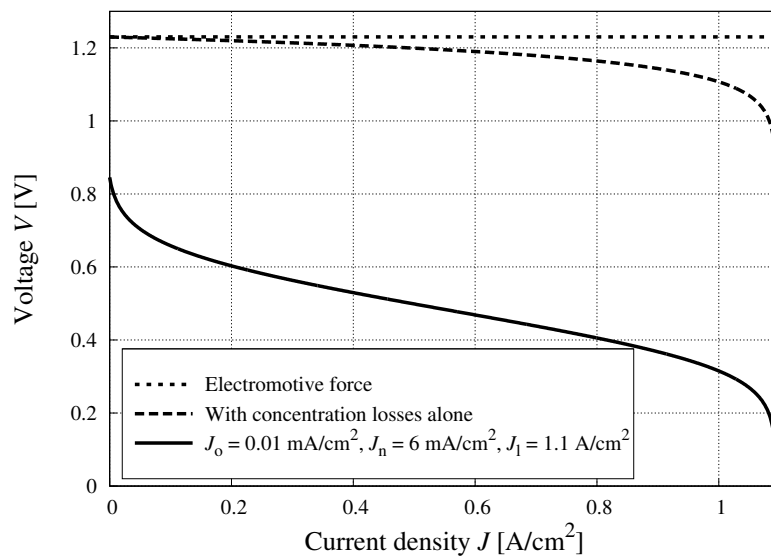
$$B = 0.05 \text{ V}. \quad (4.1.29)$$

The voltage drop due to the diffusion of the mass transport phenomenon is then:

$$v_d(j_d) = -v_p(j_d) = -B \ln \left( 1 - \frac{j_d}{J_1} \right). \quad (4.1.30)$$

The effect of concentration losses and the fuel cell output voltage, as a result of all the voltage drops, is shown in Figure 4.7. Concentration losses are particularly noticeable for high values of the fuel cell current density.

Further and more detailed information on the hydrogen partial pressure drop in a fuel cell stack can be found in [106].



**Figure 4.7.** The effect of concentration losses and the voltage of a fuel cell with all losses taken into account.

#### 4.1.5. Dynamic effects

The dynamic behaviour of a fuel cell is affected by fluid dynamic — both inside and outside the fuel cell — and electric phenomena — like the double charge layer effect.

*The double charge layer effect.* — At the interface between the electrolyte and the gas diffusion layer, both at the anode and cathode sides, two layers of charges with opposite signs are present. These two layers are separated by a very small distance, the layer interface [107]. A capacitive effect is associated to this charge layer, and represented by a capacitor. Several configurations exist; the one found in [6], which is one of the simplest and most common has been adopted here.



*Fluid dynamic effects.* — Since the reactant pressure has influence on the fuel cell voltage, also the fluid dynamic effect of the reactant should also be taken into account. However, the fuel cell system that has been used is directly connected to a medium pressure (5 atm) gas line, and pressure regulators are directly mounted on the fuel cell stack itself. So, the gas paths characterised by low pressure and high speed — i.e. high friction losses — are short. For these reasons, these effects have not been taken into account in this dissertation.

#### 4.1.6. Power density and efficiency

The power density of a fuel cell element  $q$  is defined as:

$$q(j) = v(j) \cdot j. \quad (4.1.31)$$

The efficiency of the fuel cell by itself can then be defined as the ratio between the electrical output power density  $q$  and the electrochemical input power density  $q_i$ :

$$\eta_{\text{FC}}(j) = \frac{q(j)}{q_i(j)} \quad (4.1.32)$$

and, since the electromotive force  $e$  was by definition related to the electrochemical energy the reaction can release, it becomes:

$$\eta_{\text{FC}}(j) = \frac{v(j)j}{ej} = \frac{v(j)}{e}. \quad (4.1.33)$$

This is true if the reactant mass flow that enters the fuel cell is equal to the reactant mass flow required. However, this is generally not the case. The stoichiometric ratio  $\lambda_i$  of the reactant  $i$  is defined as:

$$\lambda_i = \frac{\dot{n}_{i,i}}{\dot{n}_i} = \frac{\dot{n}_{i,i}}{\dot{n}_{i,i} - \dot{n}_{o,i}} \quad (4.1.34)$$

where  $\dot{n}_{i,i}$  is the input molar rate of the reactant  $i$ ,  $\dot{n}_i$  is its consumption rate, and  $\dot{n}_{o,i}$  is its output molar rate.

The stoichiometric ratio needs to be higher than one ( $\lambda_i > 1$ ), since this is the only way to let the produced water out of the fuel cell. This also means that the electrochemical energy of the reactants has not been used completely. So, Equation 4.1.33 can be rewritten as:

$$\eta_{\text{FC}}(j) = \frac{v(j)j}{e \lambda_{\text{H}_2} j} = \frac{v(j)}{e \lambda_{\text{H}_2}} \quad (4.1.35)$$

where  $\lambda_{\text{H}_2}$  is the stoichiometric ratio of the fuel — hydrogen.

Furthermore, the efficiency of an entire fuel cell system has to take into account all the power losses, which can be divided into constant losses  $P_{\text{L,c}}$  and losses depending on the current density  $p_{\text{L},j}$ :

$$p_{\text{L}}(j) = P_{\text{L,c}} + p_{\text{L},j}(j). \quad (4.1.36)$$

Dividing each by the total surface  $S_{\text{T}}$  of the fuel cell stack, these losses can be expressed in terms of power density:

$$q_{\text{L}}(j) = \frac{p_{\text{L}}(j)}{S_{\text{T}}} = \frac{P_{\text{L,c}}}{S_{\text{T}}} + \frac{p_{\text{L},j}(j)}{S_{\text{T}}} = Q_{\text{L,c}} + q_{\text{L},j}(j). \quad (4.1.37)$$

As an example,  $Q_{\text{L,c}}$  could represent the power density used to keep the gas solenoid valves open, and to give power to the system control unit. Instead, the current depending losses could be represented as:

$$q_{\text{L},j}(j) = V_{\text{L},j} j + r_{\text{L},j} j^2 \quad (4.1.38)$$

where the constant  $V_{\text{L},j}$ , which is measured in Volts, but is not a physical voltage, takes into account the air compressor and the cooling circuit power, while  $r_{\text{L},j}$ , which is an area specific resistance, takes into account the ohmic losses outside the fuel cell stack.

The system efficiency can then be expressed as:

$$\eta(j) = \frac{q(j) - q_{\text{L}}(j)}{q_{\text{i}}(j)} \quad (4.1.39)$$

$$= \frac{v(j)j}{e \lambda_{\text{H}_2} j} - \frac{Q_{\text{L,c}} + q_{\text{L},j}(j)}{e \lambda_{\text{H}_2} j} \quad (4.1.40)$$

$$= \frac{v(j)}{e \lambda_{\text{H}_2}} - \frac{Q_{\text{L,c}} + q_{\text{L},j}(j)}{e \lambda_{\text{H}_2} j}. \quad (4.1.41)$$

Figure 4.8 shows the fuel cell voltage  $v$ , the power density  $q$  and its efficiency  $\eta_{\text{FC}}$  function of the current density  $j$ , while Figure 4.9 shows the overall efficiency for a fuel cell system.

In the first case, in which an ideal behaviour of the system is assumed, the lower the fuel cell current density is, the higher its efficiency is, because all the losses are proportional to the current density. In the actual case, shown in the second figure, the efficiency also decreases for low values of the current density, because of the constant losses.

#### 4.1.7. Water production

The mass rate of the produced water  $\dot{m}_{\text{H}_2\text{O}}$  is calculated as:

$$\dot{m}_{\text{H}_2\text{O}} = (2M_{\text{H}} + M_{\text{O}}) \dot{n}_{\text{H}_2\text{O}} \quad (4.1.42)$$

where  $\dot{n}_{\text{H}_2\text{O}}$  is the molar rate of water produced by a single fuel cell element, and  $M_{\text{H}}$  and  $M_{\text{O}}$  are the atomic weights of hydrogen and oxygen respectively.

If 4.1.5 is substituted in 4.1.42, the following is obtained:

$$\dot{m}_{\text{H}_2\text{O}}(j) = i \frac{2M_{\text{H}} + M_{\text{O}}}{2F} = j S \frac{2M_{\text{H}} + M_{\text{O}}}{2F} \quad (4.1.43)$$

where  $S$  is the surface of a single element, and for a fuel cell stack made of  $N$  elements

$$\dot{m}_{\text{T,H}_2\text{O}}(j) = N \dot{m}_{\text{H}_2\text{O}} = j S_{\text{T}} \frac{2M_{\text{H}} + M_{\text{O}}}{2F} \quad (4.1.44)$$

where  $S_{\text{T}} = S N$  is the total surface of the stack, and where

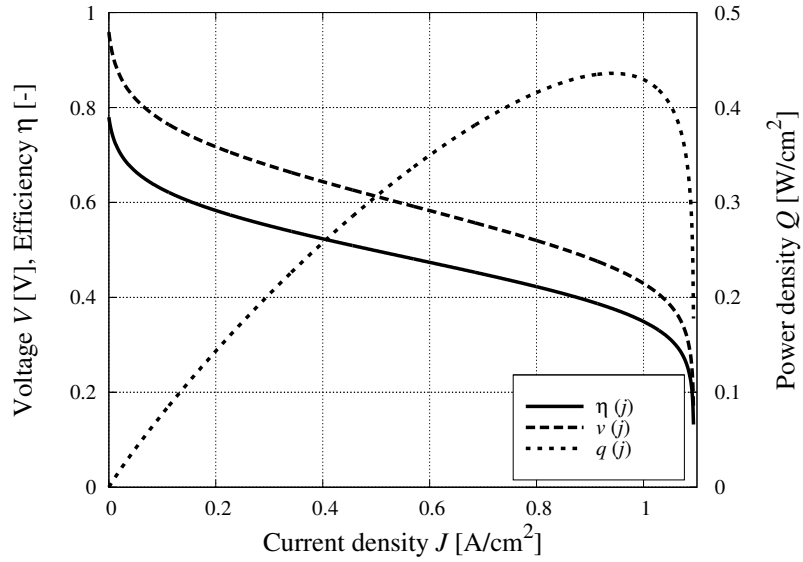
$$\frac{2M_{\text{H}} + M_{\text{O}}}{2F} = 9.336 \cdot 10^{-8} \frac{\text{kg}}{\text{A s}} = 0.336 \frac{\text{g}}{\text{A h}}. \quad (4.1.45)$$

The water production density  $\dot{o}_{\text{H}_2\text{O}}$  for a single fuel cell is:

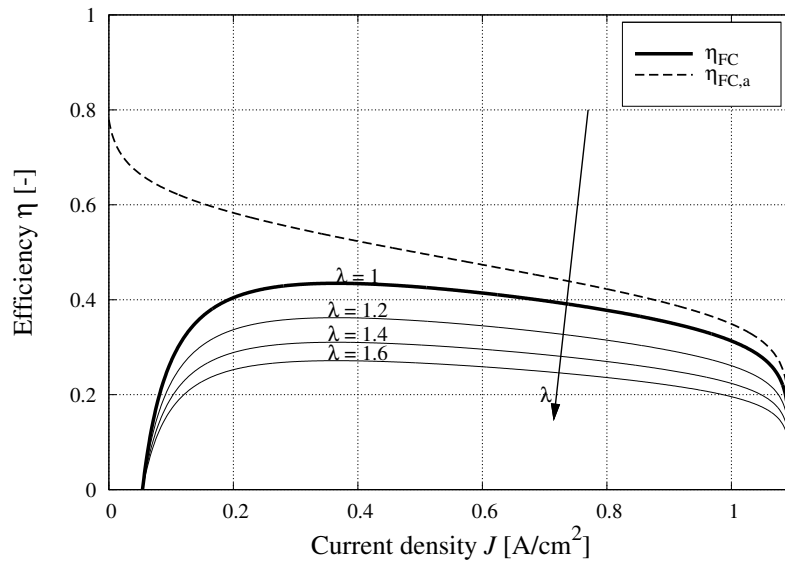
$$\dot{o}_{\text{H}_2\text{O}}(j) = \frac{\dot{m}_{\text{H}_2\text{O}}}{S} = \frac{2M_{\text{H}} + M_{\text{O}}}{2F} j. \quad (4.1.46)$$

Its plot is shown in Figure 4.10.

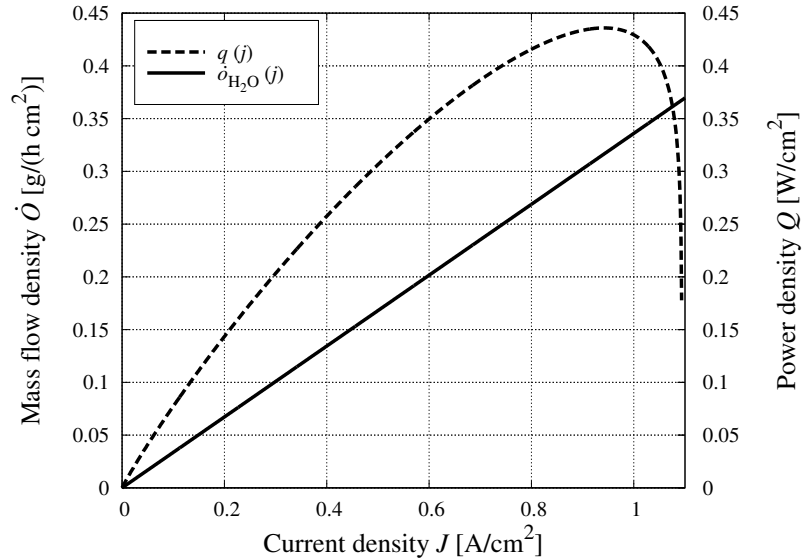
Water management for low temperature fuel cells, like PEM, is crucial and many papers have been dedicated to it [108 – 114].



**Figure 4.8.** Typical plots of fuel cell voltage  $v$ , power density  $q$  and efficiency  $\eta$  versus current density  $j$  for a low temperature PEM fuel cell.



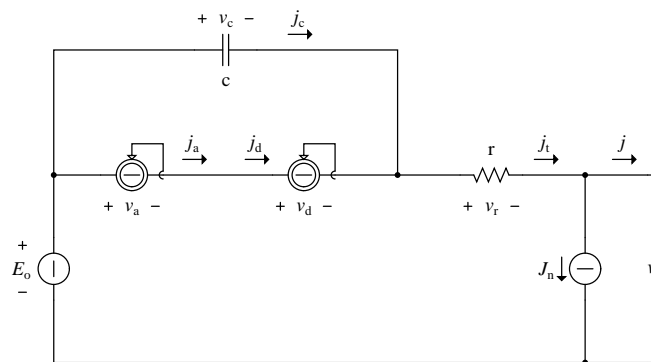
**Figure 4.9.** Efficiency plots for a single low temperature PEM fuel cell  $\eta_{FC,a}$  and for a fuel cell system  $\eta_{FC}$  for different values of the stoichiometric ratio  $\lambda$  versus current density  $j$ .



**Figure 4.10.** Density power  $q$  and water production density  $\dot{o}_{H_2O}$  versus current density  $j$  for a typical low temperature PEM fuel cell.

#### 4.1.8. Model description

*Electrical model.* — In the literature, several electrical equivalent fuel cell models exist (Section 4.1.1), based on the relations expressed in the previous sections concerning the electromotive force (Section 4.1.3) and the voltage drops (Section 4.1.4). One of the simplest is shown in Figure 4.11.



**Figure 4.11.** Electrical model of a Proton Exchange Membrane Fuel Cell (PEMFC).

Since the temperature effects are not taken into account, the electromotive force is supposed to be a constant  $e = E_0$  and represented by an ideal voltage source. The activation  $v_a(j_a)$  and diffusion  $v_d(j_d)$  voltage drops are represented by current controlled voltage sources, and the ohmic voltage drop  $v_r$  by the constant area specific resistance  $r$ . The internal current density  $J_n$  is represented by an ideal current source, and the capacitive effects by the capacitance density  $c$ . The definitions of area specific resistance and capacitance density are given in Appendix F.

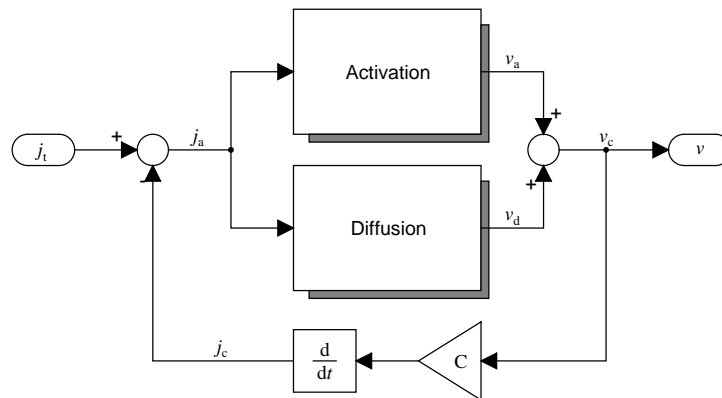
In the case of a  $N$ -element fuel cell stack whose surface is  $S$ , the behaviour of the fuel cell stack can be described by the same electrical model, once the relations between the current density  $j$  and the stack current  $i_{FC}$ , and between the cell voltage  $v$  and the stack voltage  $v_{FC}$  has been set:

$$i_{FC} = j S \quad (4.1.47)$$

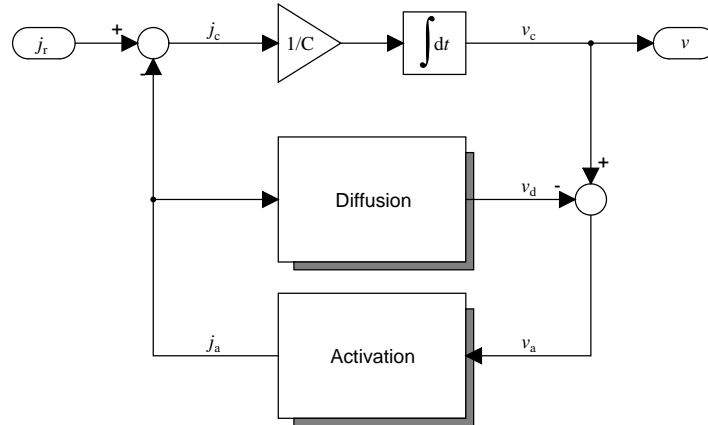
$$v_{FC} = v N. \quad (4.1.48)$$

*Block model.* — The representation of the previous electrical model in a block model can be useful for the simulation with programs such as Matlab Simulink.

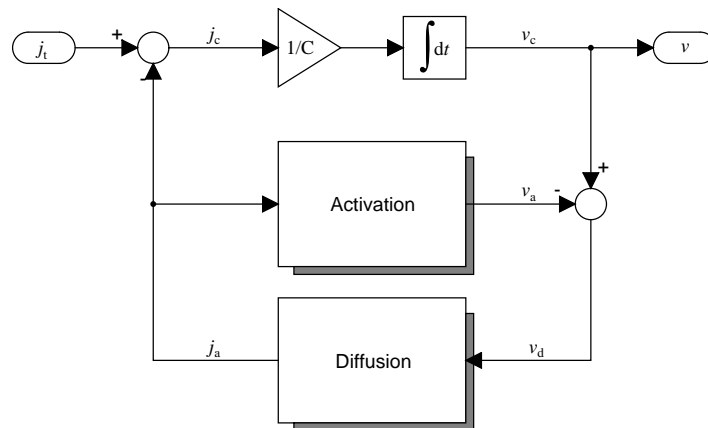
There are three different ways of expressing the electrical loop made up by the capacitor and the two controlled voltage sources, depending on how the equations concerning the capacitive effect, the activation and diffusion voltage drops are expressed.



**Figure 4.12.** First block model configuration for the capacitor, activation and diffusion voltage drop loop. The capacitive effect is represented by a derivative block.



**Figure 4.13.** Second block model configuration for the capacitor, activation and diffusion voltage drop loop. The capacitive effect is represented by an integral block. The  $j_a$  current density is a function of the activation voltage drop.



**Figure 4.14.** Third block model configuration for the capacitor, activation and diffusion voltage drop loop. The capacitive effect is represented by an integral block. The  $j_a$  current density is a function of the diffusion voltage drop.

In the first case — Figure 4.12 — the capacitor is represented by a derivative block:

$$v_c = c \frac{dj_c}{dt}. \tag{4.1.49}$$

In the second and third case — Figure 4.13 and 4.14 — the capacitor is represented by an integral block:

$$j_c = \frac{1}{c} \int v_c(t) dt. \quad (4.1.50)$$

The first solution has to be immediately excluded, since a derivative operation should be avoided in numeric simulations. The other two have been analysed in order to choose the best formulation for both the diffusion and activation blocks.

The two alternatives are:

- $j_d(v_d)$  and  $v_a(j_a)$ ;
- $v_d(j_d)$  and  $j_a(v_a)$ .

*Diffusion block.* — It can be observed that function 4.1.30, which describes this phenomenon, is not defined for  $j_d \geq J_1$ :

$$v_d(j_d) = -v_p(j_d) = -B \ln\left(1 - \frac{j_d}{J_1}\right).$$

This forces to avoid the formulation in which  $j_d$  is the input variable and  $v_d$  the output variable, and to investigate the behaviour of the inverted function, which becomes:

$$j_d(v_d) = J_1 \left(1 - e^{\frac{-v_d}{B}}\right). \quad (4.1.51)$$

Since Equation 4.1.30 is physically meaningful only for  $j_d \geq 0$ ,  $j_d = 0$  has been imposed for  $v_d < 0$ , which amounts to saying that the current in the fuel cell cannot reverse. If a negative current density were imposed by an external source, other reactions would take place, which cannot be described by the same equation, the proposed model only being valid for positive  $j_d$ .

So, the relation between  $j_d$  and  $v_d$  becomes:

$$j_d(v_d) = \begin{cases} J_1 \left(1 - e^{\frac{-v_d}{B}}\right) & v_d \geq 0 \\ 0 & v_d < 0 \end{cases} \quad (4.1.52)$$

which is always defined for  $j_d = (-\infty; +\infty)$ .



*Activation block.* — As previously done for the diffusion block, the inversion feasibility and physical meaningfulness of the equation describing the activation block will be studied.

The Tafel equation 4.1.6, which has been used to express the relation between  $v_a$  and  $j_a$ , is only defined in  $j_a = [J_0; +\infty)$ . Because of the definition of exchange current density and of activation losses,  $v_a$  is zero if  $j_a < J_0$ , leading to:

$$v_a(j_a) = \begin{cases} A \ln\left(\frac{j_a}{J_0}\right) & j_a \geq J_0 \\ 0 & j_a < J_0. \end{cases} \quad (4.1.53)$$

This represents the physical situation, in which the current density  $j_a$  — the input variable — is the cause, and the voltage drop  $v_a$  — the output variable — is the effect.

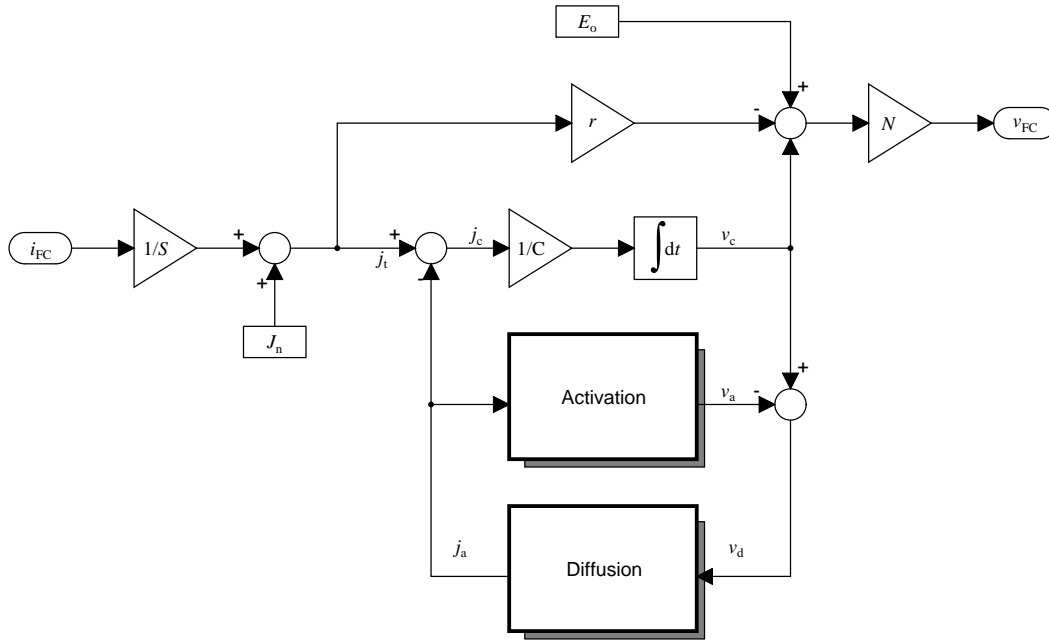
Moreover, the inversion of Equation 4.1.53 is not possible, since the function is not surjective. This excludes the formulation in which  $v_a$  is the input variable and  $j_a$  the output one.

*Conclusion.* — The previous considerations lead to choose the case shown in Figure 4.14, in which  $j_d(v_d)$  and  $v_a(j_a)$ . As a consequence, the complete model for the fuel cell stack is represented in Figure 4.15.

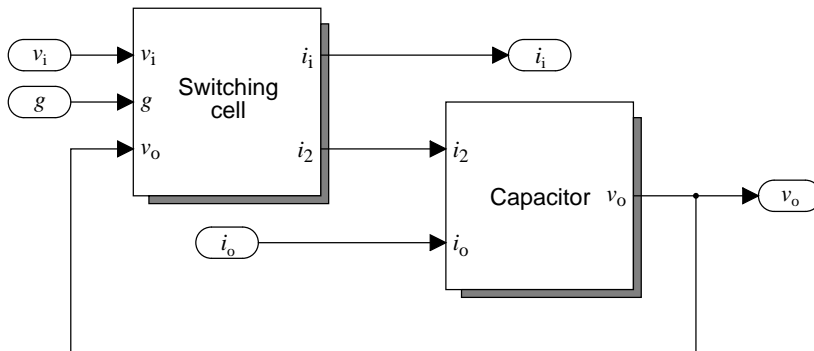
Although these functions are continuous in  $(-\infty; +\infty)$ , their derivatives are not and this could slow down the computing simulation. The solution that has been adopted to solve this issue is presented in Appendix G.

## 4.2. Power converter

The overall diagram of a power converter is described in Figure 4.16, in which the switching cell block can change according to the chosen topology, while the output capacitor block, described in Figure 4.23, stays the same.



**Figure 4.15.** Block model of a fuel cell stack after derivation from the electrical equivalent model.

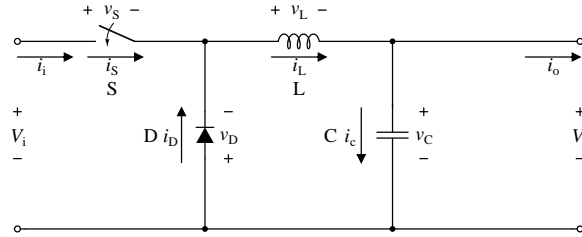


**Figure 4.16.** Main blocks that compose a power converter model, where  $v_i$  and  $v_o$  are the input and output voltages,  $i_i$  and  $i_o$  the input and output currents,  $g$  the switch command, and  $i_2 = i_c + i_o$  while  $i_c$  stands for the capacitor current.

4.2.1. Buck converter

The principle schematic of a buck converter switching cell is shown in Figure 4.17, while its block diagram is represented in Figure 4.18. They are both

valid in continuous and discontinuous conduction mode, the discontinuous mode being modelled by the saturation block and the reset input of the integrator.



**Figure 4.17.** Electric schematic of a buck converter.

They are both expressed by the following equations:

$$v_L = \begin{cases} V_i - V_o & \text{if } g = 1 \\ -V_o & \text{if } g = 0 \\ 0 & \text{if } g = 0 \wedge i_L = 0 \end{cases} \quad (4.2.1)$$

$$i_2 = i_L \quad (4.2.2)$$

$$i_1 = \begin{cases} i_L & \text{if } g = 1 \\ 0 & \text{if } g = 0 \end{cases} \quad (4.2.3)$$

where  $g$  is the switch signal command,  $v_L$  the voltage across the inductor,  $V_i$  the input voltage,  $V_o$  the output voltage,  $i_L$  the inductor current,  $i_i$  the input current, and  $i_2 = i_C + i_o$  is the sum of the capacitor current and the output current. In a buck converter  $V_i$  is always greater than  $V_o$ .

#### 4.2.2. Boost converter

The principle schematic of a boost converter switching cell is shown in Figure 4.19, while its block diagram is represented in Figure 4.20. They are both valid in continuous and discontinuous conduction mode, the discontinuous mode being modelled by the saturation block and the reset input of the integrator.

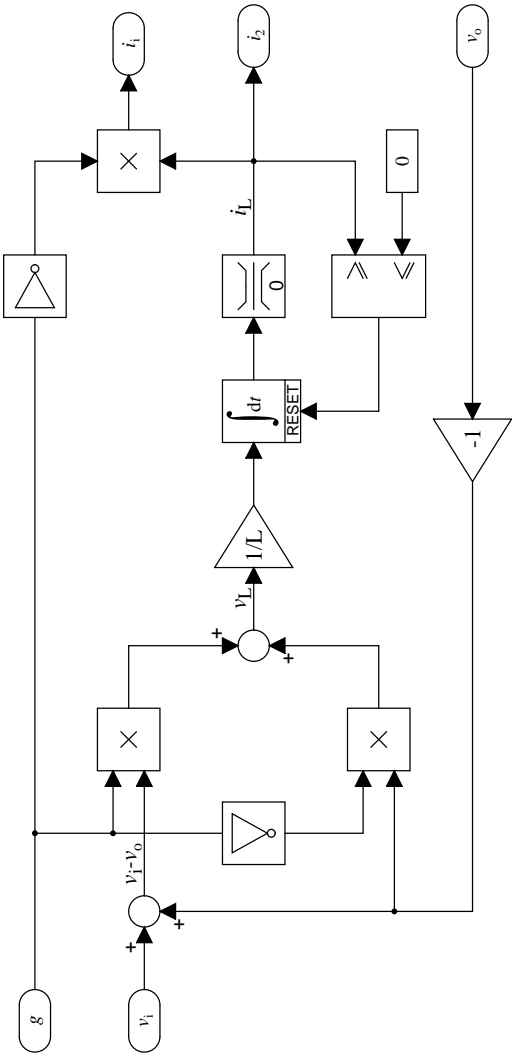
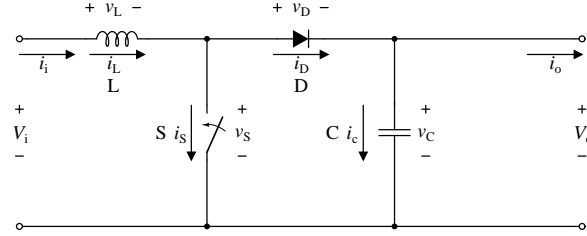


Figure 4.18. Block model of a buck converter.



**Figure 4.19.** Electric schematic of a boost converter.

They are both expressed by the following equations:

$$v_L = \begin{cases} V_i & \text{if } g = 1 \\ V_i - V_o & \text{if } g = 0 \\ 0 & \text{if } g = 0 \wedge i_L = 0 \end{cases} \quad (4.2.4)$$

$$i_2 = \begin{cases} 0 & \text{if } g = 1 \\ i_L & \text{if } g = 0 \end{cases} \quad (4.2.5)$$

$$i_i = i_L \quad (4.2.6)$$

where  $g$  is the switch signal command,  $v_L$  the voltage across the inductor,  $V_i$  the input voltage,  $V_o$  the output voltage,  $i_L$  the inductor current,  $i_i$  the input current, and  $i_2 = i_C + i_o$  is the sum of the capacitor current and the output current. In a boost converter  $V_i$  is always less than  $V_o$ .

### 4.2.3. Buck-boost converter

The principle schematic of a buck-boost converter switching cell is shown in Figure 4.21, while its block diagram is represented in Figure 4.22. They are both valid in continuous and discontinuous conduction mode, the discontinuous mode being modelled by the saturation block and the reset input of the integrator.

They are both expressed by the following equations:

$$v_L = \begin{cases} V_i & \text{if } g = 1 \\ -V_o & \text{if } g = 0 \\ 0 & \text{if } g = 0 \wedge i_L = 0 \end{cases} \quad (4.2.7)$$

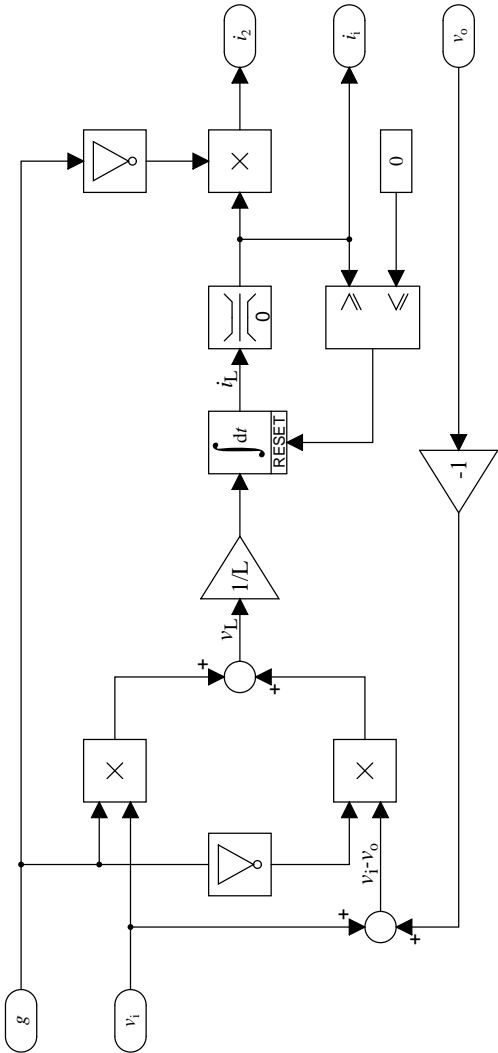
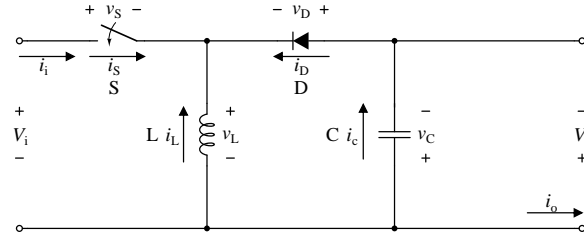


Figure 4.20. Block model of a boost converter.



**Figure 4.21.** Electric schematic of a buck-boost converter.

$$i_2 = \begin{cases} 0 & \text{if } g = 1 \\ i_L & \text{if } g = 0 \end{cases} \quad (4.2.8)$$

$$i_1 = \begin{cases} i_L & \text{if } g = 1 \\ 0 & \text{if } g = 0 \end{cases} \quad (4.2.9)$$

where  $g$  is the switch signal command,  $v_L$  the voltage across the inductor,  $V_i$  the input voltage,  $V_o$  the output voltage,  $i_L$  the inductor current,  $i_i$  the input current, and  $i_2 = i_C + i_o$  is the sum of the capacitor current and the output current. In a boost converter  $V_i$  can be either equal, less or greater than  $V_o$ .

#### 4.2.4. Output capacitor

The output capacitor integrates its current  $i_C$ , which gives the output voltage  $v_o$ , as shown in Figure 4.23 and described by:

$$i_C = i_2 - i_o \quad (4.2.10)$$

$$v_o = v_C = \frac{1}{C} \int i_C dt. \quad (4.2.11)$$

#### 4.2.5. Interleaving

If  $N_p$  switching cells are put in parallel, the structure shown in Figure 4.24 can be obtained. If the switch signal commands of the  $j$  and  $j + 1$  switching cells are shifted of  $\phi_j = \frac{2\pi}{N_p}$  rad for  $j = 1 \dots N_p$ , the whole converter is called interleaved [115].

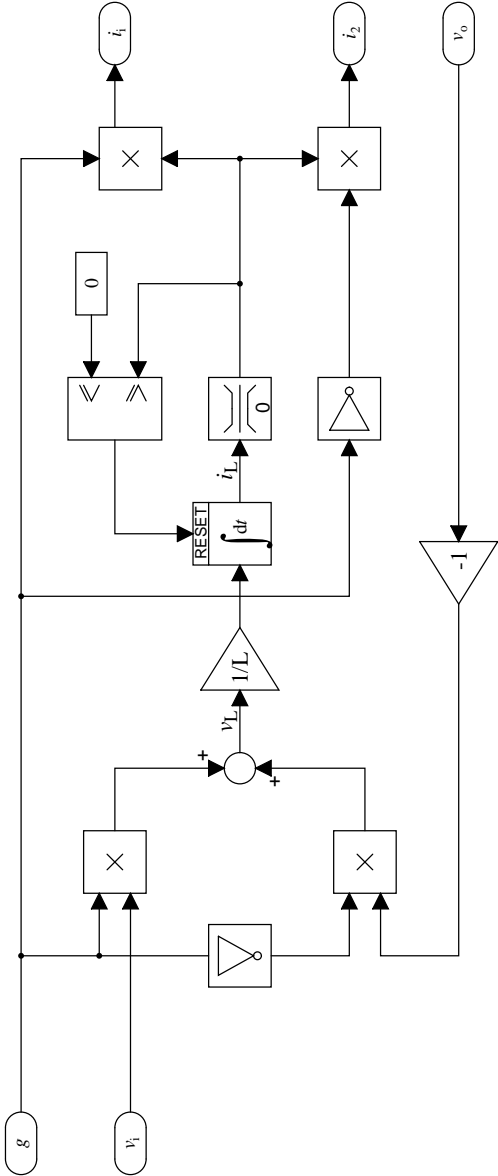
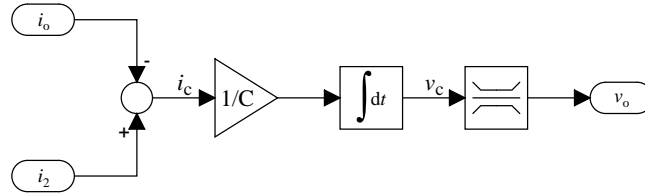
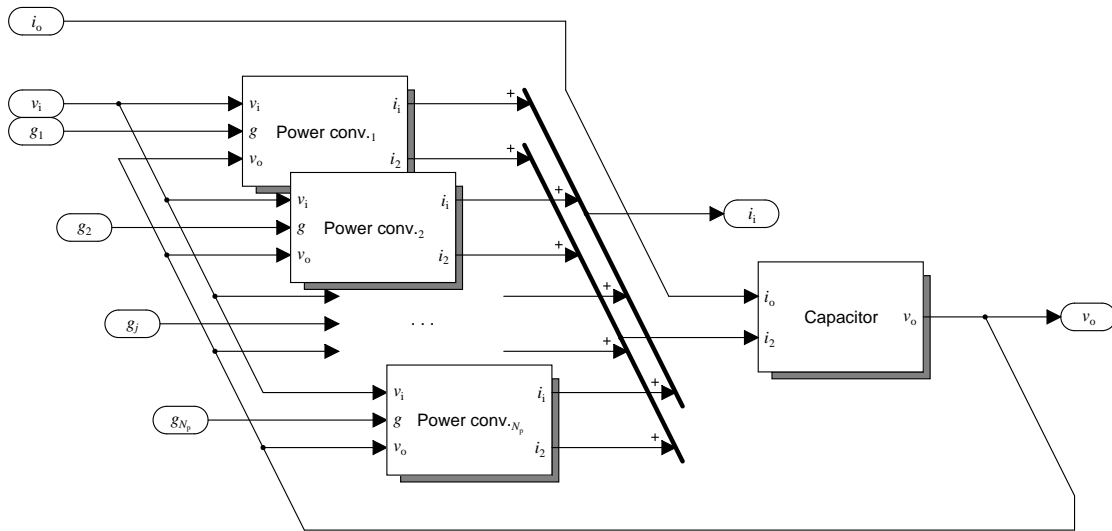


Figure 4.22. Block model of a buck-boost converter.





**Figure 4.23.** Block model of the output capacitor, valid for buck, boost and buck-boost converters.



**Figure 4.24.** Block representation of the parallel of more switching cells.

In both cases the currents  $i_1$  and  $i_2$  are described by the following sums:

$$i_1 = \sum_{j=1}^{N_p} i_{1,j} \tag{4.2.12}$$

$$i_2 = \sum_{j=1}^{N_p} i_{2,j} \tag{4.2.13}$$

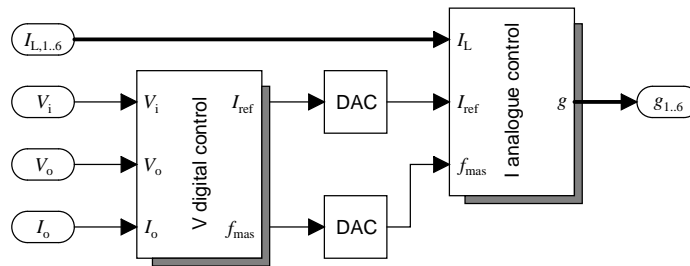
but their behaviour is completely different, as shown in Figure 4.26 for a boost, and a buck or buck-boost converter respectively.

With interleaving, smaller current ripples can be obtained, and the fundamental frequency measured at the output, in ideal conditions, is  $N_p$  times the

switching frequency, properly phase-shifting the switch signal commands of each switching cell.

### 4.3. Controller

Figure 4.25 shows the overall structure of the controller, composed of an analog inner current loop, fed by an external digital voltage loop.



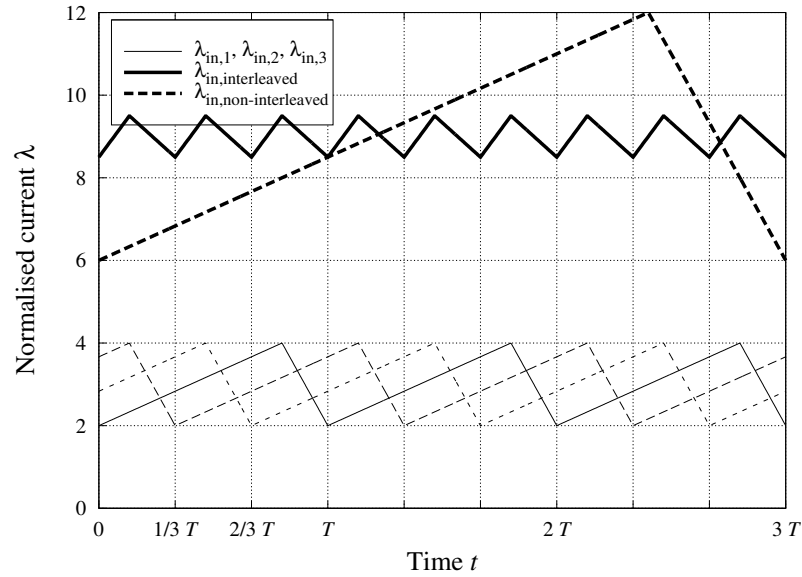
**Figure 4.25.** The overall control system, composed of the digital voltage controller and of the analog current controller. Acronyms: inductance currents ( $I_L$ ), input and output voltages ( $V_i$  and  $V_o$ ), output current ( $I_o$ ), gate commands ( $g$ ), Digital to Analog converter (DAC).

In the digital voltage control block (Figure 4.27) the current reference  $I_{ref}$  and the master frequency  $f_{mas}$  are calculated from the power converter input voltage  $V_i$ , the power converter output voltage  $V_o$  and power converter output current  $I_o$ .

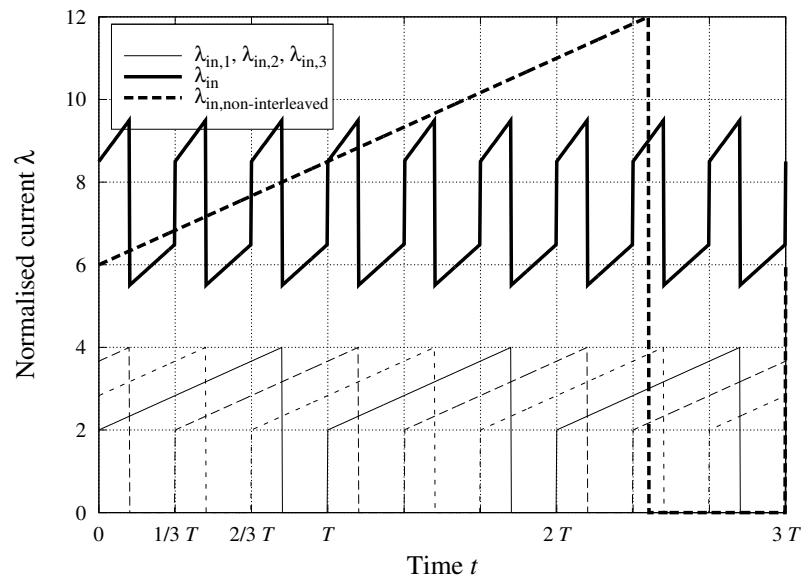
The voltage control block (Figure 4.28) is a digital PI controller, while the frequency adjustment block adapts the switching frequency of the power converter in order to keep the power converter on the border between CCM and DCM, as previously discussed.

Then, the  $I_{ref}$  and  $f_{mas}$  signals are passed to the current control block (Figure 4.31), which creates the gate commands for the power MOSFET. The “Clock generator” simply divides by  $N_p = 6$  and dispatches the frequency signal to the current controllers. The internal structure of the current controllers and of the modulators is shown in Figures 4.29 and 4.30 respectively.

The current controller is a PI controller, while the modulator block provides the constant on-time control, via a flip-flop, an integrator and a comparator.

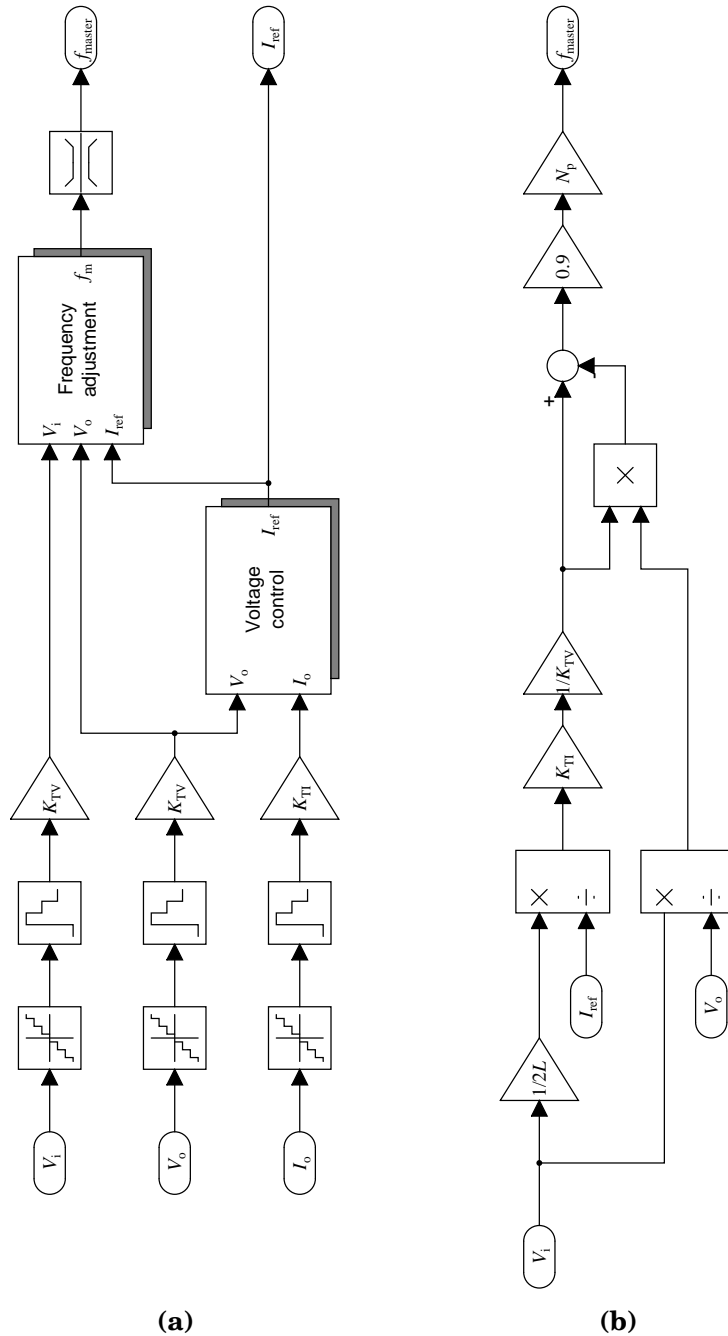


(a)

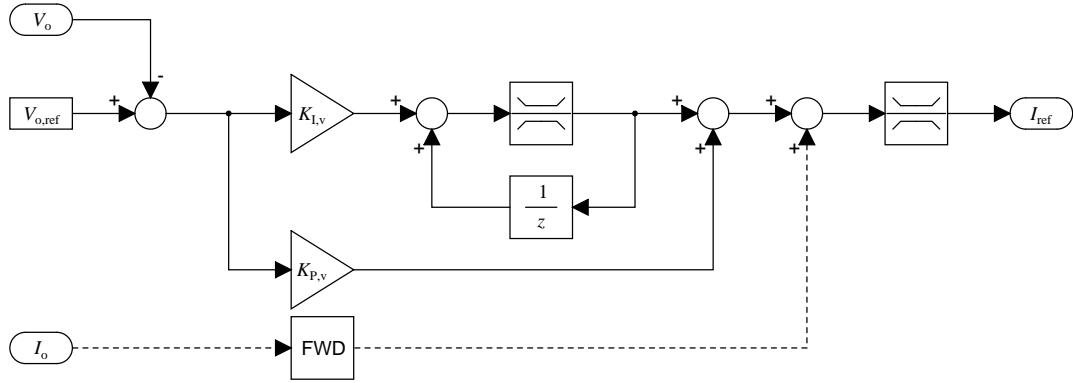


(b)

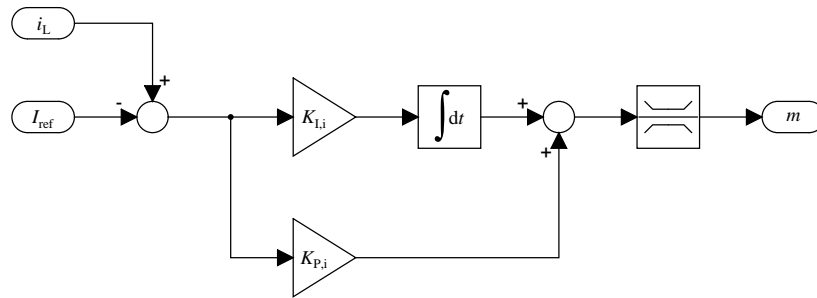
**Figure 4.26.** Normalised input current of an interleaved boost (a) and buck (b) converters (black line) and a non-interleaved boost (a) and buck (b) converters (dashed line), with the same average value and operating in CCM. The current of the different phases of the interleaved converter are plotted in grey and shown as a reference.



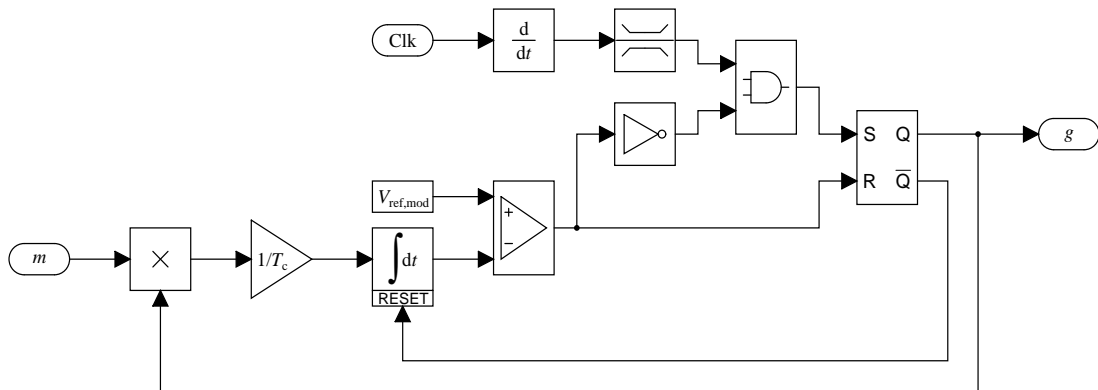
**Figure 4.27.** (a) The overall voltage digital controller, composed of the voltage control and of the frequency adjustment blocks. Acronyms: input and output voltages ( $V_i$  and  $V_o$ ), output current ( $I_o$ ), master frequency ( $f_{mas}$ ), inductance current reference ( $I_{ref}$ ). (b) The frequency adjustment block. Acronyms: input and output voltages ( $V_i$  and  $V_o$ ), master frequency ( $f_{mas}$ ).



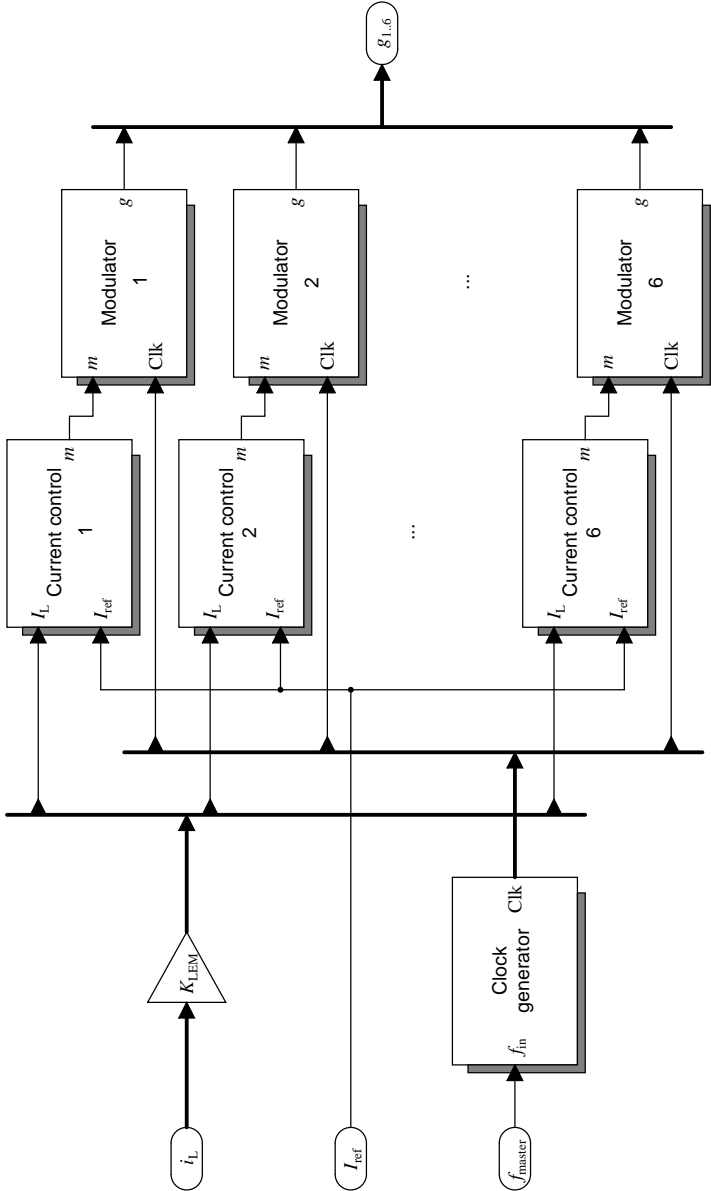
**Figure 4.28.** The digital PI voltage controller. Acronyms: output voltage and current ( $V_o$  and  $I_o$ ), output voltage reference ( $V_{o,ref}$ ), inductance current reference ( $I_{ref}$ ).



**Figure 4.29.** The analog PI current control. Acronyms: inductance current ( $i_L$ ), inductance current reference ( $I_{ref}$ ), reference signal ( $m$ ).



**Figure 4.30.** The modulator block. Acronyms: clock signal ( $Clk$ ), voltage modulator reference value ( $V_{ref,mod}$ ), gate command ( $g$ ).



**Figure 4.31.** The overall current controller, composed by six independent modulator and current control blocks, fed by a clock generator and the six current transducers. Acronyms: inductance currents ( $I_L$ ), inductance current reference ( $I_{ref}$ ), master frequency ( $f_{mas}$ ), clock signal (Clk), reference signal ( $m$ ), gate commands ( $g$ ).

#### 4.4. Conclusion

A complete model of a fuel cell system has been described. The fuel cell, the power converter and the controller models have been detailed. Thanks to this model, simulation results will be presented and compared to experimental data in Chapter 6.

The fuel cell stack and the power converter prototypes will be presented in the next chapter, along with the developed hardware required to make the fuel cell safely work.





## CHAPTER 5

### **HARDWARE**

The fuel cell stack and power converter prototypes will be illustrated in the first part of this chapter. The acquisition system which is necessary for a safe fuel cell stack operation will be presented in the second part. It has been designed to be expandable; for example, it may also provide the possibility to control the power converter in future work.

The acquisition system is interesting to describe for two main reasons:

- it shows a solution of a complex problem, like the measurement of all the fuel cell single elements' voltages, that must be isolated and which are all referred to different potentials;
- it is meant as a reference for future work on the system.

A relevant part of the hardware work consisted in building a laboratory suitable for testing fuel cell stacks and power converters. Some descriptions of it can be found in Appendix J.

## 5.1. Prototype

The fuel cell stack and the power converter prototypes will be presented in this part. The characterisation of the fuel cell stack, along with the experimental results of static and dynamic tests, will be presented in Chapter 6.

### 5.1.1. Fuel cell stack

The fuel cell stack prototype is composed of 50 elements of 325 cm<sup>2</sup> each and it has been built by Exergy Fuel Cells. It is meant to work either with hydrogen/air or hydrogen/oxygen.

Figures 5.1 and 5.2 show the fuel cell stack before the installation, while Figure 5.4 shows the fuel cell stack after installation, ready to be tested. The wires that measure every single cell voltage and that are connected to the acquisition system are noticeable in Figure 5.3.

### 5.1.2. Power converter

The actual first prototype is slightly different from the previously sized power converter, since it has been oversized for safety reason. The main differences are:

- input inductance:  $L = 2.2 \mu\text{H}$  instead of  $L = 2.4 \mu\text{H}$ ;
- input capacitor:  $C_i = 10 \mu\text{F}$ ;
- output capacitor:  $C_o = 10 \mu\text{F}$  instead of  $C_o = 28 \mu\text{F}$ ;
- switch: APT30M19JVFR ( $R_{\text{DS,on}} = 19 \text{ m}\Omega$ ,  $V_{\text{DSS}} = 300 \text{ V}$ ,  $I_{\text{D}} = 130 \text{ A}$ ) instead of APT10M11JVRU2 ( $R_{\text{DS,on}} = 11 \text{ m}\Omega$ ,  $V_{\text{DSS}} = 100 \text{ V}$ ,  $I_{\text{D}} = 142 \text{ A}$ );
- diode: STTH20002TV ( $V_{\text{F,M}} = 1.2 \text{ V}$ ) instead of APT10M11JVRU2 ( $V_{\text{F,M}} = 1.4 \text{ V}$ ).

Figure 5.5 shows all the six legs of the multiphase power converter prototype, while a detail of one phase can be seen in Figure 5.6. The control board is represented in Figure 5.7.



**Figure 5.1.** Detail of the fuel cell stack before installing it. The gas inlets with their pressure regulators and the solenoid valves are on the left of the stack. The electrical terminals are located on the top (negative) and on the bottom (positive) of the stack. The black pipes carry the coolant (demineralised water).



**Figure 5.2.** The fuel cell stack with the coolant tank, pump and radiator. On the right of the stack, there are the two outlet valves.



**Figure 5.3.** A detail of the fuel cell stack, showing 51 wires used to acquire and measure the 50 differential voltages of every single element.



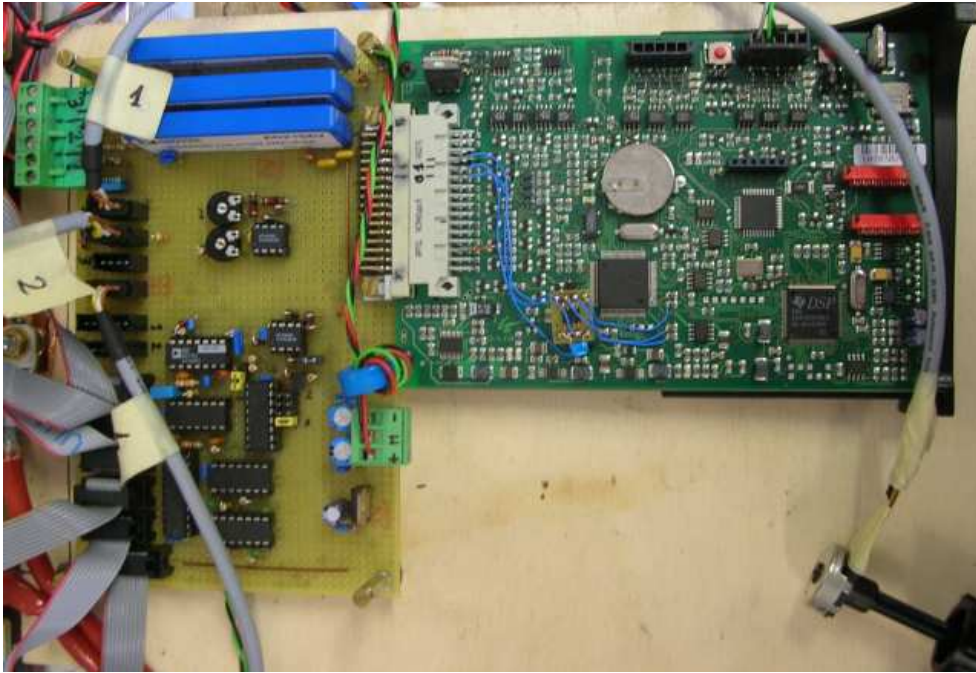
**Figure 5.4.** The fuel cell stack after installation. The inlet valves are connected to the hydrogen and oxygen systems with two flowmeters in series. The outlet valves are connected to two pipes that carry the gasses outside. The radiator has been oversized and put under the table. A 100 k $\Omega$  resistance is always connected in parallel to the stack, in order to avoid to keep it in an open circuit state.



**Figure 5.5.** The boost prototype with its input bars on the rear side and its output bars on the front side. The six modules are visible, each with its input and output capacitors, its inductance, its current sensor and its current control board.



**Figure 5.6.** A detail of one of the six modules. The MOSFET and the diode are located under the main board, in contact with the aluminium heat sink.



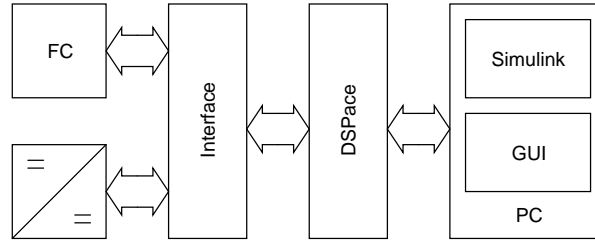
**Figure 5.7.** The control boards. The board on the left provides the logic required to dispatch the clock and the current reference signals to the modules. On the right side is the DSP board, which will implement the voltage and frequency control loops. At the present time, it is only used to prevent the output voltage rises above the maximum acceptable value.

## 5.2. Acquisition system

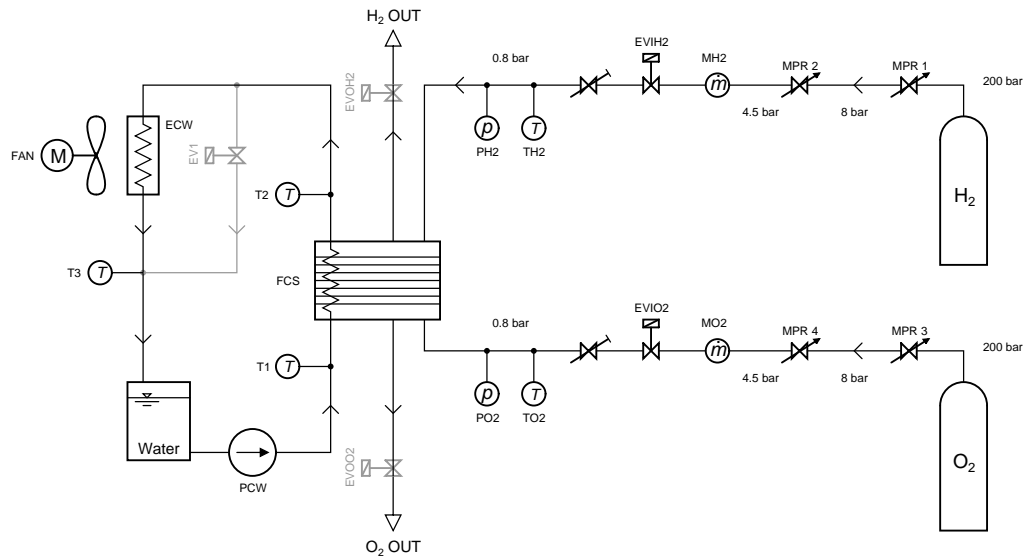
The acquisition system presented here has been conceived with the main purpose of keeping all the voltages of the fuel cell stack elements under control. Nevertheless, its design leaves the possibility open to expand it for larger fuel cell stacks and to use it to interface a computer based control system with all the hardware required by the system operation.

Figure 5.8 illustrates such a system, in which both the fuel cell stack and the power converter are connected to a computer thanks to a dSPACE board and a customised interface.

The fuel cell system is represented in Figure 5.9, with some of the variables that influence proper fuel cell stack operation. All these variables — like the ambient air temperature  $T_a$ , the cooling water temperatures  $T_1$ ,  $T_2$  and  $T_3$ , the hydrogen and oxygen input temperatures  $T_{H_2}$  and  $T_{O_2}$ , their pressures  $P_{H_2}$  and



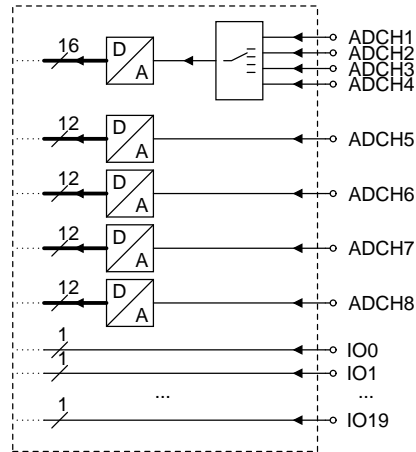
**Figure 5.8.** General diagram of the system: the fuel cell stack (FC) and the power converter are interfaced to a dSPACE board, which is programmed with Simulink and accessed via a Graphical User Interface (GUI).



**Figure 5.9.** General diagram of the fuel cell system. Acronyms: manual pressure regulator (MPR), hydrogen and oxygen Mass flow meter (MH2 and MO2), input and output solenoid Valves (EVI and EVO), hydrogen and oxygen temperature ( $T_{H_2}$ ,  $T_{O_2}$ ), hydrogen and oxygen pressures ( $P_{H_2}$ ,  $P_{O_2}$ ), water heat exchanger (ECW), water pump (PCW), water temperature ( $T_1$ ,  $T_2$ ,  $T_3$ ).

$P_{O_2}$ , the fuel cell stack voltage  $V_{FC}$  and current  $I_{FC}$  — can be acquired through adequate interfaces connected to the acquisition system. During the tests described in this thesis, these variables have been kept under control manually.

An interface system is required in order to interface all the inputs and outputs of the system with the dSPACE board, whose limited number of I/O is represented in Figure 5.10.



**Figure 5.10.** Diagram of the input stage of the DS1104 dSPACE acquisition interface.  $ADCH_1 \dots ADCH_8$  are analog inputs.  $ADCH_1 \dots ADCH_4$  are internally multiplexed.  $IO_0 \dots IO_{19}$  are digital input/output lines.

An interface system has been built, along with its bus standard and communication protocol [116]. The system has been designed keeping future expansion in mind. The twenty digital lines ( $IO_0 \dots IO_{19}$ ) allow communication between the interface cards and the dSPACE board. The 12-bit analog channels  $ADCH_5 \dots ADCH_8$  are reserved for measurements with a very high bandwidth. Instead, the 16-bit multiplexed analog channels  $ADCH_1 \dots ADCH_4$  are instead used for low bandwidth measurements. The communication bus lines, whose correspondences to the dSPACE board digital interface are shown in Table 5.1, are:

- $D_0 \dots D_3$ : digital dSPACE inputs for multiplexing digital system inputs;
- $DO_0 \dots DO_3$ : digital dSPACE outputs for multiplexing digital system outputs;
- $A_0 \dots A_7$ : board/signal address;
- SE: select/unselect signal for analog boards, lower/higher nibble for digital boards;
- IN: input/output selection signal;
- AN: analog/digital selection signal;
- F: fire (clock) signal.



Their meaning and operation are explained in what follows.

**Table 5.1.** Table of the correspondences between the digital input/output lines of the dSPACE board and the lines of the designed bus.

IO <sub>0</sub>	DI <sub>0</sub>	IO <sub>8</sub>	A <sub>0</sub>	IO <sub>16</sub>	SE
IO <sub>1</sub>	DI <sub>1</sub>	IO <sub>9</sub>	A <sub>1</sub>	IO <sub>17</sub>	IN
IO <sub>2</sub>	DI <sub>2</sub>	IO <sub>10</sub>	A <sub>2</sub>	IO <sub>18</sub>	AN
IO <sub>3</sub>	DI <sub>3</sub>	IO <sub>11</sub>	A <sub>3</sub>	IO <sub>19</sub>	F
IO <sub>4</sub>	DO <sub>0</sub>	IO <sub>12</sub>	A <sub>4</sub>		
IO <sub>5</sub>	DO <sub>1</sub>	IO <sub>13</sub>	A <sub>5</sub>		
IO <sub>6</sub>	DO <sub>2</sub>	IO <sub>14</sub>	A <sub>6</sub>		
IO <sub>7</sub>	DO <sub>3</sub>	IO <sub>15</sub>	A <sub>7</sub>		

### 5.2.1. Generic implementation of the interface

Four different types of interface boards can be designed:

- digital input interface: the total number of digital inputs is 2048, since up to 256 interfaces can be addressed, with 8 digital inputs per interface;
- digital output interface: the total number of digital outputs is 2048, since up to 256 interfaces can be addressed, with 8 digital outputs per interface;
- analog input interface: the total number of analog inputs is 1024, since up to 256 channels can be multiplexed per dSPACE analog input, with 4 dSPACE analog inputs;
- analog output interface: the total number of analog outputs is 1024, since up to 256 channels can be multiplexed per dSPACE analog output, with 4 dSPACE analog outputs.

Their implementation is addressed to in Appendix I.

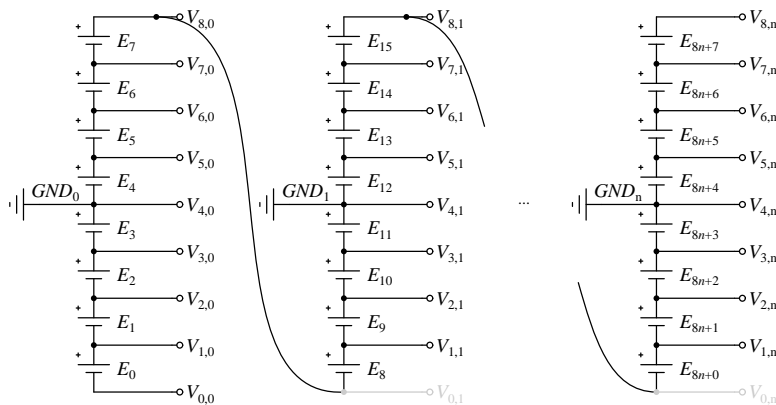
### 5.2.2. Fuel cell single element voltage measurement

The safe operation of the fuel cell stack is generally guaranteed by the measurement of the voltage of every element of the stack, even if other solutions exist [117 – 119]. This voltage can be checked against the value predicted by the mathematical model or, in a simpler way, against a fixed range.

This means measuring 50 voltages, in the range between 400 mV and 1 V during normal operation, but that can reverse in case of failure. All these voltages are referred to different potentials, which can be up to 50 V.

It has been decided to define the input voltage range between  $-2$  V and  $2$  V, which will be scaled to the output voltage range between  $10$  V and  $-10$  V.

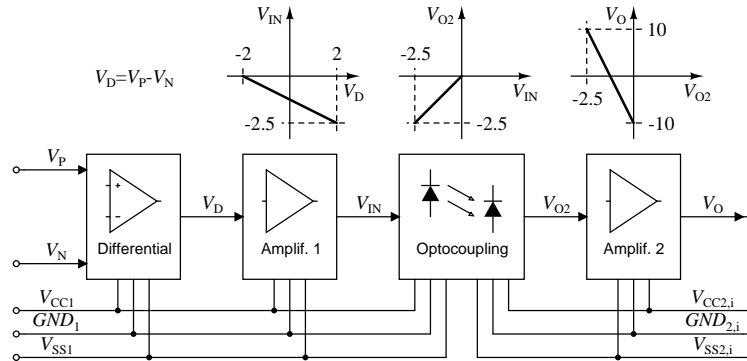
The elements of the stack have been grouped 8 by 8 and connected as shown in Figure 5.11.



**Figure 5.11.** Connections of the differential voltages of the fuel cell elements ( $E_0 \dots E_{8n+7}$ ), with their separated grounds ( $GND_0 \dots GND_n$ ).

The 8 differential signals are then amplified, optocoupled and then amplified a second time, before being sent to an analog multiplexer — controlled by a microcontroller — as represented in Figure 5.12.

The adopted modular structure allows to measure up to 1024 voltages: a multiplexer board contains 8 differential signal modules (Figure 5.14), a microcontroller controls two multiplexer boards, a rack contains up to 7 multiplexer boards, and up to 4 racks can be addressed (Figure 5.15).

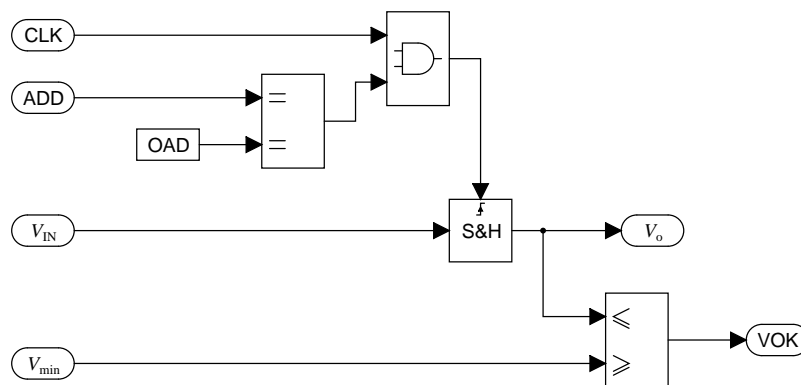


**Figure 5.12.** Fuel cell element differential voltage module. The left and right sides of the module are referred to different grounds. Acronyms: positive voltage ( $V_p$ ), negative voltage ( $V_n$ ), differential voltage ( $V_D$ ), optocoupling stage input voltage ( $V_{IN}$ ), optocoupling stage output voltage ( $V_{O2}$ ), module output voltage ( $V_o$ ).

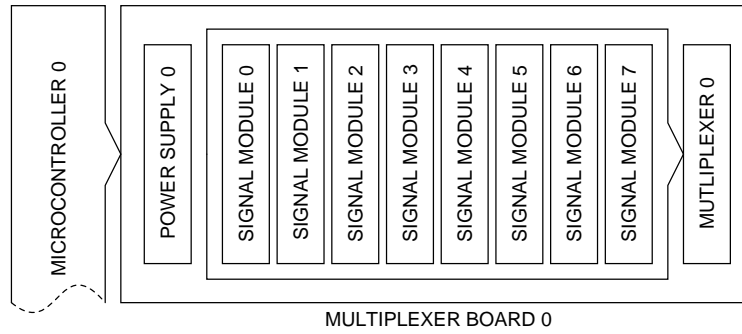
### 5.2.3. Basic software voltage control

The software demultiplexer, which scans all the addresses and acquires and saves all the fuel cell element voltages, is shown in Figures 5.16, 5.13 and 5.17.

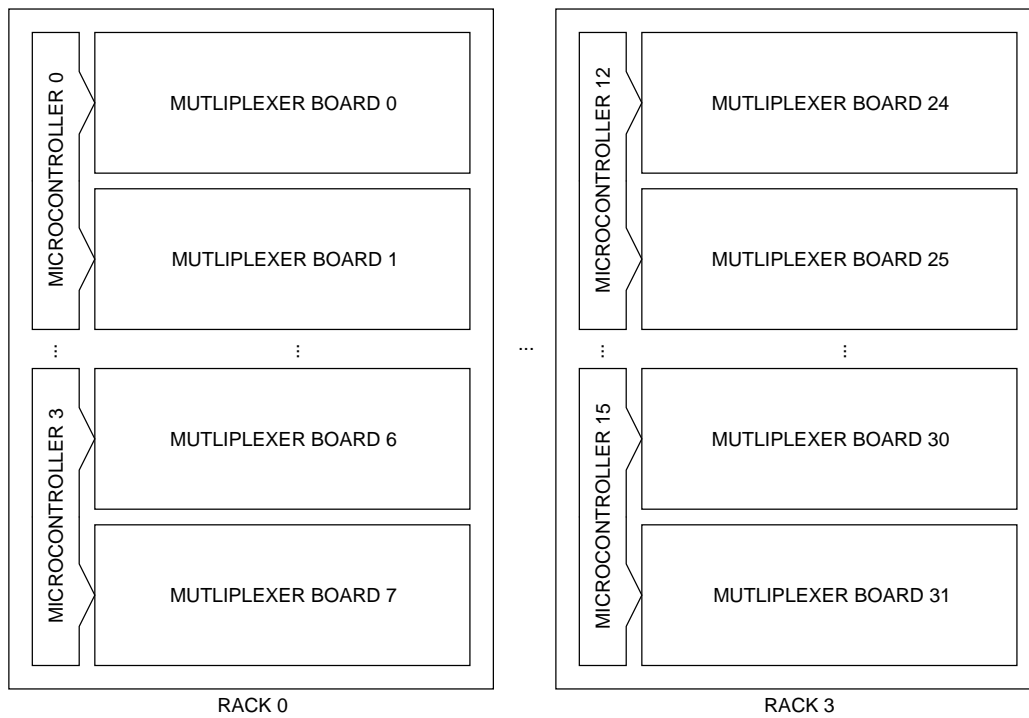
In this first simple implementation, the measured voltage is checked against a lower limit. If one voltage goes below this limit, an alarm signal is raised and the system must be manually stopped.



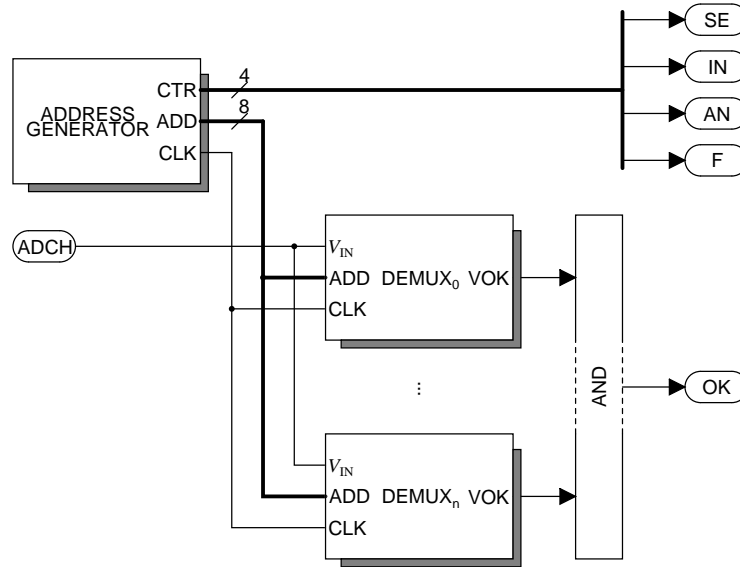
**Figure 5.13.** Block diagram of the DEMUX element. Acronyms: own address (OAD), address lines (ADD), clock line (CLK), input multiplexed voltage ( $V_{IN}$ ), output demultiplexed voltage ( $V_o$ ), lower voltage limit ( $V_{min}$ ), single voltage enable (VOK), sample and hold element (S&H).



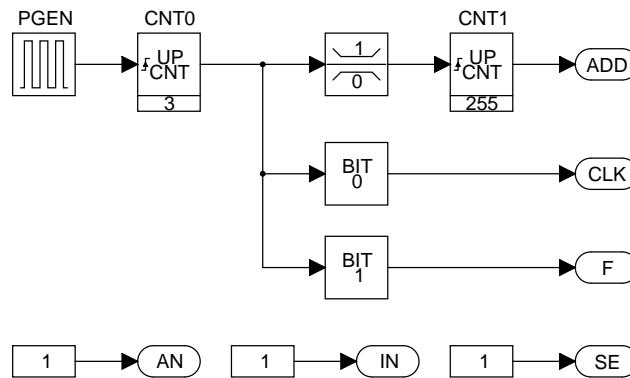
**Figure 5.14.** Representation of the multiplexer board for the acquisition of the fuel cell element voltages, with its eight signal modules, its analog multiplexer and its isolated power supply.



**Figure 5.15.** Representation of the entire system for the acquisition of the fuel cell element voltages, with the multiplexer boards, controlled by the microcontroller boards. Each microcontroller controls two multiplexer boards.



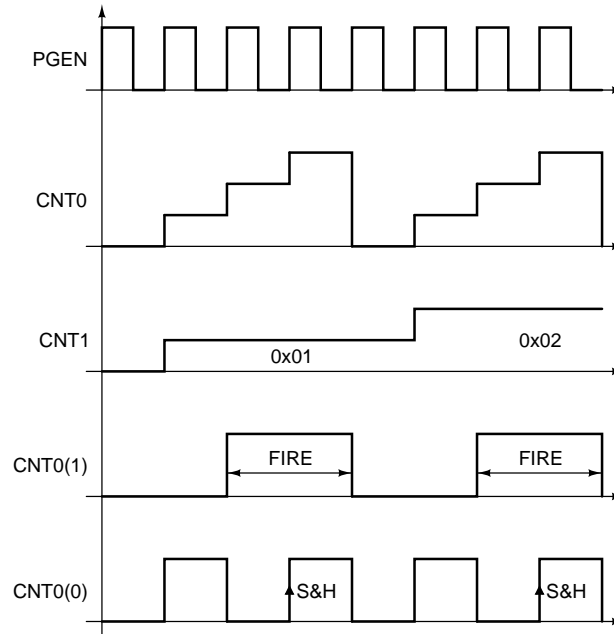
**Figure 5.16.** Block diagram of the software voltage demultiplexer and control. Acronyms: control lines (CTR), address lines (ADD), clock line (CLK), select line (SE), input line (IN), analog line (AN), fire line (F), single voltage enable (VOK), global voltage enable (OK), analog input channel (ADCH).



**Figure 5.17.** Block diagram of ADDRESS GENERATOR element. Acronyms: address lines (ADD), clock line (CLK), select line (SE), input line (IN), analog line (AN), fire line (F), up counter (UP CNT), extraction of bit  $x$  (BIT  $x$ ), pulse generator (PGEN).

#### 5.2.4. Conclusion

An expandable and modular acquisition system has been designed. It can be used to control the fuel cell element voltages, as well to command system actuators, or to acquire user inputs, or process variables.



**Figure 5.18.** Time diagram of the selection of an analog channel. Acronyms: counter (CNT), extraction of bit  $x$  (CNT ( $x$ )), pulse generator (PGEN), fire signal (FIRE), sample and hold (S&H) action.

The presented parallel bus has been designed and used in this first version, but in the future the parallel bus could be replaced by a serial bus — like the CAN (Controller Area Network) bus or the I<sup>2</sup>C (Inter-Integrated Circuit) bus — emptying digital I/O on the dSPACE system. This serial bus could then communicate to the dSPACE board via its RS232 port and a dedicated micro-controller.

The reimplementing of the DPSPACE/Simulink system with a Linux real time system would be an interesting topic to investigate. This would be possible using RTAI — the RealTime Application Interface for Linux [120] —, Scilab/Scicos — an opensource alternative to Matlab/Simulink [121] —, and the Comedi drivers — Linux drivers for many commercial input/output boards [122].

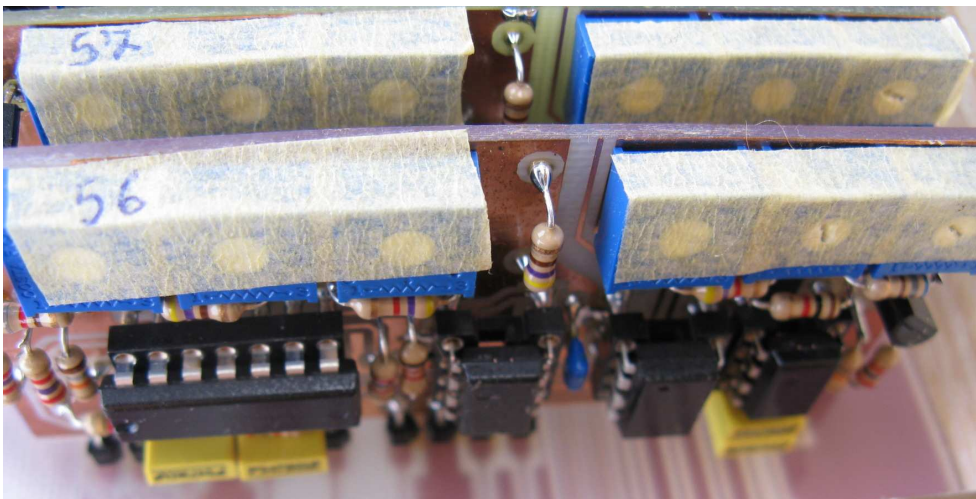
### 5.3. Conclusion

The fuel cell stack and power converter prototypes have been presented, along with the internally designed and developed modular acquisition system.

The next chapter will present the simulation and experimental results obtained from the prototypes and models described so far.

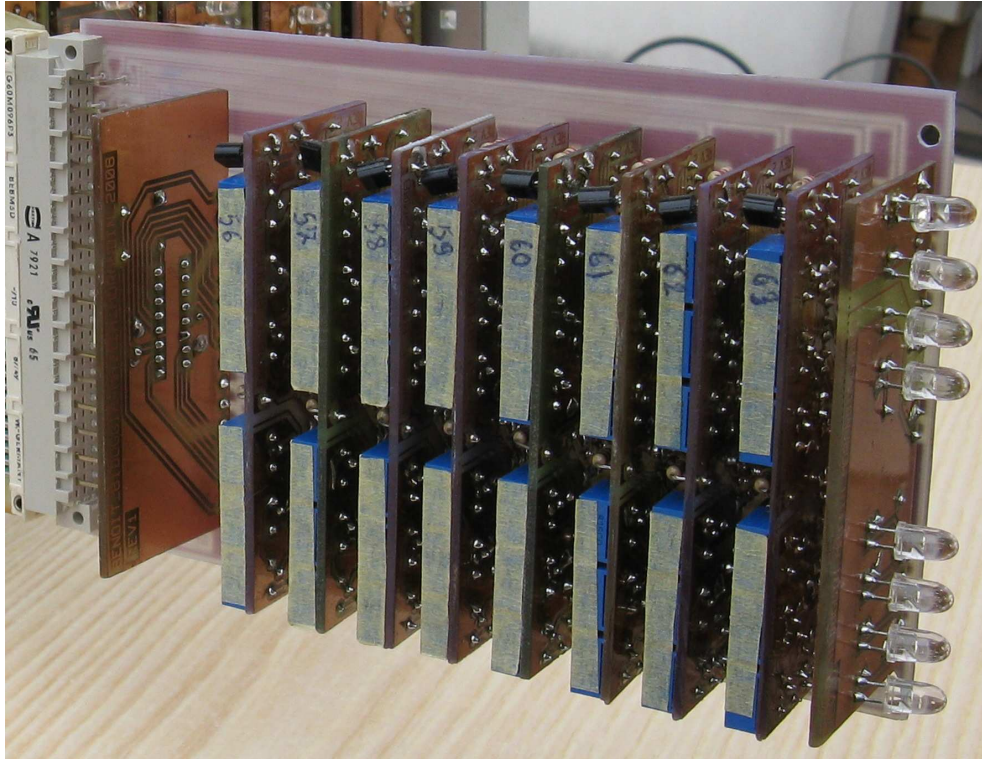


**Figure 5.19.** Picture of one of the racks for the acquisition of up to 64 fuel cell element voltages. From left to right: the first board is the microcontroller board, the other eight ones are the multiplexer boards. The LEDs on the front display the power supplies and the signal selection.

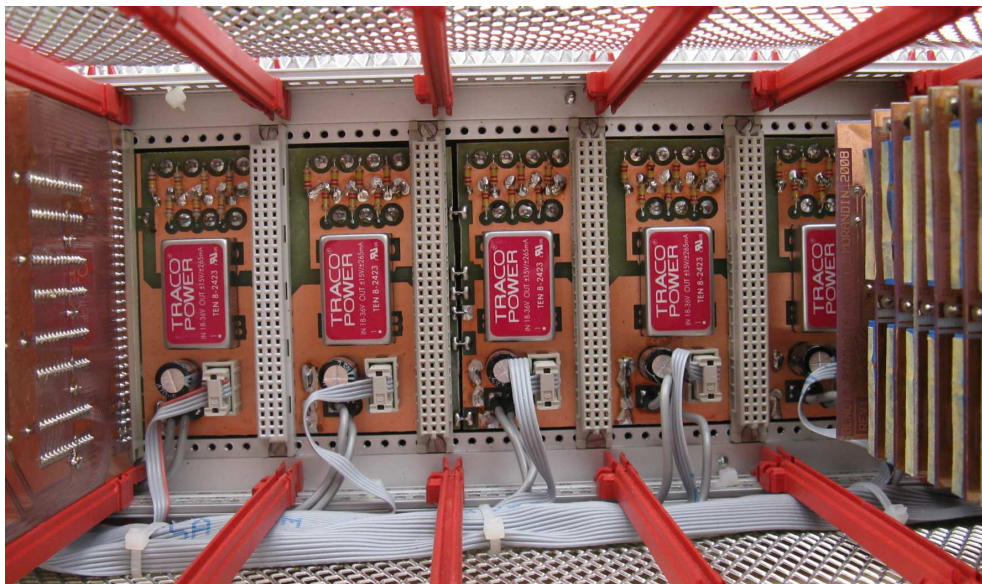


**Figure 5.20.** Detail of one the signal modules of the multiplexer board.





**Figure 5.21.** Picture of one of the multiplexer boards. From left to right: the analog multiplexer module, the eight signal modules, and the LED module.



**Figure 5.22.** Detail of the bottom of the rack with the isolated power supplies.



## CHAPTER 6

### RESULTS AND DISCUSSIONS

In the previous chapters a fuel cell system has been modelled and sized, along with all its components, namely:

- the fuel cell stack;
- the power converter;
- the control system.

The results from the simulations and the experimental tests carried out on all the single elements and on the system as a whole will be presented in this chapter. The presentation reflects the chronological and causal order:

1. experimental tests on the first fuel cell stack prototype, with characterisation of the developed model for a single element of a fuel cell;
2. simulation results of the fuel cell stack by itself, in order to better understand its dynamic behaviour, which has been analysed by stimulating the fuel cell stack with a sinusoidal current source at different frequencies;
3. experimental tests on the power converter by itself with a constant voltage power supply in order to verify its proper operation and to measure its efficiency;
4. experimental tests on the power converter connected to a power supply emulating the behaviour of the chosen fuel cell stack, in order to understand the static behaviour of the power converter in a semi-real situation;

5. simulation results of the system as a whole, under different load conditions and transients to analyse the behaviour of the whole system under different dynamic conditions;
6. experimental tests on the final version of the fuel cell stack.

The last point would have been the experimental test of the complete system, under different load conditions and transients, but a destructive fault on the fuel cell stack prevented us from reaching this point. At the moment of this writing, the fuel cell stack manufacturer is analysing the causes of the fault.

### 6.1. Fuel cell stack measurements

During the project development and collaboration with Exergy Fuel Cells, the evolution of the project and the availability of different fuel cell stacks led to test different types of fuel cell stacks. The measurements and the experimental results about the first fuel cell stack, a 325 cm<sup>2</sup> 20 elements prototype, are presented in this section. The parameters of the equation describing the static behaviour of the fuel cell have been found from these results.

#### 6.1.1. Static characteristic

The static  $V - I$  characteristic of a 325/20 stack has been measured, whose results are shown in Appendix K, along with the acquired data. They have been used to find the parameters of the static  $V - J$  equation, valid for a single fuel cell element:

$$V(J) = E_0 - (J + J_n) r - A \log\left(\frac{J + J_n}{J_0}\right) + B \log\left(1 - \frac{J + J_n}{J_1}\right) \quad (6.1.1)$$

where  $V$  is the single fuel cell element voltage,  $J$  is the current density and:

$$E_0 = 1.23 \text{ V} \quad (6.1.2)$$

$$J_n = 6 \text{ mA} \quad (6.1.3)$$

$$J_0 = 67 \mu\text{A} \quad (6.1.4)$$

$$J_1 = 1.1 \text{ A} \quad (6.1.5)$$

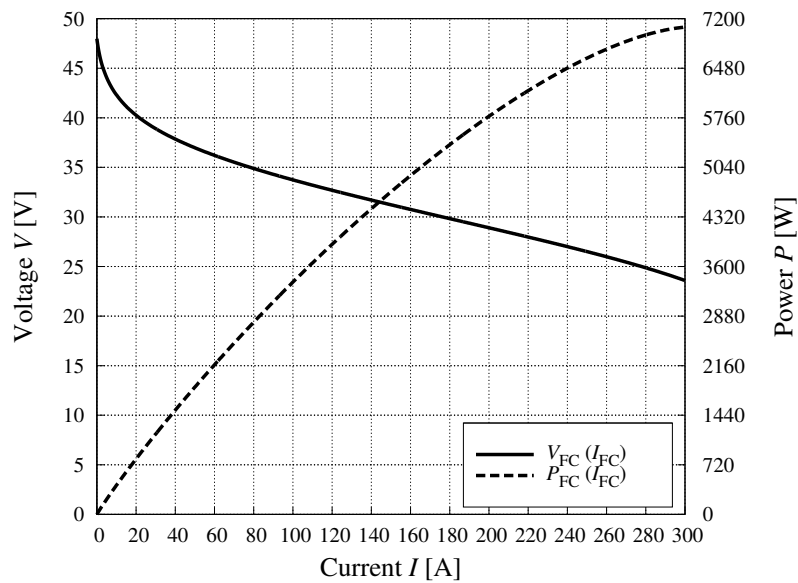
$$r = 100 \text{ m}\Omega \cdot \text{cm}^2 \quad (6.1.6)$$

$$A = 0.06 \text{ V} \quad (6.1.7)$$

$$B = 0.05 \text{ V}. \quad (6.1.8)$$

Since these parameters do not depend on the size of the stack, but only on the technology of the single fuel cell element, it is possible to use them to describe the behaviour of a fuel cell stack with a different number of cells or with a different element surface.

From Chapter 3, a 325/50 stack has been found as the most appropriate choice for this project. Its static characteristic described by Equation 6.1.1 is plotted in Figure 6.1, according to the previously derived parameters.



**Figure 6.1.** Fuel cell stack current  $I_{FC}$ , voltage  $V_{FC}$  and power  $P_{FC}$  for a 325 cm<sup>2</sup> 50 element stack.

### 6.1.2. Dynamic characteristic

In order to investigate the dynamic aspects of the fuel cell under test, a current step has been applied to the fuel cell and its voltage response has been

acquired, whose plot is shown in Appendix K. From these results the value of the capacitance density — as defined in Appendix F — equals:

$$c = 7.5 \frac{\text{mF}}{\text{cm}^2}. \quad (6.1.9)$$

As for the static test, this experiment has also been conducted on a 325/20 stack, which was available when the characterisation was done. Since the double layer capacity effect is identified by a capacitance density, it is independent from the fuel cell surface and from the number of elements of the stack. A similar procedure can be also found in [123].

The next section will deal with dynamic simulation results based on these parameters.

## 6.2. Fuel cell stack simulations

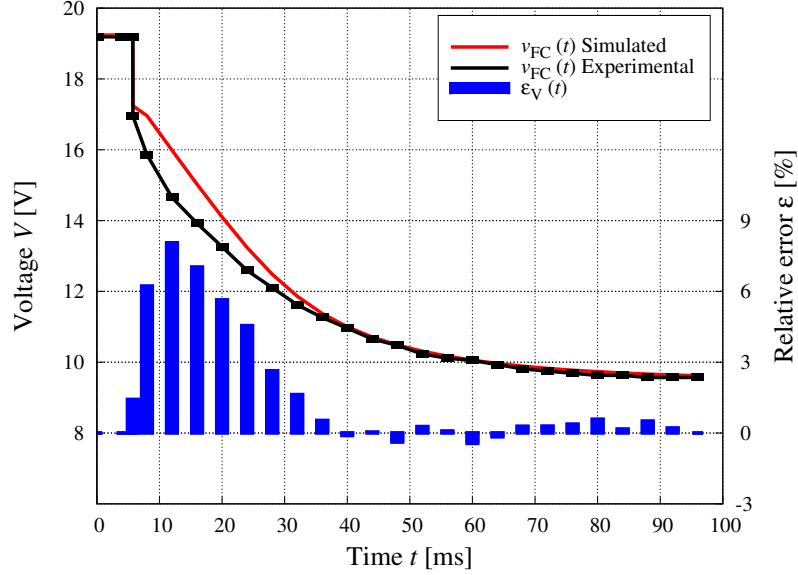
Two different types of dynamic simulations of a fuel cell stack will be presented here: the voltage response of the fuel cell to a current step and then its voltage response to sinusoidal stimuli.

### 6.2.1. Step response

The first simulation concerns the voltage response of the 325/20 fuel cell stack to a current step, which is compared with the experimental plot. They are both plotted in Figure 6.2, in which the relative error between the simulated and experimental data is also plotted.

These results come from the electric equivalent circuit used, in which the dynamic effects are represented by a single reactive element. As explained in [54], an improved model should include at least two or three capacitors: the first one representing the double layer effect, while the other ones represent the dynamic aspects related to the diffusion effects.

Despite this approximation, there still is a more than acceptable match between the simulated and experimental data. The relative error between the experimental and simulated results shows that after the first instants of



**Figure 6.2.** Simulated and experimental voltage fuel cell stack response to a 0 A–300 A current step, and relative error between the simulated and the experimental data. Fuel cell stack: 325 cm<sup>2</sup>, 20 elements. The boxes represent the absolute errors:  $\Xi_v = 0.1$  V,  $\Xi_t = 1$  ms.

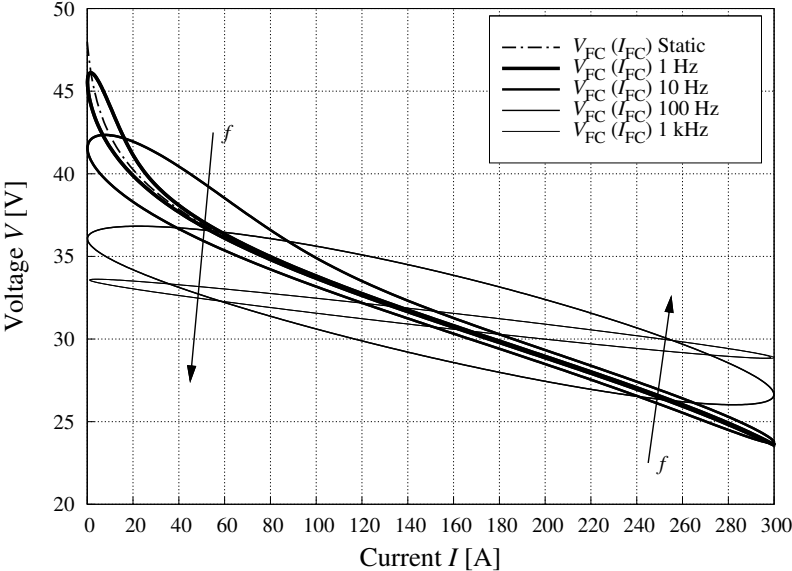
the transients, in which the relative error peak reaches 8 %, the relative error decreases very quickly and then stays under 1 %.

Although this is probably not precise enough to accurately study the mutual interactions within the commutation periods — in the range from 1  $\mu$ s to 3  $\mu$ s —, it can be used to analyse the response of the entire system to load variations, as presented further.

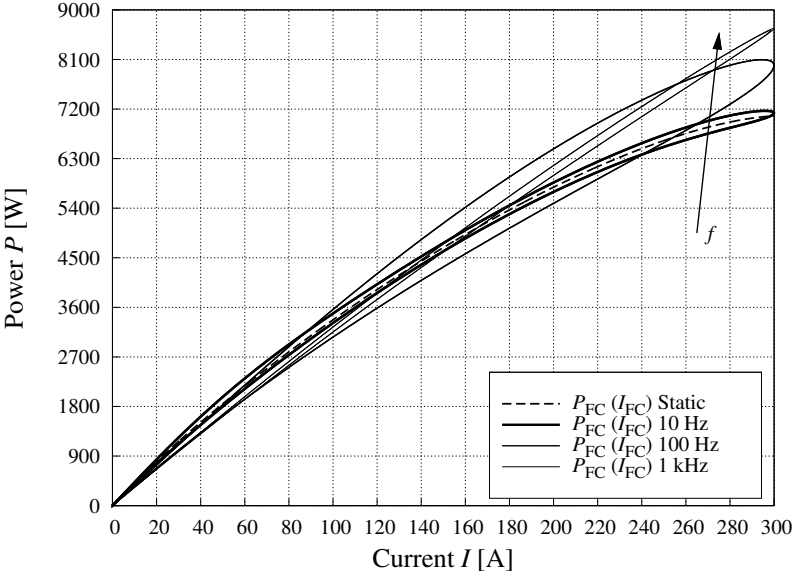
### 6.2.2. Sinusoidal stimuli

The dynamic  $V - I$  characteristic of a fuel cell can be very different from its static characteristic, depending on the current transient the fuel cell is undergoing. A way to present and study this phenomenon consists in stimulating the fuel cell with a sinusoidal current generator.

The  $V - I$  and  $P - I$  characteristics of the fuel cell stack have been traced under these conditions for different values of the sinusoidal frequency. The results are reported in Appendix K for the following frequencies: 0.1 Hz, 1 Hz, 10 Hz, 1000 Hz, 1 kHz and 10 kHz, while some of them are compared in Figure 6.3 and 6.4.



**Figure 6.3.** Voltage fuel cell stack response to a sinusoidal current injection, for different frequencies. Fuel cell stack: 325 cm<sup>2</sup>, 50 elements.



**Figure 6.4.** Power fuel cell stack response to a sinusoidal current injection, for different frequencies. Fuel cell stack: 325 cm<sup>2</sup>, 50 elements.



Figure 6.3 shows that the dynamic curve varies more and more from the static curve as the frequency increases. Now, the  $V - I$  points do not lie on the static polarisation curve anymore, but they form a closed line, meaning that the fuel cell voltage does not only depend on the fuel cell current value, but on the transients that lead to this current value as well. Furthermore, the curve becomes flatter and flatter as the frequency increases. This behaviour is also reflected in the power curve of Figure 6.4, which presents a similar behaviour.

### 6.3. Power converter measurements

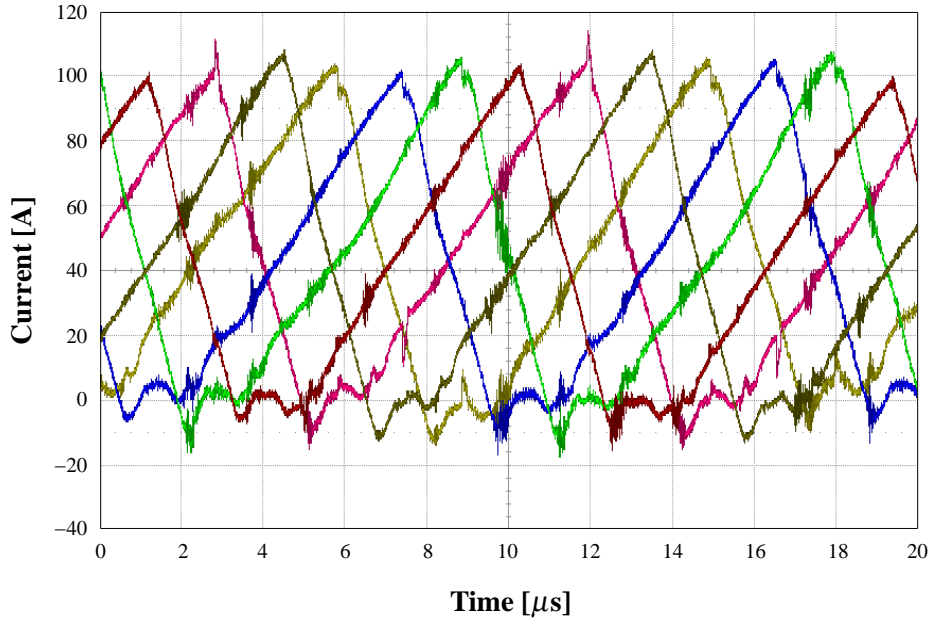
After dealing with the fuel cell stack, two different sets of experimental results on the power converter are presented in this section. The first set is about the operation of the power converter on a constant voltage power supply and is focused on the proper operation of the power converter itself. The second set concerns the operation of the power converter coupled to the chosen fuel cell stack.

#### 6.3.1. Constant voltage source test

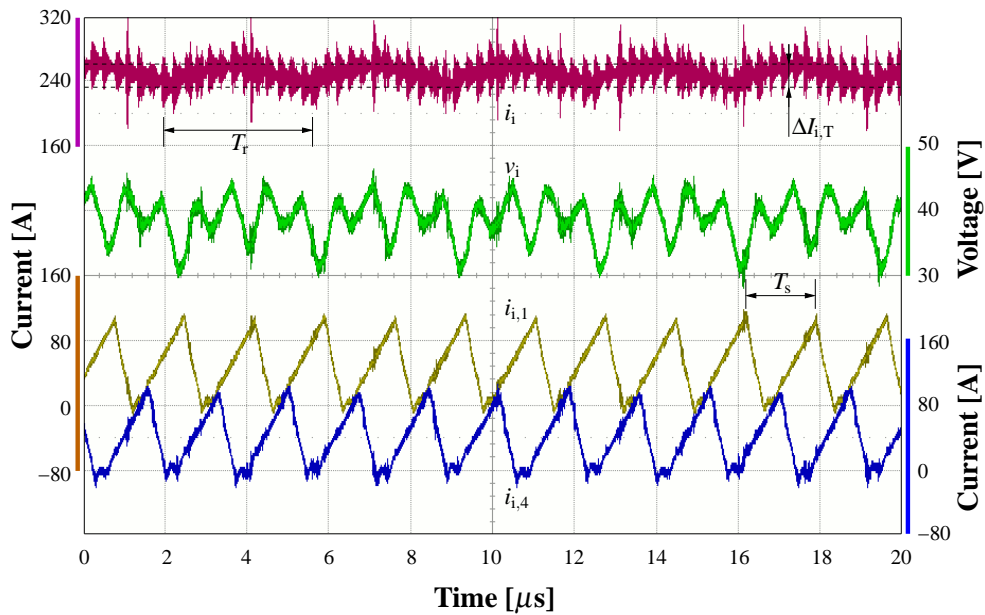
In this test, the power converter has been connected to a constant voltage power supply and tested under different load conditions. The six input currents are shown in Figure 6.5, while the average value of total input current is  $I_i = 250$  A, the average value of the input voltage  $V_i = 40$  V and the input power is then  $P_i = 10$  kW.

The differences between the modules and irregularities of the ripple of every module cause a residual current ripple with a lower frequency on the total input current  $i_i$ , as shown in Figure 6.6. The non perfect characteristic of the voltage source can be seen in this diagram, in which the input voltage  $v_i$  is not kept perfectly constant by the power supply. The same measurements for different input values are presented in Appendix K.

These tests show that the low frequency current ripple which affects the input current decreases with the input power. For the three cases presented here it is:



**Figure 6.5.** Plots of the 6 boost input currents acquired with a digital oscilloscope, under the condition of input power  $P_i = 10$  kW.



**Figure 6.6.** Plots of 2 of the 6 boost input currents, of the input voltage and of the total input current acquired with a digital oscilloscope, under the condition of input power  $P_i = 10$  kW.

- $\Delta I_{i,T} = (32 \pm 8.0)$  A, for  $P_i = 10$  kW;
- $\Delta I_{i,T} = (23 \pm 8.0)$  A, for  $P_i = 5$  kW;
- $\Delta I_{i,T} = (20 \pm 8.0)$  A, for  $P_i = 3$  kW.

All data, including the variable switching frequency  $f_s = 1/T_s$  and the low frequency period, are presented in Appendix K with their measurement errors.

After verifying the proper operation of the power converter in standard conditions, it will be tested in semi-real conditions, in which the input voltage is strongly variable and dependent on the output power, as if it were connected to a real fuel cell stack.

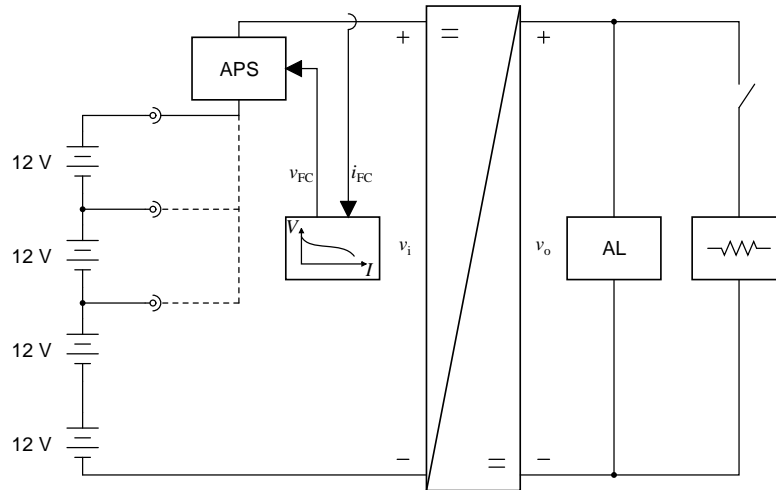
### 6.3.2. Fuel cell emulation test

In order to test the power converter in a semi-real operation, the power converter has been connected to a power supply able to emulate the behaviour of the fuel cell with a good approximation. This was useful to test the behaviour of the power converter when connected to a fuel cell stack, without having to deal with the problems a fuel cell could generate.

The emulation of the fuel cell has been carried out with an adjustable stabilised power supply in series with up to four 12V lead-acid batteries (Figure 6.7). Then, the voltage set point of the power supply has been manually set in order to make the power converter work as if it were connected to the real 325 cm<sup>2</sup> 50 element fuel cell stack, according to the static polarisation curve of such a fuel cell stack.

The load was composed of an electronic active load in parallel with a digitally controlled resistive load. The active load has been set in order to keep the output voltage to the desired value. Only the current loop of the power converter controller has been used, in order to be able to manually set the switching frequency and the switches' on-time. The converter has always been set to operate on the border between CCM and DCM.

The system has been tested in the output power range up to 3 kW, which was the maximum limit of the power supply. The most important variables — like input and output voltage and currents, output power and calculated efficiencies — are traced with their own absolute and relative errors in tables in Appendix K.



**Figure 6.7.** Electric diagram of the connection during the fuel cell emulation test. Acronyms: Adjustable Power Supply (APS), Active Load (AL).

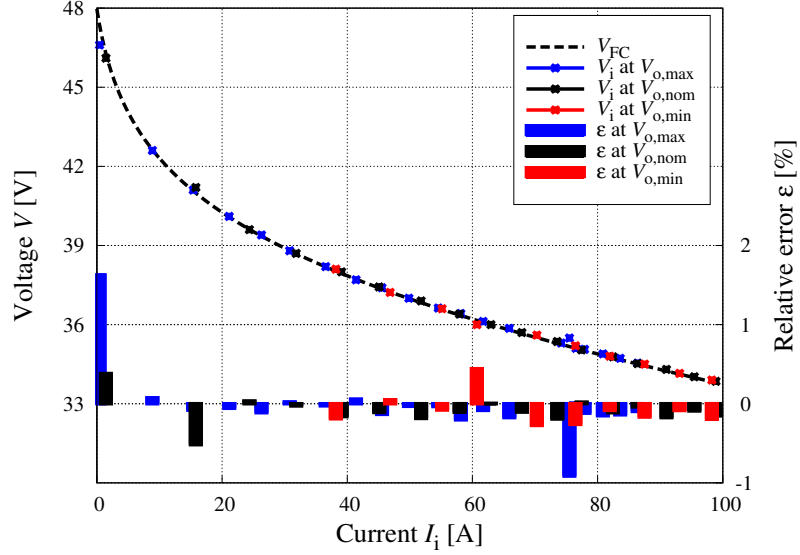
Figures 6.8 and 6.9 show the  $V - I$  and  $P - I$  points the converter has been set to work at, compared with the static  $V - I$  and  $P - I$  curves of the concerned fuel cell stack — plotted on the background — and the relative error between the experimental measurement and the theoretical curve.

The very small relative error — which is almost always less than 1 % — between the static polarisation curve and the theoretical curve of the fuel cell stack proves that the behaviour of the emulated fuel cell is quite similar to its real operation. As a consequence, these experimental data can be used as a good estimation of the actual efficiency of the converter.

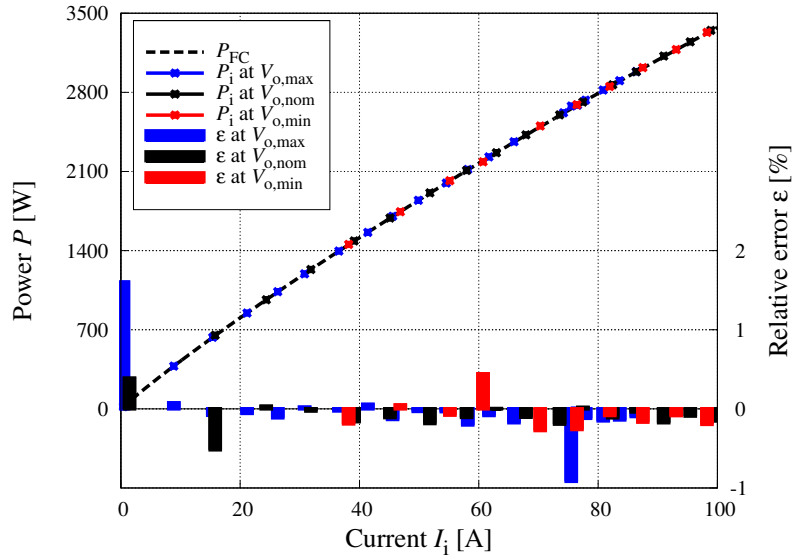
This is true in a semi steady state situation, when the transients are so slow that it can be assumed the fuel cell is working on the static polarisation curve.

Under these conditions, Figure 6.10 presents the efficiency of the power converter in the whole measurement range, for  $V_o = V_{o,M}$ ,  $V_o = V_{o,n}$ , and  $V_o = V_{o,m}$ . The single efficiencies are indicated as stars and the interpolation of the values as solid lines, while dashed lines represent the interpolation of the higher and lower error bar limits. In Appendix K, the detailed plots with all the error bars and the interpolation values are separately reported for every case.

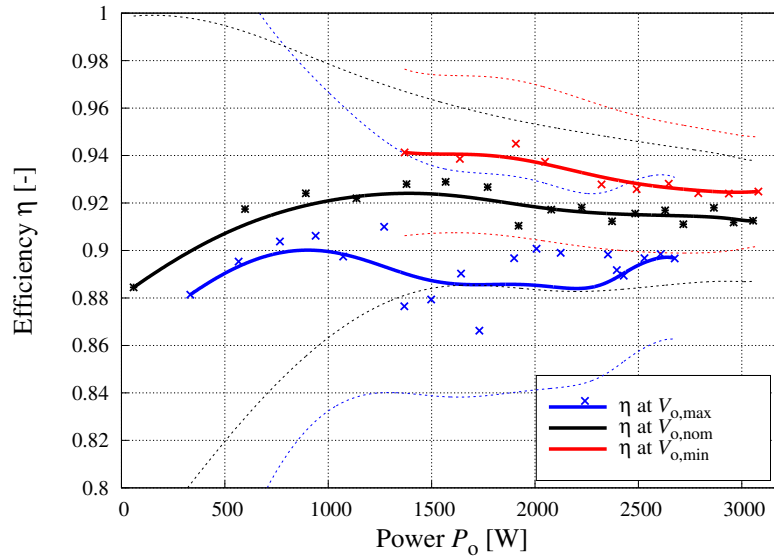
From Figure 6.10, it can be noticed that for  $P_o \geq 1000$  W the converter efficiency stays in the 84 %–98 % range with the error bars, in the whole range of out-



**Figure 6.8.** Analytical fuel cell stack voltage  $V_{FC}$  and experimental converter input voltage  $V_i$  versus fuel cell stack current and converter input current  $I_{FC} = I_i$  working points of the tested power converter, for three different values of the output voltage reference  $V_o$ :  $V_{o,m} = 42$  V,  $V_{o,n} = 48$  V and  $V_{o,M} = 60$  V. The relative error  $\varepsilon$  between  $V_{FC}$  and  $V_i$  is indicated.



**Figure 6.9.** Analytical fuel cell stack power  $P_{FC}$  and experimental converter input power  $P_i$  versus fuel cell stack current and converter input current  $I_{FC} = I_i$  working points of the tested power converter, for three different values of the output voltage reference  $V_o$ :  $V_{o,m} = 42$  V,  $V_{o,n} = 48$  V and  $V_{o,M} = 60$  V. The relative error  $\varepsilon$  between  $P_{FC}$  and  $P_i$  is indicated.



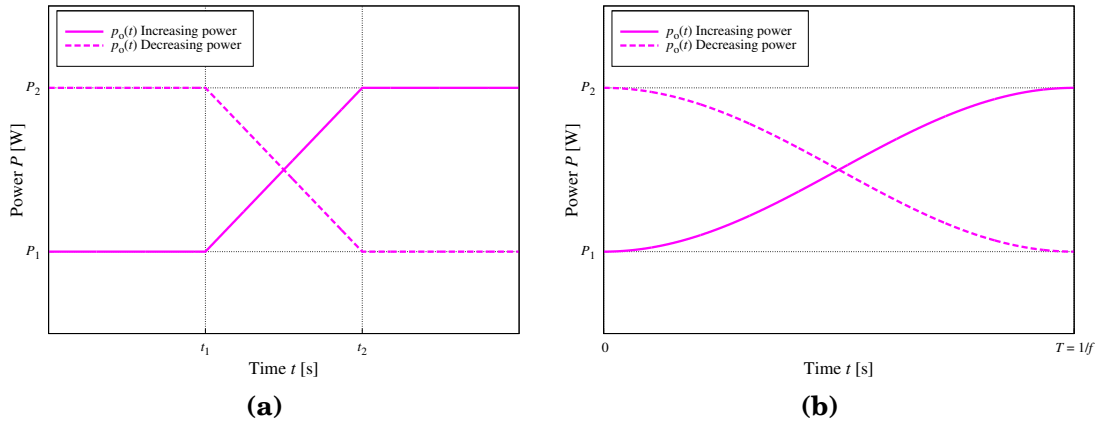
**Figure 6.10.** Experimental converter efficiency  $\eta$  versus converter output power  $P_o$ , for three different values of the output voltage reference  $V_o$ :  $V_{o,m} = 42$  V,  $V_{o,n} = 48$  V and  $V_{o,M} = 60$  V. Dashed curves represent the upper and lower limits of the error bars.

put voltage. Under  $P_o = 1000$  W, the error on the efficiency increases, making the results less meaningful.

In [40], a power converter for fuel cell applications has been presented. It shares similarities with the system studied in this thesis: they are both interleaved boost converters, even if the former consists of only 2 phases, while the latter has 6 phases. The maximum power is also slightly different, the former's maximum power being equal to 20 kW, against 5.5 kW for the latter. Nevertheless, they show comparable efficiency values — around 96 % for the former and around 92 % for the latter —, also considering the fact that the input and output voltage for the converter in [40] are higher (200 V–300 V against 25 V–60 V).

#### 6.4. Simulations of the whole system

In this section, the response of a system composed of a power converter and a fuel cell stack is simulated and analysed under different conditions of load and load transients. As shown in Figure 6.11, four different transients in the output power have been studied: step transients (Fig. 6.11 (a)) and sinusoidal transients (Fig. 6.11 (b)). For both the different transients, both the cases with positive and negative derivative have been studied: it will be shown that the system acts differently.



**Figure 6.11.** The four different transient types used to test the whole system.  $P_1$  and  $P_2$  represent the lower and higher power limits respectively,  $t_1$  and  $t_2$  the beginning and end instants of the ramp transient, and  $T = 1/f$  the period of the sinusoidal stimulus. (a) Ramp transients. (b) Sinusoidal transients.

Step transients, like the two presented in Figure 6.11 (a), are interesting because they can be frequently encountered during the normal operation of a power generator, in which loads can be connected or disconnected. Instead, studying sinusoidal transients, like the two presented in Figure 6.11 (b), provides information about the reaction of the system to a stimulus that does not present angular points, and sweeps on a wide operation range.

Furthermore, since it has been observed that the output voltage reference influences system operation, every transient has been studied for three different values of the output voltage:

- the maximum voltage,  $V_o = V_{o,M} = 60$  V;

- the nominal voltage,  $V_o = V_{o,n} = 48$  V;
- the minimum voltage,  $V_o = V_{o,m} = 42$  V.

As the studied system does not contain energy storage elements, except the ones required for the normal operation of the boost converter, the results of these simulations are also useful to understand how the system itself can react to load transients. If its dynamic performances cannot match the dynamic requirements of the load, energy storage elements need to be added.

In the tests, the output power varies in the range  $[P_{o,m}; P_{o,M}]$ , where  $P_{o,m}$  indicates the minimum output power and  $P_{o,M}$  the maximum power. This last value directly derives from the electrical requirements and is equal to:

$$P_{o,M} = 5\,500 \text{ W.} \quad (6.4.1)$$

Instead, the minimum power is a consequence of two different main issues, concerning:

- the fuel cell and boost operation: to guarantee the  $V_i < V_o$  condition required by the operation of the boost converter, where  $V_i$  and  $V_o$  are the boost input and output voltages respectively, the fuel cell must deliver a minimum power, as stated in Chapter 2;
- the minimum on-time and minimum frequency: the switches of the power converter have a minimum on-time value and the power converter cannot be operated under its minimum switching frequency, leading to a minimum transferred power.

These constraints, combined with proper safety margins, define a minimum output power equal to:

$$P_{o,m} = 2\,200 \text{ W.} \quad (6.4.2)$$

Since the output power is not an input variable for the system, the only way to achieve the desired output power was to stimulate the system by imposing the load conductance  $g_o$  defined as:

$$g_o(t) = \frac{p_o(t)}{V_o^2} \quad (6.4.3)$$



where  $p_o$  is the desired evolution of the output power and  $V_o$  is the output voltage reference. The evolution of the output power and of the conductance values imposed to the system is shown for reference in Appendix K.

The following sections will present the results of these simulations. In order to make the plots easier to read, the following conventions have been used in all figures: the output power is always plotted in magenta, while the plotted variables are coloured in:

- blue, if they refer to the test with  $V_o = V_{o,M}$ ;
- black, if they refer to the test with  $V_o = V_{o,n}$ ;
- red, if they refer to the test with  $V_o = V_{o,m}$ .

When more variable curves traced on the same plot are coincident because they illustrate close values, they have been shifted in order to highlight the differences between them. The shift values have always been indicated.

#### 6.4.1. Step transients

Step transients are the most common kind of transients that could happen during the normal operation of a power generator. Thus, six different step transients have been studied:

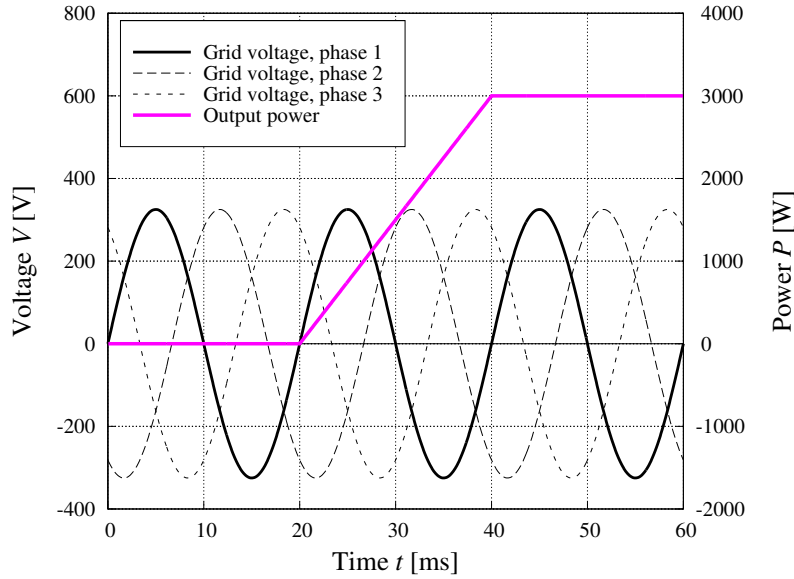
- from the minimum power  $P_{o,m}$  to the maximum power  $P_{o,M}$ , and vice versa;
- from the minimum power  $P_{o,m}$  to the average power  $P_{o,a}$ , and vice versa;
- from the average power  $P_{o,a}$  to the maximum power  $P_{o,M}$ , and vice versa;

where the average power  $P_{o,a}$  is defined as:

$$P_{o,a} = \frac{P_{o,M} + P_{o,m}}{2} = 3\,850 \text{ W} \quad (6.4.4)$$

and it has been used to analyse the operation of the system for intermediate situations, too. This is a reasonable solution, as the system is highly non linear

and it might not be a good idea to infer conclusions only from the maximum and the minimum working points.



**Figure 6.12.** Hypothesis on the power variation ramp for a standard 3 kW rectifier for telecommunication applications, compared to the grid voltage phases.

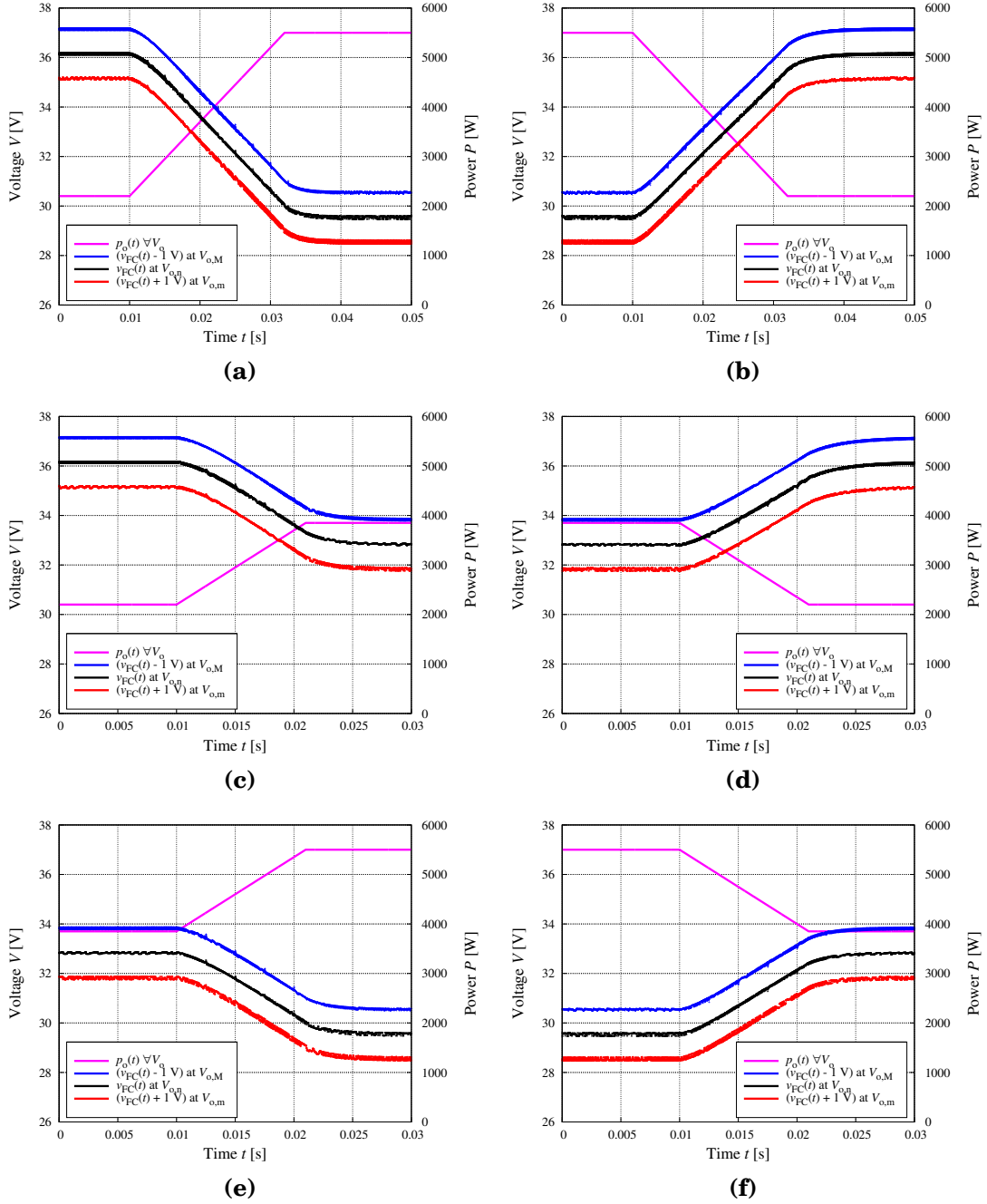
The value of the derivative of the ramp  $m_{po}$  during the step transients has been calculated considering the hypothesis that in a standard 3 kW rectifier for the telecommunication applications the power transient from 0 to the maximum power could be achieved in one period of the voltage grid, i.e. 20 ms for a 50 Hz grid, as shown in Figure 6.12, which leads to:

$$m_{po} = \frac{3 \text{ kW}}{20 \text{ s}} = 150 \frac{\text{kW}}{\text{s}}. \quad (6.4.5)$$

The results of these simulations are presented and discussed here.

#### 6.4.1.1. Fuel cell voltage response

The fuel cell voltage  $v_{FC}$  response to the output power transients is shown in Figure 6.13. The first two plots, (a) and (b), show the evolution of  $v_{FC}$  during the two transients in which the output power varies between  $P_{o,M}$  and  $P_{o,m}$ , while the other four, from (c) to (f), show the evolution of the same variable when



**Figure 6.13.** Fuel cell voltage responses to different ramp transients on the output power for three different values of the output voltage reference:  $V_{o,m}$ ,  $V_{o,n}$  and  $V_{o,M}$ . Fuel cell stack:  $325 \text{ cm}^2$ , 50 elements.

the output power varies between  $P_{o,a}$  and  $P_{o,M}$ , and between  $P_{o,a}$  and  $P_{o,m}$ . As it can be inferred from the static polarisation curve, too, the maximum fuel cell voltage corresponds to the minimum output power and vice versa.

Furthermore, since the average value of the fuel cell voltage is not affected by the output voltage reference, which only influences the voltage ripple, the fuel cell voltage plots have been shifted.

The filtering effect of the capacitive component of the fuel cell can be perceived, which smoothes the corners of the fuel cell voltage curve. It should also be noticed that the fuel cell voltage is affected by a voltage ripple, which is the fuel cell response to the current ripple present on its current and generated by the power converter.

The amplitude of the voltage ripple has different behaviour depending on the output power level and on the output voltage reference: Figure 6.13 shows that:

- for the maximum power condition, the ripple decreases when the output voltage increases, reaching its minimum when  $V_o = V_{o,M}$ ;
- for the minimum power condition, the ripple decreases when the output voltage decreases, reaching its minimum when  $V_o = V_{o,m}$ ;
- for the average power condition, the ripple is minimum for  $V_o = V_{o,n}$ , and it is higher both for  $V_o = V_{o,M}$  and for  $V_o = V_{o,m}$ .

#### 6.4.1.2. Output voltage response

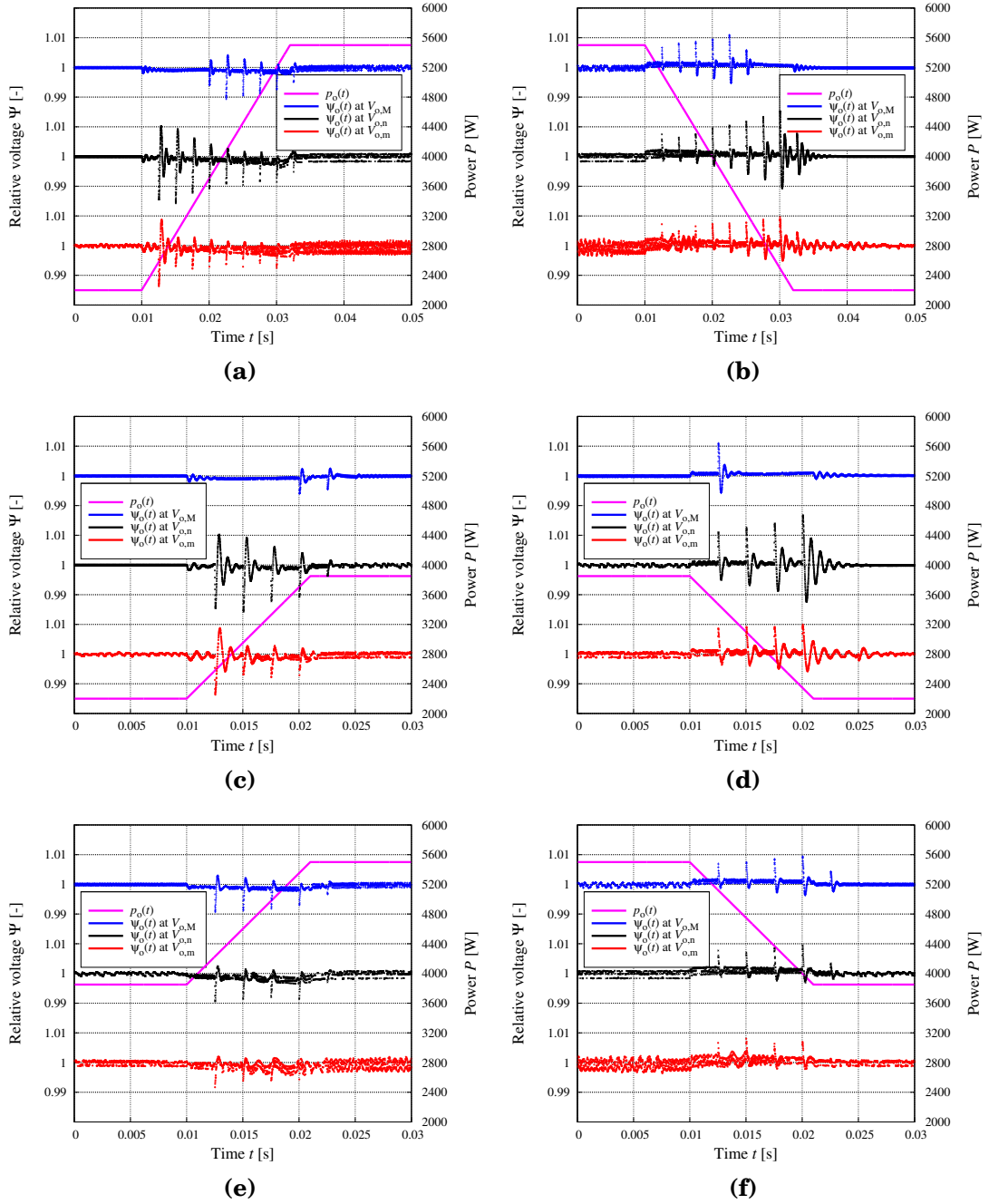
Figure 6.14 shows the relative output voltage  $\psi_o$  during the transients where  $\psi_o$  is defined as:

$$\psi_o(t) = \frac{v_o(t)}{V_o} \quad (6.4.6)$$

and where  $v_o$  is the output voltage and  $V_o$  the output voltage reference. The three plots of  $\psi_o$  for  $V_{o,M}$ ,  $V_{o,n}$  and  $V_{o,m}$  are shown on the same graphs, one under the other.

The output voltage is the resultant fo two independent responses:

- the first is the response to the output power ramp, which lasts either 11 ms or 22 ms;



**Figure 6.14.** System output voltage responses to different ramp transients on the output power for three different values of the output voltage reference:  $V_{o,m}$ ,  $V_{o,n}$  and  $V_{o,M}$ . Fuel cell stack: 325 cm<sup>2</sup>, 50 elements.

- the second is the response to the converter switching frequency steps, which are due to the digital control (cf. Figure 6.15); these transients are shorter and last around 2.5 ms.

The relative output voltage ripple increases when the output power increases, and decreases when the output voltage increases: the worst case is for  $P_o = P_{o,M}$  and  $V_o = V_{o,m}$ . Even in the worst case, the relative output voltage ripple is  $\Delta\Psi_o < 0.6\%$ , which is equivalent to  $\Delta V_o < 250$  mV. Furthermore, it should be pointed out that these results come from a model which does not contain dissipative elements, whose presence should make the output voltage ripple smaller.

The relative values of the spikes during transients are always less than 1.5 % and generally around 1 %. Since they are related to the frequency steps, they are mostly present in the first two cases in which the power step is higher and the transient lasts longer.

It is also interesting to notice that these peaks are higher during the average to minimum power transient than in the maximum to average power one. Also, all the voltage ripple spikes present a particular asymmetry: when the power derivative is positive, spikes are more extended to the negative side, while they are more extended to the positive side when the power derivative is negative.

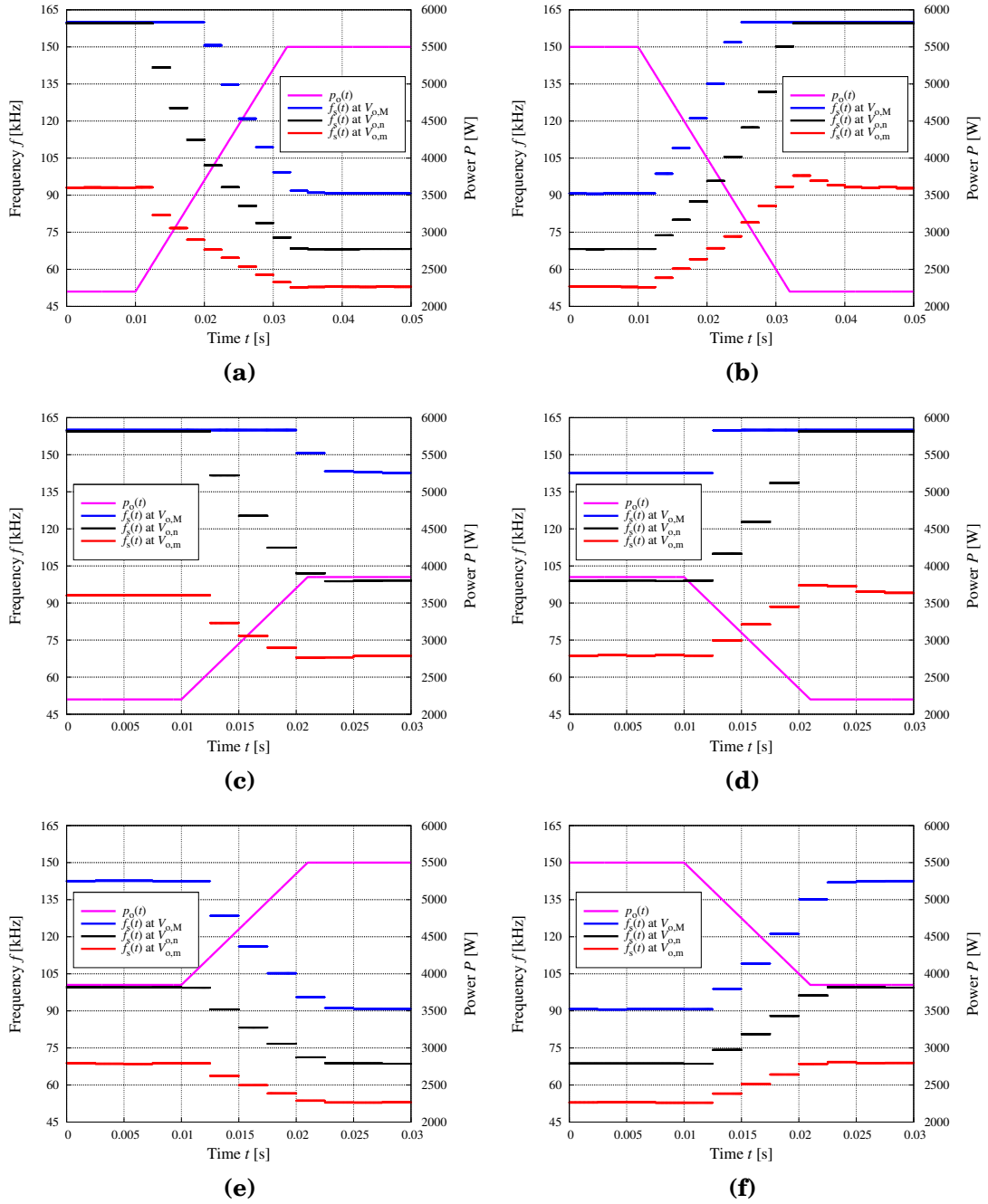
#### 6.4.1.3. *Switching frequency response*

Figure 6.15 shows the plot of the switching frequency as a function of the time during the six different studied transients. Since the control is digital, the frequency varies by steps, which generates small spikes in the output voltage, as shown in Figure 6.14.

Generally, there are no frequency undershoots, but in two cases overshoots are present. They clearly appear in the maximum and average to minimum power transients, but only for  $V_o = V_{o,m}$ . Only in these cases the frequency transient continues after the end of the output power transient.

As for the frequency values, they are not the same during the two transients with opposite derivatives, as shown in Figure 6.15 (c) and (d) for  $V_o = V_{o,M}$ . This is a general consideration, which will be analysed further on.

Figure 6.15 also shows the effect of the frequency saturation blocks:



**Figure 6.15.** Power converter switching frequency responses to different ramp transients on the output power for three different values of the output voltage reference:  $V_{o,m}$ ,  $V_{o,n}$  and  $V_{o,M}$ . Fuel cell stack:  $325 \text{ cm}^2$ , 50 elements.

- minimum power condition: the saturation upper limit is reached for  $V_{o,M}$  and  $V_{o,n}$ , but not for  $V_{o,m}$ ;
- maximum power condition: the saturation lower limit is only reached for  $V_{o,m}$ .

In all the other conditions, the switching frequency is not saturated. It varies in order to guarantee that the power converter operates on the border between CCM and DCM.

#### 6.4.1.4. Voltage-current and frequency-power maps

Figure 6.16 shows the fuel cell voltage versus current maps ((a), (c) and (e)), and the power converter switching frequency versus output power maps ((b), (d) and (f)). These plots highlight the difference in the behaviour of the power converter during the transients with opposite output power derivatives.

Since the fuel cell voltage versus current maps are mostly coincident, they have been shifted to highlight the differences between them. The shift operation was not necessary for the frequency versus power map, since switching frequencies are naturally different due to different operating conditions.

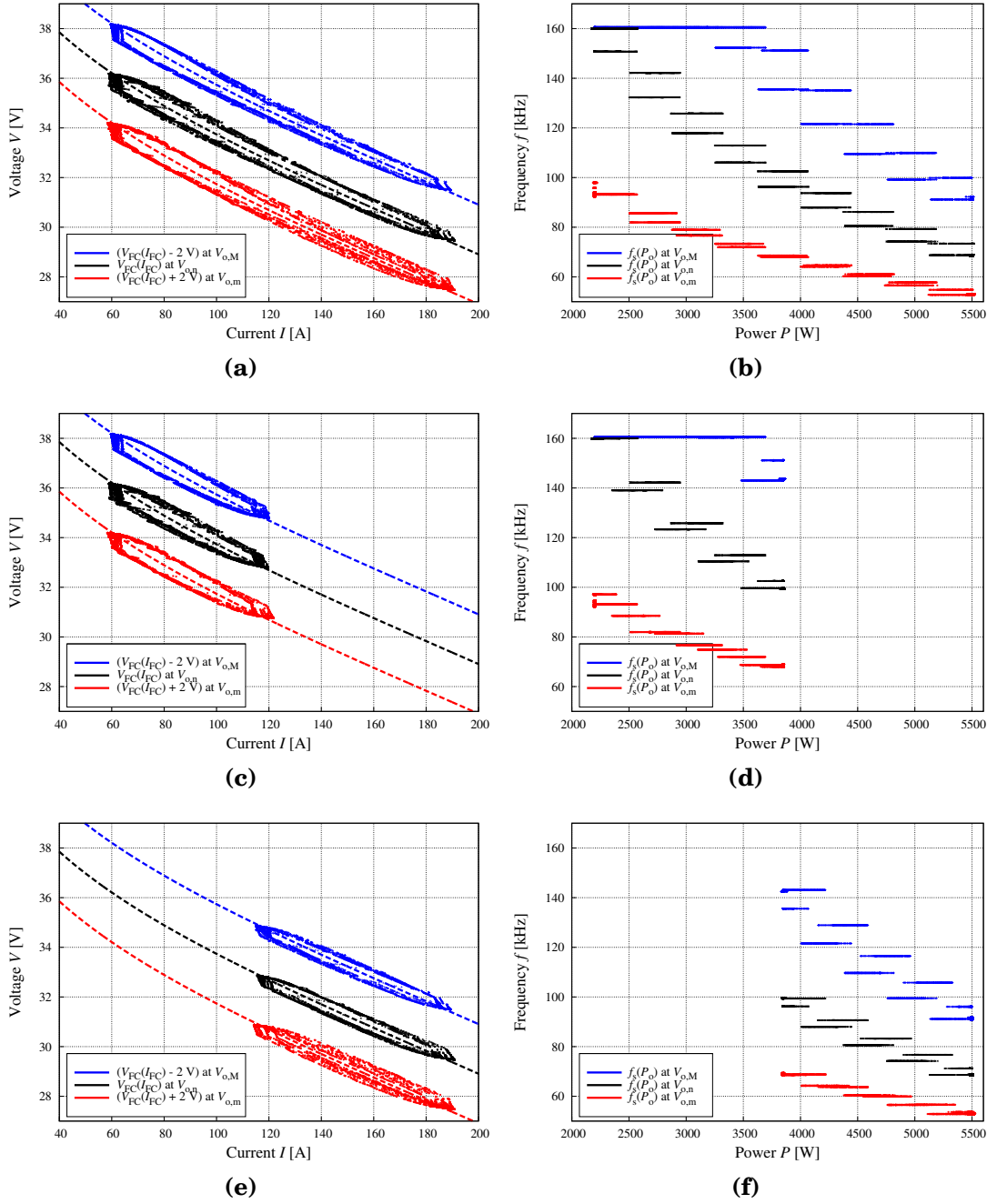
A peculiar circular shape can be observed on the voltage versus current maps: the operating points do not lie on the static polarisation curve, which is plotted as a dashed line for reference. This is due to the dynamic behaviour of the system and of the fuel cell. The steady state points are located on the right and left side of the map, where it intersects the static polarisation curve. The transient corresponding to the positive power derivative is always located above the polarisation curve, while the one corresponding to the negative power derivative is always located below it.

Both current and voltage ripple are particularly evident for higher values of the output power when  $V_o = V_{o,m}$ , which corresponds to the bottom right part of the red curves, where the map points are more dispersed.

Similar maps can be drawn for the fuel cell power versus current, but they do not provide any new information, as the power is derived from voltage and current. They are also less interesting, since points are closer to the steady state curve. They have been plotted in Appendix K for reference.

As for the switching frequency versus power maps, the same power values can correspond to different switching frequencies. This is because the fuel





**Figure 6.16.** Fuel cell voltage versus current maps (left column) and power converter switching frequency versus output power maps (right column) under different ramp transients on the output power for three different values of the output voltage reference:  $V_{o,m}$ ,  $V_{o,n}$  and  $V_{o,M}$ . Fuel cell stack:  $325\text{ cm}^2$ , 50 elements.

cell voltage depends on the transient evolution, as in the voltage versus current maps.

#### 6.4.2. Sinusoidal transients

The simulation results of transients between three different values of output power have been shown in the previous section. The intermediate states of the system will be studied by stimulating it with a continuous sinusoidal output power from the minimum power  $P_{o,m}$  to the maximum power  $P_{o,M}$  in this section.

The chosen frequency for the sinusoidal stimulus is such that the maximum power derivative is equal to half of the maximum previously defined  $m_{po,M} = 150 \text{ kW/s}$  derivative:

$$p_o(t) = P_{o,A} \sin \omega t + P_{o,o} \quad (6.4.7)$$

$$\frac{dp_o}{dt}(0) = \omega P_{o,A} = 2\pi f P_{o,A} = \frac{m_{po,M}}{2} \quad (6.4.8)$$

$$f = \frac{1}{2} \frac{m_{po,M}}{2\pi P_{o,A}} = 3.6 \text{ Hz} \cong 4 \text{ Hz} \quad (6.4.9)$$

where  $P_{o,A}$  is the amplitude value,  $P_{o,o}$  the offset value, and  $f$  the frequency of the stimulating sinusoid and where:

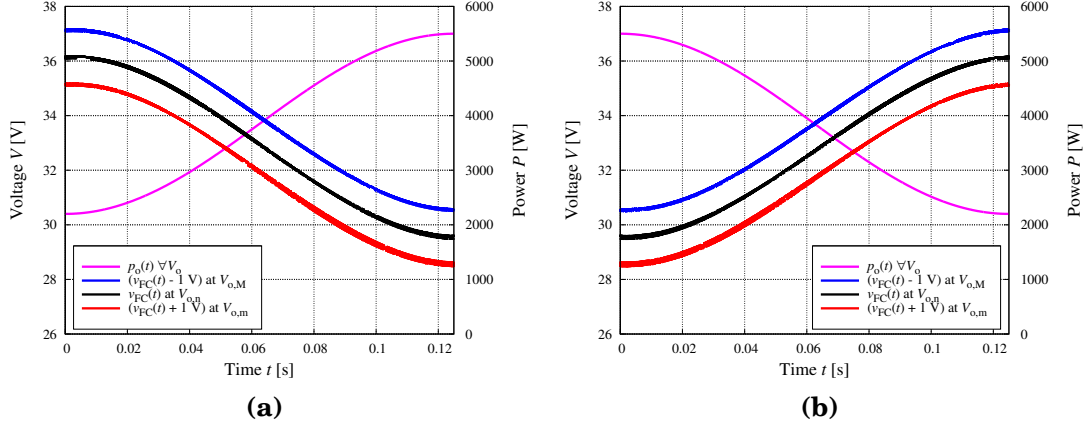
$$P_{o,A} = \frac{P_{o,M} - P_{o,m}}{2} = 3\,300 \text{ W} \quad (6.4.10)$$

$$P_{o,o} = \frac{P_{o,M} + P_{o,m}}{2} = 3\,850 \text{ W}. \quad (6.4.11)$$

This leads to transients without any angular points and whose length is equal to 125 ms, which are longer compared to 22 ms and 11 ms of the previous tests.

Some tests have also been carried out with higher frequencies to verify how the system would react. Results for  $f = 10 \text{ Hz}$  are presented in Appendix K, showing that the system is still operating properly.

Figure 6.17 shows the variation of the fuel cell voltage due to the output power variation, where the minimum voltage still corresponds to the maximum power and vice versa.



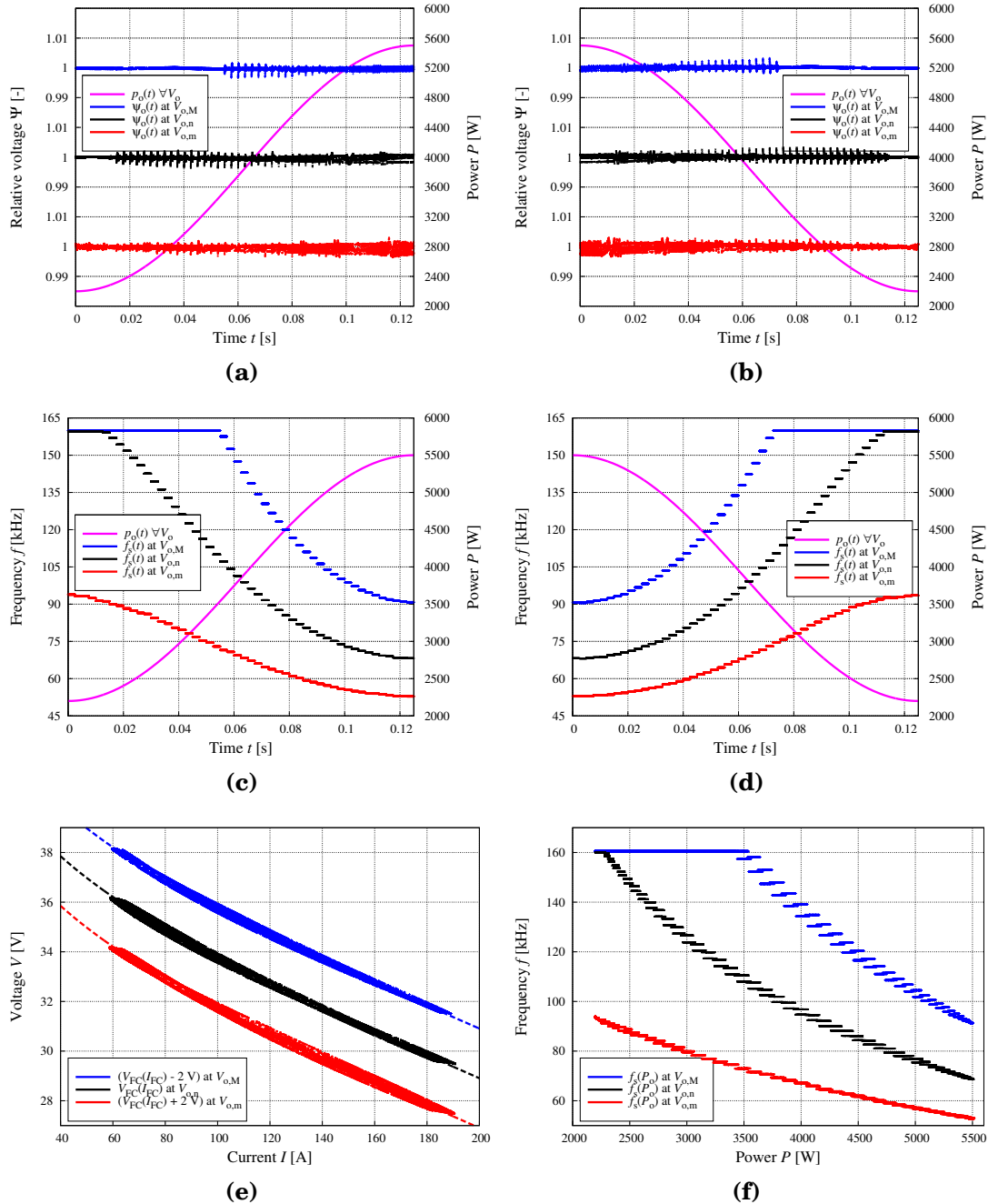
**Figure 6.17.** Fuel cell voltage responses to sinusoidal transients on the output power for three different values of the output voltage reference:  $V_{o,m}$ ,  $V_{o,n}$  and  $V_{o,M}$ . Fuel cell stack:  $325 \text{ cm}^2$ , 50 elements.

Plots (a) and (b) in Figure 6.18 show the relative output voltage  $\psi_o$  during the transients. The ripple is increasing with the output power and decreasing with the output voltage reference here too, confirming that the worst case is the one in which the output power is at its maximum and the output voltage is at its minimum.

Plots (c) and (d) show the switching frequency evolution during the transients: the frequency gradually changes and this always happens through steps because of the digital control.

Comparing plots (a) and (b) with (c) and (d) in Figure 6.18, the effect of the step frequency transients on the output voltage can be perceived. In this case, they generate small output voltage peaks, lower than 0.3 %.

The low transients lead to have a fuel cell voltage versus current map very close to the static polarisation curve (plot (e)), where the two opposite transients are not noticeable any more. Similar behaviour can be observed in plot (f) for the switching frequency versus power map, in which the switching frequencies are still different in the two transients, but very close to each other.



**Figure 6.18.** System output voltage responses (a) and (b), power converter switching frequency responses (c) and (d), fuel cell voltage versus current map (e) and power converter switching frequency versus output power map (f) under sinusoidal transients on the output power for three different values of the output voltage reference:  $V_{o,m}$ ,  $V_{o,n}$  and  $V_{o,M}$ . Fuel cell stack: 325 cm<sup>2</sup>, 50 elements.

### 6.5. Experimental results on fuel cell stack prototype

The final prototype of the fuel cell stack, constituted by 50 elements measuring  $325 \text{ cm}^2$  each, has been connected to the acquisition system described in Chapter 5 and fed with pure hydrogen and pure oxygen. As a first experiment, the fuel cell stack has been powered without any load.

Three distinct tests were performed; during each test a stable open circuit voltage and stable flows were reached, for short intervals. All the cell voltages were around 800 mV, with a total output voltage  $V_{FC} \cong 48 \text{ V}$ . Cooling water temperature increased from  $32 \text{ }^\circ\text{C}$  at the beginning to  $41 \text{ }^\circ\text{C}$  at the end of the tests.

During the third test, the hydrogen output pipe fused, determining the end of this series of experiments. The hypothesised cause behind this fault is a direct combustion between hydrogen and oxygen, due to a perforation of one or more membranes. The reason for the membrane perforation is still under research, but it could have started from the oxygen side due to some flammable impurities in the stack.

### 6.6. Conclusion

A fuel cell stack has been characterised and its model has been used to investigate the behaviour of a fuel cell stack under several dynamic conditions. The model has been integrated into a larger system, which included the model of the previously designed power converter. The performance of the system has been simulated, and the proper response of the system has been verified in its working conditions.

Then, the power converter has been tested by emulating its connection to a fuel cell stack. It behaved properly, showing a high efficiency in the whole operation range.

Future work should include the connection of the power converter to the real fuel cell stack. Then, the voltage loop of the converter controller should be closed, along with the switching frequency loop. The variable switching frequency behaviour of the system needs to be investigated further, and a control system to make the system work under the minimum power  $P_{o,m}$  should be designed as well.



## CHAPTER 7

### CONCLUSION

After an overview of fuel cell history and of the most common fuel cell types, the domains and applications in which fuel cells could be employed have been analysed. Basing on a CO<sub>2</sub> emission level criterion, applications in which the use of fuel cells can be a profitable alternative to traditional technologies have been identified.

For this purpose, four domains have been defined, split according to the role played by the fuel cell: automotive, stationary, backup and portable. The last one has not been considered in the analysis, since CO<sub>2</sub> emission reduction is not an important criterion in such systems.

It turned out that grid and battery based solutions generally present lower CO<sub>2</sub> emissions than traditional or fuel cell based solutions, even if their emission levels strictly depends on the electricity production systems. Nevertheless, fuel cell solutions can be good alternatives when it is not possible to take advantage of grid or battery based systems because the grid is not accessible or because batteries would be too heavy or too expensive. It has been proved that fuel cell systems fed with hydrogen produced from natural gas reforming are better than traditional solutions. Methanol fuel cell solutions have also been analysed and they have proved to be a good alternative too. Another advantage of methanol based solutions is the existence of a partial infrastructure. Furthermore, a domain in which fuel cells can overtake traditional technologies concerns backup applications.

After the presentation of the context, it has been shown that power electronics are getting more and more involved in the fuel cell domain, because of the requirement of adapting the electrical characteristics of the fuel cell to those required by the load.

Once fuel cells and power converters proved to be interesting research matter, the basic types of power converters that can be used in fuel cell systems have been illustrated. This was followed by a sizing and designing procedure for fuel cell systems, in which the mutual implications in the choices of the fuel cell stack and the power converter have been presented. As the field of power converters is very large, the scope of this dissertation has been restricted to non-isolated DC/DC converters, since these topologies are generally simpler, cheaper and more efficient.

The sizing and design procedure has been based on the total fuel cell active surface, which leads to a partial definition of the characteristics of the fuel cell stack and the power converter.

Other criteria have also been taken into account and have been presented, like the variation of the cost of the fuel cell system as a function of the fuel cell stack surface. Generally, the larger the element surface of a fuel cell stack is, the cheaper the stack is.

A 5 kW fuel cell backup system for telecommunication applications has been chosen as an example of the application of the exposed theoretical approach. A prototype of such a system has been sized along with all its components: the fuel cell stack, the power converter and the controller.

As the desired operation mode of the power converter is quite unusual, a quite extended analytical description of its operation in the whole current range has been reported. The power converter is characterised by a variable switching frequency which guarantees its operation on the border between CCM and DCM, and so a higher efficiency. Other related aspects have been studied, like an interesting instability phenomenon observed in the first version of the current mode control.

A complete model — composed of the fuel cell, the power converter, the controller and the load — has been developed and described in order to study the whole system.

Before dealing with the experimental and simulation results, the fuel cell stack and the power converter prototypes, along with the hardware required for a safe fuel cell stack operation, have been presented.

The description of the internally designed acquisition system has been reported since it offers a solution to the complex problem of measuring the fuel cell single element voltages, which are all referred to different potentials and must be isolated.



The results from the simulations and the experimental tests about all the single elements and about the system as a whole have been presented in the last chapter.

A fuel cell stack has been characterised and its model integrated into a larger system. The system has been simulated and proved to work properly. The power converter has also been tested in semi-real conditions, showing high efficiency in the whole operation range.

Unfortunately, it was impossible to perform the experimental test on the complete system because of a destructive fault on the fuel cell stack whose causes are still under investigation.

Future work includes the connection of the power converter to the real fuel cell stack, the improvement of the control system and its integration with the control of the fuel cell stack.



## APPENDIX A

### ENERGETICS CONSIDERATIONS

#### A.1. Efficiencies

The diagram reported in [124] has been used to determine the energetic efficiencies calculated from the primary energy sources to the final user. The cited diagram was meant to evaluate the CO<sub>2</sub> emissions for different kind of vehicles. It has been expanded in order to be used for other purposes as well. This is the list of modifications and assumptions that have been made:

- the efficiency of internal combustion engines for gasoline, natural gas and hydrogen is always the maximum and equals 23 %;
- the efficiency of internal combustion engines fed by methanol also equals 23 %;
- optimistically, the efficiency of a direct methanol fuel cell equals 35 %;
- if the final user is not a vehicle, the required power electronics has the same efficiency of the electric drive of a vehicle and equals 90 %;
- in a diesel power generator the efficiency of the alternator equals 90 %;
- the electricity produced from oil is supposed to be produced half from a traditional system, whose efficiency is 48 %, and half from a combined system, whose efficiency is 52 %, so an overall efficiency of 50 % has been assumed;

- the total efficiency of a fuel cell based CHP system equals 80 %, where 45 % is the electrical efficiency and 35 % the thermal efficiency;
- the total efficiency of a Diesel internal combustion engine based CHP system equals 60 %, where 25 % is the electrical efficiency and 35 % the thermal efficiency;
- the total efficiency of a Otto internal combustion engine based CHP system equals 58 %, where 23 % is the electrical efficiency and 35 % the thermal efficiency.

## A.2. Carbon dioxide emission calculation

Once the total process efficiency  $\mu$  is known, the energy of the primary source  $E_1$  can be calculated from the final energy  $E_2$ :

$$E_1 = \frac{E_2}{\mu} \quad (\text{A.2.1})$$

which leads to the fuel mols  $n_f$ , once the fuel higher heating value  $E_f$  and its molar mass  $A_f$  are known, being  $m_f$  the fuel mass:

$$m_f = \frac{E_1}{E_f} \quad (\text{A.2.2})$$

$$n_f = \frac{m_f}{A_f}. \quad (\text{A.2.3})$$

The emitted mols of  $\text{CO}_2$   $n_{\text{CO}_2}$ , which equal the mols of carbon in the fuel  $n_C$ , are derived from:

$$n_{\text{CO}_2} = n_C = k_C n_f \quad (\text{A.2.4})$$

where  $k_C$  represents the number of carbons atoms per fuel mol.

The  $\text{CO}_2$  total mass can be calculated once the molar mass  $A_{\text{CO}_2}$  of  $\text{CO}_2$  is provided:

$$m_{\text{CO}_2} = n_{\text{CO}_2} A_{\text{CO}_2}. \quad (\text{A.2.5})$$

CO<sub>2</sub> emissions can be expressed as a ratio between the CO<sub>2</sub> total mass and the final energy:

$$\frac{m_{\text{CO}_2}}{E_2} = k_f \frac{1}{\mu} \quad (\text{A.2.6})$$

where  $k_f$  is a constant which depends only on the fuel and equals to:

$$k_f = \frac{A_{\text{CO}_2}}{A_f} k_c \frac{1}{E_f}. \quad (\text{A.2.7})$$

Examples of values for natural gas, oil and coal are:

- natural gas:  $k_{f,g} = 50 \cdot 10^{-9} \text{ kg/J}$
- oil:  $k_{f,o} = 67 \cdot 10^{-9} \text{ kg/J}$
- coal:  $k_{f,c} = 87 \cdot 10^{-9} \text{ kg/J}$

When comparing different technologies and different sources, it can be easier to use a normalised value for the CO<sub>2</sub> emissions. In this thesis, CO<sub>2</sub> emission levels have been references to oil, leading to:

$$\mu_{\text{CO}_2,o} = \frac{\frac{m_{\text{CO}_2,o}}{E_2}}{k_{f,o}} = \frac{1}{\mu} \quad (\text{A.2.8})$$

$$\mu_{\text{CO}_2,c} = \frac{\frac{m_{\text{CO}_2,c}}{E_2}}{k_{f,o}} = \frac{k_{f,c}}{k_{f,o}} \frac{1}{\mu} = 1.3 \frac{1}{\mu} \quad (\text{A.2.9})$$

$$\mu_{\text{CO}_2,g} = \frac{\frac{m_{\text{CO}_2,g}}{E_2}}{k_{f,o}} = \frac{k_{f,g}}{k_{f,o}} \frac{1}{\mu} = 0.75 \frac{1}{\mu}. \quad (\text{A.2.10})$$

If the absolute mass of CO<sub>2</sub> emissions is needed, it can be calculated using:

$$m_{\text{CO}_2,x} = \mu_{\text{CO}_2,x} E_2 k_{f,o} \quad (\text{A.2.11})$$

where  $x$  is either o for oil, g for natural gas or c for coal.

### A.3. Primary sources of some country grid systems

In order to calculate the amount of CO<sub>2</sub> emissions due to grid electricity usage, the composition of the primary sources in the production of electricity has been looked for Italy, France and USA. These data, referred to the situation in 2006, are presented in Table A.1.

**Table A.1.** Distribution of the energy produced in Italy, France and USA across the different energy sources.

	Coal	Oil	Natural gas	Nuclear	Hydraulic	Renewable	Other
	[%]	[%]	[%]	[%]	[%]	[%]	[%]
USA	49	1.60	20	19.3	7.1	2.4	0.70
France	3.9	1.80	3.8	78	11.1	1.30	0
Italy	15.3	7.9	60	0	13.8	2.7	0

While data for France and USA directly come from [125, 126], in the Italian case they have been deduced from the total production found in [127], divided into thermoelectric, hydraulic, and renewable. Reference [128] provides the composition of the thermoelectric Italian power plant systems, and so the total thermoelectric energy has been divided according to the composition of the thermoelectric system.

In the three cases, but specifically for Italy, the import/export production has not been considered, since it was impossible to know its composition.

## APPENDIX B

### THE BEGINNING OF ELECTRICAL LIGHTING

At the end of the 19<sup>th</sup> century, a wide choice of different lighting solutions had to share their market with other non electrical solutions, like gas and oil lighting systems. As an example, reference [129, p. 809] is quoted, where a comparison between different lighting solutions was done.

*“Nous donnerons d’abord dans le tableau suivant les dépenses afférentes aux modes d’éclairage autres que l’éclairage électrique.*

*Ces chiffres ont été données par M. Lecomte au Congrès international du gaz en 1900. [...]*

*Il ressort néanmoins de ces essais que de tous les modes d’éclairage autres que l’éclairage électrique, le plus économique est l’éclairage à incandescence par le gaz. [...]*

*Il résulte de ces chiffres que, de tous les systèmes d’éclairage, le plus économique est l’éclairage avec lampe à arc à flamme.”*

“We will give in the following table the outcome of lighting systems other than electric lighting.

These values were provided by Mr. Lecomte at the international gas congress in 1900. [...]

The result of these tests is that among all the lighting systems other than electric, the cheapest is the gas incandescent lighting. [...]

The result of these data is that among all the lighting systems, the cheapest is electric lighting with flame arc lamps.”

This second quotation is about the cost of tungsten lamps in comparison to carbon filament lamps, which were cheaper, but whose lifetime was shorter [129, p. 845].

*“Depuis quelques années on a réussi à remplacer le filament de charbon de la lampe à incandescence par des filaments d’autres substances réfractaires et on a pu obtenir ainsi des lampes à consommation spécifique moins élevée que celle des lampes à filament de charbon.*

*En revanche le prix d’achat de ces nouvelles lampes est très supérieur à celui de la lampe à filament de charbon.”*

“For some time we have succeeded in substituting the coal filament of the incandescent lamp with filaments of other refractory substances and then we have obtained lamps with lower specific consumption than coal filament lamps.

Despite this, the cost of these new lamps is far higher than the cost of coal filament lamps.”



## APPENDIX C

### STATISTICS ON PUBLISHED ARTICLES

Elsevier's search criteria:

- search engine: Science Direct's;
- terms: "fuel cells";
- journals: all (included articles in press);
- subject: all sciences.

IEEE's search Criteria:

- search engine: IEEEExplore;
- terms: "fuel cells";
- fields: all.

The total number of published articles ( $n_{T,1}$  and  $n_{T,2}$ ) and the number of published articles about fuel cells ( $n_1$  and  $n_2$ ) have been found for each year. Then, the ratios  $\pi_1$  and  $\pi_2$  have been calculated as:

$$\pi_1 = \frac{n_1}{n_{T,1}} \quad (\text{C.1})$$

$$\pi_2 = \frac{n_2}{n_{T,2}}. \quad (\text{C.2})$$

Data are presented in Tables C.1 and C.2.

**Table C.1.** Data about articles concerning fuel cells published by Elsevier.

<b>Year</b>	$n_{T,1}$	$n_1$	$\pi_1$	<b>Year</b>	$n_{T,1}$	$n_1$	$\pi_1$
[a]	[-]	[-]	[%]	[a]	[-]	[-]	[%]
1959	16 207	1	0.006 2	1984	141 044	34	0.024
1960	17 931	4	0.022	1985	150 831	21	0.013 9
1961	20 264	2	0.009 9	1986	154 406	35	0.023
1962	22 944	4	0.017 4	1987	165 330	22	0.013 3
1963	28 035	7	0.025	1988	172 925	37	0.021
1964	30 852	8	0.026	1989	184 141	33	0.017 9
1965	34 057	7	0.021	1990	195 539	74	0.038
1966	36 865	7	0.019	1991	208 294	49	0.024
1967	42 991	11	0.026	1992	212 304	113	0.053
1968	46 902	22	0.047	1993	219 653	70	0.032
1969	49 740	12	0.024	1994	229 980	129	0.056
1970	55 297	7	0.012 7	1995	274 645	113	0.041
1971	59 156	20	0.034	1996	281 811	199	0.071
1972	66 383	21	0.032	1997	297 216	233	0.078
1973	71 847	11	0.015 3	1998	284 577	328	0.115
1974	76 217	3	0.003 9	1999	264 517	370	0.140
1975	79 572	8	0.010 1	2000	276 760	481	0.174
1976	84 352	17	0.020	2001	289 101	572	0.198
1977	85 807	10	0.011 7	2002	291 711	839	0.29
1978	94 110	11	0.011 7	2003	332 634	880	0.26
1979	100 937	15	0.014 9	2004	354 897	1 218	0.34
1980	110 276	16	0.014 5	2005	362 109	1 333	0.37
1981	117 524	22	0.018 7	2006	399 532	1 994	0.50
1982	122 900	9	0.007 3	2007	413 471	1 872	0.45
1983	135 653	27	0.019 9	2008	448 191	2 254	0.50

**Table C.2.** Data about articles concerning fuel cells published by the IEEE.

<b>Year</b>	$n_{T,2}$	$n_2$	$\pi_2$	<b>Year</b>	$n_{T,2}$	$n_2$	$\pi_2$
[a]	[-]	[-]	[%]	[a]	[-]	[-]	[%]
1959	2 016	0	0	1984	11 482	1	0.008 7
1960	1 787	0	0	1985	14 303	0	0
1961	1 990	1	0.050	1986	13 611	0	0
1962	2 308	2	0.087	1987	14 613	1	0.006 8
1963	3 790	9	0.24	1988	27 330	7	0.026
1964	3 486	6	0.172	1989	30 361	31	0.102
1965	4 451	6	0.135	1990	35 873	40	0.112
1966	5 152	5	0.097	1991	41 154	6	0.014 6
1967	4 775	1	0.021	1992	40 949	12	0.029
1968	5 455	3	0.055	1993	47 818	20	0.042
1969	5 823	2	0.034	1994	52 977	19	0.036
1970	5 512	1	0.018 1	1995	52 620	18	0.034
1971	6 160	0	0	1996	59 318	37	0.062
1972	6 282	0	0	1997	63 512	38	0.060
1973	6 802	2	0.029	1998	65 146	17	0.026
1974	6 418	0	0	1999	69 750	37	0.053
1975	7 664	3	0.039	2 000	72 106	78	0.108
1976	7 248	1	0.013 8	2 001	72 631	82	0.113
1977	8 837	5	0.057	2 002	83 425	113	0.135
1978	8 781	1	0.011 4	2 003	97 357	132	0.136
1979	10 330	1	0.009 7	2 004	123 094	240	0.195
1980	9 314	0	0	2 005	137 310	259	0.189
1981	11 969	5	0.042	2 006	153 943	334	0.217
1982	10 613	1	0.009 4	2 007	164 723	402	0.244
1983	11 766	4	0.034	2 008	110 178	222	0.201



## APPENDIX D

### FUEL CELL EQUATIONS

#### D.1. Molar rates and current

The relations between the molar rates of the different species involved in the fuel cell reactions are:

$$\dot{n}_{\text{H}^+} = \dot{n}_{\text{e}^-} \quad (\text{D.1.1})$$

$$\dot{n}_{\text{H}_2} = \frac{1}{2} \dot{n}_{\text{e}^-} \quad (\text{D.1.2})$$

$$\dot{n}_{\text{H}_2\text{O}} = \frac{1}{2} \dot{n}_{\text{e}^-} \quad (\text{D.1.3})$$

$$\dot{n}_{\text{O}_2} = \frac{1}{4} \dot{n}_{\text{e}^-} \quad (\text{D.1.4})$$

where  $\dot{n}_{\text{H}^+}$  is the molar rate of the protons flowing through the membrane,  $\dot{n}_{\text{e}^-}$  the molar rate of the electrons in the external electric circuit,  $\dot{n}_{\text{H}_2}$  and  $\dot{n}_{\text{O}_2}$  the hydrogen and oxygen consumption rates, and  $\dot{n}_{\text{H}_2\text{O}}$  the water production rate.

Since the charge of an electron is  $q_e = 1.602 \cdot 10^{-19}$  C and the Avogadro number, which is the number of elements in a mole, is  $N_A = 6.022 \cdot 10^{23} \text{ 1/mol}$ , the charge of a mole of electrons is  $F = q_e N_A = 96\,485 \text{ C/mol}$  (Faraday constant).

So, the relation between the current and the electron mole rate is:

$$i = \dot{n}_{\text{e}^-} F \quad (\text{D.1.5})$$

and so the relations between electron  $\dot{n}_{e^-}$  and proton  $\dot{n}_{H^+}$  molar rates and current are:

$$\dot{n}_{e^-} = \frac{i}{F} \quad (\text{D.1.6})$$

$$\dot{n}_{H^+} = \frac{i}{F} \quad (\text{D.1.7})$$

Between hydrogen and oxygen flow rates, and water production are:

$$\dot{n}_{H_2} = \frac{i}{2F} \quad (\text{D.1.8})$$

$$\dot{n}_{O_2} = \frac{i}{4F} \quad (\text{D.1.9})$$

$$\dot{n}_{H_2O} = \frac{i}{2F} \quad (\text{D.1.10})$$

## D.2. Electromotive force

The Gibbs free energy, defined as the “energy available to do external work, neglecting any work done by changes in pressure and/or volume” [6], must be illustrated. It is indicated with  $g$ .

The Gibbs energy, enthalpy and entropy of formation are used in the following, meaning that “the zero energy point is defined as pure elements, in the normal state, at Standard Temperature and Pressure (STP)” [6]. The symbols used are  $g_f$ ,  $h_f$  and  $s_f$ , but it is more practical to refer these quantities to a mole of matter, using their molar counterparts  $\bar{g}_f$ ,  $\bar{h}_f$  and  $\bar{s}_f$ .

In a chemical reaction the released energy can be represented by the variation of the Gibbs free energy of formation  $\Delta\bar{g}_f$ :

$$\Delta\bar{g}_f = \left( \bar{g}_{f,H_2O} \right) - \left( \bar{g}_{f,H_2} + \frac{1}{2} \bar{g}_{f,O_2} \right) \quad (\text{D.2.1})$$

where  $\bar{g}_{f,H_2O}$ ,  $\bar{g}_{f,H_2}$ , and  $\bar{g}_{f,O_2}$  are the Gibbs free energies of formation of the produced water, the reactant hydrogen and the reactant oxygen respectively.

On the other hand, the electric work  $w_e$  spent by one mole of electrons along an electric circuit in a presence of a difference of potential  $e$ , from anode to cathode, is:

$$w_e = q_e N_A e = F e. \quad (\text{D.2.2})$$

The sum of the electric work and the energy released by the reaction must be null:

$$\Delta \bar{g}_f + 2w_e = 0 \quad (\text{D.2.3})$$

where the total electric work is  $2w_e$  since two moles of electrons are released in the reaction.

This leads to:

$$e = -\frac{\Delta \bar{g}_f}{2F}. \quad (\text{D.2.4})$$

In order to calculate  $e$ , the Gibbs molar free energy  $\bar{g}$  can be expressed as a function of of molar enthalpy  $\bar{h}$ , molar entropy  $\bar{s}$  and temperature  $T$ :

$$\bar{g} = \bar{h} - T \bar{s}. \quad (\text{D.2.5})$$

So, changes in the Gibbs molar free energy  $\Delta \bar{g}$  at constant temperature can be expressed:

$$\Delta \bar{g} = \Delta \bar{h} - T \Delta \bar{s}. \quad (\text{D.2.6})$$

It is the same for the Gibbs molar free energy of formation:

$$\Delta \bar{g}_f = \Delta \bar{h}_f - T \Delta \bar{s}_f. \quad (\text{D.2.7})$$

The molar enthalpy and entropy of formation for the two semi-reactions 4.1.1 and 4.1.2 are defined as:

$$\Delta \bar{h}_f = \left( \bar{h}_{f,\text{H}_2\text{O}} \right) - \left( \bar{h}_{f,\text{H}_2} + \frac{1}{2} \bar{h}_{f,\text{O}_2} \right) \quad (\text{D.2.8})$$

$$\Delta \bar{s}_f = \left( \bar{s}_{f,\text{H}_2\text{O}} \right) - \left( \bar{s}_{f,\text{H}_2} + \frac{1}{2} \bar{s}_{f,\text{O}_2} \right). \quad (\text{D.2.9})$$

Molar enthalpy and entropy are functions of pressure and temperature; at the standard pressure  $P_0$  they are only function of temperature:

$$\bar{h}_i(T) = \bar{H}_{T_0,i} + \int_{T_0}^T \bar{c}_{p,i}(T) dT \quad (\text{D.2.10})$$

$$\bar{s}_i(T) = \bar{S}_{T_0,i} + \int_{T_0}^T \frac{1}{T} \bar{c}_{p,i}(T) dT \quad (\text{D.2.11})$$

where  $\bar{c}_{p,i}$  is the molar heat capacity at constant pressure: it is highly non linear, but approximations for particular temperature ranges exist.  $\bar{H}_{T_0,i}$  and  $\bar{S}_{T_0,i}$  are experimentally measured and can be found in tables [6].

Thus, at the standard pressure  $P_0$  the electromotive force is only a function of temperature,  $e(T)$ , while pressure effects are included using the concept of activity of a reaction.

In a reaction of the kind:



where  $\text{J}, \text{K}, \text{M}$  are the species and  $j, k, m$  are their stoichiometric numbers, the activities  $a_{\text{J}}, a_{\text{K}}, a_{\text{M}}$  of the three species can be introduced, where the activity is a dimensionless quantity. A definition of activity can be found in [130].

The activity of the species are calculated in different ways, whether they are in the form of an ideal gas  $a_{\text{G}}$ , water steam  $a_{\text{S}}$  or liquid water  $a_{\text{W}}$ :

$$a_{\text{G}} = \frac{p_{\text{G}}}{P} \quad (\text{D.2.13})$$

$$a_{\text{S}} = \frac{p_{\text{S}}}{P} \quad (\text{D.2.14})$$

$$a_{\text{W}} = 1 \quad (\text{D.2.15})$$

where  $p_{\text{G}}$  is the partial pressure of the gas,  $p_{\text{S}}$  is the steam pressure,  $P$  is a reference pressure of the species or of the mixture, and  $a_{\text{W}} = 1$  since liquid water is incompressible.

The variation of the Gibbs free energy of formation  $\Delta \bar{g}_f$  for the reaction D.2.12 can be expressed as:

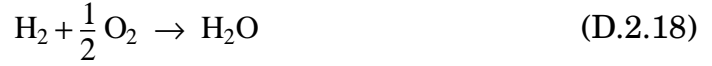


$$\Delta \bar{g}_f = \Delta \bar{g}_{o,f} + \Delta \bar{g}_{a,f} \quad (\text{D.2.16})$$

where  $\Delta \bar{g}_{o,f}$  is the variation of the Gibbs free energy of formation calculated at the STP ( $T_0, P_0$ ) and  $\Delta \bar{g}_{a,f}$  is the variation of the Gibbs free energy of formation due to the activity variation, which can be calculated in terms of activities:

$$\Delta \bar{g}_{a,f} = -R T \ln \left( \frac{a_J^j a_K^k}{a_M^m} \right). \quad (\text{D.2.17})$$

For a PEMFC the global reaction, which is the sum of the two semi-reactions 4.1.1 and 4.1.2, is:



and the variation of the Gibbs free energy of formation related to the activities of this reaction is:

$$\Delta \bar{g}_{a,f} = -R T \ln \left( \frac{a_{\text{H}_2} a_{\text{O}_2}^{\frac{1}{2}}}{a_{\text{H}_2\text{O}}} \right). \quad (\text{D.2.19})$$

Since the electromotive force  $e$  is directly proportional to the variation of the Gibbs free energy of formation, it can be expressed as:

$$e = -\frac{\Delta \bar{g}_f}{2F} = -\frac{\Delta \bar{g}_{o,f}}{2F} - \frac{\Delta \bar{g}_{a,f}}{2F} = E_0 + \Delta e_a \quad (\text{D.2.20})$$

where  $E_0$  is the electromotive force at the STP ( $P_0, T_0$ ), and  $\Delta e_a$  is the variation of the electromotive force due to the activity variation, which is related to the variation of the species' partial pressure:

$$\Delta e_a = -\frac{\Delta \bar{g}_{a,f}}{2F} = \frac{R T}{2F} \ln \left( \frac{a_{\text{H}_2} a_{\text{O}_2}^{\frac{1}{2}}}{a_{\text{H}_2\text{O}}} \right). \quad (\text{D.2.21})$$

The activities for gaseous hydrogen  $a_{\text{H}_2}$ , gaseous oxygen  $a_{\text{O}_2}$  and water  $a_{\text{H}_2\text{O}}$ , assuming that gaseous hydrogen and oxygen behave like ideal gases and that water is only in steam form, are:

$$a_{\text{H}_2} = \frac{p_{\text{H}_2}}{P_0} \quad (\text{D.2.22})$$

$$a_{\text{O}_2} = \frac{p_{\text{O}_2}}{P_0} \quad (\text{D.2.23})$$

$$a_{\text{H}_2\text{O}} = \frac{p_{\text{H}_2\text{O}}}{P_0} \quad (\text{D.2.24})$$

where  $p_{\text{H}_2}$ ,  $p_{\text{O}_2}$  and  $p_{\text{H}_2\text{O}}$  are the partial pressures of hydrogen on the anode side, and oxygen and water steam on the cathode side, and equal:

$$p_{\text{H}_2} = \gamma_{\text{H}_2} p_A \quad (\text{D.2.25})$$

$$p_{\text{O}_2} = \gamma_{\text{O}_2} p_C \quad (\text{D.2.26})$$

$$p_{\text{H}_2\text{O}} = \gamma_{\text{H}_2\text{O}} p_C \quad (\text{D.2.27})$$

where  $p_A$  and  $p_C$  are the anode and cathode gas pressures, and  $\gamma_{\text{H}_2}$ ,  $\gamma_{\text{O}_2}$  and  $\gamma_{\text{H}_2\text{O}}$  are the concentrations of hydrogen, oxygen and water steam.

The variation of the electromotive force can be rewritten as the sum of two factors:

$$\Delta e_a = \frac{R T}{2F} \ln \left( \frac{\gamma_{\text{H}_2} \gamma_{\text{O}_2}^{\frac{1}{2}}}{\gamma_{\text{H}_2\text{O}}} \right) + \frac{R T}{4F} \ln \left( \frac{p_A^2}{p_C P_0} \right) = \Delta e_c + \Delta e_p \quad (\text{D.2.28})$$

where:

$$\Delta e_c = \frac{R T}{2F} \ln \left( \frac{\gamma_{\text{H}_2} \gamma_{\text{O}_2}^{\frac{1}{2}}}{\gamma_{\text{H}_2\text{O}}} \right) \quad (\text{D.2.29})$$

$$\Delta e_p = \frac{R T}{4F} \ln \left( \frac{p_A^2}{p_C P_0} \right) \quad (\text{D.2.30})$$

and where  $\Delta e_c$  and  $\Delta e_p$  are the variations of the electromotive force due to the species concentrations and pressure variations respectively. In the next section,  $\Delta e_c$  will be rewritten as a function of the fuel cell current, and called mass transport or diffusion voltage drop.

Furthermore, since the pressures on the anode and on cathode side have to be equal  $p_A = p_C = p_{op}$  during normal operation in order to avoid membrane damages,  $\Delta e_p$  becomes:

$$\Delta e_p = \frac{R T}{4F} \ln\left(\frac{p_{op}}{P_0}\right). \quad (\text{D.2.31})$$

This shows that the higher the pressure is the higher the electromotive force will be.



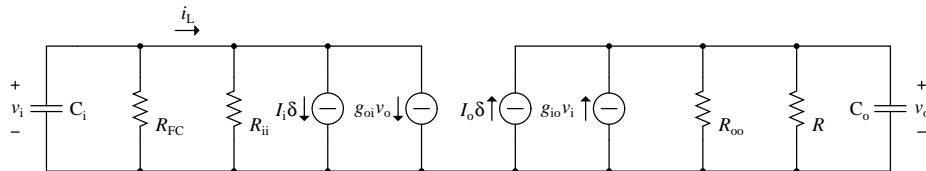
## APPENDIX E

### CONTROL IMPLEMENTATION DETAILS

#### E.1. Current control implementation

The small signal model shown in Figure E.1, valid for a single phase boost converter operating in DCM, can be used for the current controller design.

In the definition of the model,  $1/N_p$  of the total input and output capacitances have been considered. This is an approximation, as the input and phase capacitances can be considered in parallel in multi phase converters only as long as the interconnection stray inductances can be considered negligible. This is true only for frequencies well below the resonance frequency of the phase capacitance and interconnection inductance. However, as the layout of the converter was studied to minimise interconnection inductance, the validity range of the model is expected to be sufficiently wide. The model is based on the linearisation by perturbation of the following non-linear relations, involving the converter input and output electrical variables, measured in the operating point of interest:



**Figure E.1.** Small signal equivalent circuit for the boost converter operating in Discontinuous Conduction Mode (DCM).

$$I_{L,a} = \frac{V_i}{2L f_s} \frac{V_o}{V_o - V_i} \delta^2 \quad (\text{E.1.1})$$

$$I_{d,a} = \frac{1}{2L f_s} \frac{V_i^2}{V_o - V_i} \delta^2 \quad (\text{E.1.2})$$

where  $I_{L,a}$  and  $I_{d,a}$  are the average inductance and diode currents respectively,  $L$  the inductance value,  $f_s$  the switching frequency,  $V_i$  and  $V_o$  the input and output voltage, and  $\delta = \delta_s$  the switch duty cycle.

From Equations E.1.1 and E.1.2, the following small signal gains can be derived:

$$I_i = \frac{\partial I_{L,a}}{\partial \delta} = \frac{\delta}{L f_s} \frac{V_i V_o}{V_o - V_i} \quad (\text{E.1.3})$$

$$g_{ii} = \frac{1}{R_{ii}} = \frac{\partial i_L}{\partial v_i} = \frac{\delta^2}{2L f_s} \frac{V_o^2}{(V_o - V_i)^2} \quad (\text{E.1.4})$$

$$g_{oi} = \frac{\partial i_L}{\partial v_o} = - \frac{\delta^2}{2L f_s} \frac{V_i^2}{(V_o - V_i)^2} \quad (\text{E.1.5})$$

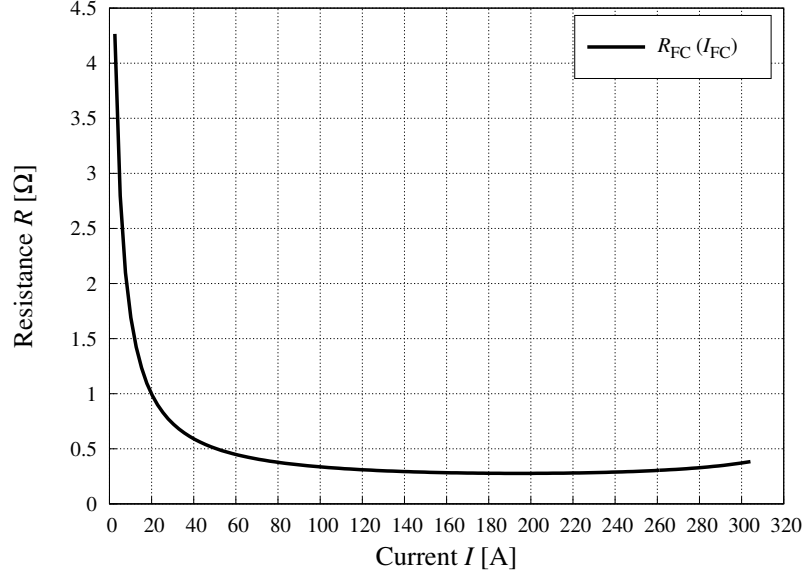
$$I_o = \frac{\partial i_d}{\partial \delta} = \frac{\delta}{L f_s} \frac{V_i^2}{V_o - V_i} \quad (\text{E.1.6})$$

$$g_{io} = \frac{\partial i_d}{\partial v_i} = \frac{\delta^2}{2L f_s} \frac{V_i(2V_o - V_i)}{(V_o - V_i)^2} \quad (\text{E.1.7})$$

$$g_{oo} = \frac{1}{R_{oo}} = \frac{\partial i_d}{\partial v_o} = - \frac{\delta^2}{2L f_s} \frac{V_i^2}{(V_o - V_i)^2} \quad (\text{E.1.8})$$

In the model of Figure E.1, the input generator has been represented by its small signal output resistance  $R_{FC}$ , obtained as the local slope of the fuel cell  $V - I$  characteristic in the operating point of interest. The variation of  $R_{FC}$  function of the fuel cell current  $I_{FC}$  is shown in Figure E.2.

The last resistance of the model ( $R$ ) is the representation of the electrical load applied to the power supply. Considering the model of Figure E.1, it is possible to derive the transfer function required for the controller design. It is the transfer function between the small signal variations of the duty-cycle  $\delta$  and those of the average input current  $I_{L,a}$ . This is defined by:



**Figure E.2.** Fuel cell equivalent resistance  $R_{FC}$  versus fuel cell current  $I_{FC}$ .

$$G_{ID}(s) = \frac{I_{L,a}(s)}{\delta(s)} = \frac{A_N + s B_N + s^2 C_N}{A_D + s B_D + s^2 C_D} \quad (\text{E.1.9})$$

where:

$$A_N = (1 - g_{ii} R_{ii})(I_i + I_o g_{oi} R_o) \quad (\text{E.1.10})$$

$$B_N = I_i (R_{ii} C_i + R_o C_o) + R_{ii} R_o (C_i g_{oi} I_o - C_o g_{ii} I_i) \quad (\text{E.1.11})$$

$$C_N = I_i R_{ii} R_o C_i C_o \quad (\text{E.1.12})$$

$$A_D = 1 + g_{oi} g_{io} R_{ii} R_o \quad (\text{E.1.13})$$

$$B_D = R_{ii} C_i + R_o C_o \quad (\text{E.1.14})$$

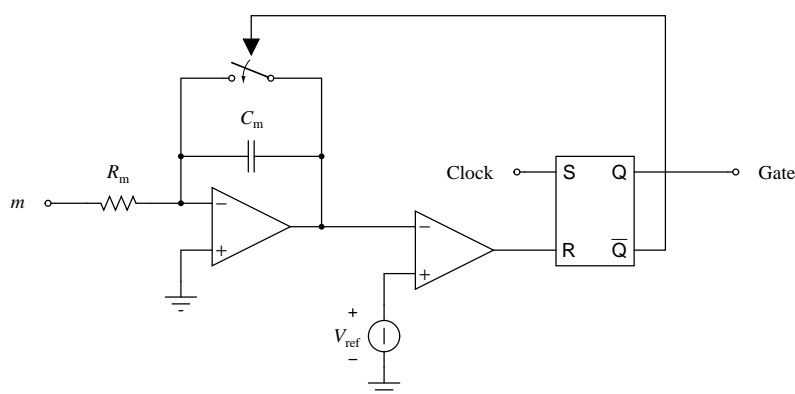
$$C_D = R_{ii} R_o C_i C_o \quad (\text{E.1.15})$$

and where  $R_{ii}$  and  $R_o$  represent the equivalent resistances defined as:

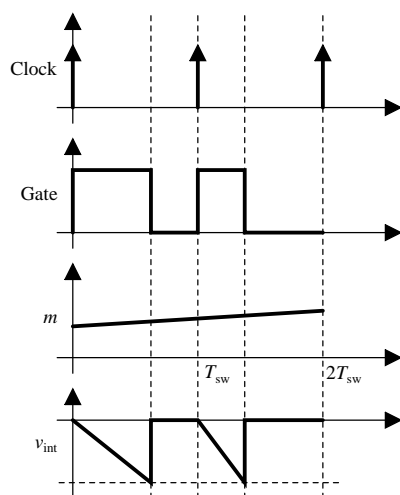
$$R_i = R_{FC} \parallel R_{ii} \quad (\text{E.1.16})$$

$$R_o = R_{oo} \parallel R. \quad (\text{E.1.17})$$

Considering the constant on-time modulator implementation, it is possible to derive the small signal transfer function between the current controller output  $m$  and the duty-cycle  $\delta$ . A schematic representation of the modulator is shown in Figure E.3, while Figure E.4 shows the fundamental signals involved in the modulator operation.



**Figure E.3.** Simplified schematic of the constant on-time modulator. Acronym: input signal  $m$ , reference voltage  $V_{\text{ref}}$ .



**Figure E.4.** Constant on-time modulator basic operation signals versus time  $t$ . Acronym: input signal  $m$ , integrator output voltage  $v_{\text{int}}$ , switching period  $T_s$ .

At any clock pulse, the signal  $m$  is integrated from zero with a given time constant. At the same time, the gate signal for the power switch is set high.



The integrator output is sent to a comparator, which compares it with a constant voltage reference. After a time delay that is linked to  $m$  by the following equations:

$$T_{\text{on}} = \frac{R_m C_m V_{\text{ref}}}{m} \quad (\text{E.1.18})$$

$$\delta = \frac{R_m C_m V_{\text{ref}} f_s}{m} \quad (\text{E.1.19})$$

the integrator output reaches the reference voltage. Therefore, the comparator's output changes state, forcing the flip-flop to change its state. The gate pulse is then terminated. At the same time, the integrator is reset so that a similar cycle can start at the following clock pulse.

Perturbing Equation E.1.19 with respect to  $m$ , we can derive the following small signal gain:

$$\frac{\partial \delta}{\partial m} = - \frac{R_m C_m V_{\text{ref}} f_s}{M^2} = - \frac{\delta}{M} \quad (\text{E.1.20})$$

that relates the current controller output signal variations to the duty-cycle ones.  $M$  represents the steady state value of  $m$  in the operating point of interest. It should be noted that the analysis above refers to a fixed frequency modulator operation. In case of a variable switching frequency, the analysis is generally no longer applicable. However, if the frequency variation is relatively slow, the same considerations can be made, assuming a quasi-stationary operation for the modulator.

Moreover, it is common practice to increase the modulator small signal model including some form of delay representation, in order to take into account its non-instantaneous dynamic behaviour. If a sudden variation of  $m$  takes place immediately after the gate pulse ends, it will have no effect on the modulator operation until the next clock pulse. Therefore, a certain delay is inherent in the modulator operation, whose exact modelling is not actually required.

As a first order approximation, the transfer function between  $m$  and  $\delta$  can be expressed by:

$$G_M(s) = - \frac{R_m C_m V_{\text{ref}} f_s}{M^2} \frac{1 - s \frac{T_s}{4}}{1 + s \frac{T_s}{4}} \quad (\text{E.1.21})$$

where a first order Padé approximation of a delay equal to half of the switching period has been considered.

Summing up the results above, the compensator for the current loop can be designed. The transfer function to compensate is the product of Equations E.1.9 and E.1.21 and will be designated as  $G_{TC}(s)$ . The design of the PI compensator can be done according to the following relations:

$$\tau_{PI} = \frac{k_P}{k_I} = \frac{1}{\omega_{CR}} \tan \left[ m_\phi - \frac{\pi}{2} - \arg(G_{TC}(j \omega_{CR})) \right] \quad (E.1.22)$$

$$k_I = \frac{\omega_{CR}}{\left| G_{TC}(j \omega_{CR}) \right| \sqrt{1 + (\omega_{CR} \tau_{PI})^2}} \quad (E.1.23)$$

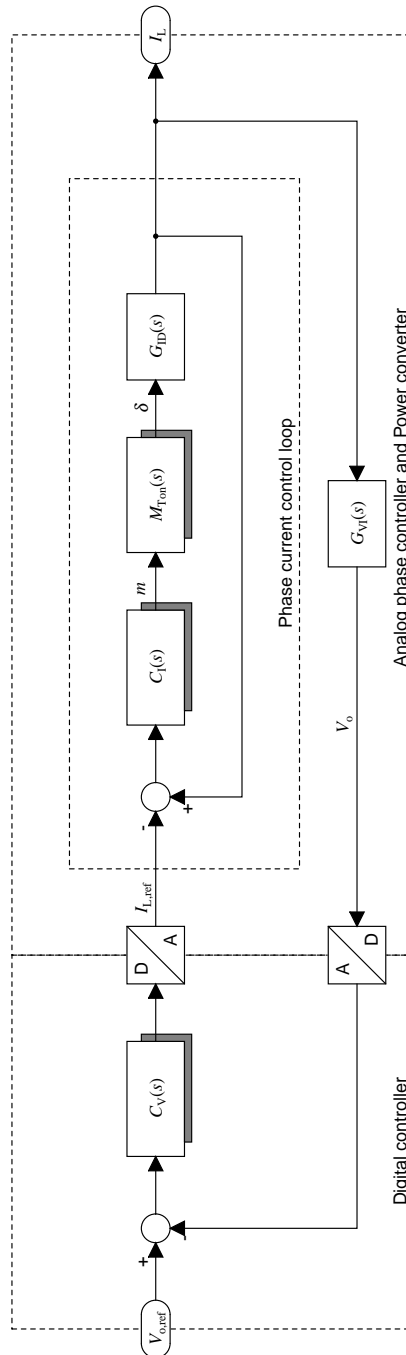
$$k_P = k_I \tau_{PI} \quad (E.1.24)$$

where  $m_\phi$  and  $\omega_{CR}$  represent the desired phase margin and cross-over frequency respectively. It is worth noting that in the present analysis, transducers have not been considered. Of course, these need to be accounted for in the practical controller design.

## E.2. Output voltage control implementation

Once the current control loop has been implemented, the voltage loop can be analysed. In this implementation, the output voltage controller has been implemented digitally, using a Digital to Analog (D/A) converter to generate the current reference. The general control organisation for any converter phase is the one schematically represented in Figure E.5. This is the case of a mixed signal control implementation, in which a purely analog current control loop is controlled by a digital voltage regulator again of PI type. The fully digital control option has been considered and discarded because of the need to operate with a relatively high and variable switching frequency. Furthermore, implementing six independent current loops would lead to a considerable control system complexity and would require high performance digital hardware. In this way a much simpler and more cost effective solution has been realised.

A continuous time equivalent of the digital system, that has been obtained by using the zero order hold approximation, has been considered in order to design the output voltage compensator. In the continuous time domain, the transfer function which must be compensated is the cascade connection of the



**Figure E.5.** Overview of the control organisation. The current reference is provided by an outer digital voltage controller through a D/A converter. The phase current controller is made up of an analog PI compensator and a constant on-time modulator.

one linking the converter input current  $I_{L,a}$  to the output voltage  $V_o$ , designated as  $G_{VI}(s)$  in Figure E.5, and the closed loop transfer function between the voltage regulator output  $I_{L,ref}$  and  $i_L$ . The latter can be derived from the previously presented current controller design and is indicated as  $W_I(s)$  in what follows. The former can be derived by referring to the small signal equivalent circuit represented in Figure E.6, in which the inductor current  $i_L$  is treated as an exogenous input, as it is controlled by the inner current loop.

As in the case of the current controller design, the six converter phases are treated as if they were independent, which is only approximately correct from the voltage controller standpoint. Indeed, one of the advantages of the interleaving solution is that the current controller response to perturbations is distributed across the modulation period. This may lead to shorter response delay with respect to the solution with several converters connecting in parallel. This means that the equivalent bandwidth of the interleaved current controlled boost modules is somewhat larger than that of a single phase. This effect is not taken into account in the model, therefore leading to a slightly conservative compensator design.

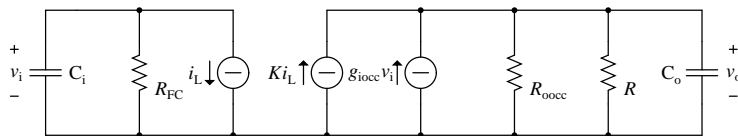
The controlled current source gains of the model shown in Figure E.6 have been calculated, as in the previous case, by perturbing the large signal non-linear relation of the current controlled boost converter:

$$I_{d,a} = I_{L,a} \frac{V_i}{V_o}. \quad (\text{E.2.1})$$

This leads to:

$$K = \frac{\partial I_{d,a}}{\partial I_{L,a}} = \frac{V_i}{V_o} \quad (\text{E.2.2})$$

$$g_{io,cc} = \frac{\partial I_{d,a}}{\partial V_i} = \frac{I_{L,a}}{V_o} \quad (\text{E.2.3})$$



**Figure E.6.** Small signal equivalent circuit for the current controller boost converter.

$$g_{oo,cc} = -\frac{1}{R_{oo,cc}} = \frac{\partial I_{d,a}}{\partial V_o} = -\frac{I_{L,a} V_i}{V_o^2} \quad (\text{E.2.4})$$

Basing on the above definitions and on the circuit of Figure E.6, the  $G_{VI}(s)$  transfer function can be derived:

$$G_{VI}(s) = \frac{V_o(s)}{I_{L,a}(s)} = \frac{R_{o,cc} (K (1 + s R_{FC} C_i) - g_{io,cc} R_{FC})}{(1 + s R_{o,cc} C_o)(1 + s R_{FC} C_i)}. \quad (\text{E.2.5})$$

The transfer function which has to be compensated can now be derived by multiplying Equation E.2.5 and the closed loop transfer function of the current controller  $W_I(s)$  that links the control signal  $I_{L,ref}$  and the converter inductor current. The continuous time voltage PI compensator can be designed by applying the same procedure outlined for the current controller case, basing on the desired phase margin and crossover frequency specifications. The effect of the implicit holder delay needs to be properly taken into account in specifying the phase margin. The digital PI gains were obtained by discretisation of the continuous time PI; different methods were considered, namely the Euler and Tustin ones [131].

### E.3. Conclusion

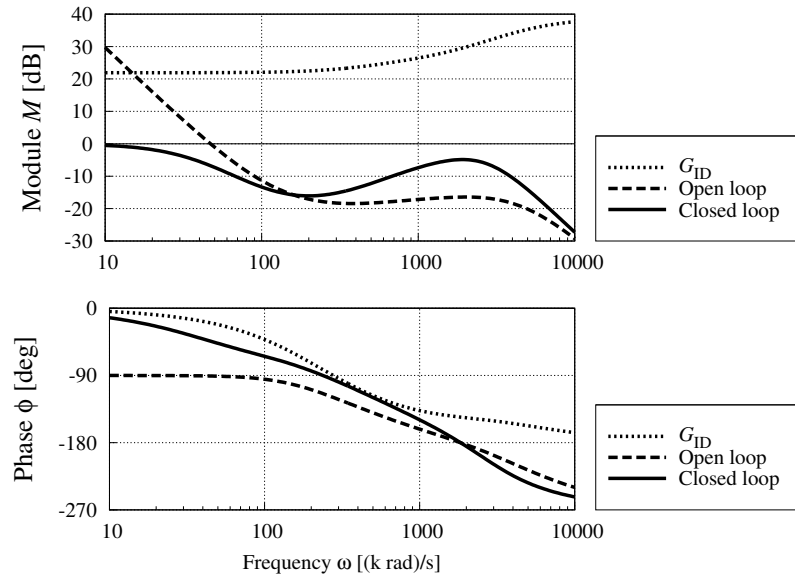
The design procedure explained above was successfully applied with respect to the nominal operating point of the converter: an input voltage of 28 V and an input current of 220 A, corresponding to the nominal load condition, nominal output voltage of 48 V and target efficiency of 0.9. The controller parameters for the analog current loop are:

- current transducer and DAC gain:  $0.02 \text{ } \frac{\text{A}}{\text{V}}$ ;
- target crossover frequency: 7 500 Hz;
- target phase margin:  $90^\circ$ ;
- proportional gain:  $k_{P,i} = 0.117 \text{ } 4$ ;
- integral gain:  $k_{I,i} = 14.721 \cdot 10^3 \text{ } \frac{\text{rad}}{\%}$ .

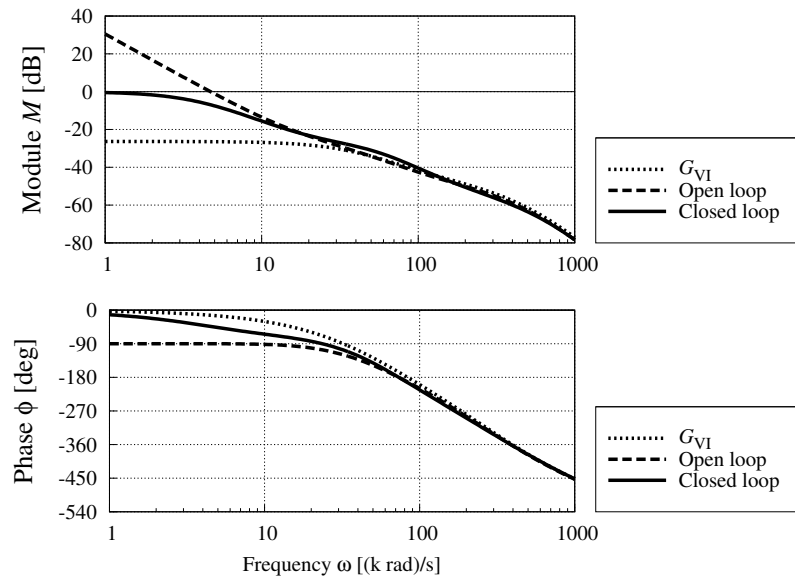
The controller parameters for the digital voltage control loop, in which a 20 kHz sampling frequency was considered, are:

- voltage transducer and DAC gain:  $0.5 \text{ V/V}$ ;
- target crossover frequency: 750 Hz;
- target phase margin:  $90^\circ$ ;
- proportional gain:  $k_{P,v} = 0.9357$ ;
- integral gain:  $k_{I,v} = 17.131 \cdot 10^3 \text{ rad/s}$ ;
- Euler proportional gain:  $k_{P,v}^E = 0.9357$ ;
- Euler integral gain:  $k_{I,v}^E = 0.8566 \text{ rad/s}$ ;
- Tustin proportional gain:  $k_{P,v}^T = 0.5074$ ;
- Tustin integral gain:  $k_{I,v}^T = 0.8566 \text{ rad/s}$ .

Figures E.7 and E.8 concludes this presentation on the control design by showing the open and closed loop gains of the current and voltage regulators.



**Figure E.7.** Design of the current controller. Bode diagrams of the converter transfer function  $G_{ID}(s)$ , open loop current gain, closed loop current gain.



**Figure E.8.** Design of the voltage controller. Bode diagrams of the converter transfer function  $G_{VI}(s)$ , open loop voltage gain, closed loop voltage gain.





## APPENDIX F

### AREA SPECIFIC AND DENSITY VARIABLES

Quantities are often referred to the fuel cell surface, in the study of fuel cells. Some of them already exist in the literature, while new names have been coined for others.

#### F.1. Area specific resistance

It is indicated with  $r$  and defined as:

$$v = r j \quad (\text{F.1.1})$$

where  $v$  is a voltage and  $j$  a current density. Its unit measure in the SI is:

$$[r] = \Omega \cdot \text{m}^2. \quad (\text{F.1.2})$$

#### F.2. Conductance density

It is indicated with  $s$  and defined as:

$$j = s v \quad (\text{F.2.1})$$

where  $v$  is a voltage and  $j$  a current density. Its unit measure in the SI is:

$$[s] = \frac{\text{S}}{\text{m}^2}. \quad (\text{F.2.2})$$

**F.3. Capacitance density**

It is indicated with  $c$  and defined as:

$$j = c \frac{dv}{dt} \quad (\text{F.3.1})$$

where  $v$  is a voltage and  $j$  a current density. Its unit measure in the SI is:

$$[c] = \frac{\text{F}}{\text{m}^2}. \quad (\text{F.3.2})$$

**F.4. Area specific inductance**

It is indicated with  $l$  and defined as:

$$v = l \frac{dj}{dt} \quad (\text{F.4.1})$$

where  $v$  is a voltage and  $j$  a current density. Its unit measure in the SI is:

$$[l] = \text{H} \cdot \text{m}^2. \quad (\text{F.4.2})$$

## APPENDIX G

### STEP AND LOG FUNCTIONS WITH CONTINUOUS DERIVATIVE

The functions expressed by Eq. 4.1.52 and 4.1.53 are  $C^0(\mathbf{D})$  functions — continuous functions with non-continuous derivatives in their domain  $\mathbf{D}$ . This could slow down the numerical computing.<sup>1</sup>

A good approximation of these functions to  $C^\infty(\mathbf{D})$  functions using only  $C^\infty(\mathbf{D})$  functions — continuous functions with their derivatives continuous in  $\mathbf{D}$ , where  $\mathbf{D}$  can be  $\mathbf{R}$  or  $\mathbf{R}$  minus a point — will be presented.

The previous functions can be written as:

$$f(x) = F_1(x) \cdot f_1(x) + F_2(x) \cdot f_2(x) + \dots + F_n(x) \cdot f_n(x) \quad (\text{G.1})$$

where  $F_1 \dots F_n$  are unitary step functions and  $f_1 \dots f_n$  are  $C^\infty(\mathbf{R})$  functions.

These unitary step functions have been approximated with  $C^\infty(\mathbf{R})$  functions of the type:

$$F_i(x) = \frac{1}{\pi} \arctan(k(x - x_0)) + \frac{1}{2} \quad (\text{G.2})$$

where  $k$  is sufficiently high. The plot of this function for different values of  $k$  is drawn in Figure G.1.

*Activation loss equation.* — Taking into account the previous considerations, the equation for the activation loss block becomes:

---

<sup>1</sup>The following notation has been used:  $\mathbf{D}$  indicates the domain of a function, while  $\mathbf{R}$  indicates the set of real numbers.

$$v_a(j_a) = \left[ A \ln \left( \frac{j_a}{J_0} \right) \right] \left[ \frac{1}{\pi} \arctan k (j_a - J_0) + \frac{1}{2} \right]. \quad (\text{G.3})$$

*Diffusion loss equation.* — Taking into account the previous considerations, the equation for the diffusion loss block becomes:

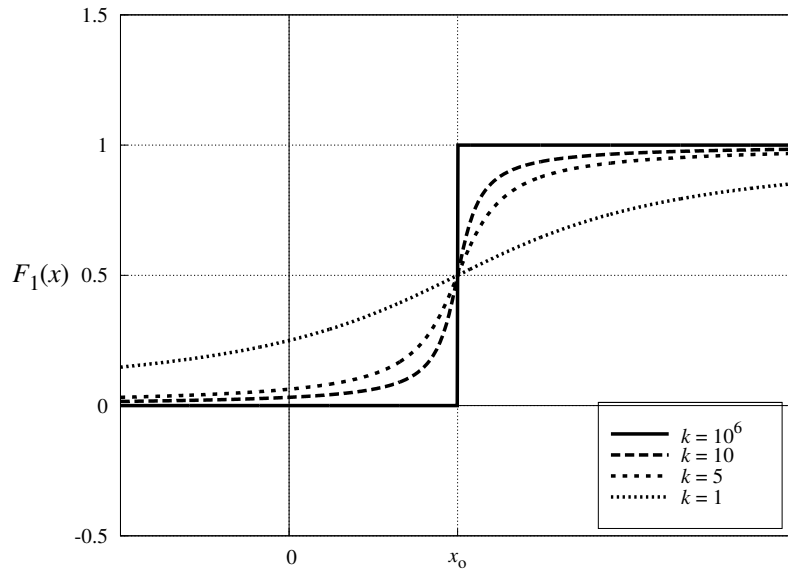
$$j_d(v_d) = J_1 \left[ 1 - e^{-\frac{v_d}{B}} \right] \left[ \frac{1}{\pi} \arctan k v_d + \frac{1}{2} \right]. \quad (\text{G.4})$$

*Extension to square waves.* — The former approach can also be applied to square waves, as in Figure G.2, where:

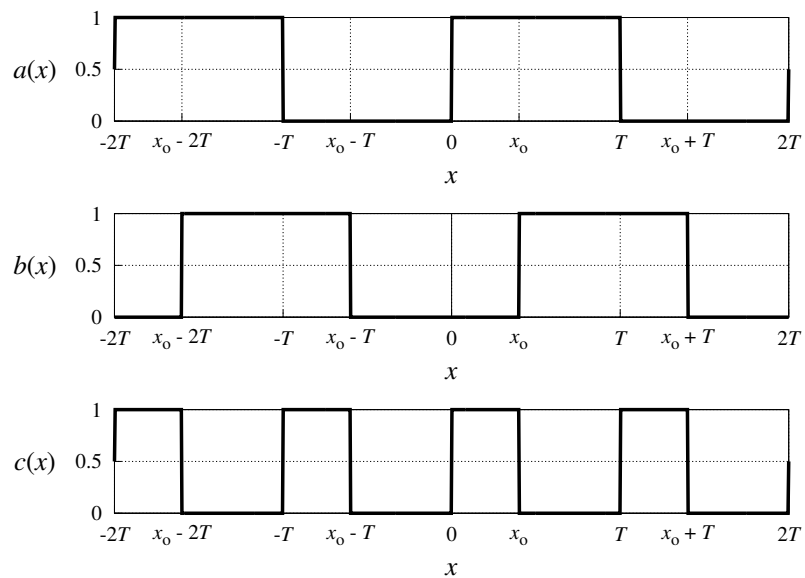
$$a(x) = \frac{1}{\pi} \arctan k \sin 2\pi x + \frac{1}{2} \quad (\text{G.5})$$

$$b(x) = \frac{1}{\pi} \arctan k \sin(2\pi x - x_0) + \frac{1}{2} \quad (\text{G.6})$$

$$c(x) = \left| a(x) - b(x) \right| = \frac{1}{\pi} \left| \arctan k \sin 2\pi x - \arctan k \sin(2\pi x - x_0) \right|. \quad (\text{G.7})$$



**Figure G.1.** Approximation of a step function using continuous functions, with different values of the parameter  $k$ .



**Figure G.2.** Approximation of square waves using continuous functions.



## APPENDIX H

### CONVERTER SIZING DETAILS

Some details about the converter's input inductor design will be presented in this appendix. The inductor core is an ETD 44/22/15 with 3C90 material from Ferroxcube [132, 133].

#### H.1. Input inductor sizing

Ungapped permeability:  $A_L = 3\,800 \cdot 10^{-9}$  H

Permeability tolerance: 0.25

Relative material permeability:  $\mu_e = 1\,800$

Core cross section area:  $A_c = 173 \cdot 10^{-6}$  H<sup>2</sup>

Central leg diameter:  $D_c = 15.2 \cdot 10^{-3}$  m

Core volume:  $V_e = 17\,800 \cdot 10^{-9}$  m<sup>3</sup>

Magnetic path average length:  $l_e = 101 \cdot 10^{-3}$  m

Winding average length:  $l_{w,a} = 77 \cdot 10^{-3}$  m

Rectangular window area:  $A_w = 216 \cdot 10^{-6}$  m<sup>2</sup>

Window length:  $l_w = 29.5 \cdot 10^{-3}$  m

Window height:  $h_w = 8.4 \cdot 10^{-3}$  m

Conductor width:  $w_{Cu} = 0.025$  m

Double of the skin depth:  $2D_p = 622.4 \mu\text{m}$

Conductor thickness:  $t_{\text{Cu}} = 0.5 \text{ mm}$

Conductor cross section:  $S_{\text{Cu}} = w_{\text{Cu}} t_{\text{Cu}} = 12.5 \text{ mm}^2$

Number of paralleled conductors:  $N_c = 1$

Winding equivalent cross section:  $S_w = N_c S_{\text{Cu}} = 12.5 \text{ mm}^2$

Conductor rms current density:  $J_{\text{L,rms}} = \frac{I_{\text{L,rms}}}{S_w} = 3.44 \text{ A/mm}^2$

Winding equivalent thickness:  $t_w = N_c t_{\text{Cu}} = 500 \mu\text{m}$

Isolation layer thickness:  $t_i = 500 \mu\text{m}$

Maximum number of windings:  $N_{t,M} = \text{floor}\left(\frac{h_w - t_i}{t_w + t_i}\right) = 7$

Winding DC resistance:  $R_{w,DC} = \rho_{\text{Cu,T}} \frac{l_{w,a}}{S_w} = 142 \text{ m}\Omega$

Winding power losses:  $P_{w,l} = R_{w,DC} I_{\text{L,rms}}^2 = 0.262 \text{ W}$

Maximum allowed magnetic induction:  $B_M = 250 \text{ mT}$

Per winding inductance:  $A_L(N_t) = \frac{B_M A_e}{I_{\text{L,pk}} N_t}$ ;  $A_L(1) = 0.57 \mu\text{H}$

Maximum achievable inductance:  $L_M(N_t) = A_L(N_t) N_t^2$

Inductance values obtainable for different numbers of windings, and induction level equal to  $B_M$ :

$$L_M(2) = 1.131 \mu\text{H}$$

$$L_M(3) = 1.697 \mu\text{H}$$

$$L_M(4) = 2.263 \mu\text{H}$$

$$L_M(5) = 2.829 \mu\text{H}$$

$$L_M(N_{t,M}) = 3.96 \mu\text{H}$$

Number of windings required:  $N_t = 4$

Air gap design on the central leg:

$$c_1(N_s) = \frac{2L_n}{\pi\mu_0 N_s^2}$$



$$t_g(N_s) = (c_1(N_s) - D_c) - \sqrt{(c_1(N_s) - D_c)^2 - D_c^2}$$

$$t_g(N_t) = 1.931 \text{ mm}$$

Inductance verification:

$$\text{Air gap reluctance: } \mathfrak{R}_g(N_t) = \frac{t_g(N_t)}{\pi \mu_0 \frac{(t_g(N_t) + D_c)^2}{4}}$$

$$\text{Achieved inductance: } L_a(N_t) = \frac{N_t^2}{\mathfrak{R}_g(N_t)}; L_a(N_t) = 2.4 \text{ } \mu\text{H}$$

Maximum induction verification:

$$B_{M,l} = L_a(N_t) \frac{I_{L,pk}}{N_t A_e} = 0.265 \text{ T}$$

## H.2. Core power density interpolation function

An interpolating function has been created in order to automatically calculate the core power losses of the input inductor. The core power losses can then be expressed as a function of the fuel cell current  $I_{FC}$  and of the output voltage  $V_o$ .

$$X(I_{FC}, V_o) = \log\left(\frac{B_{AC}(I_{FC}, V_o)}{\text{mT}}\right)$$

$$X(I_{FC,n}, V_{o,n}) = 2.122$$

$$F_s(I_{FC}, V_o) = \frac{f_s(I_{FC}, V_o)}{25} \text{ kHz}$$

$$F_s(I_{FC,n}, V_{o,n}) = 2.41$$

$$Y(I_{FC}, V_o) = 2.73 (X(I_{FC}, V_o) - 2) + 1.33 (F_s(I_{FC}, V_o) - 0.6)^{0.29}$$

$$Y(I_{FC,n}, V_{o,n}) = 1.914$$

$$P_V(I_{FC}, V_o) = 10^{Y(I_{FC}, V_o)} \text{ kW/m}^3$$

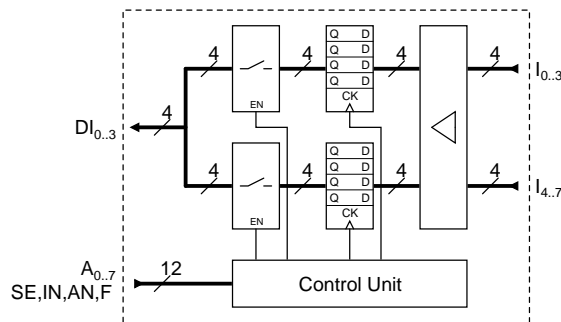
$$P_V(I_{FC,n}, V_{o,n}) = 82.03 \cdot 10^3 \text{ kW/m}^3$$

## APPENDIX I

### GENERIC IMPLEMENTATION OF THE INPUT/OUTPUT INTERFACE

#### I.1. Digital input interface

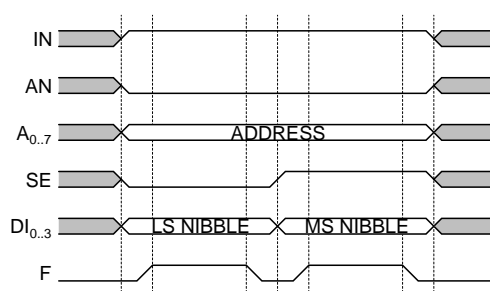
The generic implementation of the digital input interface is shown in Figure I.1. Each interface allows to acquire 8 digital inputs  $l_0 \dots l_7$ , to buffer them and to split them into the most and less significant nibbles, before sending them to the digital input bus  $Dl_0 \dots Dl_3$ . When data is not being sent, the outputs need to be kept in the high impedance state.



**Figure I.1.** Diagram of the generic digital input interface. Acronyms: digital inputs ( $l_0 \dots l_7$ ), bus input lines ( $Dl_0 \dots Dl_3$ ), address lines ( $A_0 \dots A_7$ ), control lines (SE, IN, AN, F), enable signal (EN), clock signal (CK).

The control unit receives and interprets the address and the control lines.

Their meaning is shown in Figure I.2: IN must be kept high to select an input interface, AN must be kept low to select a digital interface,  $A_0 \dots A_7$  must provide a valid address, SE must be low at first and high later on to indicate the transmission of the less and most significant nibbles respectively.  $D_0 \dots D_3$  are the two nibbles being sent, and F must be raised twice, the first time to ask for the transmission of the first nibble, and the second time for the second one.



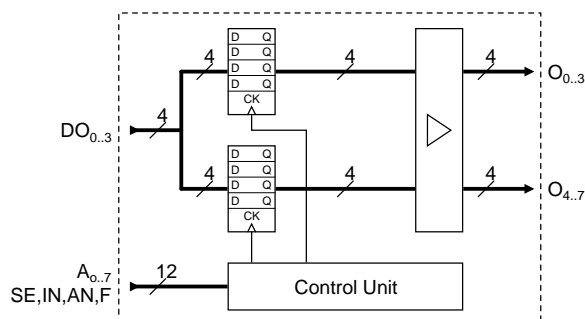
**Figure I.2.** Time diagram of the transmission towards a digital input interface. Acronyms: most/less significant (MS/LS), bus input lines ( $D_0 \dots D_3$ ), address lines ( $A_0 \dots A_7$ ), MS/LS selection line (SE), input selection line (IN), analog selection line (AN), fire line (F).

The total number of digital inputs is 2048, since up to 256 interfaces can be addressed, with 8 digital inputs per interface.

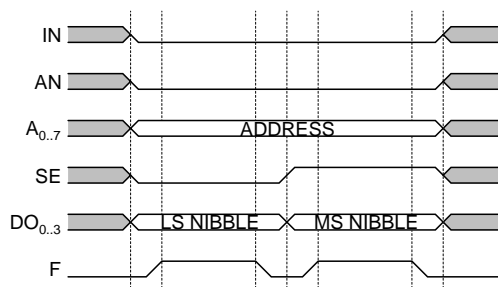
## I.2. Digital output interface

The generic implementation of the digital output interface is shown in Figure I.3. Each interface allows to set 8 digital output  $O_0 \dots O_7$ , to buffer them and to rebuild them from the most and less significant nibbles, coming from the digital output bus  $DO_0 \dots DO_3$ .

The control unit receives and interprets the address and the control lines. Their meaning is shown in Figure I.4: IN must be kept low to select an output interface, AN must be kept low to select a digital interface,  $A_0 \dots A_7$  must provide a valid address, SE must be low first and high later on to indicate the transmission of the less significant and most significant nibbles respectively.  $D_0 \dots D_3$  are the two nibbles being received, and F must be raised twice, the first time to inform about the transmission of the first nibble, and the second time for the second one.



**Figure I.3.** Diagram of the generic digital output interface. Acronyms: digital outputs ( $O_0 \dots O_7$ ), bus output lines ( $DO_0 \dots DO_3$ ), address lines ( $A_0 \dots A_7$ ), control lines (SE, IN, AN, F), clock signal (CK).



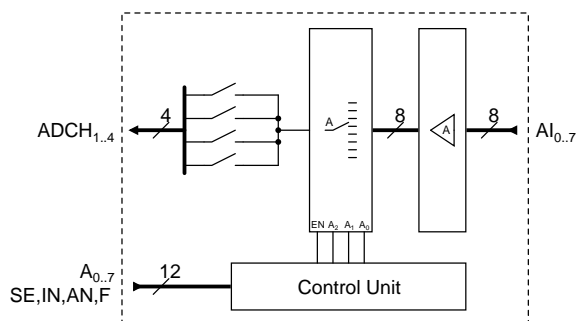
**Figure I.4.** Time diagram of the transmission towards a digital output interface. Acronyms: most/less significant (MS/LS), bus output lines ( $DO_0 \dots DO_3$ ), address lines ( $A_0 \dots A_7$ ), MS/LS selection line (SE), input selection line (IN), analog selection line (AN), fire line (F).

The total number of digital outputs is 2048, since up to 256 interfaces can be addressed, with 8 digital outputs per interface.

### I.3. Analog input interface

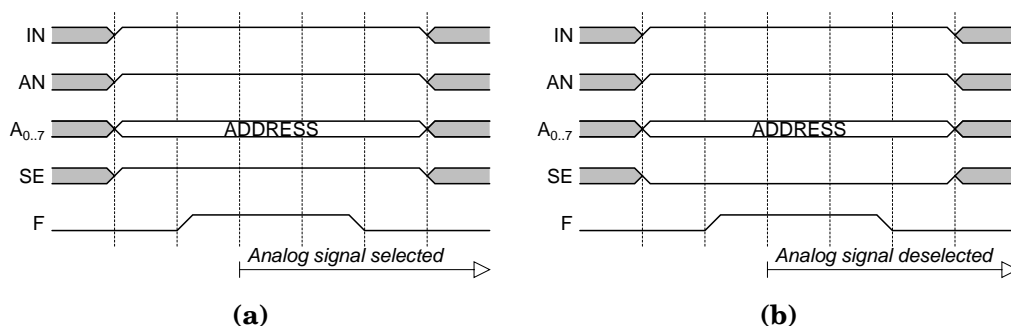
The generic implementation of the analog input interface is shown in Figure I.5. Each interface allows to multiplex 8 analog inputs  $A_0 \dots A_7$  and to send the selected one to one of the four analog channels  $ADCH_1 \dots ADCH_4$ . When data is not being sent, the outputs need to be kept in the high impedance state.

The control unit receives and interprets the address and the control lines. Their meaning is shown in Figures I.6 (a) and (b): IN must be kept high to



**Figure I.5.** Diagram of the generic analog input interface. Acronyms: analog inputs ( $A_0 \dots A_7$ ), analog input channels ( $ADCH_1 \dots ADCH_4$ ), address lines ( $A_0 \dots A_7$ ), control lines (SE, IN, AN, F), clock signal (CK).

select an input interface, AN must be kept high to select an analog interface,  $A_0 \dots A_7$  must provide a valid address, SE must be high to connect — and low to disconnect — the addressed analog channel to the hardware programmed input channel. F must be raised to actually execute the command.

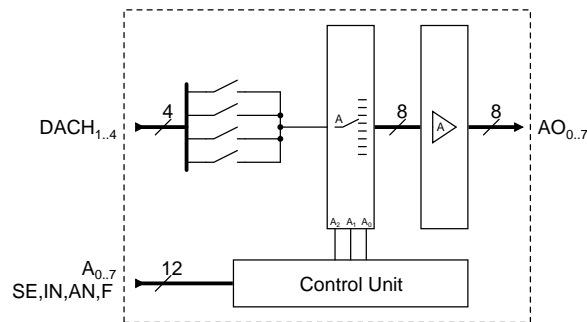


**Figure I.6.** Time diagram of the selection (a) and deselection (b) of an analog input channel. Acronyms: address lines ( $A_0 \dots A_7$ ), MS/LS selection line (SE), input selection line (IN), analog selection line (AN), fire line (F).

The total number of analog inputs is 1024, since up to 256 channels can be multiplexed per dSPACE analog input, with 4 dSPACE analog inputs.

#### I.4. Analog output interface

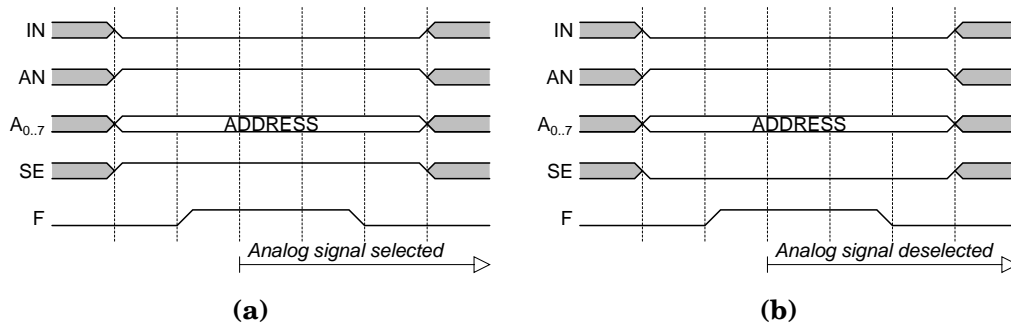
The generic implementation of the analog output interface is shown in Figure I.7. Each interface allows to demultiplex 8 analog outputs  $AO_0 \dots AO_7$  and to send the selected one to one of the four analog channels  $DACH_1 \dots DACH_4$ .



**Figure I.7.** Diagram of the generic analog output interface. Acronyms: analog outputs ( $AO_0 \dots AO_7$ ), analog output channels ( $DACH_1 \dots DACH_4$ ), address lines ( $A_0 \dots A_7$ ), control lines (SE, IN, AN, F), clock signal (CK).

The control unit receives and interprets the address and the control lines. Their meaning is shown in Figures I.8 (a) and (b): IN must be kept low to select an output interface, AN must be kept high to select an analog interface,  $A_0 \dots A_7$  must provide a valid address, SE must be high to connect — and low to disconnect — the addressed analog channel to the hardware programmed output channel. F must be raised to actually execute the command.

The total number of analog outputs is 1024, since up to 256 channels can be multiplexed per dSPACE analog output, with 4 dSPACE analog outputs.



**Figure I.8.** Time diagram of the selection (a) and deselection (b) of an analog output channel. Acronyms: address lines ( $A_0 \dots A_7$ ), MS/LS selection line (SE), input selection line (IN), analog selection line (AN), fire line (F).



## APPENDIX J

### THE FUEL CELL POWER ELECTRONICS LABORATORY

A new laboratory has been built and organised to work with fuel cell stack and power electronics. An office container especially conceived to operate fuel cells has been designed: it has no windows, but several openings to ensure good ventilation. Useful information on the practical realisation of hydrogen and oxygen systems can be found in [134, 135].



**Figure J.1.** The container in the courtyard of the Department of Information Engineering (DEI) of the University of Padova. Its surface is equal to 9.6 m<sup>2</sup>. It is connected to the department electrical grid ( $P_{e,M} = 20$  kW) and to the department Local Area Network (LAN).



**Figure J.2.** The table on the right is for the computerised controller system. The table on the left is for the fuel cell stack being tested.



**Figure J.3.** The table on the right is for the fuel cell stack under test. The table on the left is for the power electronics converter connected to the fuel cell stack.



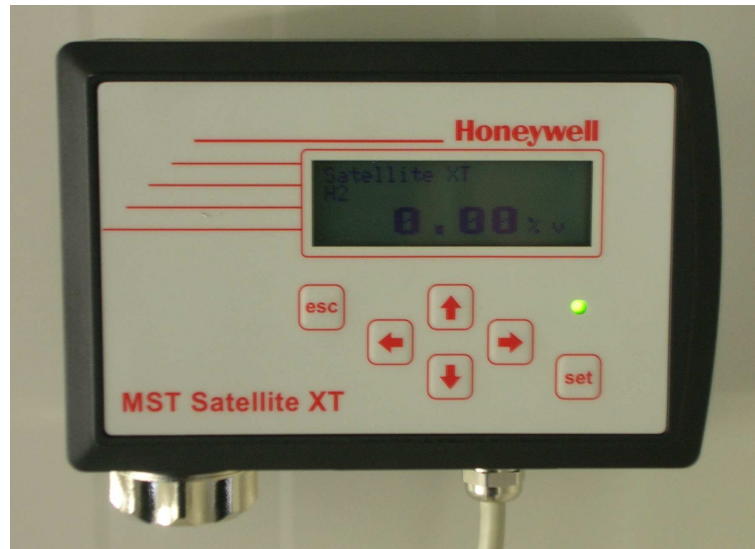
**Figure J.4.** The table on the left is for the power electronics converter connected to the fuel cell stack. The table on the right is for the fuel cell stack begin tested.



**Figure J.5.** The gas safety system. On the left are the hydrogen and oxygen concentration measurement units. On the right is the panel with all the safety controls (green lights). The gas solenoid valves (red lights) are open only if all the safety controls are passed.



**Figure J.6.** Main electric panel.



**Figure J.7.** Hydrogen concentration sensor.



**Figure J.8.** Hydrogen and oxygen concentration measurement units.



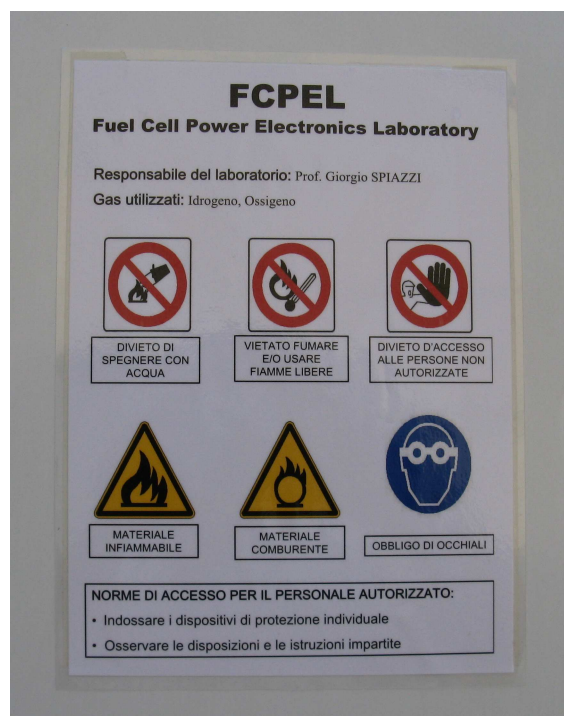
**Figure J.9.** Fuel cell stack and fittings before installation.



**Figure J.10.** High and medium pressure hydrogen fittings.



**Figure J.11.** Oxygen and hydrogen cylinder cabinets. The cylinder in use must have the yellow label “*Bombola in uso*” (“Cylinder in use”). The new cylinder must have the yellow label “*Bombola carica*” (“Full cylinder”). Empty cylinders must have the red label “*Bombola scarica*” (“Empty cylinder”).



**Figure J.12.** Safety signs inside and on the door of the laboratory.





## APPENDIX K

### RESULT DETAILS

Some details about experimental and simulation results are presented in this appendix.

#### **K.1. Fuel cell stack measurements**

Table K.1 and Figure K.1 show the first static measurements carried out on a 325 cm<sup>2</sup> 50 element stack. The voltage response to a current step for the fuel cell stack being tested is shown in Figure K.2.

#### **K.2. Fuel cell simulations**

The simulation results obtained by stimulating the fuel cell model with a sinusoidal current generator with different frequencies are shown in Figure K.3.

#### **K.3. Power converter measurements**

The first measurements about the power converter, with a constant voltage power supply, are represented by the plots shown in Chapter 6 and in Figures K.4 and K.5. The ripple amplitudes and frequencies are summed up in Table K.2.

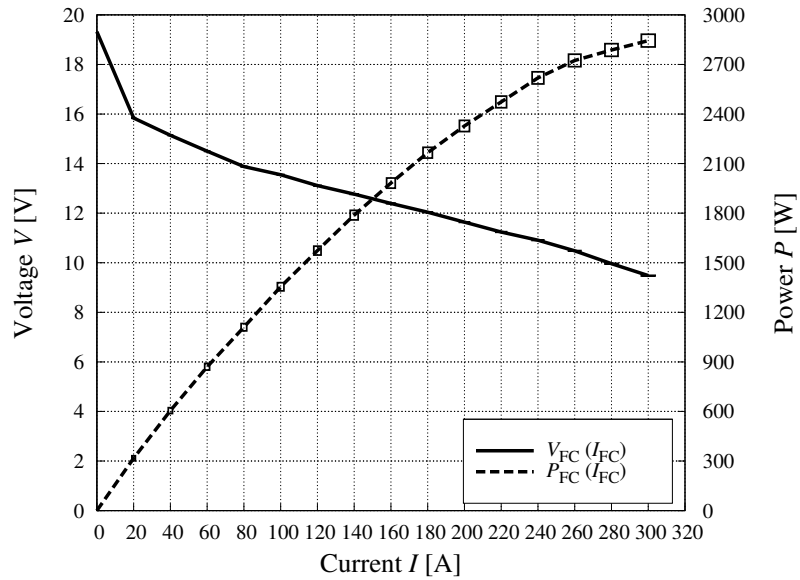
**Table K.1.** Fuel cell stack current  $I_{FC}$ , voltage  $V_{FC}$  and power  $P_{FC}$  on a 325 cm<sup>2</sup> 20 element stack. (a) Data, (b) Plot. Average temperature of the stack: 44 °C. The boxes represent the absolute errors.

$I_{FC}$	$\Xi_I$	$V_{FC}$	$\Xi_V$	$P_{FC}$	$\Xi_P$
[A]	[A]	[V]	[V]	[W]	[W]
0	0	19.3	0.01	0	0
20	0.95	15.8	0.01	320	15.3
40	1.15	15.1	0.01	610	17.8
60	1.35	14.5	0.01	870	20
80	1.55	13.9	0.01	1 110	22
100	1.75	13.6	0.01	1 350	25
120	2.0	13.1	0.01	1 570	27
140	2.2	12.8	0.01	1 790	29
160	2.4	12.4	0.01	2 000	31
180	2.6	12.0	0.01	2 200	32
200	2.8	11.6	0.01	2 300	34
220	3.0	11.2	0.01	2 500	35
240	3.2	10.9	0.01	2 600	37
260	3.4	10.5	0.01	2 700	38
280	3.6	10.0	0.01	2 800	38
300	3.8	9.5	0.01	2 800	39

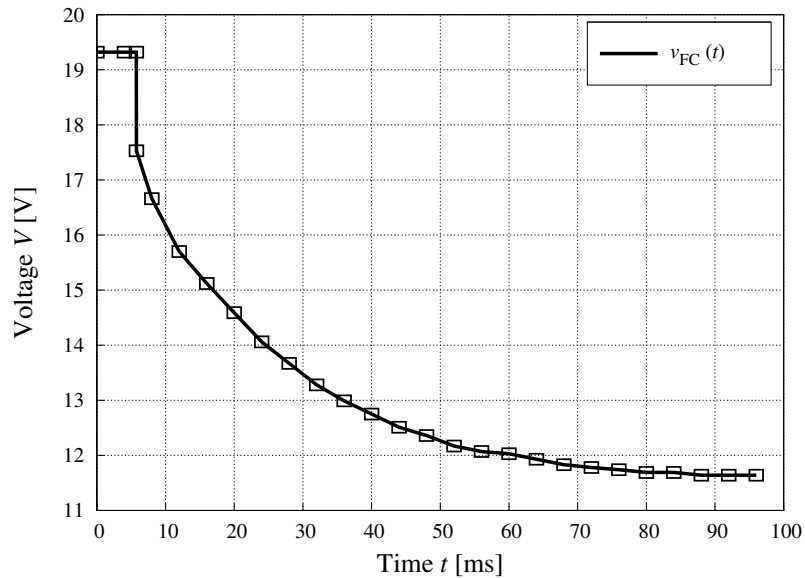
**Table K.2.** Data related to the low frequency ripple of the total input current, where  $P_i$  is the input power,  $\Delta I_{i,T}$  is the total input current ripple,  $f_r$  is the low frequency of the ripple,  $f_s$  is the switching frequency for every phase, and  $f_t$  is the total apparent switching frequency.

$P_i$	$\Delta I_{i,T}$	$\Xi$	$\epsilon$	$f_r$	$\Xi$	$\epsilon$	$f_s$	$\Xi$	$\epsilon$	$f_t$	$\Xi$	$\epsilon$
[kW]	[A]	[A]	[%]	[kHz]	[kHz]	[%]	[kHz]	[kHz]	[%]	[kHz]	[kHz]	[%]
10	32	8	25	58	3.4	5.9	116	12.9	11.1	697	77	11.1
5	23	8	35	64	4	6.3	83	6.9	8.3	500	41	8.3
3	20	8	40	63	4	6.3	108	12	11.1	649	72	11.1

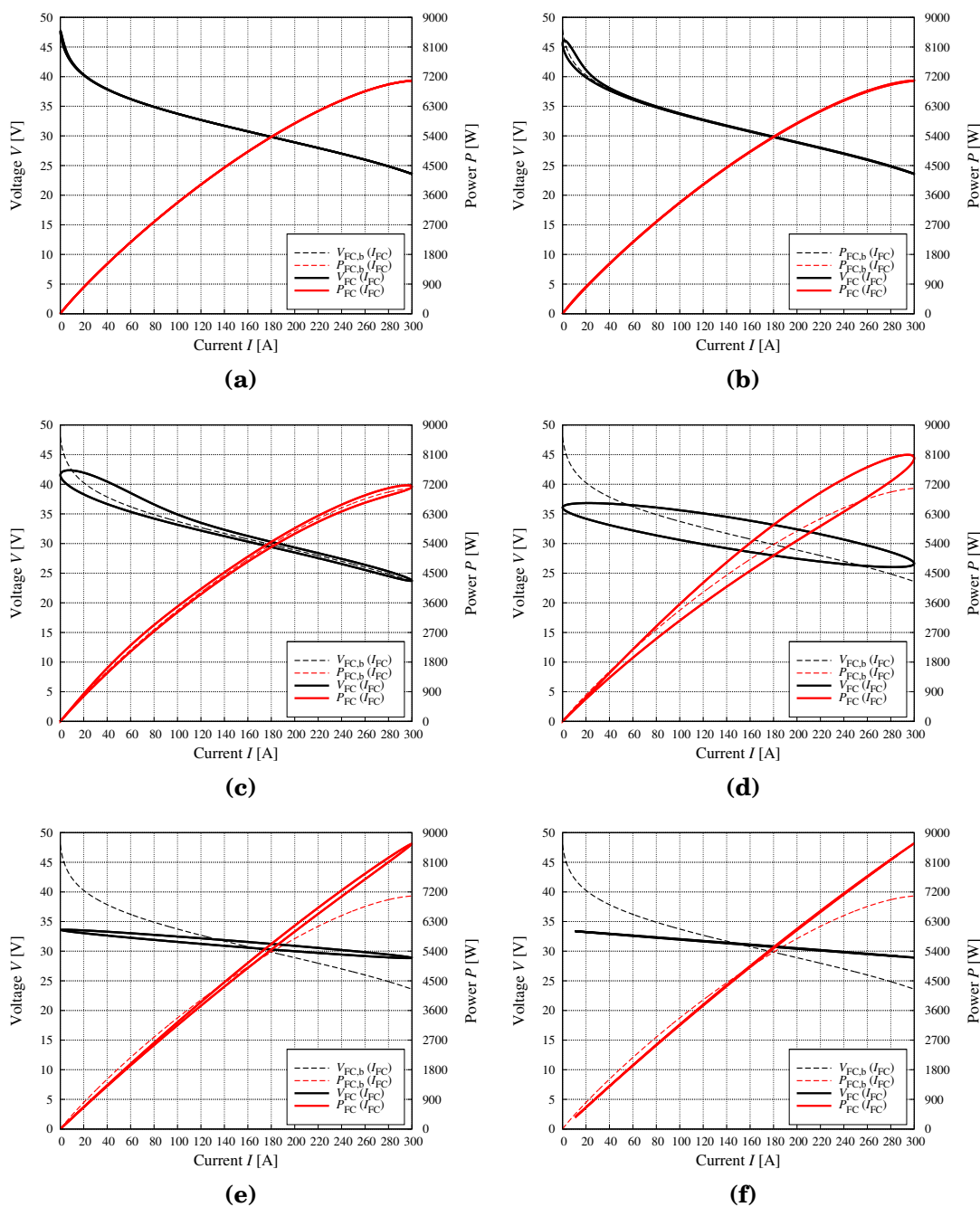
Figure K.6 and Tables K.3, K.4 and K.5 show the experimental results about the power converter powered by a power supply emulating the static behaviour of a fuel cell stack.



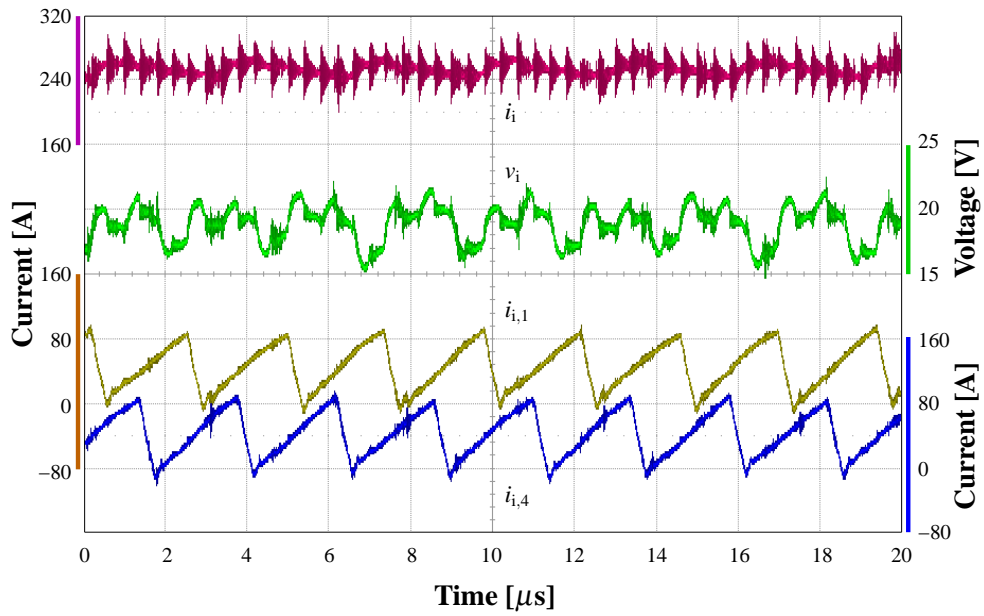
**Figure K.1.** Fuel cell stack current  $I_{FC}$ , voltage  $V_{FC}$  and power  $P_{FC}$  on a  $325 \text{ cm}^2$  20 element stack. (a) Data, (b) Plot. Average temperature of the stack:  $44 \text{ }^\circ\text{C}$ . The boxes represent the absolute errors.



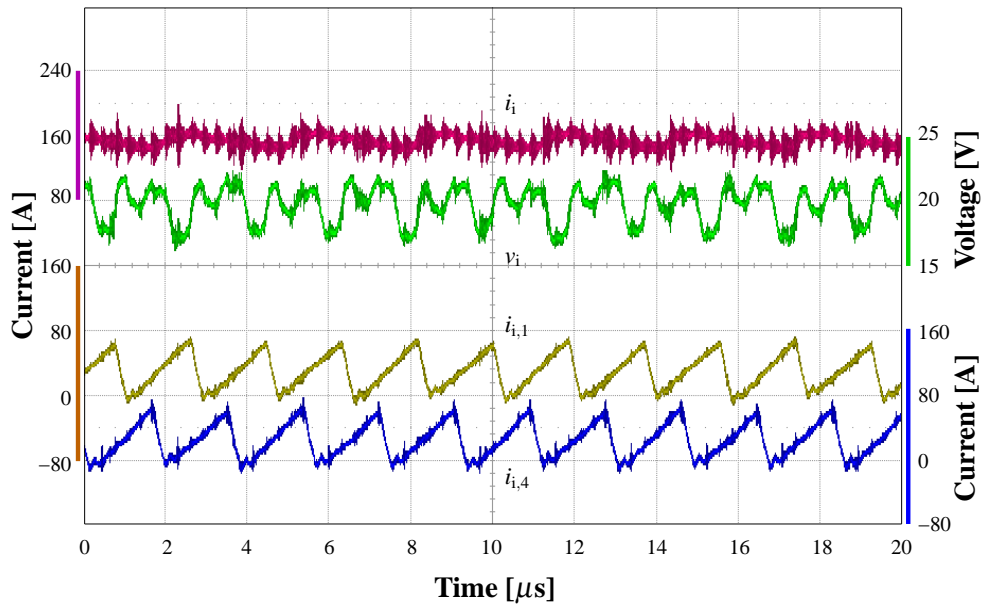
**Figure K.2.** Voltage fuel cell stack response to a 0 A–300 A current step. Experimental data ( $v_{FC}$ ). Fuel cell stack:  $325 \text{ cm}^2$ , 20 elements. The boxes represent the absolute errors:  $\Xi_v = 0.1 \text{ V}$ ,  $\Xi_t = 1 \text{ ms}$ .



**Figure K.3.** Voltage fuel cell stack response to a sinusoidal current injection, whose parameters are: amplitude 150 A, offset 150 A, frequency: (a) 0.1 Hz, (b) 1 Hz, (c) 10 Hz, (d) 100 Hz, (e) 1 kHz, (f) 10 kHz. Results from Matlab/Simulink simulation. Fuel cell stack: 325 cm<sup>2</sup>, 50 elements.



**Figure K.4.** Plots of the 6 boost input currents acquired with a digital oscilloscope, on condition of input power  $P_i = 5$  kW.



**Figure K.5.** Plots of the 6 boost input currents acquired with a digital oscilloscope, on condition of input power  $P_i = 3$  kW.

**Table K.3.** Converter input voltage  $V_i$ , input current  $I_i$ , output power  $P_o$  and efficiency  $\eta_{PC}$ , with their respective absolute errors  $\Xi_{V,i}$ ,  $\Xi_{I,i}$ ,  $\Xi_{P,o}$ ,  $\Xi_{\eta,PC}$ , and relative errors  $\epsilon_{V,i}$ ,  $\epsilon_{I,i}$ ,  $\epsilon_{P,o}$ ,  $\epsilon_{\eta,PC}$ . Voltage output reference  $V_o = 42$  V.

$V_i$	$\Xi_{V,i}$	$\epsilon_{V,i}$	$I_i$	$\Xi_{I,i}$	$\epsilon_{I,i}$	$P_o$	$\Xi_{P,o}$	$\epsilon_{P,o}$	$\eta_{PC}$	$\Xi_{\eta,PC}$	$\epsilon_{\eta,PC}$
[V]	[V]	[%]	[A]	[A]	[%]	[W]	[W]	[%]	[-]	[-]	[%]
38	0.050	0.131	38	0.125	0.33	1 370	45	3.3	0.94	0.040	3.7
37	0.050	0.134	47	0.125	0.27	1 640	45	2.8	0.94	0.030	3.2
37	0.050	0.137	55	0.125	0.23	1 910	67	3.5	0.94	0.040	3.9
36	0.050	0.139	61	0.125	0.21	2 000	67	3.3	0.94	0.030	3.6
36	0.050	0.140	70	0.125	0.178	2 300	67	2.9	0.93	0.030	3.2
35	0.050	0.142	76	0.125	0.164	2 500	67	2.7	0.93	0.030	3.0
35	0.050	0.144	82	0.125	0.153	2 600	68	2.6	0.93	0.030	2.9
35	0.050	0.145	88	0.125	0.143	2 800	78	2.8	0.92	0.030	3.1
34	0.050	0.146	93	0.125	0.134	2 900	68	2.3	0.92	0.020	2.6
34	0.050	0.148	98	0.125	0.127	3 100	68	2.2	0.92	0.020	2.5

**Table K.4.** Converter input voltage  $V_i$ , input current  $I_i$ , output power  $P_o$  and efficiency  $\eta_{PC}$ , with their respective absolute errors  $\Xi_{V,i}$ ,  $\Xi_{I,i}$ ,  $\Xi_{P,o}$ ,  $\Xi_{\eta,PC}$ , and relative errors  $\epsilon_{V,i}$ ,  $\epsilon_{I,i}$ ,  $\epsilon_{P,o}$ ,  $\epsilon_{\eta,PC}$ . Voltage output reference  $V_o = 48$  V.

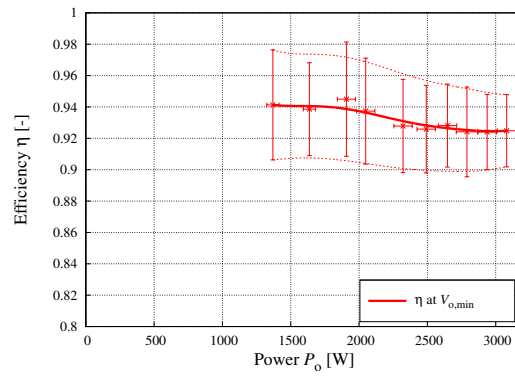
$V_i$	$\Xi_{V,i}$	$\epsilon_{V,i}$	$I_i$	$\Xi_{I,i}$	$\epsilon_{I,i}$	$P_o$	$\Xi_{P,o}$	$\epsilon_{P,o}$	$\eta_{PC}$	$\Xi_{\eta,PC}$	$\epsilon_{\eta,PC}$
[V]	[V]	[%]	[A]	[A]	[%]	[W]	[W]	[%]	[-]	[-]	[%]
46	0.050	0.109	1.45	0.125	8.7	59	56	96	0.88	0.110	12.9
41	0.050	0.121	15.8	0.125	0.79	600	50	8.3	0.92	0.080	9.2
40	0.050	0.126	24	0.125	0.51	890	50	5.6	0.92	0.060	6.3
39	0.050	0.129	32	0.125	0.39	1 140	50	4.4	0.92	0.050	5.0
38	0.050	0.132	39	0.125	0.32	1 380	51	3.7	0.93	0.040	4.1
37	0.050	0.134	45	0.125	0.28	1 570	51	3.2	0.93	0.030	3.7
37	0.050	0.136	52	0.125	0.24	1 770	51	2.9	0.93	0.030	3.3
36	0.050	0.137	58	0.125	0.22	1 920	75	3.9	0.91	0.040	4.3
36	0.050	0.139	63	0.125	0.20	2 100	76	3.6	0.92	0.040	4.0
36	0.050	0.140	68	0.125	0.184	2 200	76	3.4	0.92	0.030	3.7
35	0.050	0.141	74	0.125	0.170	2 400	76	3.2	0.91	0.030	3.5
35	0.050	0.143	77	0.125	0.161	2 500	76	3.1	0.92	0.030	3.4
35	0.050	0.144	82	0.125	0.152	2 600	76	2.9	0.92	0.030	3.2
35	0.050	0.145	86	0.125	0.145	2 700	76	2.8	0.91	0.030	3.1
34	0.050	0.146	91	0.125	0.137	2 900	77	2.7	0.92	0.030	3.0
34	0.050	0.147	95	0.125	0.131	3 000	77	2.6	0.91	0.030	2.9
34	0.050	0.148	99	0.125	0.126	3 100	77	2.5	0.91	0.030	2.8

**Table K.5.** Converter input voltage  $V_i$ , input current  $I_i$ , output power  $P_o$  and efficiency  $\eta_{PC}$ , with their respective absolute errors  $\Xi_{V,i}$ ,  $\Xi_{I,i}$ ,  $\Xi_{P,o}$ ,  $\Xi_{\eta,PC}$ , and relative errors  $\epsilon_{V,i}$ ,  $\epsilon_{I,i}$ ,  $\epsilon_{P,o}$ ,  $\epsilon_{\eta,PC}$ . Voltage output reference  $V_o = 60$  V.

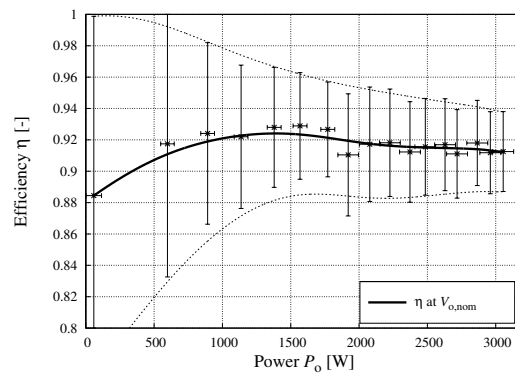
$V_i$ [V]	$\Xi_{V,i}$ [V]	$\epsilon_{V,i}$ [%]	$I_i$ [A]	$\Xi_{I,i}$ [A]	$\epsilon_{I,i}$ [%]	$P_o$ [W]	$\Xi_{P,o}$ [W]	$\epsilon_{P,o}$ [%]	$\eta_{PC}$ [–]	$\Xi_{\eta,PC}$ [–]	$\epsilon_{\eta,PC}$ [%]
47	0.050	0.107	0.43	0.125	29	20	3.0	15.2	1.00	0.45	45
43	0.050	0.117	8.9	0.125	1.41	330	62	18.5	0.88	0.180	20
41	0.050	0.122	15.4	0.125	0.81	570	62	10.9	0.90	0.110	11.9
40	0.050	0.125	21	0.125	0.59	770	62	8.1	0.90	0.080	8.8
39	0.050	0.127	26	0.125	0.48	940	62	6.6	0.91	0.070	7.2
39	0.050	0.129	31	0.125	0.41	1070	62	5.8	0.90	0.060	6.4
38	0.050	0.131	37	0.125	0.34	1270	63	4.9	0.91	0.050	5.4
38	0.050	0.133	41	0.125	0.30	1370	63	4.6	0.88	0.040	5.0
37	0.050	0.134	46	0.125	0.27	1500	63	4.2	0.88	0.040	4.6
37	0.050	0.135	50	0.125	0.25	1640	93	5.7	0.89	0.050	6.1
37	0.050	0.137	55	0.125	0.23	1730	93	5.4	0.87	0.050	5.7
36	0.050	0.137	58	0.125	0.22	1900	93	4.9	0.90	0.050	5.3
36	0.050	0.138	62	0.125	0.20	2000	93	4.6	0.90	0.040	5.0
36	0.050	0.139	66	0.125	0.190	2100	93	4.4	0.90	0.040	4.7
35	0.050	0.141	76	0.125	0.166	2200	94	4.2	0.84	0.040	4.5
35	0.050	0.142	74	0.125	0.169	2400	94	4.0	0.90	0.040	4.3
35	0.050	0.142	77	0.125	0.163	2400	94	3.9	0.89	0.040	4.2
35	0.050	0.143	78	0.125	0.161	2400	94	3.9	0.89	0.040	4.2
35	0.050	0.143	81	0.125	0.155	2500	94	3.7	0.90	0.040	4.0
35	0.050	0.144	84	0.125	0.150	2600	94	3.6	0.90	0.040	3.9
35	0.050	0.145	86	0.125	0.145	2700	94	3.5	0.90	0.030	3.8

#### K.4. Simulation of the whole system

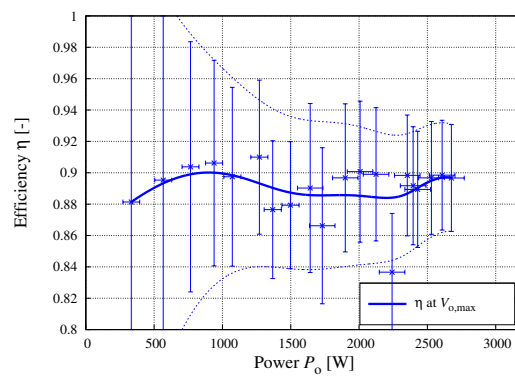
During the simulations of the whole system, the input variable stimulating the system is the output conductance  $g_o$ , whose plots are given for the different transients that have been studied in Figures K.7, K.8 and K.9.



(a)



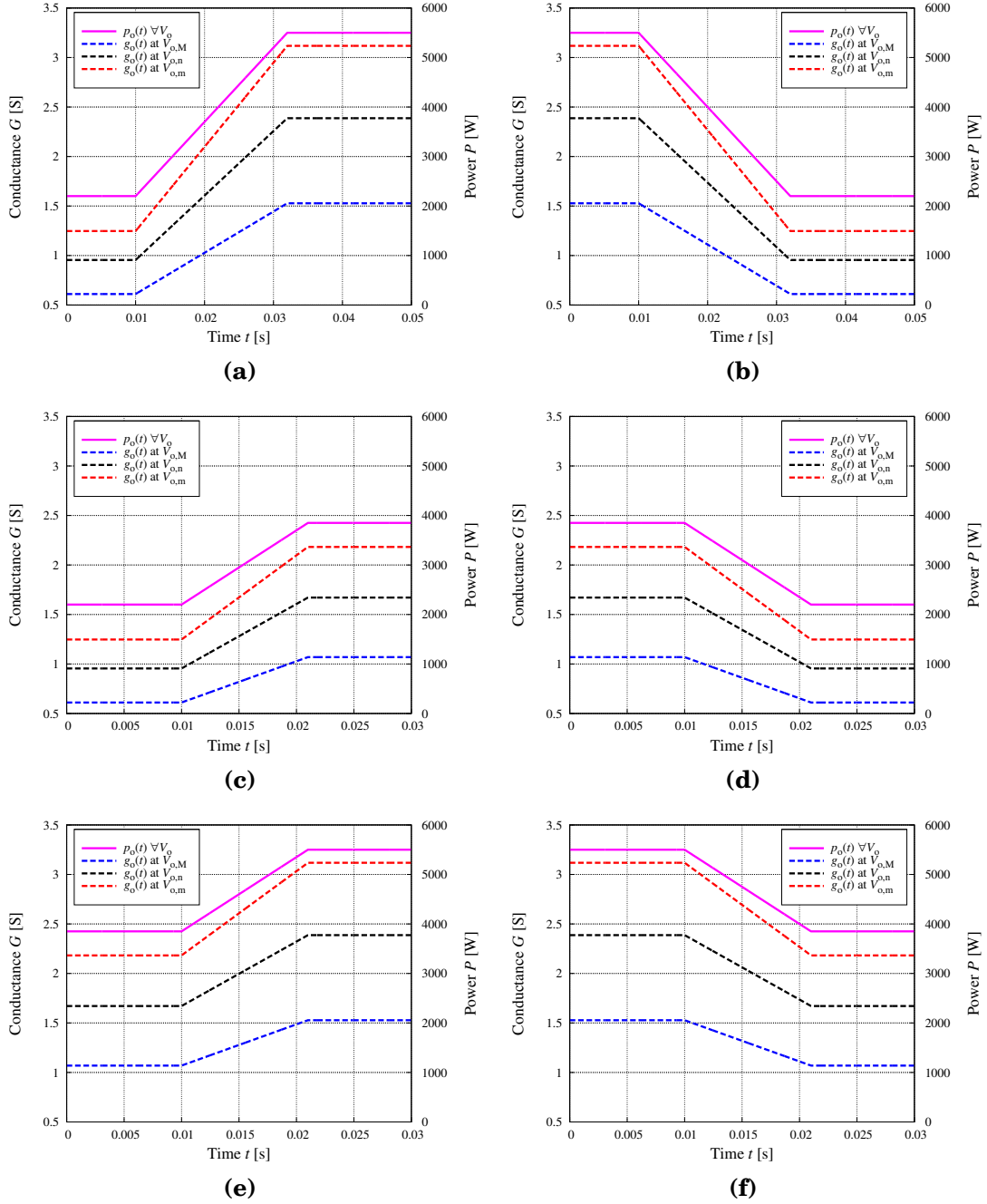
(b)



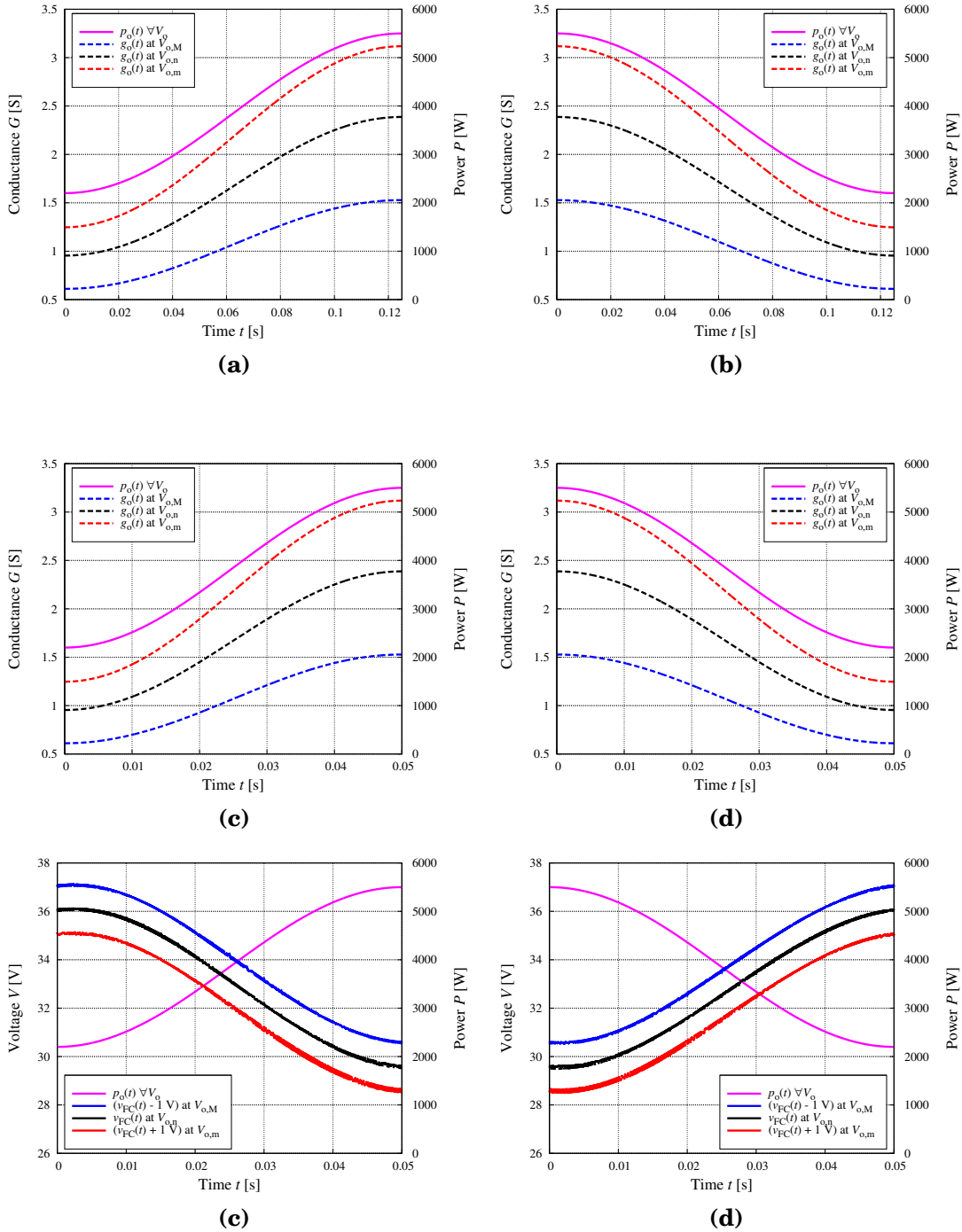
(c)

**Figure K.6.** Experimental converter efficiency  $\eta$  versus converter output power  $P_o$ , for output voltage (a)  $V_{o,m} = 42$  V, (b)  $V_{o,m} = 48$  V, (c)  $V_{o,m} = 60$  V. Error bars are indicated.

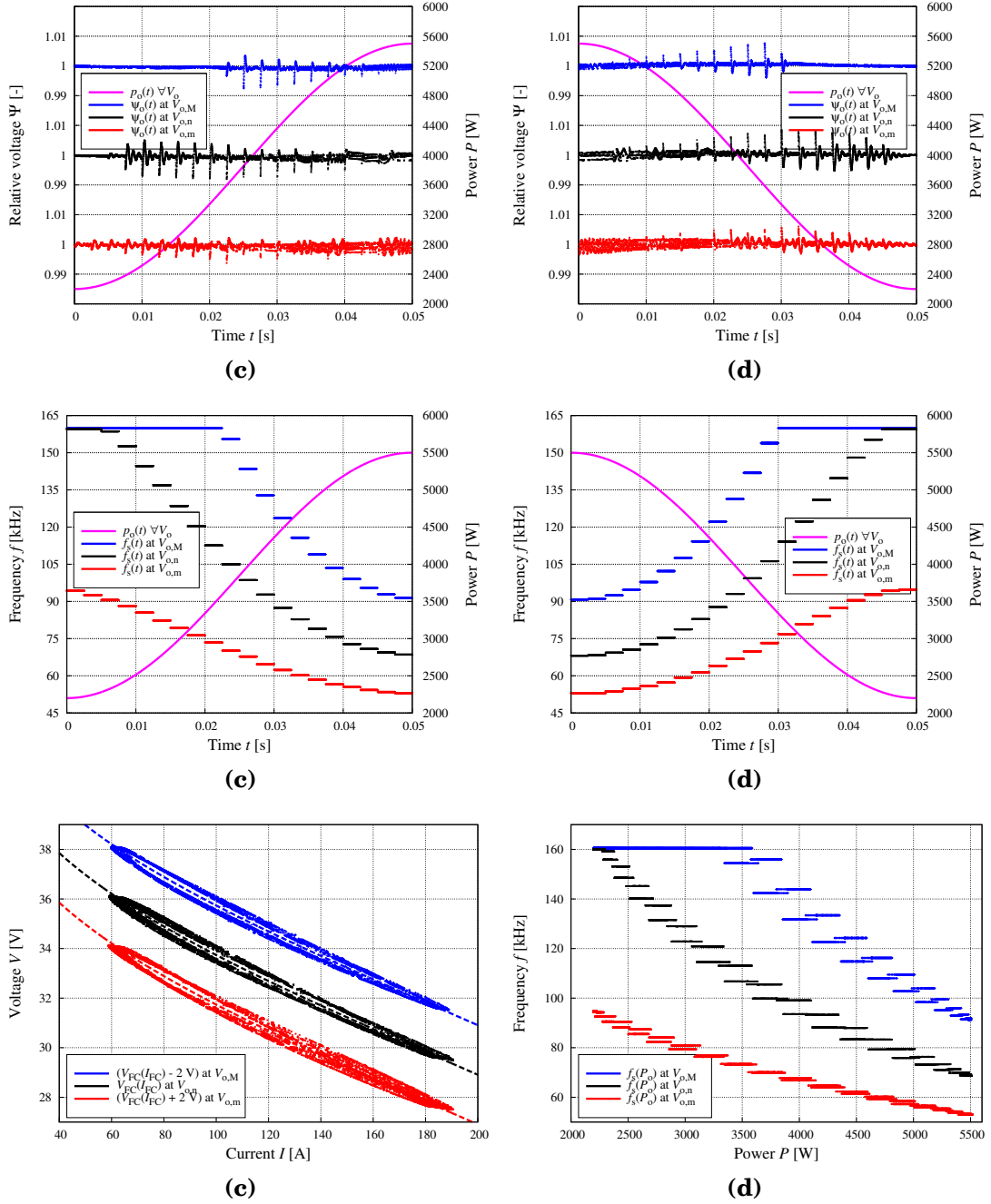




**Figure K.7.** Output conductance of the system for the different ramp transients for three different values of the output voltage reference:  $V_{o,m}$ ,  $V_{o,n}$  and  $V_{o,M}$ . Fuel cell stack: 325 cm<sup>2</sup>, 50 elements.



**Figure K.8.** Output conductance (a), (b) of the system for the 4 Hz sinusoidal transient tests. Output conductance (c), (d) of the system and fuel cell voltage responses (e), (f) for the 10 Hz sinusoidal transient tests. For three different values of the output voltage reference:  $V_{o,m}$ ,  $V_{o,n}$  and  $V_{o,M}$ . Fuel cell stack: 325 cm<sup>2</sup>, 50 elements.



**Figure K.9.** System output voltage responses (a) and (b), power converter switching frequency responses (c) and (d), fuel cell voltage versus current map (e) and power converter switching frequency versus output power map (f) for the 10 Hz sinusoidal transient tests. For three different values of the output voltage reference:  $V_{o,m}$ ,  $V_{o,n}$  and  $V_{o,M}$ . Fuel cell stack: 325 cm<sup>2</sup>, 50 elements.



## REFERENCES

- [1] M. Farooque, H.C. Marum, “Fuel cells—the clean and efficient power generators”, *IEEE, Proceedings of the IEEE*, vol. 89, n. 12, pp. 1819–1829, December 2001.
- [2] G. Hoogers, et al., *Fuel Cell Technology Handbook*. CRC Press LLC, Boca Raton, Florida, 2003.
- [3] E.I. Ortiz-Rivera, A.L. Reyes-Hernandez, R.A. Febo, “Understanding the history of fuel cells”, *IEEE, Proceedings of the Conference on the History of Electric Power*, pp. 117–122, August 2007.
- [4] G.L. Lapini, “Produzione e distribuzione dell’energia elettrica (Electrical energy production and distribution in Italy)”, last visit on October 28, 2008. [http://www.storiadimilano.it/citta/milanotecnica/eletricita/eletricita\\_link2.htm](http://www.storiadimilano.it/citta/milanotecnica/eletricita/eletricita_link2.htm).
- [5] U. Schmitt, “Nernst Lamp”, last visit on October 28, 2008. <http://www.nernst.de/lamp/nernstlamp.htm>.
- [6] J. Larminie, A. Dicks, *Fuel Cell Systems Explained*. John Wiley and Sons, Chichester, England, 2000.
- [7] K. Prater, “The renaissance of the solid polymer fuel cell”. *Journal of Power Sources*, vol. 29, n. 1–2, pp. 239–250, January 1990.
- [8] M.W. Verbrugge, “Methanol diffusion in perfluorinated ion-exchange membranes”. *Journal of the Electrochemical Society*, vol. 136, n. 2, pp. 417–423, February 1989.
- [9] J.C. Amphlett, R.M. Baumert, R.F. Mann, B.A. Peppley, P.R. Roberge, “Performance modeling of the Ballard Mark IV solid polymer electrolyte fuel cell. I. Mechanistic model development”. *Journal of the Electrochemical Society*, vol. 142, n. 1, pp. 1–8, January 1995.

- [10] J.C. Amphlett, R.M. Baumert, R.F. Mann, B.A. Peppley, P.R. Roberge, "Performance modeling of the Ballard Mark IV solid polymer electrolyte fuel cell. II. Empirical model development". *Journal of the Electrochemical Society*, vol. 142, n. 1, pp. 9–15, January 1995.
- [11] "PEM Fuel Cells", Smithsonian Institution, last visit on October 27, 2008. <http://americanhistory.si.edu/fuelcells/pem/pemmain.htm>.
- [12] K. Ledjeff-Hey, A. Heinzl, "Critical issues and future prospects for solid polymer fuel cells". *Journal of Power Sources*, vol. 61, n. 1–2, pp. 125–127, July-August 1996.
- [13] "Solid Oxide Fuel Cells", Smithsonian Institution, last visit on October 27, 2008. <http://americanhistory.si.edu/fuelcells/so/sofcmmain.htm>.
- [14] "Honda FCX Clarity", American Honda Motor Co., Inc., last visit on October 27, 2008. <http://automobiles.honda.com/fcx-clarity>.
- [15] Young Ho Seo, Young-Ho Cho, "Micro direct methanol fuel cells and their stacks using a polymer electrolyte sandwiched by multi-window microcolumn electrodes". *Sensors and Actuators A: Physical*, vol. 150, n. 1, pp. 87–89, March 2009.
- [16] S. Wagner, S. Krumbholz, R. Hann, H. Reichl, "Influence of structure dimensions on self-breathing micro fuel cells". *Journal of Power Sources*, vol. 190, n. 1, pp. 76–82, May 2009.
- [17] *Fuel Cell Handbook*, U.S. Department of Energy, under contract no. DE-AM26-99FT40575, Fifth Edition. EG&G Services Parsons, Inc.. National Energy Technology Laboratory, Office of Fossil Energy, Morgantown, West Virginia, October 2000.
- [18] M.S. Wilson, S. Gottesfeld, "High performance catalyzed membranes of ultra-low Pt loadings for polymer electrolyte fuel cells". *Journal of the Electrochemical Society*, vol. 139, n. 2, pp. L28–L30, February 1992.
- [19] H.A. Gasteiger, J.E. Panels, S.G. Yan, "Dependence of PEM fuel cell performance on catalyst loading". *Journal of Power Sources*, vol. 127, n. 1–2, pp. 162–171, March 2004.
- [20] S.D. Knight, K.D. Colbow, J. St.-Pierre, D.P. Wilkinson, "Aging mechanisms and lifetime of PEFC and DMFC". *Journal of Power Sources*, vol. 127, n. 1–2, pp. 127–134, March 2004.
- [21] H. Mera, T. Takata, "High-performance fibers". *Ullmann's Encyclopedia of Industrial Chemistry*, June 2000.

- [22] A.R. Korsgaard, R. Refshauge, M.P. Nielsen, M. Bang, S.K. Kær, “Experimental characterization and modeling of commercial polybenzimidazole-based MEA performance”. *Journal of Power Sources*, vol. 162, n. 1, pp. 239–245, November 2006.
- [23] “Elsevier at a glance”, Elsevier B.V., last visit on September 21, 2009. [http://www.elsevier.com/wps/find/intro.cws\\_home/ata glance](http://www.elsevier.com/wps/find/intro.cws_home/ata glance).
- [24] M.L. Perry, T.F. Fuller, “A historical perspective of fuel cell technology in the 20th century”. *Journal of the Electrochemical Society*, vol. 149, n. 7, pp. 59–67, June 2002.
- [25] B. Bidoggia, T. Lequeu, J.-C. Le Bunetel, A. Schellmanns, L. Ventura, S. Buso, G. Spiazzi, “Systèmes hybrides de génération de moyenne puissance : applications stationnaires aux énergies renouvelables (Medium power hybrid generation systems: stationary applications for renewable energies)”, *Proceedings of EPF, Électronique de Puissance du Futur Conference*, pp. 6, July 2006.
- [26] L.D. Paulson, “Will fuel cells replace batteries in mobile devices?”. *Computer*, vol. 36, n. 11, pp. 10–12, November 2003.
- [27] C.K. Dyer, “Fuel cells for portable applications”. *Journal of Power Sources*, vol. 106, n. 1–2, pp. 31–34, April 2002.
- [28] S.R. Bull, “Renewable energy today and tomorrow”, *IEEE, Proceedings of the IEEE*, vol. 89, n. 8, pp. 1216–1226, August 2001.
- [29] J.P. Meyers, “Fundamental issues in subzero PEMFC startup and operation”, *U.S. DOE, Department of Energy, Proceedings of Freeze Workshop*, February 2005.
- [30] R.E. Morgan, “Bridge-chopper inverter for 400 cps sine wave power”. *IEEE Transactions of Aerospace*, vol. 2, n. 2, pp. 993–997, April 1964.
- [31] S. Rahman, Kwa-Sur Tam, “A feasibility study of photovoltaic-fuel cell hybrid energy system”. *IEEE Transactions on Energy Conversion*, vol. 3, n. 1, pp. 50–55, March 1988.
- [32] W.J. Lueckel, L.G. Eklund, S.H. Law, “Fuel cells for dispersed power generation”. *IEEE Transactions on Power Apparatus and Systems*, vol. PAS-92, n. 1, pp. 230–236, January 1973.
- [33] C.V. Chi, D.R. Glenn, S.G. Abens, “Development of a fuel cell power source for bus”, *IEEE, Proceedings of IECEC, International Energy Conversion Engineering Conference*, vol. 3, pp. 308–313, August 1990.

- [34] G.V. Sukumara, A. Parthasarathy, V.R. Shankar, "Fuel cell based uninterruptible power sources", *IEEE, Proceedings of PEDS, Power Electronics and Drive Systems Conference*, vol. 2, pp. 728–733, June 1997.
- [35] N. Kato, T. Murao, K. Fujii, T. Aoki, S. Muroyama, "1 kW portable fuel cell system based on PEFCs". TELESCON, Telecommunications Energy Special Conference, *IEEE, Proceedings of TELESCON, Telecommunication Energy Special Conference*, pp. 209–213, May 2000.
- [36] Rong-Jong Wai, Rou-Yong Duan, Jeng-Dao Lee, Li-Wei Liu, "High-efficiency fuel-cell power inverter with soft-switching resonant technique". *IEEE Transaction on Energy Conversion*, vol. 20, n. 2, pp. 485–492, June 2005.
- [37] G.K. Andersen, C. Klumpner, S.B. Kjær, F. Blaabjerg, "A new green power inverter for fuel cells", *IEEE, Proceedings of PESC, Power Electronics Specialists Conference*, vol. 2, pp. 727–733, June 2002.
- [38] Yaosuo Xue, Liuchen Chang, S.B. Kjær, J. Bordonau, T. Shimizu, "Topologies of single-phase inverters for small distributed power generators: an overview". *IEEE Transactions on Power Electronics*, vol. 19, n. 5, pp. 1305–1314, September 2004.
- [39] Xuancai Zhu, Dehong Xu, Ping Wu, Guoqiao Shen, Pingping Chen, "Energy management design for a 5kW fuel cell distributed power system", *IEEE, Proceedings of APEC, Applied Power Electronics Conference and Exposition*, pp. 291–297, February 2008.
- [40] Xudong Huang, Xiaoyan Wang, Ferrel, J., Nergaard, T., Jih-Sheng Lai, Xingyi Xu, Lizhi Zhu, "Parasitic ringing and design issues of high power interleaved boost converters", *IEEE, Proceedings of PESC, Power Electronics Specialists Conference*, vol. 1, pp. 30–35, June 2002.
- [41] L. Palma, M.H. Todorovic, P. Enjeti, "A high gain transformer-less DC-DC converter for fuel-cell applications", *IEEE, Proceedings of PESC, Power Electronics Specialists Conference*, pp. 2514–2520, June 2005.
- [42] Dachuan Yu, S. Yuvarajan, "Modeling and performance studies of a fuel-cell powered boost converter", *IEEE, Proceedings of INTELEC, International Telecommunication Energy Conference*, pp. 713–717, September 2004.
- [43] J.-N. Marie-Françoise, H. Gualous, A. Berthon, "DC to DC converter with neural network control for on-board electrical energy management", *IEEE, Proceedings of IPEMC, International Power*



- Electronics and Motion Control Conference*, vol. 2, pp. 521–525, August 2004.
- [44] Y. Lembeye, Viet Dang Bang, G. Lefèvre, J.-P. Ferrieux, “Novel half-bridge inductive DC-DC isolated converters for fuel cell applications”. *IEEE Transactions on Energy Conversion*, vol. 24, n. 1, pp. 203–210, March 2009.
- [45] Haiping Xu, Li Kong, Xuhui Wen, “Fuel cell power system and high power DC-DC converter”. *IEEE Transactions on Power Electronics*, vol. 19, n. 5, pp. 1250–1255, September 2004.
- [46] G. Spiazzi, S. Buso, G.M. Martins, J.A. Pomilio, “Single phase line frequency commutated voltage source inverter suitable for fuel cell interfacing”, vol. 2, pp. 734–739, June 2002.
- [47] G.M. Martins, J.A. Pomilio, S. Buso, G. Spiazzi, “Three-phase low-frequency commutation inverter for renewable energy systems”. *IEEE Transactions on Industrial Electronics*, vol. 53, n. 5, pp. 1522–1528, October 2006.
- [48] Shu Wang, Y. Lembeye, J.-P. Ferrieux, “Design and implementation of a high switching frequency digital controlled SMPS”, pp. 219–223, June 2007.
- [49] T. Lequeu, G. Kalvelage, P. Aubin, “An innovating topology of power converter: serial and parallel auto regulated configuration (SPARC)”. *IEEE Transactions on Industry Applications*, vol. 40, n. 2, pp. 632–641, March–April 2004.
- [50] N. Mohan, T.M. Undeland, W.P. Robbins, *Power Electronics — Converters, Applications and Design*, Second Edition. John Wiley and Son, Inc., 1995.
- [51] R. Erickson, D. Maksimovic, *Fundamental of Power Electronics*, Second Edition. Kluwer Academic Publishers, 2004.
- [52] R.S. Gemmen, “Analysis for the effect of inverter ripple current on fuel cell operation condition”. *Journal of Fluids Engineering*, vol. 125, n. 3, pp. 576–586, May 2003.
- [53] B. Wahdame, L. Girardot, D. Hissel, F. Harel, X. François, D. Candusso, M.C. Péra, L. Dumercy, “Impact of power converter current ripple on the durability of a fuel cell stack”, *IEEE, Proceedings of ISIE, International Symposium on Industrial Electronics*, pp. 1495–1500, July 2008.
- [54] G. Fontès, *Modélisation et caractérisation de la pile PEM pour l’étude des interactions avec les convertisseurs statiques (Modelling and char-*

- acterization of the PEM fuel cell in order to study the interactions with static power converters*). Ph.D. thesis, Institut National Polytechnique de Toulouse, Toulouse, France, September 2005.
- [55] W.J. Choi, P.N. Enjeti, J.W. Howze, “Development of an equivalent circuit model of a fuel cell to evaluate the effects of inverter ripple current”, *IEEE, Proceedings of APEC, Applied Power Electronics Conference and Exposition*, vol. 1, pp. 335–361, 2004.
- [56] J.-P. Ferrieux, F. Forest, *Alimentations à découpage, convertisseurs à résonance (Switching power supplies, resonant converters)*, Principes, composants, modélisation (Principles, components, modelling), 3ème édition. DUNOD, Paris, 1999.
- [57] G. Spiazzi, D. Tagliavia, S. Spampinato, “DC-DC flyback converters in the critical conduction mode: a re-examination”, *Conference record of the IEEE Industry Applications Conference*, vol. 4, pp. 2426–2432, October 2000.
- [58] B. Bidoggia, G. Spiazzi, S. Buso, T. Lequeu, L. Ventura, “Design of a fuel cell based backup system for telecoms applications”, *IEEE, Proceedings of INTELEC, International Telecommunications Energy Conference*, pp. 1–8, September 2008.
- [59] P. Rinaldi, G.M. Veca, “The hydrogen for base radio stations”, *IEEE, Proceedings of INTELEC, International Telecommunication Energy Conference*, pp. 288–292, September–October 2007.
- [60] M.L. Perry, S. Kotso, “A back-up power solution with no batteries”, *IEEE, Proceedings from INTELEC, International Telecommunication Energy Conference*, pp. 210–217, September 2004.
- [61] W.F. Smith, J. Giancaterino, “Telecom back-up power systems based upon PEM regenerative fuel cell technology”, *IEEE, Proceedings from INTELEC, International Telecommunication Energy Conference*, pp. 657–661, October 2001.
- [62] W. Choi, P. Enjeti, J.W. Howze, “Fuel cell powered UPS systems: design considerations”, *IEEE, Proceedings of PESC, Power Electronics Specialist Conference*, vol. 1, pp. 385–390, June 2003.
- [63] T. Jacobs, J. Beukes, “Suitability of fuel cell technology for electricity utility standby power applications”, *IEEE, Proceedings of INTELEC, International Telecommunication Energy Conference*, pp. 1–7, September 2006.

- [64] A. Torrelli, G. Calzetti, A. Orlando, P. Magnanini, G. Gagliardi, “Field testing of fuel cells systems as backup power for italian telecommunication sites”, *IEEE, Proceedings of INTELEC, International Telecommunication Energy Conference*, pp. 108–115, September–October 2007.
- [65] G. Gianolio, I. Rosso, P. Cherchi, F. Pedrazzo, A. Torrelli, G. Calzetti, S. Gamarino, “Fuel cell based power system for backup applications: Telecom Italia and other field test results”, *IEEE, Proceedings of INTELEC, International Telecommunication Energy Conference*, pp. 280–287, September–October 2007.
- [66] A. Tomasi, R. Marin, “Fuel cell backup solutions in BTS station: First project in Italy”, *IEEE, Proceedings of INTELEC, International Telecommunication Energy Conference*, pp. 116–121, September–October 2007.
- [67] A. Tomasi, A. Torelli, “Fuel cells as backup power for Italian telecommunication sites: first year of working life”, *IEEE, Proceedings of INTELEC, International Telecommunication Energy Conference*, pp. 122–125, September–October 2004.
- [68] J.C. Amphlett, E.H. de Olivera, R.F. Mann, P.R. Roberge, A. Rodrigues, J.P. Salvador, “Dynamic interaction of a proton exchange membrane fuel cell and a lead-acid battery”. *Journal of Power Sources*, vol. 65, n. 1–2, pp. 173–178, March–April 1997.
- [69] S.J. Andreasen, L. Ashworth, I.N.M. Remón, S.K. Kær, “Directly connected series coupled HTPEM fuel cell stacks to a Li-ion battery DC bus for a fuel cell electrical vehicle”. *International Journal of Hydrogen Energy*, vol. 33, n. 23, pp. 7137–7145, December 2008.
- [70] A. Rowe, Xianguo Li, “Mathematical modeling of proton exchange membrane fuel cells”. *Journal of Power Sources*, vol. 102, n. 1–2, pp. 82–96, December 2001.
- [71] J.C. Amphlett, R.F. Mann, B.A. Peppley, P.R. Roberge, A. Rodrigues, “A model predicting transient responses of proton exchange membrane fuel cells”. *Journal of Power Sources*, vol. 61, n. 1–2, pp. 183–188, August 1996.
- [72] M. Eikerling, A.A. Kornyshev, “Modelling the performance of the cathode catalyst layer of polymer electrolyte fuel cells”. *Journal of Electroanalytical Chemistry*, vol. 453, n. 1–2, pp. 89–106, August 1998.

- [73] Shan-Hai Ge, Bao-Lian Yi, "A mathematical model for PEMFC in different flow modes". *Journal of Power Sources*, vol. 124, n. 1, pp. 1–11, October 2003.
- [74] R.P. Iczkowski, M.B. Cutlip, "Voltage losses in fuel cell cathodes". *Journal of the Electrochemical Society*, vol. 127, n. 7, pp. 1433–1440, July 1980.
- [75] Jung S. Yi, T.V. Nguyen, "An along-the-channel model for proton exchange membrane fuel cells". *Journal of the Electrochemical Society*, vol. 145, n. 4, pp. 1149–1159, April 1998.
- [76] M.F. Serincan, S. Yesilyurt, "Transient analysis of proton electrolyte membrane fuel cells (PEMFC) at start-up and failure", *Wiley, Proceedings of Fuel Cell Forum 2005 II*, vol. 7, n. 2, pp. 118–127, November 2006.
- [77] M.W. Verbrugge, R.F. Hill, "Ion and solvent transport in ion-exchange membranes. I. A macrohomogenous mathematical model". *Journal of the Electrochemical Society*, vol. 137, n. 3, pp. 886–893, March 1990.
- [78] M.W. Verbrugge, R.F. Hill, "Transport phenomena in perfluorosulfonic acid membranes during the passage of current". *Journal of the Electrochemical Society*, vol. 137, n. 4, pp. 1131–1138, April 1990.
- [79] D.M. Bernardi, M.W. Verbrugge, "A mathematical model of a solid polymer electrolyte fuel cell". *Journal of the Electrochemical Society*, vol. 139, n. 9, pp. 2477–2490, September 1992.
- [80] D.M. Bernardi, M.W. Verbrugge, "Mathematical model of a gas diffusion electrode bonded to a polymer electrolyte". *AIChE Journal*, vol. 37, n. 8, pp. 1151–1163, June 1991.
- [81] T.E. Springer, T.A. Zawodzinski, S. Gottesfeld, "Polymer electrolyte fuel cell model". *Journal of The Electrochemical Society*, vol. 138, n. 8, pp. 2334–2342, August 1991.
- [82] C. Wang, M.H. Nehrir, S.R. Shaw, "Dynamic models and model validation for PEM fuel cells using electrical circuits". *IEEE Transactions on Energy Conversion*, vol. 20, n. 2, pp. 442–451, June 2005.
- [83] J. Kim, S-M. Lee, S. Srinivasan, C.E. Chamberlin, "Modeling of proton exchange membrane fuel cell performance with an empirical equation". *Journal of the Electrochemical Society*, vol. 142, n. 8, pp. 2670–2674, August 1995.

- [84] J. Hamelin, K. Agbossou, A. Laperrière, F. Laurencelle, T.K. Bose, “Dynamic behavior of a PEM fuel cell stack for stationary applications”. *International Journal of Hydrogen Energy*, vol. 26, n. 6, pp. 625–629, June 2001.
- [85] R.F. Mann, J.C. Amphlett, B.A. Peppley, C.P. Thurgod, “Application of Butler-Volmer equations in the modelling of activation polarization for PEM fuel cells”. *Journal of Power Sources*, vol. 161, n. 2, pp. 775–781, October 2006.
- [86] R.F. Mann, J.C. Amphlett, M.A.I. Hooper, H.M. Jensen, B.A. Peppley, P.R. Roberge, “Development and application of a generalised steady-state electrochemical model for a pem fuel cell”. *Journal of Power Sources*, vol. 86, n. 1–2, pp. 173–180, March 2000.
- [87] G. Squadrito, G. Maggio, E. Passalacqua, F. Lufrano, A. Patti, “An empirical equation for polymer electrolyte fuel cell (PEFC) behaviour”. *Journal of Applied Electrochemistry*, vol. 29, n. 12, pp. 1449–1455, December 1999.
- [88] T.E. Springer, M.S. Wilson, S. Gottesfeld, “Modeling and experimental diagnostics in polymer electrolyte fuel cells”. *Journal of the Electrochemical Society*, vol. 140, n. 12, pp. 3513–3526, December 1993.
- [89] A. Haddad, R. Bouyekhf, A. El Moudni, M. Wack, “Non-linear dynamic modeling of proton exchange membrane fuel cell”. *Journal of Power Sources*, vol. 163, n. 1, pp. 420–432, December 2006.
- [90] J. Haubrock, G. Heideck, Z. Styczynski, “Dynamic investigation on proton exchange membrane fuel cell systems”, *IEEE, Proceedings of PES Meeting, Power Engineering Society*, pp. 1–6, June 2007.
- [91] W. Friede, S. Raël, B. Davat, “Mathematical model and characterization of the transient behavior of a PEM fuel cell”. *IEEE Transactions on Power Electronics*, vol. 19, n. 5, pp. 1234–1241, September 2004.
- [92] J.M. Correa, F.A. Farret, V.B. Popov, J.B. Parizzi, “Influence of the modeling parameters on the simulation accuracy of proton exchange membrane fuel cells”, *IEEE, Proceedings of Power Tech Conference*, vol. 2, pp. 8, June 2003.
- [93] Kong Xing, A.M. Khambadkone, “Dynamic modeling of fuel cell with power electronic current and performance analysis”, *IEEE, Proceedings of PEDS, Power Electronics and Drive Systems*, vol. 1, pp. 607–612, November 2003.

- [94] Dachuan Yu, S. Yuvarajan, "A Novel Circuit Model for PEM Fuel Cells", *IEEE, Proceedings of APEC, Applied Power Electronics Conference and Exposition*, vol. 1, pp. 362–366, February 2004.
- [95] P. Famouri, R.S. Gemmen, "Electrochemical circuit model of a PEM fuel cell", *IEEE, Proceedings of Power Engineering Society General Meeting*, vol. 3, pp. 1436–1440, July 2003.
- [96] Chao-Yang Wang, "Fundamental models for fuel cell engineering". *Chemical Reviews*, vol. 104, n. 10, pp. 4727–4766, September 2004.
- [97] A. Biyikoglu, "Review of proton exchange membrane fuel cell models". *International Journal of Hydrogen Energy*, vol. 30, n. 11, pp. 1181–1212, September 2005.
- [98] R. Cownden, M. Nahon, M.A. Rosen, "Modelling and analysis of a solid polymer fuel cell system for transportation applications". *International Journal of Hydrogen Energy*, vol. 26, n. 6, pp. 615–623, June 2001.
- [99] S. Caux, J. Lachaize, M. Fadel, P. Shott, L. Nicod, "Modelling and control of a fuel cell system and storage elements in transport applications". *Journal of Process Control*, vol. 15, n. 4, pp. 481–491, June 2005.
- [100] W. Turner, M. Parten, D. Vines, J. Jones, T. Maxwell, "Modeling a PEM fuel cell for use in a hybrid electric vehicle", *IEEE, Proceedings of Vehicular Technology Conference*, vol. 2, pp. 1385–1388, May 1999.
- [101] S. Akella, N. Sivashankar, S. Gopalswamy, "Model-based systems analysis of a hybrid fuel cell vehicle configuration", *IEEE, Proceedings of American Control Conference*, vol. 3, pp. 1777–1782, June 2001.
- [102] S. Pischinger, C. Schönfelder, J. Ogrzewalla, "Analysis of dynamic requirements for fuel cell systems for vehicle applications". *Journal of Power Sources*, vol. 154, n. 2, pp. 420–427, March 2006.
- [103] M.T. Iqbal, "Simulation of a small wind fuel cell hybrid energy system". *Renewable Energy*, vol. 8, n. 4, pp. 511–522, April 2003.
- [104] J.S. Newman, *Electrochemical Systems*. Prentice-Hall, Inc., Englewood Cliffs, New Jersey, 1973.
- [105] S.S. Kocha, J.D. Yang, Jung S. Yi, "Characterization of gas crossover and its implications in PEM fuel cells". *AIChE Journal*, vol. 52, n. 5, pp. 1916–1925, May 2006.
- [106] Pucheng Pei, Minggao Ouyang, Wei Feng, Languang Lu, Haiyan Huang, Jinhui Zhang, "Hydrogen pressure drop characteristics in a fuel

- cell stack". *International Journal of Hydrogen Energy*, vol. 31, n. 3, pp. 371–377, March 2006.
- [107] J. O'M. Bockris, A.K.N. Reddy, M. Gamboa-Aldeco, *Modern Electrochemistry 2*, Fundamentals of Electrodeics, Second Edition. Kluwer Academic Publishers, New York, 2001.
- [108] M. Eikerling, Yu.I. Kharkats, A.A. Kornyshev, Yu.M. Volkovich, "Phenomenological theory of electro-osmotic effect and water management in polymer electrolyte proton-conducting membranes". *Journal of the Electrochemical Society*, vol. 145, n. 8, pp. 2684–2699, August 1998.
- [109] Falin Chen, Yu-Guang Su, Chyi-Yeou Soong, Wei-Moon Yan, Hsin-Sen Chu, "Transient behavior of water transport in the membrane of a PEM fuel cell". *Journal of Electroanalytical Chemistry*, vol. 566, n. 1, pp. 85–93, May 2004.
- [110] T.F. Fuller, J. Newman, "Water and thermal management in solid-polymer-electrolyte fuel cells". *Journal of the Electrochemical Society*, vol. 140, n. 5, pp. 1218–1225, May 1993.
- [111] Nguyen, T.V., White, R.E., "A water and heat management model for proton-exchange-membrane fuel cells". *Journal of the Electrochemical Society*, vol. 140, n. 8, pp. 2178–2186, August 1993.
- [112] H.H. Voss, D.P. Wilkinson, P.G. Pickup, M.C. Johnson, V. Basura, "Anode water removal: a water management and diagnostic technique for solid polymer fuel cells". *Electrochimica Acta*, vol. 40, n. 3, pp. 321–328, February 1995.
- [113] Fang-Bor Weng, Ay Su, Chun-Ying Hsu, Chi-Yuan Lee, "Study of water-flooding behaviour in cathode channel of a transparent proton-exchange membrane fuel cell". *Journal of Power Sources*, vol. 157, n. 2, pp. 674–680, July 2006.
- [114] Baschuk, J.J., Xianguo, Li, "Modelling of Polymer Electrolyte Membrane Fuel Cells With Variable Degrees of Water Flooding". *Journal of Power Sources*, vol. 86, pp. 181–196, 2000.
- [115] Dang Bang Viet, Y. Lembeye, J.-P. Ferrieux, J. Barbaroux, Y. Avenas, "New high power-high ratio non isolated DC-DC boost converter for fuel cell applications", *IEEE, Proceedings of PESC, Power Electronics Specialists Conference*, pp. 1–7, June 2006.
- [116] B. Bidoggia, T. Lequeu, L. Ventura, G. Spiazzi, S. Buso, "Système de contrôle et de supervision numérique pour pile à combustible (Dig-

- ital control and monitor system for fuel cells)", *Proceedings of EPF, Électronique de Puissance du Futur Conference*, pp. 5, July 2008.
- [117] E. Ramschak, V. Peinecke, P. Prenninger, T. Schaffer, V. Hacker, "Detection of fuel cell critical status by stack voltage analysis". *Journal of Power Sources*, vol. 157, n. 2, pp. 837–840, July 2006.
- [118] Xiaozhi Yuan, Haijiang Wang, Jian Colin Sun, Jiujun Zhang, "AC impedance technique in PEM fuel cell diagnosis—A review". *International Journal of Hydrogen Energy*, vol. 32, n. 17, pp. 4365–4380, December 2007.
- [119] A. Narjiss, D. Depernet, F. Gustin, D. Hissel, A. Berthon, "Design and control of a fuel cell DC/DC converter for embedded applications", *IEEE, Proceedings of EPE, European Conference on Power Electronics and Applications*, pp. 1–10, September 2007.
- [120] "RTAI — RealTime Application Interface for Linux", Politecnico di Milano, Dipartimento di Ingegneria Aerospaziale, last visit on April 2, 2009. <https://www.rtai.org>.
- [121] "Scilab, the open source platform for numerical computation", INRIA, Institut National de Recherche en Informatique et en Automatique, last visit on April 2, 2009. <http://www.scilab.org>.
- [122] D. Schleef, F.M. Hess, I. Abbott, "Comedi, Linux COntrol and MEasurement Interface", last visit on April 2, 2009. <http://www.comedi.org>.
- [123] G. Bucci, F. Ciancetta, E. Fiorucci, E. Rotondale, F. Vegliò, "Experimental validation of a PEM fuel cell dynamic model", *IEEE, Proceedings of SPEEDAM, International Symposium on Power Electronics, Electrical Drives, Automation and Motion*, pp. 546–551, May 2006.
- [124] L. Guzzella, "Control oriented modeling of fuel-cell based vehicles", *NSF, ASME, DSCD, IEEE CSS, Presentation of NSF Workshop on the Integration of Modeling and Control for Automotive Systems*, pp. 8, June 1999.
- [125] "Net Generation by Energy Source by Type of Producer", EIA — Energy Information Administration — Official Energy Statistics from the U.S. Government, last visit on September 21, 2009. <http://www.eia.doe.gov/cneaf/electricity/epa/epat1p1.html>.
- [126] L'électricité en France en 2008 (Electricity in France in 2008). Chiffres & statistiques (Numbers & statistics). Tech. Rep. 40 (June 2009), Commissariat général au développement durable. <http://>



*www.developpement-durable.gouv.fr/energie/statisti/pdf/elec-analyse-stat.pdf.*

- [127] Dati Statistici sull'energia elettrica in Italia (Statistical data concerning the electrical energy in Italy). Dati generali, 2007. Tech. Rep. (2007), Terna Rete Elettrica Nazionale. *http://www.terna.it/LinkClick.aspx?fileticket=OnkycVUaLqs%3d.*
- [128] “Produzione di energia elettrica in Italia (Electrical energy production in Italy)”, Wikipedia, The Free Encyclopedia, last visit on November 11, 2008. *http://it.wikipedia.org/wiki/Produzione\_di\_energia\_elettrica\_in\_Italia.*
- [129] J. Laffargue, L. Jumau, *Manuel Pratique du Monteur Électricien (Practical handbook for electricians)*, Bibliothèque des actualités industrielles n° 51, Quatorzième édition revue et augmentée par Lucien Jumau. Bernard Tignol, Paris.
- [130] Kaufman, M., *Principle of thermodynamics*. Marcel Dekker, Inc., New York, 2002.
- [131] S. Buso, P. Mattavelli, *Digital Control in Power Electronics*, Synthesis Lectures on Power Electronics. Morgan & Claypool publishers, San Rafael, California, 2006.
- [132] Ferroxcube. Ferroxcube 3C90 Material specification, pages 104–107. Tech. Rep. (September 2008).
- [133] Ferroxcube. Ferroxcube ETD44/22/15 ETD cores and accessories, pages 1–5. Tech. Rep. (September 2008).
- [134] *Safety Standard for Oxygen and Oxygen Systems*, Guidelines for Oxygen System Design, Materials Selection, Operations, Storage, and Transportation, NSS 1740.15. Office of Safety and Mission Assurance. NASA — National Aeronautics and Space Administration, Washington, D.C., January 1996.
- [135] *Safety Standard for Hydrogen and Hydrogen Systems*, Guidelines for Hydrogen System Design, Materials Selection, Operations, Storage, and Transportation, NSS 1740.16. Office of Safety and Mission Assurance. NASA — National Aeronautics and Space Administration, Washington, D.C., February 1997.